Pump asymmetry compensation in an atom-optomechanical hybrid system

Dissertation

zur Erlangung des Doktorgrades
an der Fakultät für Mathematik, Informatik und Naturwissenschaften
Fachbereich Physik
der Universität Hamburg

vorgelegt von
Jakob Jan Butlewski
aus Hamburg

Hamburg
2023

Gutachter der Dissertation:	Prof. Dr. Klaus Sengstock Prof. Dr. Roland Wiesendanger
Zusammensetzung der Prüfungskomission:	Prof. Dr. Roman Schnabel Prof. Dr. Klaus Sengstock Prof. Dr. Roland Wiesendanger Prof. Dr. Ludwig Mathey Prof. Dr. Ralf Riedinger
Vorsitzender der Prüfungskomission:	Prof. Dr. Roman Schnabel
Datum der Disputation:	13.06.2023
Vorsitzender des Promotionsausschusses:	Prof. Dr. Günter H. W. Sigl
Leiter des Fachbereichs:	Prof. Dr. Wolfgang J. Parak
Dekan der Fakultät für Mathematik, Informatik und Naturwissenschaften:	Prof. Dr.-Ing. Norbert Ritter

Abstract

The investigation of hybrid systems consisting of ultracold atoms and micro-mechanical resonators provides access to detection, cooling and quantum control of mechanical motion, which promotes the understanding of the classical to quantum transition and has potential applications in high-precision metrology and quantum-level signal transduction.

In this thesis experiments that couple the vibrational motion of a trampoline resonator inside an optical cavity to the motion of laser cooled ^{87}Rb atoms are presented. The interaction is mediated by a coherent light field that is reflected from the mechanical element and forms a 1D optical lattice at the site of the atoms. An inherent property of such systems is the pump asymmetry in the lattice that arises from this reflection, which can lead to an instability of the hybrid system and deteriorate the coupling for large atomic densities in an attractive lattice potential.

This thesis investigates how the asymmetry in the lattice can be compensated, whether the compensation prevents the occurrence of the instability and if that leads to an increase of the coupling strength. First, a numerical simulation of the system is used to identify the reason for the instability and study the possibility to suppress it by utilizing an additional lattice beam. Subsequently, coupling experiments in attractive and repulsive lattice potentials for different pump asymmetries are presented. The coupling strength is evaluated by means of the sympathetic cooling process and is compared to the performance of our uncompensated repulsive lattice. We observe a suppression of the hybrid instability, which enables coupling experiments in the attractive lattice potential at high atomic densities for the first time. However, we do not witness an improvement of the coupling strength over the asymmetric lattice. This can be seen from the minimal measured mode temperatures $T^{\mathrm{PAC}} = (2.91 \pm 0.66)\,\mathrm{K}$ with pump asymmetry compensation compared to $T^{\mathrm{noPAC}} = (1.50 \pm 0.34)\,\mathrm{K}$ without compensation, where the resonator is initially at room temperature.

Another investigation that was conducted over the course of this thesis is the preparation and tomography of conditional mechanical states using short light pulses. The pulsed interaction takes place on time scales much shorter than the mechanical oscillation period and allows for position measurements with a precision that can surpass the standard quantum limit. The scheme enables the production of squeezed states of mechanical motion and their reconstruction by means of tomography. We performed first pulsed experiments in our system and were able to resolve a width of the mechanical motional state of $\sigma_{\mathrm{cond}} = (137 \pm 4)\,\mathrm{fm}$, which corresponds to the 32-fold width of the ground state of our resonator.

Zusammenfassung

Die Untersuchung hybrider Systeme aus ultrakalten Atomen und mikromechanischen Oszillatoren ermöglicht es, die mechanische Bewegung zu detektieren, zu kühlen und auf dem Quantenniveau zu kontrollieren. Damit fördert diese das Verständnis des Übergangs vom klassischen zum Quantenverhalten und zeigt mögliche Anwendungen in der Hochpräzisionsmetrologie und Einzelquanten-Signalweitergabe auf.
Im Rahmen dieser Arbeit werden Experimente vorgestellt, in denen die Vibrationsbewegung eines Trampolinoszillators innerhalb eines optischen Resonators an die Bewegung von lasergekühlten ^{87}Rb Atomen gekoppelt wird. Die Wechselwirkung wird dabei durch ein kohärentes Lichtfeld vermittelt, das durch Reflexion am mechanischen Element ein 1D optisches Gitter am Ort der Atome bildet. Eine besondere Eigenschaft solcher Systeme ist die aus der Reflexion resultierende Pumpasymmetrie des Gitters. Diese kann für hohe atomare Dichten in einem attraktiven Gitterpotential zur Instabilität des hybriden Systems führen und die Kopplung beeinträchtigen.
Diese Arbeit geht den Fragestellungen nach wie eine Kompensation der Asymmetrie des Gitters möglich ist sowie ob dies den Eintritt der Instabilität verhindert und dadurch zu einer stärkeren Kopplung führt. Dazu wird zunächst in einer numerischen Simulation des Systems die Ursache für die Instabilität identifiziert und die Möglichkeit ihrer Unterdrückung durch Zuhilfenahme eines zusätzlichen Gitterstrahls untersucht. Anschließend werden Kopplungs-Experimente in attraktiven und repulsiven Gitterpotentialen bei unterschiedlichen Pumpasymmetrien vorgestellt. Die Kopplungsstärke wird anhand des sympathetischen Kühlprozesses bewertet und mit dem Verhalten in unserem unkompensierten repulsiven Gitter verglichen. Wir beobachten eine Unterdrückung der hybriden Instabilität, was uns erstmalig ermöglicht Kopplungs-Experimente in einem attraktiven Gitterpotential mit hohen Atomdichten zu realisieren. Allerdings können wir keine Verbesserung der Kopplungstärke gegenüber dem asymmetrischen Gitter feststellen. Dies macht sich in der minimal gemessenen Modentemperatur $T^{\mathrm{PAC}} = (2.91 \pm 0.66)\,\mathrm{K}$ mit Pumpasymmetrie-Kompensation gegenüber $T^{\mathrm{noPAC}} = (1.50 \pm 0.34)\,\mathrm{K}$ ohne Kompensation bemerkbar, wobei der Resonator sich vor der Kopplung bei Raumtemperatur befindet.
Eine weitere Untersuchung, die im Rahmen dieser Arbeit stattgefunden hat, ist die konditionale Zustandspräparation und Tomographie des mechanischen Oszillators mit kurzen Lichtpulsen. Die gepulste Interaktion spielt sich dabei auf Zeitskalen unterhalb der mechanischen Schwingungsperiode ab und ermöglicht Positionsmessungen des Oszillators mit einer Präzision unterhalb des Standard-Quantenlimits. Dabei ist es möglich, gequetschte Zustände der mechanischen Bewegung zu erzeugen und diese mittels tomographischer Methoden abzubilden. Wir haben erste gepulste Messungen in unserem System durchgeführt und konnten den Bewegungszustand des Oszillators mit einer minimalen Breite von $\sigma_{\mathrm{cond}} = (137 \pm 4)\,\mathrm{fm}$ auflösen, was der 32-fachen Grundzustandsbreite des Oszillators entspricht.

Publikationen

Im Rahmen dieser Arbeit sind die folgenden Veröffentlichungen entstanden.

Publications

The following research articles have been published in the course of this thesis.

- P. Rohse, J. Butlewski, F. Klein, T. Wagner, C. Friesen, A. Schwarz, R. Wiesendanger, K. Sengstock and C. Becker: “A cavity optomechanical locking scheme based on the optical spring effect", Review of Scientific Instruments **91**, 103102 (2020), ISSN 10897623.

Contents

Chapter 1

Introduction

For one century quantum physics was a phenomenon reserved for scientists only but has lately become accessible to a broader audience. In the last two or three decades we observed a consequent and continuous evolution towards applications and technologies based on quantum physics. Finally, quantum technology is now highly recognized by the general public and private investors as well as federal funding agencies invest a vast amount of money to accelerate and consolidate this emerging new technological field. The realization of ideas like quantum computing [1–4], quantum communication and cryptography [5, 6], quantum enhanced sensing [7–9] as well as quantum simulation of complex systems [10, 11] have been anticipated for a long time and finally started to become reality. This is accomplished by the rapidly evolving abilities to experimentally manipulate and control quantum dynamics in a variety of systems. These range from photons [12, 13], individual electron and nuclear spins [14–16] over single atoms [17, 18] and ions [19], as well as ensembles of atoms [20] to mesoscopic superconducting [21, 22] and nanomechanical devices [23, 24].

However, the technological progress is confronted with challenges that complicate scaling up the system size and performance and thus hinder the realization of efficient real-world applications. On the one hand, decoherence destroys the produced quantum states and therefore demands decoupling of the systems from their environment [25], for example by placing them in ultra-high vacuum and/or cryogenic environment. On the other hand, each of the aforementioned systems is very well suited to perform a specific task: photons can be conveniently transported over long distances and are therefore ideal to transmit quantum information; weakly interacting spins have long coherence times and may be employed as a quantum memory to store information and the dynamics of electronic states of atoms or electric charges in superconducting elements enable computation and processing of the information that is encoded in their respective quantum states [26]. Yet, for many applications [2, 6] it is desirable to combine storage, processing and transfer of information, which until now, none of the systems is capable to provide on its own.

The solution is to combine different physical systems with complementary functionalities to *hybrid quantum systems* (HQSs), which enable the required multitasking capabilities [27–29]. Early ideas for HQSs were inspired by the field of quantum information processing and communication and suggested coupling of superconducting qubits via a microwave interface [21, 28] to other quantum systems with longer coherence times and

optical transitions [30–36]. Soon, the advances in the control of micro- and nanomechanical resonators [23, 24] qualified these systems also as suitable interfaces [37–40]. Moreover, due to the possibility to design functionalized resonators, which respond to weak electric, magnetic, Van-der-Waals and radiation pressure forces they experienced considerable attention in theoretical proposals that analyse them as hybrid coupling partners [41–48]. Indeed, mechanical resonators turned out to be an excellent constituent of hybrid systems as they are found in numerous experimental realizations, where they are coupled to semiconductor quantum dots [49, 50], spins [51–55], superconducting circuits [56–59] and atomic ensembles [60–65].

In this context, the research focus of our experiment lies on the investigation of a hybrid atom-mechanical system. The combination of these two platforms holds great potential for future hybrid quantum systems [26] and applications in quantum metrology [7, 66]. Due to the high controllability of trapped, ultracold atomic systems and the possibility to prepare them in collective many-body states with long coherence times [67] it is feasible to realize interaction schemes based on coupling to the center of mass motion [45, 68–70] or the total spin of the ensemble [43, 48], as both degrees of freedom can be treated as harmonic oscillators. While the former exhibits oscillation frequencies in the kHz range, governed by the trapping geometry, the latter offers a rich level structure with transition frequencies between the energy levels that range from the MHz to GHz regime. This provides substantial flexibility in the choice of the resonator, depending on the coupling scheme that is employed. Furthermore, both schemes rely on a long-range interaction that is mediated by light and allows to place the individual systems in designated environments. These form closed subsystems that can be modified and investigated independently.
Of special interest for us is the *light-mediated* interaction between the subsystems. While the interaction with light is unavoidable for cooling and trapping of the atoms it can also be exploited for precision measurements of the atomic position or the internal atomic state by mapping these quantities onto a phase shift or an intensity modulation that can be determined using interferometric techniques [66] or sensed by a mechanically compliant element. Analogously, mechanical motion can be influenced by interaction with light via radiation pressure and imprints a phase shift proportional to the mechanical oscillation amplitude onto the light [24]. These phase shifts form the base for the main subject of investigation in this thesis as they are responsible for the mediation of the atom-mechanical interaction.

First related experiments employed the motion of trapped atoms in an optical lattice formed by back-reflection from a mechanical resonator in free space to attenuate its oscillation by dynamical back-action [71]. The light-mechanics interaction was substantially enhanced by placing the resonator inside an optical cavity and enabled the observation of sympathetic cooling of the resonator by laser-cooled atoms [62, 65]. To further increase the coupling strength more atoms were loaded into the lattice, which led to the emergence of a dynamical instability, especially in attractive lattice potentials [72–74]. It prevented approaching the strong coupling regime where the coupling rate exceeds the dissipation in the system. Reaching this regime is of vital importance for the realization of a true quantum hybrid system, as it permits coherent energy

exchange on the single excitation level between the systems. The occurrence of the instability was attributed to light-mediated collective atomic motion in optical lattices - a phenomenon already investigated theoretically in 1D optical lattices [75, 76]. The key point for the appearance of the collective excitation is an imbalanced lattice, which in fact is inherent to all aforementioned atom-resonator coupling experiments. Since the mechanical resonator (in a cavity) exhibits a finite reflectivity (on resonance) the back-reflected lattice beam only carries a fraction of the incident beam's power, which results in an imbalanced lattice.
Consequently, the investigation of the influence of the pump asymmetry (power imbalance) on the collective behaviour in the lattice is of great interest. It bears the answer to the pressing question whether the number of atoms, which participate in the coupling, can be increased and if the instability can be avoided by altering the pump power imbalance. This would potentially enhance the coupling strength and enable to enter the strong coupling regime. In addition it could alleviate the limitations from preceding experiments that aimed at direct coupling of a BEC to the resonator [77]. These prospects motivated us to elaborate a scheme that allows to compensate the reduced power in the back-reflected lattice beam by utilizing an auxiliary lattice beam.

In this work we utilize a numerical simulation to investigate how the phase modulation introduced by the motion of the mechanical resonator affects the response of the atoms in the optical lattice and how this response changes with the pump asymmetry. We identify a transition from a stable operating regime towards the hybrid instability. The stable regime is characterized by an out-of-phase backaction from the atoms onto the resonator, whereas the instability regime is governed by a detrimental phase lag of the

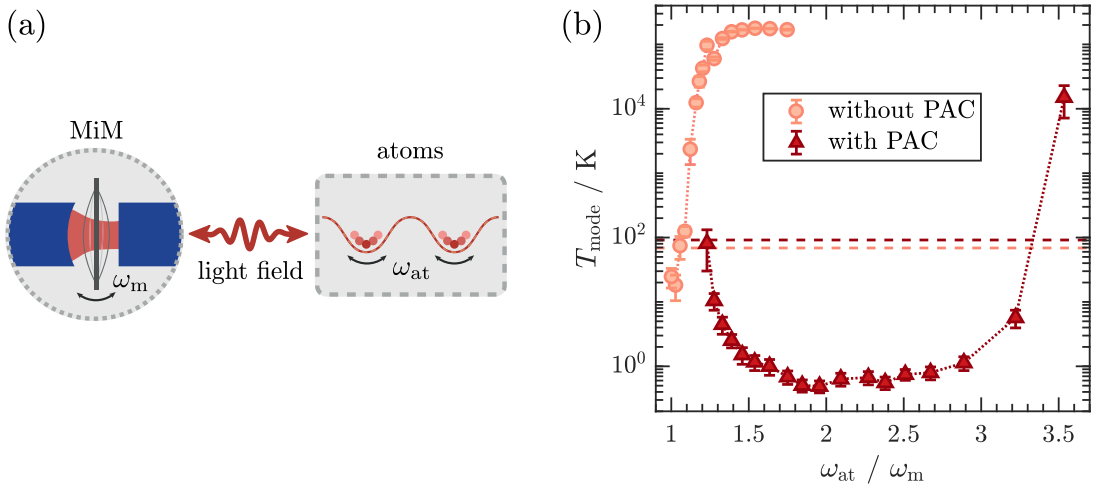

Figure 1.1: Sympathetic cooling in attractive lattice potential with and without pump asymmetry compensation. (a): Sketch of the light mediated interaction between the membrane in the middle (MiM) system and the atomic system. For resonant coupling the mechanical and atomic oscillation frequencies must coincide $\omega_m = \omega_{at}$. **(b):** Mode temperature T_{mode} of the mechanical resonator during a coupling experiment as a function of the lattice depth. The lattice depth is expressed by means of the atomic trapping frequency ω_{at} in units of the resonator frequency ω_m. Detailed description follows in chapter 3.

backaction response ultimately leading to exponential heating of the resonator. We further show that an auxiliary lattice beam can be used to contribute to the stabilization of the lattice for increasing atom numbers. Motivated by this theoretical investigation we examine the capability of the auxiliary lattice beam to stabilize the lattice also in the experiment. We compare the performance of the initial asymmetric lattice to the lattice with pump asymmetry compensation (PAC) and find that the auxiliary lattice beam indeed enables coupling experiments in certain lattice configurations that did not allow for sympathetic cooling before (see figure 1.1). However, the lattice configuration with the highest coupling rate turns out to be still asymmetric after all and does not suffice to enter the strong coupling regime, which would enable ground state cooling.

An alternative route to prepare the mechanical resonator in a quantum state, can be achieved without participation of atoms in the process. An exceptional feature of our MiM system is its very large linewidth κ that exceeds the resonator frequency by orders of magnitude ($\kappa \gg \omega_\mathrm{m}$) and places the system far in the unresolved sideband regime [24]. This allows to probe the resonator motion instantaneously in a pulsed rather than a continuous manner by utilizing pulse lengths τ much shorter than the resonator's oscillation period ($\tau \ll 2\pi/\omega_\mathrm{m}$). The benefit of such a snap-shot of the mechanical motion, is that the back-action introduced by the measurement pulse is completely transferred to the unmeasured momentum quadrature, thus yielding a quantum non-demolition measurement [78]. By using multiple, accurately timed pulses it is even possible to reduce the entropy of the mechanical state as was proposed and experimentally verified already [79, 80]. This technique allows to determine the resonator position within one oscillation period with an accuracy better than the zero-point motion of the resonator, which is equivalent to an effective phonon occupation below unity. Moreover, it provides a method to fully reconstruct the motional quantum state of the resonator by means of tomography. This poses one of the most promising routes in optomechanics to explore non-classicality at a macroscopic scale [81].

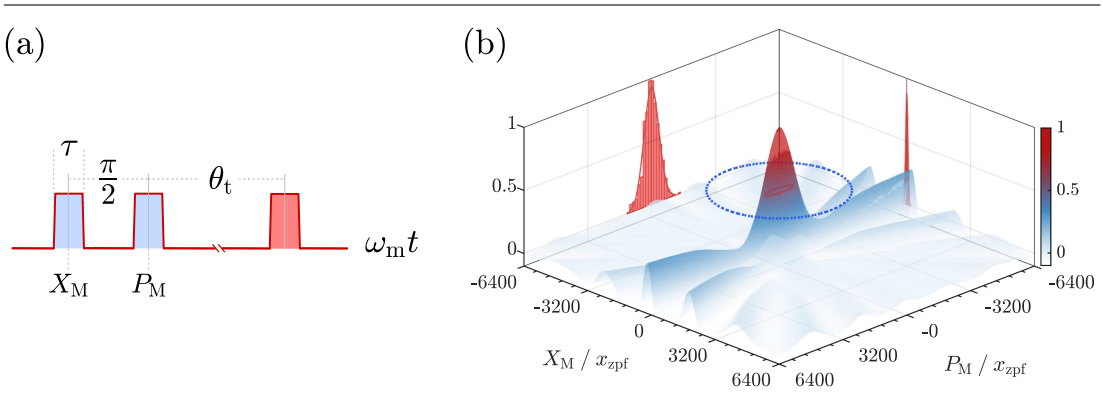

Figure 1.2: Reconstructed conditional mechanical state after pulsed preparation. **(a):** Utilized pulse scheme for conditional state preparation and measurement. Two pulses of duration $\tau \ll 2\pi/\omega_\mathrm{m}$ separated by a quarter mechanical oscillation period $\pi/2$ are used for the state preparation. A third pulse after variable time t measures the state at the tomography angle $\theta_\mathrm{t} = \omega_\mathrm{m} t$. **(b):** Reconstructed mechanical state after state tomography. The pulsed preparation scheme reduced the width of the conditional state (red ellipse) below the width of the initial thermal state (blue circle). Detailed description follows in chapter 4.

We investigate the applicability of this measurement scheme to our experimental setup and present the necessary modifications. Further, we present the first results of a pulsed position measurement in our MiM system in form of a tomographic reconstruction of the motional state.

The thesis is structured as follows:

Ch. 2 – The atom-optomechanical hybrid system

The second chapter introduces the experimental setup of our hybrid atom-mechanical system. It gives a general overview of all relevant techniques and parts of the setup that are used for the measurements presented in the subsequent chapters. Moreover, it contains an investigation of the observable Faraday rotation in our atomic ensemble that could potentially be used as an interface for coupling to atomic spin states.

Ch. 3 – Coupling experiments in a pump asymmetry compensated lattice

The third chapter covers our approach to compensate the pump asymmetry in our optical lattice to avoid the hybrid instability. After a brief introduction about the employed sympathetic cooling mechanism the theoretical aspects of asymmetrically pumped 1D optical lattices are presented and the necessity to compensate the asymmetry in our system is motivated. From these considerations a numerical simulation is derived that illustrates the origin of the hybrid instability. Furthermore, the setup of the auxiliary lattice is presented and characterized. Finally, the sympathetic cooling in the compensated lattice is compared to the uncompensated case.

Ch. 4 – From continuous to pulsed preparation and measurement

In the final chapter the concept of pulsed optomechanics and conditional state preparation is introduced. The relevant changes to the experimental setup are discussed and characterized, followed by the presentation of the first conditional state preparation and reconstruction results that were obtained in our MiM system.

Chapter 2

The atom-optomechanical hybrid system

This chapter describes the experimental setup of our hybrid atom-optomechanical system, which consists of ultra-cold ^{87}Rb atoms coupled to a cryogenic MiM device via laser light. In the following, all parts of the system that are relevant for the measurements presented in subsequent chapters are introduced. The chapter closes with an investigation of the observable Faraday rotation in our setup that could potentially be used for hybrid coupling to atomic spin degrees of freedom.

Ultra-cold atoms and mechanical resonators are particularly versatile platforms and therefore remarkably well suited as constituents for the creation of a hybrid system. Each system on its own is a fascinating subject that can be formed and manipulated in multiple ways and is capable of displaying quantum features when prepared in the right way. Although both systems are of very different nature the combination of both allows to exploit their individual assets. For the atoms a plethora of methods to manipulate their internal states e.g. optical pumping [82] or radio-frequency techniques [83], their interaction strength with magnetic fields via Feshbach-resonances [84], as well as their motional states by trapping in strong dipole potentials [85], e.g. optical tweezers or lattices [86] are at hand. They allow for the preparation of the atoms in various quantum states [67], which enabled implementing entanglement [87], non-classical motional states [88] and a quantum memory [89] in ultra-cold atomic systems. Mechanical resonators on the other hand can be specifically designed to exhibit certain resonating modes or band gaps, depending on their shape and size, that are tailored to the individual experimental requirements [90]. Moreover, their design influences the possible coupling mechanisms that can be applied. Their miniature size renders the observation of quantum effects on macroscopic objects feasible [91, 92], possibly even at room temperature [93–95].
In the following sections the individual parts of our experimental setup will be discussed. The focus will lie on subjects that are related to the investigations presented later or that were changed or added during the course of this thesis. For more details on the initial design considerations see [74, 77, 96, 97].

2.1 Cold atom apparatus

In our experiment we use a ^{87}Rb machine for the preparation of ultra-cold atoms that was planned and set up by A. Bick and C. Staarmann [96, 97]. Here, the main features of the machine shall be outlined.
In order to achieve a considerable coupling strength in a coupling scheme based either on internal or external degrees of freedom, a large number of atoms that participate in the coupling is necessary. The machine was designed to produce samples with large atom numbers in a magneto optical trap (MOT) or a Bose-Einstein condensate (BEC) in a robust way and with short cycle times. This is realized in a 2D/3D MOT configuration that has proven to be very successful in our group. It provides high vapour pressures in the 2D MOT and therefore allows for fast loading rates in the 3D MOT. At the same time excellent background pressure conditions in the 3D MOT region can be maintained that are required to increase the lifetime of the later produced BECs. The atoms are cooled on the D_2 line $|5^2S_{1/2}, F = 2\rangle \rightarrow |5^2P_{3/2}, F' = 3\rangle$, which does not provide a closed cycle. Therefore, an additional repumping laser is employed. A scheme of the laser system used for cooling and detection of the atomic sample is depicted in figure 2.1. The experimental apparatus is placed on a vibration isolated optical table next to the cryostat and provides excellent optical access (300 degrees) for the preparation and control beams. An overview drawing of the ^{87}Rb machine is shown in figure 2.3.

2D/3D MOT setup. The UHV environment for the preparation of the atoms consists of two glass cells on top of each other, separated by a differential pumping stage that

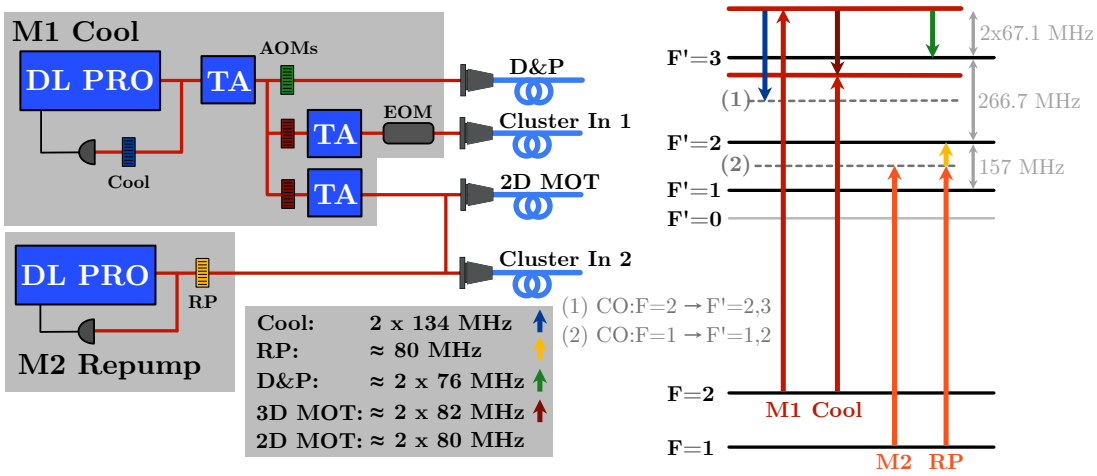

Figure 2.1: Sketch of the laser system used for cooling and detection of ^{87}Rb. The laser system consists of two master lasers, one for cooling and one for repumping of the atoms. Both are locked via Doppler-free absorption spectroscopy to crossover transitions (dashed lines on the right). The cooling laser seeds a tapered amplifier (TA), whose output is split in a detection and pushing branch (D&P) and further amplified in a 2D MOT branch and a 3D MOT branch (Cluster In 1). The repumping laser is split and coupled into separate fibers for the 2D MOT and the 3D MOT (Cluster In 2). In the experiment detection and pushing beams are coupled into separate fibers as well. The frequencies of the respective beams are tuned using AOMs either in single or double pass configuration.

allows for pressure differences of up to three orders of magnitude between the cells. In the first stage the atoms are trapped from a background gas in a 2D MOT formed by two retro-reflected, elliptical beams (see panel (a) in figure 2.3). Next, the atoms are transferred through the pumping stage into the lower glass cell ($p < 1 \cdot 10^{-11}$mbar) using a near resonant pushing beam and caught in a 3D MOT (see panel (b) in figure 2.3). The lower glass cell is surrounded by a set of large water-cooled coils to generate magnetic fields for the MOT and the magnetic trap as well as three pairs of compensation coils, one for each spatial direction [96].

BEC in the magnetic trap. A typical experimental sequence is depicted in figure 2.2 and takes less then 30 s. The 3D MOT is loaded for less then 10 s and collects $N_{\mathrm{MOT}} \approx 1 \cdot 10^{10}$ atoms with a temperature close to the Doppler temperature $T_{\mathrm{D}} = \hbar\Gamma/2k_{\mathrm{B}} = 146\,\mu\mathrm{K}$. Subsequently, the atoms are further cooled in an optical molasses to $T_{\mathrm{mol}} \approx 10\,\mu\mathrm{K}$ and loaded into an isotropic magnetic trap overlapped with a homogeneous Helmholtz field (hybrid 4D-cloverleaf trap [97]). The trap is then compressed by lowering the homogeneous field and the atoms are cooled for 15 s by radio-

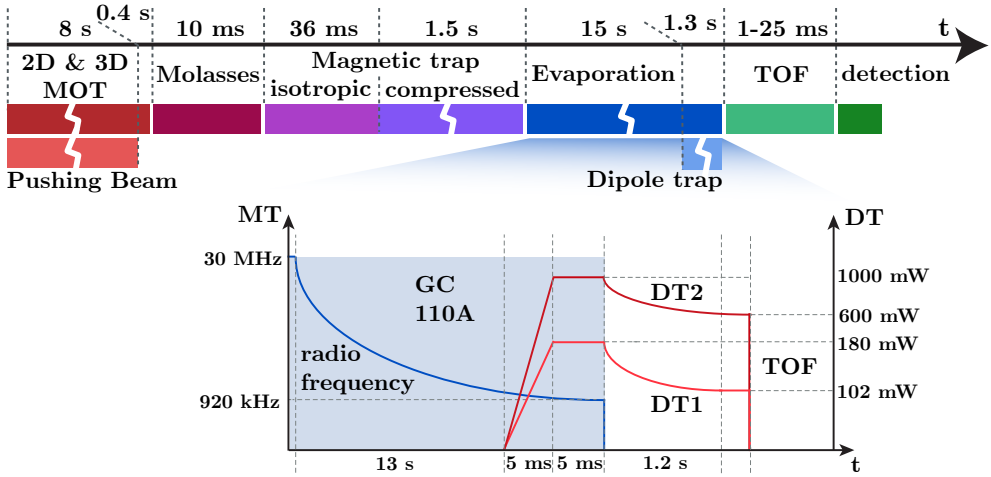

Figure 2.2: Experimental sequence to produce a ^{87}Rb BEC in the magnetic or dipole trap. The atoms are transferred by means of the resonant pushing beam from the 2D MOT to the 3D MOT. After a short molasses phase for sub-Doppler cooling the atoms are loaded into the isotropic magnetic trap which is subsequently compressed for the radio-frequency evaporation stage. Either the evaporation is performed until a BEC is obtained in the magnetic trap, or the atoms are loaded into an optical dipole trap before the end of the evaporation ramp where a second, optical evaporation phase takes place. At the end of the evaporation the atoms are released from the trap and imaged after a variable time-of-flight (TOF) phase. The lower part depicts a more detailed view of the production of a BEC in the dipole trap. The shaded area shows the initial radio-frequency evaporation phase in the magnetic trap (MT). The final frequency of 920 kHz is slightly higher than the typical value for creating a BEC in the MT (typically 860 kHz). Shortly before switching of the gradient coils (GC) of the MT, the dipole trap (DT) beams DT1 and DT2 are ramped up to a power of 180 mW and 1 W, respectively. After the radio-frequency sweep is finished the MT is switched of and a second evaporation stage in the dipole trap is performed by exponentially ramping down the beam powers. Subsequently, the DT is switched of and the atoms are imaged after a variable TOF phase.

frequency evaporation to quantum degeneracy. The resulting BECs have a particle number of $N_{\mathrm{BEC,MT}} \approx 1.4 \cdot 10^5$ without any noticeable thermal fraction.

BEC in the dipole trap. For experiments aiming at the coupling of internal atomic degrees of freedom to a mechanical resonator the atoms need to be held in a state independent trapping potential. We realize this potential through a far red detuned, crossed optical dipole trap (see panel (c) in figure 2.3), which is also convenient for pure BEC experiments and characterization measurements like the calibration of the coupling lattice (section 2.2.1). The trapping beams have circular beam waists of $\mathrm{w_{DT1}} = 52\,\mu\mathrm{m}$ and $\mathrm{w_{DT2}} = 242\,\mu\mathrm{m}$ and are derived form a Nd:YAG laser operating at $\lambda_{\mathrm{DT}} = 1064\,\mathrm{nm}$. The experimental sequence for the creation of a BEC in the dipole trap is similar to the sequence for a magnetic trap BEC (see figure 2.2). Before the end of the evaporation phase in the magnetic trap, the atoms are loaded into the dipole trap and the radio-frequency evaporation stops at a slightly higher frequency. The magnetic trap is switched off and the final evaporation step is performed solely in the dipole trap by lowering the beam intensities exponentially until a BEC with a particle number of $N_{\mathrm{BEC,DT}} \approx 7 \cdot 10^4$ without any noticeable thermal fraction remains. The potential of the dipole trap leads to an elongated cigar like shape of the BEC and exhibits radial trapping frequencies of $(\omega_y, \omega_z) = 2\pi \cdot (144, 105)\,\mathrm{Hz}$, where gravity points along the z-direction (for $P_{\mathrm{DT1}} = 100\,\mathrm{mW}, P_{\mathrm{DT2}} = 1\,\mathrm{W}$). Due to the larger waist of beam DT2, compared to DT1, the axial trapping frequency along the x-direction is only $\omega_x \approx 2\pi \cdot 12\,\mathrm{Hz}$ and can be tuned by adjusting the power of beam DT2 after evaporation. In this way atomic samples that are elongated along the x-direction of the almost co-propagating coupling beam can be realized. A BEC that is held in the dipole trap after evaporation has a lifetime of $\tau_{1/e} \approx 17\,\mathrm{s}$.

2.2 Coupling and detection laser system

The link that connects the two constituents of our hybrid atom-mechanical system is the light field that produces the long-range interaction. Both the coupling beam and the detection beam, which is used to measure the mechanical displacement, are derived from the same dedicated laser system. It is based on a titanium-sapphire laser (TiSa) with a wide wavelength tuning range including the D_2 line ($\lambda_{\mathrm{air}} = 780.0\,\mathrm{nm}$) and the D_1 line ($\lambda_{\mathrm{air}} = 794.8\,\mathrm{nm}$) [98] of the ^{87}Rb atoms that makes it applicable for different coupling and detection schemes of the cold atoms. A sketch of the laser system is depicted in figure 2.4. The TiSa is locked internally using an etalon dither lock and a temperature-isolated reference cavity to increase its stability. Since we are working at a detuning $|\Delta_{\mathrm{at,L}}| \lesssim 1\,\mathrm{GHz}$, close to the atomic resonance, small frequency drifts of the laser change the lattice depth experienced by the atoms [85]. To allow for an absolute frequency stability, the TiSa can be locked to a transfer cavity (linewidth $\approx 3\,\mathrm{MHz}$) via a Pound-Drever-Hall (PDH) lock, visible in the top line of figure 2.4. A homebuilt electro-optic modulator (EOM) creates the necessary sidebands at $\approx 10\,\mathrm{MHz}$.
Using a small amount of the ^{87}Rb cooling light, which already has sidebands from a PDH lock to the atomic transition, the transfer cavity itself is stabilized to the cooling

laser. The TiSa can therefore be locked to the atomic resonance in units n_{FSR} of the transfer cavity's free spectral range (FSR), which further improves the lasers short-term frequency stability to below 1 MHz. By locking the laser to every FSR from $n_{\mathrm{FSR}} = -9$ to $+6$ with respect to the cooling laser and measuring the beat signal of the two, the FSR was determined using a linear fit to [96]:

$$\Delta\nu = n_{\mathrm{FSR}} \times (997.544 \pm 0.004)\,\mathrm{MHz} \tag{2.1}$$

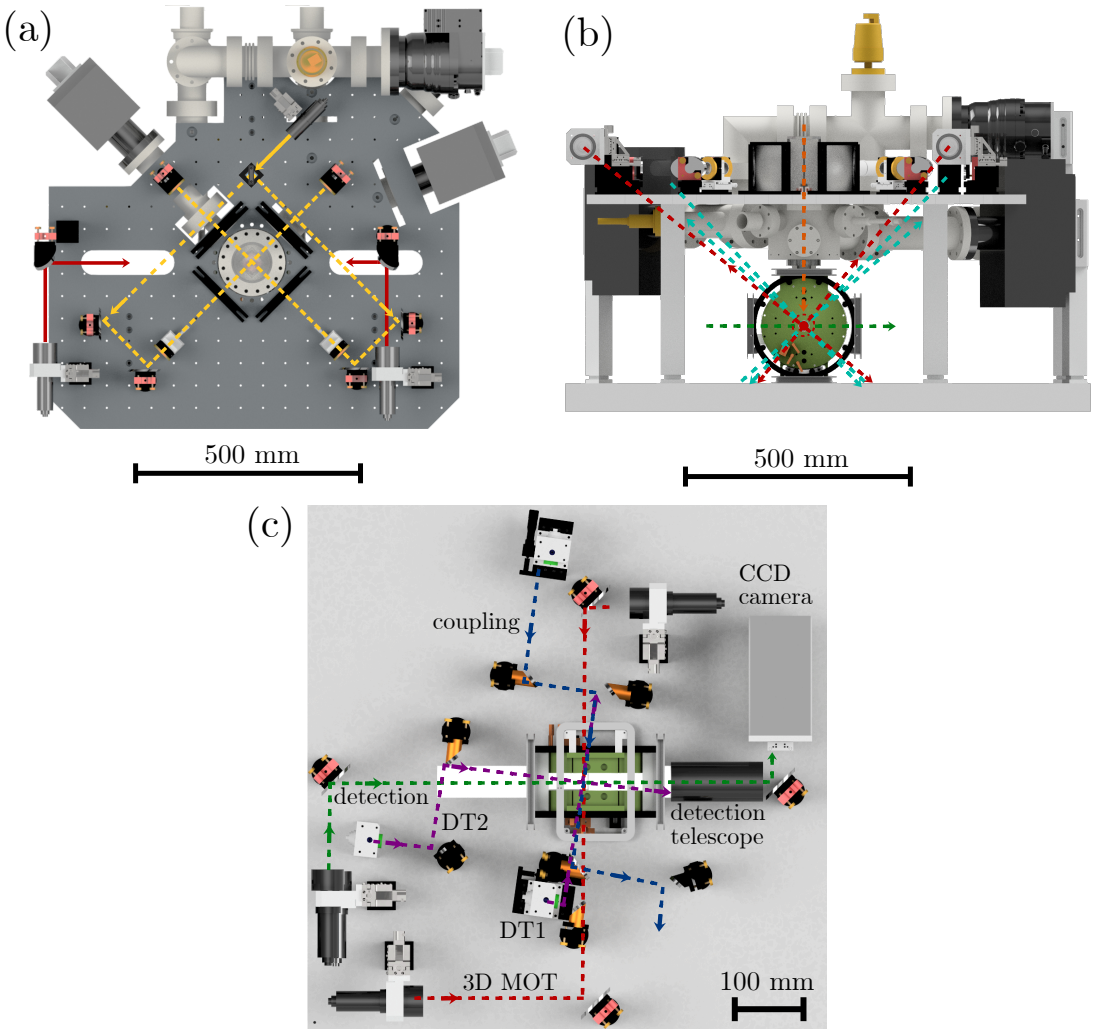

Figure 2.3: Drawing of the experimental apparatus to produce a ^{87}Rb BEC. (a) Top view of the 2D MOT breadboard. Yellow lines depict the 2D MOT beam path. The beams are expanded to an elliptical shape by cylindrical telescopes and back-reflected after passage through the glass cell. Red lines depict the 3D MOT beams. **(b)** Side view showing the upper glass cell and lower glass cell surrounded by the magnetic trap (green housing). A compensation coil cage is placed around the magnetic trap. The coloured lines depict the respective beams: red - 3D MOT beams, orange - pushing beam, green - detection beam for absorption imaging and cyan - 2D lattice in bowtie configuration. **(c)** Top view of the lower 3D MOT breadboard. The purple lines show the two perpendicular dipole trap beams DT1 and DT2 and the blue line depicts the coupling lattice that propagates under a small angle to the DT1 beam. The green beam denotes the detection beam and red shows the axial 3D MOT beams.

When the transfer lock is not used the laser frequency is subject to a slow drift on the order of 50 MHz per hour. However, if needed the frequency can be held stable within 5 MHz by manual readjustment of the locking electronics, where the accuracy is limited by the digital quantization of the used wavemeter. Most of the experiments presented in this thesis were performed without the transfer lock, as it proved to be more convenient to tune the lattice depth by varying the detuning of the lattice rather than the power due to the power dependent optical spring effect. Nevertheless, the transfer-lock is an essential tool for the lattice depth calibration that has to be performed on a daily basis, as the reading of the wavemeter is prone to temperature and humidity drifts.
The main laser output is divided into three branches (see figure 2.4):

Coupling beam - The coupling between atoms and mechanical resonator is mediated by a 1D optical lattice that is created by back-reflection of the coupling beam off the resonator inside the cavity. The beam can be intensity controlled using a home-built analog control box, which stabilizes the signal from a photodiode to an analog reference signal by application of feedback on the radio-frequency (RF) input of the coupling beam acousto-optic modulator (AOM). This is established by modulating the DC component of the 80 MHz sinusoidal RF drive signal with the control signal via a mixer before feeding it to a high power AOM amplifier. The analog reference signal is supplied by the experiment control and can be used to stabilize the lattice power P_{lat} or ramp it between desired values. Using a fast RF-switch in the RF signal path of the AOM driver the lattice light can be rapidly switched on and off, which enables to create short light pulses with minimum durations on the order of 100 ns and a cycle-to-cycle pulse power stability of 0.3 % [74]. Such pulses allow for the alignment of the lattice by Kapitza-Dirac diffraction or for non-adiabatic lattice loading as described in [77]. The coupling light is guided to the experiment through a single mode fiber that is mounted in a fiber polarization controller (FPC). Using a polarizing beam splitter (PBS) after the fiber we can split off a fraction of the beam power to derive the auxiliary beam (see section 3.4.1). The coupling light then passes the atomic sample and is coupled into another single mode (SM) fiber that guides it to the cavity inside the cryostat. Again, a FPC is used to adjust the polarization of the back-reflected lattice beam. The intensity of the back-reflex can then be monitored on a dedicated photodiode.

Feedback beam - The feedback beam is used to apply an optical damping force to the mechanical resonator that reduces its kinetic energy. It is guided to the experiment in a polarization maintaining (PM) fiber and passes a fiber-optic amplitude modulator. The beam can be intensity controlled via the bias input of the modulator and is always locked to the 50 % working point[1]. The signal that is used to drive the intensity modulation at the RF input is derived from the homodyne signal. The beam is then coupled to the MiM system via an SM fiber and enters the cavity from the curved side.

Homodyne beam - To determine the mechanical displacement and measure the state of the mechanical resonator with interferometric precision we apply a phase-sensitive

[1] Point between the minimum and maximum transmission of the modulator where the largest modulation depth can be achieved.

homodyne detection scheme. The detection beam can be intensity controlled via an AOM in a similar way as described for the coupling beam. It is guided by a PM fiber to the experiment and is split there into a local oscillator (LO) and a signal beam. The signal beam is coupled into the fiber cavity with its polarization perpendicular to the polarization of the coupling beam. Upon reflection from the resonator the beam collects a phase that is modulated at the resonator frequency. After returning from the cavity the signal beam is mixed with the LO on a PBS. At a subsequent PBS the superimposed beams are split with equal contributions to be measured on a balanced photo detector[2]. A piezo-mirror is used to adjust the relative phase between signal and LO beam that determines which quadrature component is measured. The resulting signal is fed to a lock-in amplifier and is used to derive the feedback cooling signal as well as the error signal for the optical spring lock (see section 2.3.2). For the pulsed optomechanics experiments we introduced a fiber-optic amplitude modulator in the homodyne branch as well, as we will need it for the generation of short light pulses with arbitrary spacing and shape (see chapter 4).

[2]HCA-S from *Femto*, bandwidth DC...1 MHz, gain 28.5 kV/W, NEP 1.1 pW/$\sqrt{\text{Hz}}$

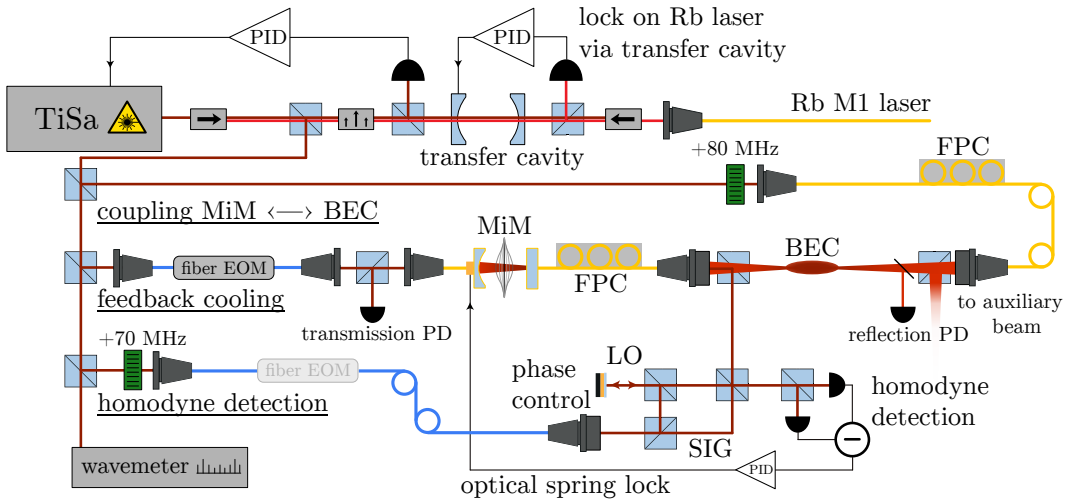

Figure 2.4: Laser system for coupling and detection of the MiM device. The TiSa laser (MBR 110 from *Coherent* - pumped by Verdi V18 from *Coherent*) can be locked relative to the ^{87}Rb D_2 line by use of a transfer cavity (FPI 100 from *Toptica*), which is locked to the M1 cooling laser of the rubidium laser system. From the laser three branches are derived: (1) the coupling beam that interfaces the mechanical resonator in the MiM device with the ^{87}Rb atoms, (2) a feedback cooling beam for optical damping of the resonator, (3) a beam for balanced homodyne detection of the resonator motion. A wavemeter (WS6-600 from *HighFinesse*) is employed to monitor the TiSa wavelength. The coupling and homodyne beam are both frequency shifted by 80 MHz and 70 MHz with AOMs, respectively. The AOMs are also used for intensity control of both beams. Coupling and homodyne beam are coupled with perpendicular polarizations from the planar side into the cavity, which allows a better mode match with the cavity field [74, 99] and a steeper phase response as a function of the cavity-light detuning [96]. All depicted cubes are polarizing beam splitters - wave plates are omitted for clarity.

2.2.1 Coupling lattice setup

For the realization of a resonant interaction between the mechanical resonator and the atomic sample the atomic trapping frequency ω_{at} along the 1D lattice has to be matched to the mechanical resonance frequency $\omega_{\mathrm{m}} \approx 2\pi \cdot 154\,\mathrm{kHz}$. For optical lattices the lattice depth is commonly quoted in units of the recoil energy [98]

$$E_{\mathrm{rec}} = \frac{\hbar^2 k_{\mathrm{lat}}^2}{2m_{\mathrm{Rb}}} \tag{2.2}$$

of the used atomic species, where m_{Rb} denotes its mass and $k_{\mathrm{lat}} = 2\pi/\lambda_{\mathrm{lat}}$ is the wave number of the lattice light. Each lattice well can be approximated by a harmonic potential with a trapping frequency

$$\omega_{\mathrm{at}} = \sqrt{\frac{2V_{\mathrm{lat}}k_{\mathrm{lat}}^2}{m_{\mathrm{Rb}}}}, \tag{2.3}$$

which results in a trap depth of $V_{\mathrm{lat}} \approx 411 E_{\mathrm{rec}}$, if the resonance condition $\omega_{\mathrm{at}} = \omega_{\mathrm{m}}$ is met. This is a very deep lattice that can be realized with various combinations of laser power and detuning. Commonly, far detuned lattices are used, which would require several hundred milliwatts of laser power. Due to the fact that our lattice is created by retro-reflecting a laser beam from an object in a cryogenic environment, we can not afford such high powers as they would massively heat up the MiM system. Therefore, we are limited to lattice powers $P_{\mathrm{lat}} < 1\,\mathrm{mW}$. As the lattice depth scales as $V_{\mathrm{lat}} \propto I_0/\Delta_{\mathrm{at,L}}$, where I_0 is the peak intensity of the laser beam and $\Delta_{\mathrm{at,L}}$ the detuning of the laser from the atomic resonance, we can reach the needed lattice depth by using near-resonant light. In our experiments we use a detuning on the order of $\Delta_{\mathrm{at,L}} \lesssim 1\,\mathrm{GHz}$ and a small waist size $\mathrm{w}_{\mathrm{lat}} = 76\,\mu\mathrm{m}$ of the lattice beams to increase the intensity at the position of the atoms.

Optical setup: The experimental setup of the coupling lattice is shown in figure 2.5. It depicts the lattice setup that was used in [74, 77] and forms the basis of our study of the asymmetric coupling lattice. For the experiments performed during the course of this thesis several changes have been made to the setup that will be described in detail in section 3.4.1. The coupling beam is derived from the TiSa laser and frequency shifted by 80 MHz using an AOM. This allows for ramping and regulating the beam intensity along with fast switching ($\tau_{\mathrm{r,f}} \approx 50\,\mathrm{ns}$) for the generation of short light pulses. For total light extinction the beam can be blocked with a shutter before it enters the PM fiber that guides it to the experiment, which is crucial to avoid near resonant photon scattering during the BEC cycle. At the experiment the coupling beam is then shaped by a telescope that consists of a collimating lens, a PBS for polarization cleaning and a focusing lens that result in a working distance of $\approx 50\,\mathrm{cm}$. For fine adjustment of the focal position with respect to the position of the BEC in the optical dipole trap, the telescope is mounted on a translation stage that allows to move it along the direction of the outgoing beam. The lateral alignment is done with differential micrometer screws at the dichroic mirror in front of the glass cell. In contrast to the second dichroic mirror behind the glass cell this mirror substrate is coated in-house to have a reflec-

tivity of $R_{780} = 9.7\,\%$ at 780 nm, which allows for picking up the transmitted light for the intensity control of the beam. Since the reflectivity of the substrate proved to be slightly wavelength dependent we use a second identical substrate in front of the intensity control PD to suppress this parasitic effect. Otherwise the calibrated control signal would yield deviant lattice powers at the site of the atoms for changing wavelengths. The dichroic mirrors are needed to transmit the optical dipole trap beam DT1 ($\lambda_{\mathrm{DT}} = 1064\,\mathrm{nm}$), which is aligned almost parallel to the coupling beam, while the coupling light is reflected. After passing the glass cell the beam is coupled into a PM fiber that leads to the cryostat using an identical telescope as on the incident side. Again the telescope is placed on a translation stage and a differential mirror holder is employed to allow for fine alignment of the back-reflected beam. Via the reflection port of the PBS in the cryostat telescope the homodyne beam is superimposed with the lattice beam and coupled into the cryostat fiber, whose end forms the planar side of the fiber cavity. After reflection from the fiber cavity in the MiM device both beams leave the telescope through their respective ports.

The back-reflected coupling beam interferes with the incident beam and forms an 1D optical lattice at the position of the atoms. Considering the fiber coupling efficiency, optical losses at the optics as well as the finite reflectivity on resonance $\sigma_{\mathrm{cav}} = 0.54$ of the cavity one finds that only $\approx 30\,\%$ of the incident light are reflected back onto the atoms. This is an inherent property of our experimental setup and leads to the instability that will be discussed in detail in section 3.4.1.
The fraction of the back-reflected beam that is transmitted through the 10/90 substrate is monitored on the lattice back-reflex photodiode. This signal is used for monitoring the coupling efficiency into the cryostat, the cavity signals (cavity alignment, tuning on resonance, cavity length measurement, etc.) and the time evolution of the lattice power during experimental cycles.
Not shown in figure 2.5 is the additional 2D lattice that can be applied in the plane perpendicular to the direction of the coupling lattice. It is formed by two beams with $\lambda_{2D} = 1064\,\mathrm{nm}$ and was used in experiments performed with T. Wagner [77] to counteract the heating of the BEC in the dipole trap by scattering of blue detuned coupling lattice photons and enabled to see a coupling effect of the resonator motion to a BEC.

Lattice alignment: To make sure that the lattice is optimally aligned within the MOT we use a BEC for the alignment, as it is produced approximately at the center of the MOT and allows for a much more precise adjustment, due to its small size of only a few micrometers. The alignment is performed by blocking the cryostat telescope port, such that no coupling light is back-reflected. Next the coupling beam is adjusted to be red detuned by $\Delta_{\mathrm{F=3}} \approx -250\,\mathrm{GHz}$ and the power is set to $P_{\mathrm{lat}} = 3\,\mathrm{mW}$. With this settings the coupling beam exhibits a strong enough attractive potential to pull the BEC out of the dipole trap if it is close enough[3]. After evaporation in the dipole trap the coupling beam is switched on for 2 ms and subsequently all optical potentials are switched off. The atoms are imaged after 20 ms time of flight. If the coupling beam

[3]For the rough alignment blue detuned light can be used to maximize the losses in the BEC due to the repulsive dipole potential.

is not well aligned the atoms are pulled out of their position in the dipole trap. The alignment of the coupling beam is optimal, when its influence on the BEC position (compared to the position without lattice pulse) is minimal. Once the incident beam is properly aligned the light has to be coupled into the cryostat fiber. When the fiber coupling is optimized the alignment onto the atoms is continued using the Kapitza-Dirac diffraction method described in [74, 77, 100]. One should already see a diffraction pattern when short lattice pulses are applied. From here the alignment is optimized by maximizing the Kapitza-Dirac diffraction into the first momentum order, while slightly readjusting the fiber coupling.

Lattice depth calibration: In order to calibrate our lattice depth we use Kapitza-Dirac diffraction measurements. For that, a BEC is prepared and held in the dipole trap and subsequently irradiated using short pulses of lattice light with variable duration on the order of tens of microseconds. During that process photons from either lattice beam are redistributed into its counter-propagating correspondent, which leads to a

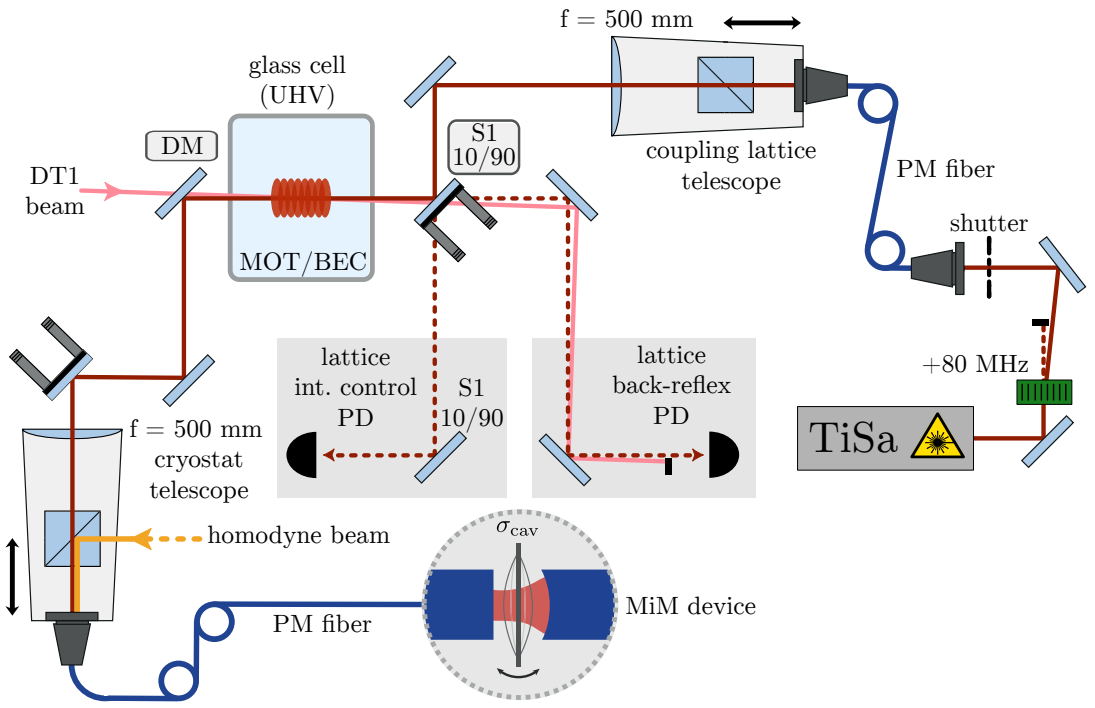

Figure 2.5: Coupling lattice setup. Sketch of the setup for the 1D lattice for coupling ultracold atoms to a mechanical resonator in a MiM system. The light from the TiSa is blue shifted 80 MHz by an AOM and coupled to a PM fiber that is connected to the incident beam telescope (fiber collimator 60FC-L-4-M20L-02 with beam $\varnothing = 3.6$ mm and focusing lens 13M-S500-05-S from *Schäfter+Kirchhoff*, working distance: 49.2 cm). The telescope is mounted on a translation stage for fine adjustment of the distance to the BEC. The beam is aligned onto the BEC with dichroic mirrors that allow transmission of the optical dipole trap beam DT1, which propagates almost parallel to the coupling lattice. For lateral fine alignment of the lattice beam mirror mounts with differential micrometer screws are used. After passing the glass cell the beam is coupled through an identically constructed telescope to the cryostat fiber (AR coated end-facet for improved incoupling efficiency). Figure adapted from [100].

momentum transfer of two times the lattice light's photon momentum

$$\Delta p = \pm 2 p_{\mathrm{lat}} = \pm 2 \hbar k_{\mathrm{lat}} = \pm 4 \pi \hbar / \lambda_{\mathrm{lat}}. \tag{2.4}$$

During the interaction time the atoms experience Rabi oscillations between different momentum orders. Hence, for varying interaction time their momentum distribution changes. The atoms are released from the trap at the end of the lattice pulse and their momentum distribution after the interaction is measured using time of flight imaging (see upper panel in figure 2.6). For deeper lattices also higher order scattering processes ($p = n\Delta p$, $n \in \mathbb{N}$) start to become important. Since their Rabi frequencies differ, the resulting interference of all the coherent scattering processes leads to a non-trivial evolution of momentum orders. By evaluating the distribution of atoms across all different momenta as a function of the atom-lattice interaction time the lattice depth $s = V_{\mathrm{lat}}/E_{\mathrm{rec}}$ can be extracted [101, 102]. For that, the solution of the time dependent Schrödinger equation for a matter wave (BEC) in a periodic potential (1D-lattice) is calculated numerically and fitted to the distribution of the momentum orders (see lower panel in figure 2.6) [74, 102].
We use measurements at moderate lattice depths $V_{\mathrm{lat}} \lesssim 30\, E_{\mathrm{rec}}$ to extrapolate them to higher lattice depths as a function of lattice power and detuning. As in our system the intensities of the counter-propagating lattice beams are not equal and can change independently from each other (e.g. by tuning the the MiM cavity on resonance) we need a model that includes the near resonant detuning, the incident lattice beam power P_{inc} and the reflected power P_{ref} [85, 98, 102]:

$$V_{\mathrm{lat}} = \frac{4c^2\sqrt{P_{\mathrm{inc}} P_{\mathrm{ref}}}}{\mathrm{w_{inc}} \mathrm{w_{ref}}} \left[\frac{\Gamma_{\mathrm{D_1}}}{\omega_{\mathrm{D_1}}^3} \frac{1}{\Delta_{\mathrm{D_1}}} + 2 \frac{\Gamma_{\mathrm{D_2}}}{\omega_{\mathrm{D_2}}^3} \left(\frac{1}{20 \Delta_{\mathrm{D_2,F'=1}}} + \frac{1}{4 \Delta_{\mathrm{D_2,F'=2}}} + \frac{7}{10 \Delta_{\mathrm{D_2,F'=3}}} \right) \right]. \tag{2.5}$$

Here, $\mathrm{w_{inc}}$ and $\mathrm{w_{ref}}$ denote the beam waists of the incident and back-reflected beams, $\omega_{\mathrm{D_1}}$ is the (optical) resonance frequency of the atomic $\mathrm{D_1}$ transition and $\Delta_{\mathrm{D_1}}$ is the detuning of the lattice light to that transition. The hyperfine splitting of this transition can be neglected as it is much smaller than the detuning. For the $\mathrm{D_2}$ transition however, the hyperfine splitting has to be regarded and $\Delta_{\mathrm{D_2},F'=i}$ is the detuning of the lattice light to the respective transition from the $|5^2\mathrm{S}_{1/2}, \mathrm{F} = 2\rangle$ ground state to the $|5^2\mathrm{P}_{3/2}, \mathrm{F}' = i\rangle$ excited state. Each $\mathrm{D_2}$ hyperfine transition is weighted with its relative hyperfine transition strength factor [98]. To determine the actual detuning of the lattice light we calibrate our wavemeter in the following way:
The TiSa, from which the lattice light is derived, is transfer-locked to a cavity that is stabilized on the rubidium M1 cooling laser (see figure 2.4). This laser is blue detuned from the $|5^2\mathrm{S}_{1/2}, \mathrm{F} = 2\rangle \rightarrow |5^2\mathrm{P}_{3/2}, \mathrm{F}' = 3\rangle$ transition by $2\times$ 66.809 MHz, which is the frequency of the double-pass AOM that is used to tune the cooling laser into resonance with the atoms for absorption imaging. Furthermore, the coupling lattice is blue detuned from the raw TiSa output by 80 MHz. Hence, if the TiSa is locked to the transfer cavity by multiple $n_{\mathrm{FSR}} \in \mathbb{N}$, the lattice beam has a frequency of

$$\omega_{\mathrm{lat}}/2\pi = \omega_{2,3}/2\pi + 2 \times 66.809\,\mathrm{MHz} + 80\,\mathrm{MHz} + n_{\mathrm{FSR}} \times \mathrm{FSR}. \tag{2.6}$$

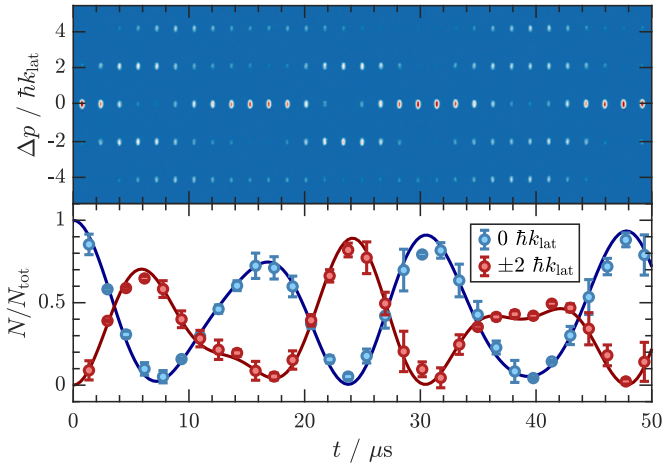

Figure 2.6: Exemplary lattice depth calibration measurement. Upper panel: Short lattice pulses of variable duration (depicted on horizontal axis) are applied to a BEC in the dipole trap and the resulting diffraction pattern is imaged after 20 ms time-of-flight. **Lower panel:** Circles denote the relative atom numbers in the respective momentum orders for a given pulse length. The solid lines depict fits to the data using the solution of the time dependent Schrödinger equation of the system (calculations can be found in [74, 102]). From the fit, the measured lattice depth can be extracted.

The displayed wavemeter reading corresponding to this frequency can then be used to calculate the relative detuning of other wavemeter readings to this frequency. And with that an absolute detuning from the atomic resonance can be derived for any adjusted wavelength[4].
Once the absolute detuning is determined the expected lattice depth for a given lattice power can be calculated using equation (2.5). By comparison of the measured lattice depth with the expected lattice depth we arrive at our lattice calibration factor

$$c_{\mathrm{cal}} = \frac{s_{\mathrm{lat,meas}}}{s_{\mathrm{lat,theo}}}. \tag{2.7}$$

Ideally this factor should be close to unity, however numerous experimental imperfections (e.g. wavefront errors, axial and transversal misalignment, polarization mismatch, etc.) lead to a smaller value. We use this quantity in two ways: 1) to gauge the quality of the current lattice alignment, 2) to correct all extrapolated lattice depths, in order to arrive at the actual lattice depth for given parameters.

2.2.2 Homodyne detection

When we place a mechanical resonator inside a cavity and illuminate it with light of constant frequency ω_{L} the resonator motion changes the cavity resonance ω_{cav} periodically (see figure 2.13) due to the optomechanical coupling discussed in section 2.3.1. This can equivalently be seen as a modulation of the detuning Δ between laser and cavity and results in a phase modulation of the reflected beam at the mechanical resonance frequency. Thus, in order to measure the motion i.e. the displacement of the resonator a phase sensitive detection scheme is needed. Furthermore, for feedback cooling of mechanical motion the detection noise plays a decisive role. Homodyne detection

[4]This wavemeter calibration has to be performed on a daily basis as the wavemeter output follows ambient temperature and humidity drifts.

is capable of fulfilling both requirements, it enables to measure any quadrature of the light field and can be quantum noise limited [103, 104].
While direct detection of a single beam on a balanced detector cannot differentiate between quadratures and therefore always measures the in-phase (amplitude) quadrature, the addition of a stable phase reference beam (local oscillator) allows to measure at an arbitrary relative phase and hence gives access to any quadrature. To realize a homodyne detector the local oscillator must have the same frequency as the signal. Practically this is realized by deriving both beams from the same laser. The signal amplitude can be expressed by

$$\alpha_{\mathrm{sig}}(t) = \alpha_{\mathrm{sig}} + \delta X_{\mathrm{sig}}(t) + i\delta Y_{\mathrm{sig}}(t), \tag{2.8}$$

with α_{sig}, $\delta X_{\mathrm{sig}}(t)$ and $\delta Y_{\mathrm{sig}}(t) \in \mathbb{R}$. The quadratures δX_{sig} and δY_{sig} are the amplitude and phase fluctuations around a steady-state value α. Similarly, the local oscillator amplitude can be written as

$$\alpha_{\mathrm{lo}}(t) = [\alpha_{\mathrm{lo}} + \delta X_{\mathrm{lo}}(t) + i\delta Y_{\mathrm{lo}}(t)]e^{i\phi_{\mathrm{lo}}}, \tag{2.9}$$

where ϕ_{lo} is an arbitrary but fixed phase between the signal and local oscillator beam that can be controlled by changing the path length of the LO branch in the interferometer. Both beams are superimposed spatially again, are then split on a 50/50 beam splitter and sent to two ports of a differential photo detector. The fields at the respective detector ports are described by

$$\begin{aligned}
\alpha_{D_1}(t) &= \sqrt{\frac{1}{2}}\alpha_{\mathrm{lo}}(t) + \sqrt{\frac{1}{2}}\alpha_{\mathrm{sig}}(t), \\
\alpha_{D_2}(t) &= \sqrt{\frac{1}{2}}\alpha_{\mathrm{lo}}(t) - \sqrt{\frac{1}{2}}\alpha_{\mathrm{sig}}(t),
\end{aligned} \tag{2.10}$$

where the minus sign arises from the π-phase shift experienced by one of the fields upon reflection at the beam splitter [104]. For the photocurrents obtained from the measured intensities this yields

$$\begin{aligned}
i_{D_1}(t) &= |\alpha_{D_1}(t)|^2 = \frac{1}{2}\left(|\alpha_{\mathrm{lo}}(t)|^2 + \alpha_{\mathrm{lo}}(t)\alpha^*_{\mathrm{sig}}(t) + \alpha^*_{\mathrm{lo}}(t)\alpha_{\mathrm{sig}}(t) + |\alpha_{\mathrm{sig}}(t)|^2\right), \\
i_{D_2}(t) &= |\alpha_{D_2}(t)|^2 = \frac{1}{2}\left(|\alpha_{\mathrm{lo}}(t)|^2 - \alpha_{\mathrm{lo}}(t)\alpha^*_{\mathrm{sig}}(t) - \alpha^*_{\mathrm{lo}}(t)\alpha_{\mathrm{sig}}(t) + |\alpha_{\mathrm{sig}}(t)|^2\right).
\end{aligned} \tag{2.11}$$

We consider that the local oscillator beam is far more intense than the signal beam: $|\alpha_{\mathrm{lo}}|^2 \gg |\alpha_{\mathrm{sig}}|^2$. If we insert equations (2.8) and (2.9) into (2.11) we can then neglect terms of the form $\alpha_{\mathrm{sig}}\delta X$ and similar, as well as terms containing two quadrature components. With that approximation we arrive at

$$\begin{aligned}
i_{D_1}(t) &\approx \frac{1}{2}\alpha^2_{\mathrm{lo}} + \alpha_{\mathrm{lo}}\delta X_{\mathrm{lo}}(t) + \alpha_{\mathrm{lo}}\alpha_{\mathrm{sig}}\cos(\phi_{\mathrm{lo}}) + \alpha_{\mathrm{lo}}\delta X_{\mathrm{sig}}(t)\cos(\phi_{\mathrm{lo}}) + \alpha_{\mathrm{lo}}\delta Y_{\mathrm{sig}}(t)\sin(\phi_{\mathrm{lo}}), \\
i_{D_2}(t) &\approx \frac{1}{2}\alpha^2_{\mathrm{lo}} + \alpha_{\mathrm{lo}}\delta X_{\mathrm{lo}}(t) - \alpha_{\mathrm{lo}}\alpha_{\mathrm{sig}}\cos(\phi_{\mathrm{lo}}) - \alpha_{\mathrm{lo}}\delta X_{\mathrm{sig}}(t)\cos(\phi_{\mathrm{lo}}) - \alpha_{\mathrm{lo}}\delta Y_{\mathrm{sig}}(t)\sin(\phi_{\mathrm{lo}}).
\end{aligned} \tag{2.12}$$

The homodyne signal is then given by the current difference at the two detector ports

$$i_-(t) = i_{D_1}(t) - i_{D_2}(t) \approx 2\alpha_{\mathrm{lo}}\alpha_{\mathrm{sig}}\cos(\phi_{\mathrm{lo}}) + 2\alpha_{\mathrm{lo}}\left[\delta X_{\mathrm{sig}}(t)\cos(\phi_{\mathrm{lo}}) + \delta Y_{\mathrm{sig}}(t)\sin(\phi_{\mathrm{lo}})\right]. \tag{2.13}$$

This current $i_-(t)$ scales with the local oscillator amplitude, but its quadrature fluctuations or noise are completely suppressed. On the other hand the power of the signal beam has negligible influence as long as it is small compared to the power of the local oscillator. The phase ϕ_{lo} determines which of the two quadratures (or which combination of both) is measured. Since the information about the mechanical resonator is encoded in the phase quadrature of the signal beam we want to measure $\delta Y_{\mathrm{sig}}(t)$, which is realized by choosing $\phi_{\mathrm{lo}} = \pm\pi/2$.
Homodyne detection allows to perform very sensitive measurements of the amplitude and phase quadrature of the light field and can be therefore applied in quantum optics to reconstruct the full quantum state of a system. In chapter 4 we will discuss the reconstruction of the state of our mechanical resonator. However, we cannot probe the resonator directly but rather measure the light field that has interacted with it. As we measure only the displacement quadrature we have to rely on the fact that the resonator behaves like a harmonic oscillator and that the equipartition theorem is valid.
The measurements performed in chapter 3 are weak continuous measurements. In contrast to a strong projective measurement (at high detection power) that determines the state of the resonator almost arbitrarily precise but also completely destroys it by the measurement, a weak measurement extracts less information about the system per time but is non-destructive [105]. Even though the motional state of the resonator is not destroyed by a weak measurement it still exerts a backaction force onto the resonator that grows with increasing probe power. At the same time the measurement imprecision is reduced at higher probe powers due to the improved signal to noise ratio as can be seen in figure 2.7. There is an optimal detection power, where both contrary effects are in balance. This point is called the standard quantum limit (SQL) and represents a fundamental uncertainty principle [23, 24, 104].
Nevertheless, more advanced position measurement methods have been developed that allow in principle to surpass this limit and measure the mechanical motion with precision below the SQL, either by evading the backaction [78] or by clever cancellation of the noise at the detector [106]. The difficulty to realize these schemes is emphasized

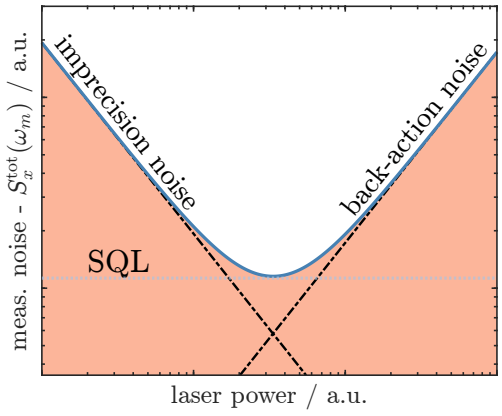

Figure 2.7: The standard quantum limit of displacement sensing. Total measured noise power spectral density (PSD) $S_x^{\mathrm{tot}}(\omega_{\mathrm{m}})$ of a mechanical resonator evaluated at the mechanical noise peak as a function of detection power. At low powers the measured noise is dominated by the measurement imprecision and at higher powers by the measurement backaction. The point of minimum noise defines the standard quantum limit (dashed grey line). Both axes have logarithmic scaling.

by the fact that interferometric displacement measurements with a precision below the SQL have been realized only in the last few years on optomechanical platforms employing nanomechanical resonators [107] or kilogram-scale test masses [108].
Another path to beat the SQL is to move from continuous to pulsed or stroboscopic measurements [109] where the interaction of the probe with the resonator is much shorter than a period of its mechanical motion. In this case the back-action transferred to the mechanical momentum does not have enough time to evolve into position noise and therefore allows for a sub-SQL measurement. This will be treated in more detail in chapter 4.

Experimental realization: In order to achieve quantum noise limited detection precision and cancellation of the classical LO noise the homodyne setup must be carefully balanced. For that the amplitudes and the wave front curvatures of the signal and LO beam should be ideally identical. This implies that both beams travel comparable distances and experience similar optical components such as lenses and mirrors. Also these components should be of high quality i.e. the use of lenses with dedicated coatings and mirrors with excellent reflectivities is mandatory to avoid optical losses wherever possible - otherwise vacuum noise is added and the noise suppression is deteriorated. To judge the quality of the alignment the normalized fringe visibility

$$\mathcal{V} = \frac{VIS}{VIS_{\text{perfect}}} \tag{2.14}$$

can be measured, where $VIS = (I_{\max} - I_{\min})/(I_{\max} + I_{\min})$ is calculated from the measured maximum and minimum intensities of the interference pattern and $VIS_{\text{perfect}} = 2\sqrt{I_{\text{sig}} I_{\text{lo}}}/(I_{\text{sig}} + I_{\text{lo}})$ is the expected fringe visibility that can be calculated from the respective beam intensities of signal and LO. The quality of the whole homodyne detection can be described by an overall efficiency [104]

$$\eta_{\text{hd}} = \eta_{\text{det}} \mathcal{V}^2 \tag{2.15}$$

where η_{det} denotes the quantum efficiency of the photo detector. It is defined as

$$\eta_{\text{det}} = \frac{hc}{\lambda e} \cdot \frac{I_{\text{diode}}}{P_{\text{opt}}} \tag{2.16}$$

where $e = 1.602 \times 10^{-19}\,\text{C}$ is the elementary charge and λ is the used wavelength. The photo sensitivity $I_{\text{diode}}/P_{\text{opt}}$ is sometimes specified by the manufacturer or can be obtained from fitting $V_{\text{out,diode}}/R$ plotted against the applied power P_{opt} for several P_{opt}.

The homodyne detection setup used for the measurements in chapter 3 was built by T. Wagner and is still operated in a similar state to the one presented in [74, 77] (see figure 2.8). The detection light is split into an LO and signal beam on a plate beam splitter. The former one is coupled to the MiM setup where the resonator motion is encoded in its phase upon back-reflection. Subsequently, the signal beam is superimposed with the LO on a PBS. The phase of the LO can be adjusted by changing the optical path length in the LO branch using a piezo mirror. As there are no perfect 50/50 beam splitters

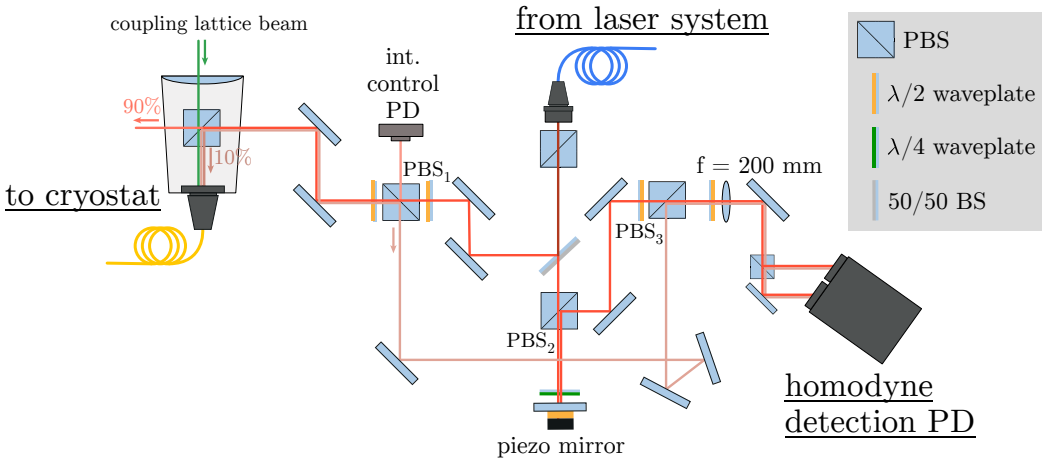

Figure 2.8: Balanced homodyne detection setup. The homodyne light is collimated to a beam diameter of $\varnothing = 3.6\,\mathrm{mm}$ using a 60FC-L-4-M20L-02 fiber collimator from *Schäfter + Kirchhoff*, polarization cleaned and subsequently split on a 50/50 non-polarizing beam splitter into signal and LO beam. At PBS_1 a small fraction of the signal beam is reflected and used for the intensity control. The remaining fraction is guided to the cryostat telescope where 10 % of the arriving signal light are reflected and coupled together with the lattice beam into the cryostat fiber. After back-reflection from the MiM device the signal beam is guided via PBS_1 to PBS_3 where it is superimposed with the LO beam again. The LO beam passes PBS_2 and is retro-reflected from a piezo mirror (HPSt 150/14-10/12 from *Piezomechanik*), which is used to adjust the relative phase between signal and LO beam. Once both beams are spatially overlapped on PBS_3 they are split equally in power and sent onto a customized differential photo detector from *Femto* (DC...1 MHz, gain 28.5 kV/W, NEP 1.1 $\mathrm{pW}/\sqrt{\mathrm{Hz}}$, $\eta_{\mathrm{det,780nm}} = 0.86$) which generates a voltage signal proportional to the mechanical resonator displacement.

in reality we use a combination of two PBS to achieve the best possible balancing of our homodyne signal. After the beams are overlapped with perpendicular polarizations on the first PBS a $\lambda/2$ waveplate is used to rotate their polarization axes by 45° before the beams are split with equal intensities and polarizations at the second PBS. Subsequently, each beam carries a relative phase dependent interference signal that is composed of the signal and LO contributions and impinges on one port of a differential photo detector. The detector was installed at an angle of 45° to the beams in order to avoid back-reflection and parasitic interference effects that might occur under normal incidence. A small fraction of the light is reflected from the glass windows in front of the photodiodes, which is recorded on another detector (not shown in figure 2.8) and used to derive the phase-lock signal.

Homodyne calibration: In order to convert the measured homodyne signal U_{hd} into a displacement x_{m} of the mechanical resonator the homodyne detector has to be calibrated. The used method is described in detail in [74, 110] and will only be briefly outlined here. We are interested in the amount of signal change in the homodyne voltage per displacement of the resonator $\partial U_{\mathrm{hd}}/\partial x_{\mathrm{m}}$. It can be written as the product of three quantities

$$\frac{\partial U_{\mathrm{hd}}}{\partial x_{\mathrm{m}}} = \frac{\partial \omega_{\mathrm{cav}}}{\partial x_{\mathrm{m}}} \frac{\partial \phi_{\mathrm{x}}}{\partial \omega_{\mathrm{cav}}} \frac{\partial U_{\mathrm{hd}}}{\partial \phi_{\mathrm{x}}}, \tag{2.17}$$

where $\partial\omega_{\mathrm{cav}}/\partial x_{\mathrm{m}} = g_{\mathrm{m}}$ is the optomechanical coupling that describes the change of the cavity resonance frequency for a given resonator displacement. This change of resonance frequency is related to a phase change in the light reflected from the cavity $\partial\phi_{\mathrm{x}}/\partial\omega_{\mathrm{cav}}$, which in turn alters the voltage on the homodyne detector $\partial U_{\mathrm{hd}}/\partial\phi_{\mathrm{x}}$. The calibration is based on two steps:
First, the resonator position within the cavity is changed at constant cavity length L_{cav} to determine the phase change per resonator position $\frac{\partial\phi_{\mathrm{x}}}{\partial x_{\mathrm{m}}} = \frac{\partial\omega_{\mathrm{cav}}}{\partial x_{\mathrm{m}}}\frac{\partial\phi_{\mathrm{x}}}{\partial\omega_{\mathrm{cav}}}$. This is done by changing the position of both cavity mirrors around the resonator position by the same amount[5] and in the same direction. The resulting phase change is derived from the reflection signal of the MiM cavity. For that we fit the reflected intensity with the expression for a cavity resonance [99, 110]

$$I_{\mathrm{ref,norm}}(x_{\mathrm{m}}) = \left|\frac{\sqrt{R_1} - e^{4\pi i x_{\mathrm{m}}}\sqrt{R_2}}{1 - e^{4\pi i x_{\mathrm{m}}}\sqrt{R_1 R_2}}\right|^2, \tag{2.18}$$

where the cavity mirror reflectivities R_1 and R_2 are used as free fit parameters (left panel in figure 2.9). The corresponding phase response is given by

$$\phi_{\mathrm{x}} = \mathrm{Im}\left(\sqrt{R_1}\frac{e^{4\pi i x_{\mathrm{m}}}(1-R_1)\sqrt{R_2}}{e^{4\pi i x_{\mathrm{m}}}\sqrt{R_1 R_2} - 1}\right) \tag{2.19}$$

and is calculated with the values obtained from the fit. The calibration factor $\partial\phi_{\mathrm{x}}/\partial x_{\mathrm{m}}$ is derived from the slope of the phase response function around $x_{\mathrm{m}} = 0$ (right panel in figure 2.9).
The second calibration step is to determine the homodyne voltage per phase change $\partial U_{\mathrm{hd}}/\partial\phi_{\mathrm{x}}$, which is done by scanning the phase of the local oscillator by multiples of 2π (using the phase-lock piezo). The scan results in a sinusoidal interference signal with a peak-to-peak voltage U_{pp} and a maximum slope of $\partial U_{\mathrm{hd}}/\partial\phi_{\mathrm{x}} = U_{\mathrm{pp}}/2$ [110]. While $\partial\phi_{\mathrm{x}}/\partial x_{\mathrm{x}}$ is a fixed quantity of the aligned MiM system, the quantity $\partial U_{\mathrm{hd}}/\partial\phi_{\mathrm{x}}$ depends on many critical parameters (e.g. fiber coupling, alignment of the homodyne detection, used photo detector, etc.). Therefore, U_{pp} is measured on a daily basis to obtain the homodyne calibration

$$\frac{\partial U_{\mathrm{hd}}}{\partial x_{\mathrm{m}}} = \frac{\partial\phi_{\mathrm{x}}}{\partial x_{\mathrm{m}}} \cdot \frac{U_{\mathrm{pp}}}{2}. \tag{2.20}$$

The measurement depicted in figure 2.9 is just an exemplary one and its result was used in chapter 4. Throughout the thesis measurements were performed at different cryostat temperatures. Each change in temperature leads to a thermally induced length change of the cavity and, depending on magnitude of the length change, a modified intra-cavity position of the resonator. Thus, it is necessary to realign the MiM system each time, which can result in an altered homodyne calibration. Furthermore, also different balanced detectors were used, depending on the measurement scenario. After each change to the system a new calibration was performed and the corresponding calibration will always be mentioned in the respective sections.

[5] By applying the independently measured piezo calibration (see section 2.3.1).

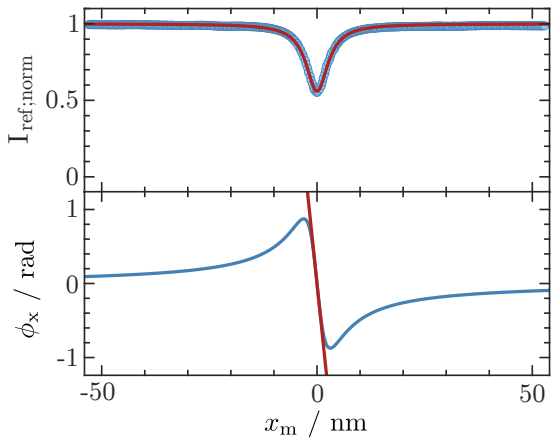

Figure 2.9: Cavity scan measurement used to calibrate the homodyne detection. Normalized reflected intensity $I_{\mathrm{ref,norm}}$ and phase ϕ_{x} as a function of the resonator position x_{m}. **Upper panel:** The measured data (blue) is fitted using equation (2.18) (red), resulting in effective mirror reflectivities $R_1 = 0.917$ and $R_2 = 0.988$. **Lower panel:** Using the fit results and equation (2.19) the phase response of the cavity is calculated (blue line). A linear fit around the cavity resonance (red line) yields the calibration factor $|\frac{\partial \phi_{\mathrm{x}}}{\partial x_{\mathrm{m}}}| = (0.56 \pm 0.01)\,\mathrm{rad/nm}$.

2.2.3 Feedback cooling

One major challenge in the use of mechanical resonators for quantum applications is their coupling to the thermal environment, which acts as a source of classical noise and leads to a finite average phonon occupation of the resonator. This classical noise can obscure the quantum behaviour of the resonator. Thus, it is of vital importance to cool these resonators close to their motional ground state and minimize the phonon noise in the system. One common and powerful approach in cavity optomechanics is to use resolved sideband cooling [56, 111, 112]. It works with resonators of all kinds and for arbitrary resonance frequencies ω_{m} as long as they exceed the linewidth κ of the surrounding cavity (good cavity limit: $\omega_{\mathrm{m}} > \kappa$). In our case this scheme is not applicable since our system operates deep in the sideband unresolved regime (bad cavity limit: $\kappa \gg \omega_{\mathrm{m}}$). In this regime the optical readout field instantaneously responds to changes in the mechanical motion, thus enabling measurement-based feedback cooling. Indeed, in the past few years feedback cooling has proven to be a suitable tool for cooling mechanical resonators to the quantum mechanical groundstate [113]. Recently, we approached the ground state quite close by feedback cooling as well, reaching a final phonon occupation of $n_{\mathrm{m}} = 3.8 \pm 0.1$ [77]. Meanwhile, other groups almost managed to reach the groundstate by feedback cooling from room-temperature [114, 115]. The technique also was applied to qubits, facilitating controlled quantum state stabilization [116].
In the course of this thesis feedback cooling is used as a tool for deterministic state preparation rather than cooling to the lowest possible phonon occupations.

The lowest vibrational mode of our mechanical resonator can be well approximated by a harmonic oscillator with resonance frequency ω_{m}, effective mass m_{eff} and damping rate (mechanical linewidth) $\Gamma_{\mathrm{m}} = \omega_{\mathrm{m}}/Q$, whose motion is described by $x(t)$. It is subject to three stochastic forces: a thermal force F_{th} associated with the ambient environment, a back-action force F_{ba} associated with the coupling of the resonator to the measurement device, and a feedback force F_{fb} that controls the resonator. The dynamics of the system

are described by the Langevin equation [117]

$$m_{\mathrm{eff}}(\ddot{x} + \Gamma_{\mathrm{m}}\dot{x} + \omega_{\mathrm{m}}^2 x) = F_{\mathrm{th}} + F_{\mathrm{ba}} + F_{\mathrm{fb}} \tag{2.21}$$

$$\overset{FT}{\Rightarrow} \underbrace{m_{\mathrm{eff}}(\omega_{\mathrm{m}}^2 - \omega^2 - i\omega\Gamma_{\mathrm{m}})}_{:=\chi_{\mathrm{m}}(\omega)^{-1}}\tilde{x} = \tilde{F}_{\mathrm{th}} + \tilde{F}_{\mathrm{ba}} + \tilde{F}_{\mathrm{fb}}, \tag{2.22}$$

where $\chi_{\mathrm{m}}(\omega)$ is the intrinsic mechanical susceptibility and FT denotes a Fourier transformation from time to frequency domain[6]. The back-action and feedback forces can be modelled as

$$\tilde{F}_{\mathrm{ba}} = -\chi_{\mathrm{ba}}(\omega)^{-1}\tilde{x} + \tilde{F}_{\mathrm{ba,th}} \tag{2.23}$$

$$\tilde{F}_{\mathrm{fb}} = -\chi_{\mathrm{fb}}(\omega)^{-1}\tilde{y} + \tilde{F}_{\mathrm{fb,th}}. \tag{2.24}$$

Both expressions consist of a dynamic component, characterized by a linear susceptibility, that contains correlations with the resonator's position and an effective thermal component. The dynamic component of the back-action force manifests itself in the high-Q ($\omega_{\mathrm{m}} \gg \Gamma_{\mathrm{m}}$), bad-cavity ($\kappa \gg \omega_{\mathrm{m}}$) limit relevant to our experiment as a shifted mechanical frequency (the optical spring effect, see section 2.3.2) and passive cold damping. Here, both effects can be neglected, as they vanish for the considered case of resonant probe light ($\Delta_{\mathrm{cav,L}} = 0$). For the feedback force the dynamic component can be regarded as a filter that affects the measured position $\tilde{y} = \tilde{x} + \tilde{x}_{\mathrm{imp}}$, where $\tilde{x}_{\mathrm{imp}}$ is the measurement imprecision added by the detector. Substituting equations (2.23) and (2.24) into (2.22) and omitting χ_{ba}^{-1} as mentioned above, the real resonator position $\tilde{x}$ and the measured position $\tilde{y}$ can be expressed as

$$(\chi_{\mathrm{m}}^{-1} + \chi_{\mathrm{fb}}^{-1})\tilde{x} = \tilde{F}_{\mathrm{th}} + \tilde{F}_{\mathrm{ba,th}} + \tilde{F}_{\mathrm{fb,th}} - \chi_{\mathrm{fb}}^{-1}\tilde{x}_{\mathrm{imp}} \tag{2.25}$$

$$(\chi_{\mathrm{m}}^{-1} + \chi_{\mathrm{fb}}^{-1})\tilde{y} = \underbrace{\tilde{F}_{\mathrm{th}} + \tilde{F}_{\mathrm{ba,th}} + \tilde{F}_{\mathrm{fb,th}}}_{:=\tilde{F}_{\mathrm{tot}}} + \chi_{\mathrm{m}}^{-1}\tilde{x}_{\mathrm{imp}}. \tag{2.26}$$

In the equations above one can identify an inverse effective mechanical susceptibility $\chi_{\mathrm{eff}}^{-1} := \chi_{\mathrm{m}}^{-1} + \chi_{\mathrm{fb}}^{-1}$ that describes how the response of the resonator is altered due to feedback. When compared with the bare mechanical susceptibility one finds that the resonators spring constant $k_{\mathrm{m}} = m_{\mathrm{eff}}\omega_{\mathrm{m}}^2$ is altered by the real part of the feedback filter to

$$k'_{\mathrm{m}} = k_{\mathrm{m}}\left(1 + \frac{\mathrm{Re}[\chi_{\mathrm{fb}}^{-1}]}{k_{\mathrm{m}}}\right) = k_{\mathrm{m}}(1 + g_{\mathrm{d}}) \tag{2.27}$$

On the other hand the imaginary part of of the filter affects the resonator damping, which results in

$$\Gamma'_{\mathrm{m}} = \Gamma_{\mathrm{m}}\left(1 - \frac{\mathrm{Im}[\chi_{\mathrm{fb}}^{-1}]}{m_{\mathrm{eff}}\omega\Gamma_{\mathrm{m}}}\right) = \Gamma_{\mathrm{m}}(1 + g_{\mathrm{v}}). \tag{2.28}$$

Since the former effect is purely position dependent and the latter effect is velocity

[6]The Fourier transform via $\tilde{x}(\omega) = \int_{-\infty}^{\infty} x(t)e^{i\omega t}dt$ is used here.

dependent we introduced the displacement and velocity proportional feedback gains g_d and g_v, respectively. Equivalently, the feedback filter function can now be expressed through these feedback gains:

$$\chi_\mathrm{fb}^{-1} \;=\; k_\mathrm{m} \cdot g_\mathrm{d} - i m_\mathrm{eff} \omega \Gamma_\mathrm{m} \cdot g_\mathrm{v}. \tag{2.29}$$

Using equations (2.25) and (2.26) that describe the real resonator displacement $\tilde{x}(\omega)$ and the in-loop detected displacement $\tilde{y}(\omega)$ under the influence of the total force F_tot and the susceptibility χ_eff the power spectral densities (PSD) $S_\mathcal{O}(\omega) = \langle|\mathcal{O}(\omega)|^2\rangle$ of these resonator positions in the feedback loop can be calculated. For the real resonator displacement $\tilde{x}$ the single-sided PSD can be calculated as

$$\begin{aligned} S_\mathrm{x}(\omega) &= \langle \tilde{x}(\omega)\tilde{x}^*(\omega)\rangle \\ &= |\chi_\mathrm{eff}(\omega)|^2 \left(\langle \tilde{F}_\mathrm{tot}(\omega)\tilde{F}^*_\mathrm{tot}(\omega)\rangle + |\chi_\mathrm{fb}(\omega)|^{-2} \langle \tilde{x}_\mathrm{imp}(\omega)\tilde{x}^*_\mathrm{imp}(\omega)\rangle \right) \\ &= |\chi_\mathrm{eff}(\omega)|^2 \left(S_\mathrm{F}^\mathrm{tot}(\omega) + |\chi_\mathrm{fb}(\omega)|^{-2} S_\mathrm{x}^\mathrm{imp}(\omega) \right), \end{aligned} \tag{2.30}$$

where the cross terms including $F_\mathrm{tot}(\omega)$ and $x_\mathrm{imp}(\omega)$ vanish because the thermal noise and the detector noise are uncorrelated. One can see that the resonator position PSD consists of a contribution from the thermal noise force and the imprecision noise that is fed back to the resonator. Similarly, the PSD of the measured displacement $\tilde{y}$ can be calculated to

$$S_\mathrm{y}(\omega) \;=\; |\chi_\mathrm{eff}(\omega)|^2 \left(S_\mathrm{F}^\mathrm{tot}(\omega) + |\chi_\mathrm{m}(\omega)|^{-2} S_\mathrm{x}^\mathrm{imp}(\omega) \right). \tag{2.31}$$

It is clearly not just the sum of the real resonator displacement PSD $S_\mathrm{x}(\omega)$ and the imprecision noise PSD $S_\mathrm{x}^\mathrm{imp}(\omega)$. Instead it becomes apparent that the feedback loop creates correlations between the noise and the real resonator displacement.

To evaluate the effect of feedback cooling on the mode temperature T_mode of the resonator we use the obtained equations for the susceptibility $\chi_\mathrm{eff}(\omega)$ and the feedback

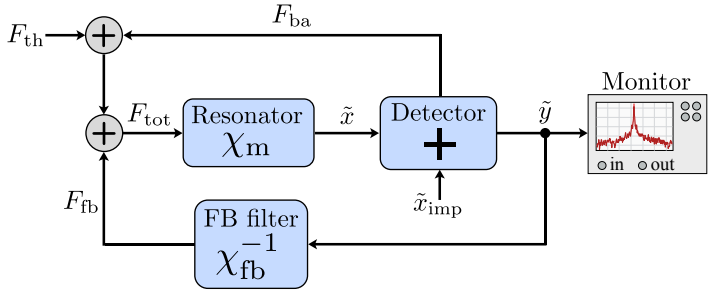

Figure 2.10: Schematic representation of the feedback loop. A thermal noise force F_th drives the resonator and its action is converted by the mechanical susceptibility χ_m to a displacement $\tilde{x}$. Upon detection, noise $\tilde{x}_\mathrm{imp}$ is introduced, which results in an additional back-action force F_ba that leads to the measured *in-loop detection signal* $\tilde{y} = \tilde{x} + \tilde{x}_\mathrm{imp}$. This signal is processed by the feedback filter χ_fb^{-1} to derive the feedback force F_fb. All these contributions add up to the total force F_tot that governs the dynamics of the system.

filter function $\chi_{\mathrm{fb}}(\omega)$ expressed through the gains g_{d} and g_{v}:

$$|\chi_{\mathrm{fb}}(\omega)|^{-2} = (k_{\mathrm{m}} g_{\mathrm{d}})^2 + (m_{\mathrm{eff}}\omega\Gamma_{\mathrm{m}} g_{\mathrm{v}})^2 \tag{2.32}$$

$$|\chi_{\mathrm{eff}}(\omega)|^{2} = \frac{1}{m_{\mathrm{eff}}^2\left[\left(\omega_{\mathrm{m}}^2\left(1+g_{\mathrm{d}}\right)-\omega^2\right)^2+\left(\omega\Gamma_{\mathrm{m}}\left(1+g_{\mathrm{v}}\right)\right)^2\right]}. \tag{2.33}$$

According to the equipartition theorem the mode temperature is given by [23]:

$$T_{\mathrm{mode}} = \frac{m_{\mathrm{eff}}\omega_{\mathrm{m}}^2}{k_{\mathrm{B}}}\langle x_{\mathrm{m}}^2\rangle = \frac{m_{\mathrm{eff}}\omega_{\mathrm{m}}^2}{k_{\mathrm{B}}}\cdot\frac{1}{2\pi}\int_0^\infty S_{\mathrm{x}}(\omega)\mathrm{d}\omega \tag{2.34}$$

Evaluating this formula using equation (2.30) expressed by (2.32) and (2.33) yields:

$$\begin{aligned} T_{\mathrm{mode}} &= \frac{\omega_{\mathrm{m}}^2}{2\pi m_{\mathrm{eff}}k_{\mathrm{B}}}S_{\mathrm{F}}^{\mathrm{tot}}\int_0^\infty\frac{1}{\left(\omega_{\mathrm{m}}'^2-\omega^2\right)^2+\left(\omega\Gamma_{\mathrm{m}}'\right)^2}\mathrm{d}\omega \\ &+ \frac{\omega_{\mathrm{m}}^2}{2\pi m_{\mathrm{eff}}k_{\mathrm{B}}}S_{\mathrm{x}}^{\mathrm{imp}}\int_0^\infty\frac{g_{\mathrm{d}}^2k_{\mathrm{m}}^2+g_{\mathrm{v}}^2\left(m\omega\Gamma_{\mathrm{m}}\right)^2}{\left(\omega_{\mathrm{m}}'^2-\omega^2\right)^2+\left(\omega\Gamma_{\mathrm{m}}'\right)^2}\mathrm{d}\omega, \end{aligned} \tag{2.35}$$

where $\omega_{\mathrm{m}}' = \omega_{\mathrm{m}}\sqrt{1+g_{\mathrm{d}}}$ and $\Gamma_{\mathrm{m}}' = \Gamma_{\mathrm{m}}\left(1+g_{\mathrm{v}}\right)$. $S_{\mathrm{F}}^{\mathrm{tot}}$ and $S_{\mathrm{x}}^{\mathrm{imp}}$ are assumed constant (a very good approximation for reasonable resonator parameters). By solving the integrals[7] the mode temperature can be calculated as a function of the feedback gains g_{d} and g_{v}:

$$T_{\mathrm{mode}} = \underbrace{\frac{T_{\mathrm{bath}}}{\left(1+g_{\mathrm{d}}\right)\left(1+g_{\mathrm{v}}\right)}}_{\text{cold spring/damping}} + \underbrace{\left[\frac{k_{\mathrm{m}}\omega_{\mathrm{m}}Q}{4k_{\mathrm{B}}}\frac{g_{\mathrm{d}}^2}{\left(1+g_{\mathrm{d}}\right)\left(1+g_{\mathrm{v}}\right)}\right.}_{T\,\sim\,g_{\mathrm{d}}} + \underbrace{\left.\frac{k_{\mathrm{m}}\omega_{\mathrm{m}}}{4k_{\mathrm{B}}Q}\frac{g_{\mathrm{v}}^2}{1+g_{\mathrm{v}}}\right]}_{T\,\sim\,g_{\mathrm{v}}}S_{\mathrm{x}}^{\mathrm{imp}} \tag{2.36}$$

From the first term of the equation one can see that for positive gains $g_{\mathrm{d,v}} > 0$ feedback cooling occurs ($T_{\mathrm{mode}} < T_{\mathrm{bath}}$). However, as the first term approaches zero for large gains the last two terms proportional to g_{d}^2 and g_{v}^2 will lead to an increase in temperature originating from the detection noise that is fed back to the resonator. Thus, the mode temperature exhibits a global minimum for $g_{\mathrm{d,v}} \in (0,\infty)$. In our experimental setup the displacement proportional term does not lead to cooling at all [74] due to the high Q-factor ($\approx 9\cdot 10^7$) of our resonator and in fact only adds a parasitic heating effect. Hence, we need to avoid it completely in the experiment. This can be done by adjusting the feedback phase $\phi_{\mathrm{fb}} = \arg(\chi_{\mathrm{fb}})$. For purely velocity dependent feedback one needs to exploit the imaginary part of the filter function χ_{fb}^{-1} which is realized for $\phi_{\mathrm{fb}} = \pi/2$. Experimentally, the phase is adjusted by the feedback signal delay, which in our case is done in the lock-in amplifier that processes the signal.

Finally, the minimum achievable temperature for $g_{\mathrm{d}} = 0$ can be determined by

$$\frac{\partial T_{\mathrm{mode}}}{\partial g_{\mathrm{v}}} = 0 \;\Rightarrow\; g_{\mathrm{v,opt}} = \sqrt{1+\frac{4k_{\mathrm{B}}QT_{\mathrm{bath}}}{k_{\mathrm{m}}\omega_{\mathrm{m}}S_{\mathrm{x}}^{\mathrm{imp}}}} - 1 \approx \sqrt{\frac{4k_{\mathrm{B}}QT_{\mathrm{bath}}}{k_{\mathrm{m}}\omega_{\mathrm{m}}S_{\mathrm{x}}^{\mathrm{imp}}}} := A$$

[7] Using $\frac{\pi}{2\Gamma\omega_{\mathrm{m}}^2} = \int_0^\infty \frac{\mathrm{d}\omega}{\left(\omega_{\mathrm{m}}^2-\omega^2\right)^2+(\omega\Gamma)^2}$ and $\frac{\pi}{2\Gamma} = \int_0^\infty \frac{\omega^2\mathrm{d}\omega}{\left(\omega_{\mathrm{m}}^2-\omega^2\right)^2+(\omega\Gamma)^2}$

$$\Rightarrow T_{\mathrm{mode}}(g_{\mathrm{v,opt}}) \approx \frac{2T_{\mathrm{bath}}}{A} = \omega_{\mathrm{m}}\sqrt{m_{\mathrm{eff}}\Gamma_m S_{\mathrm{x}}^{\mathrm{imp}} T_{\mathrm{bath}}/k_{\mathrm{B}}} \tag{2.37}$$

We find that for optimal feedback cooling it is beneficial to have a low detection noise and work at low bath temperatures. Moreover, the used resonator should have a large Q-factor and a low mass.

2.3 Cryogenic optomechanical setup

The central component of the optomechanical part of our experiment is the cryogenic membrane-in-the-middle (MiM) system. It consists of an asymmetric, plano-concave fiber Fabry-Pérot cavity that encloses a high stress silicon-nitride trampoline resonator [93, 94]. The asymmetry of the cavity refers to the cavity mirrors that have different reflectivities, allowing for a non-zero reflectivity on resonance. This feature provides the back-reflection from the cavity that is needed for the bi-directional interaction with the atomic system. The mode matched cavity is formed by two coated optical fibers that can be aligned with sub-micrometer precision using an individual 5-axis goniometer for each fiber (see figure 2.11). Details on the properties and the fabrication process of such fiber cavities are presented in [99, 118]. For detailed properties of the fiber cavity used in the course of this thesis refer to [74]. The optical axis of the fibers is oriented along gravity, perpendicular to the plane of the resonator. While the fibers are fully moveable, the resonators position is fixed to the cavity housing. It sits on a removable copper shuttle that can be used to exchange different resonators under UHV and even cryogenic conditions. The cavity must be aligned around the resonator with a transversal precision of $\approx 200\,\mathrm{nm}$ and a longitudinal precision of a few tens of nanometers to ensure optimal mode match and sufficient optomechanical coupling.
This is done by positioning the upper, planar terminated fiber at a distance of $\approx 5\,\mu\mathrm{m}$ from the resonator. In the vicinity of the fiber the wavefronts of the intra-cavity are planar and thus can be efficiently reflected from the resonator into the cavity mode. The fiber is used to couple the detection and coupling light into the cavity. On the other side, the lower, curved end fiber is placed $\approx 17\,\mu\mathrm{m}$ away from the resonator and is used to deliver the feedback cooling beam. The whole assembly is situated in a $^3\mathrm{He}/^4\mathrm{He}$ dilution refrigerator and the cavity device is connected directly to its mixing chamber allowing to reduce the temperature of the MiM device down to 500 mK. Further details on the cryogenic implementation of the MiM structure and all parts of the MiM device can be found in [119]. However, during the course of this thesis we had technical issues with the ^{3}He pump and encountered multiple blockages inside the cryogenic unit of the refrigerator, which made it necessary to perform several warm-up cycles. The reason for the blockages at our experiment could not be fully identified yet, but similar problems appeared at other experiments in adjacent laboratories as well. Presumably, they were caused by residual impurities in the used liquid helium after liquefaction of the recovered helium gas. For this reason the experiments presented in chapter 3 were performed at room-temperature.

2.3.1 Trampoline resonator in a MiM configuration

The field of cavity optomechanics [24] aims at producing and controlling quantum states of mechanical motion by exploiting the tools of quantum optics. This is facilitated by the similarity of the two fields that reflects in two facts: first, the quantum description of a single-mode of an optical field is equivalent to that of an harmonic oscillator and second, the interaction between light and mechanics can be of non-linear (Kerr-type) nature if the light confined in a cavity is modified by the mechanical motion [120]. The latter can be observed e.g. in the prototypical optomechanical setup of a cavity with a mechanically compliant end mirror, where radiation-pressure pushes the cavity mirrors apart. The deformation of the cavity affects its resonance frequency and hence the stored energy, which results in optical back-action that creates a coupling between the mechanical motion and the cavity mode. Most optomechanical systems are modifications of this simple scheme.
The great benefit of not using a mechanical resonator as a cavity end mirror is at hand - it alleviates the stringent requirement of combined exceptional optical and mechanical properties in a single object. Instead, by placing an extremely sensitive micro-mechanical resonator with large Q-factor inside a high-finesse cavity the beneficial properties of both objects can be utilized. Since the resonators are mostly optically flat and very thin ($d \approx 50\,\mathrm{nm} \ll \lambda$) they scatter photons in a well-defined direction, allowing for stable high-finesse modes in the MiM scheme. By placing the resonator at a node of the intra-cavity field, purely dispersive, linear optomechanical coupling can be created. In this configuration the cavity detuning Δ depends linearly on the resonator displacement x_m. By changing the resonator position to an anti-node of the intra-cavity field quadratic dispersive coupling $\sim x_\mathrm{m}^2$ can be created that would render direct energy measurements of the resonator possible [121].
The MiM system is a versatile and frequently used optomechanical setup composed of a

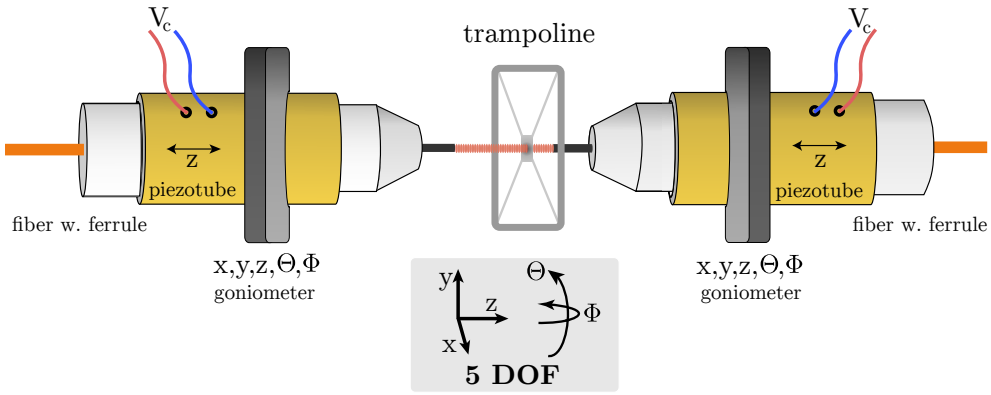

Figure 2.11: Sketch of the MiM setup. The MiM system is formed by two fibers that are aligned around the trampoline resonator. Each fiber is aligned using a 5-axis goniometer. The fibers are glued into ferules that are mounted in piezo tubes for scanning the cavity and tuning it on resonance. The planar fiber (closer to the trampoline) exhibits a nominal reflectivity $|r_1|^2 = 0.907 \pm 0.004$, while the curved fibers holds $|r_2|^2 = 0.994 \pm 0.001$ and has a radius of curvature of approximately 50 µm [97]. The cavity has a total length of $\approx 22.5\,\mu\mathrm{m}$. Figure adapted from [100].

thin dielectric membrane that is placed inside a Fabry-Pérot resonator [121–124]. It has been utilized to sense radiation pressure shot noise through mechanical motion [125], for mechanical ground state cooling [126], as well as sympathetic cooling [62, 65] and quantum back-action-evading measurements [64] in hybrid atomic-mechanical systems. More recently MiM systems have been employed to demonstrate measurement-based quantum control [113], strong coupling of atomic spins to mechanical motion [127] and spin feedback cooling [128]. MiM systems equipped with ultracoherent, soft clamped photonic shield resonators could also enable ground state cooling from room temperature in the near future [115].

Trampoline resonator

Trampoline resonators are tethered membranes that are suspended by four strings of material from the corners of a quadratic frame (see figure 2.11 and 2.12). They were first reported in [93, 94] and developed to enter the optomechanical quantum regime from room temperature. Their design idea is based on the goal to create mechanical elements that experience the lowest possible force noise which in thermal equilibrium can be described by the corresponding power spectral density [23]

$$S_{\mathrm{F}}^{\mathrm{th}} = 4k_{\mathrm{B}}T_{\mathrm{bath}}\Gamma_{\mathrm{m}}m_{\mathrm{eff}}. \tag{2.38}$$

From equation (2.38) it is evident that this requires a low resonator mass m_{eff} and a large quality factor $Q = \omega_{\mathrm{m}}/\Gamma_{\mathrm{m}}$.

At the same time a high mode frequency is desirable, since the quality factor-frequency product dictates the condition to reach the quantum realm from room temperature

$$Q \cdot f_{\mathrm{m}} > \frac{k_{\mathrm{B}}T_{\mathrm{room}}}{h}. \tag{2.39}$$

If the condition is fulfilled the system operates in the quantum coherent oscillation (QCO) regime and one can calculate the number of coherent oscillations that the resonator can undergo before a phonon enters the system

$$N_{\mathrm{osc}} = \frac{\omega_{\mathrm{m}}}{\Gamma_{\mathrm{th}}} = \frac{2\pi \cdot f_{\mathrm{m}}}{\Gamma_{\mathrm{m}} \cdot n_{\mathrm{th}}} = \frac{Qf_{\mathrm{m}}h}{k_{\mathrm{B}}T_{\mathrm{bath}}}, \tag{2.40}$$

where Γ_{th} is the thermal decoherence rate caused by coupling to a thermal bath.
Our resonator was designed by H. Zhong using finite element simulation based on the findings in [93, 94] and fabricated by *Norcada*. It is made from high stress (800 MPa) silicon nitride (Si_3N_4), which allows for low light absorption at $\lambda = 780\,\mathrm{nm}$ and can be fabricated in almost any desired shape. The rigid silicon frame has a size of $5\,\mathrm{mm} \times 5\,\mathrm{mm}$ and a thickness of $(500 \pm 25)\,\mu\mathrm{m}$. A window of $1\,\mathrm{mm} \times 1\,\mathrm{mm}$ contains the $d = (50 \pm 5)\,\mathrm{nm}$ thick resonator, whose pad has a side length of $(115 \pm 10)\,\mu\mathrm{m}$ and thus is just slightly narrower than the tips of the cavity fibers. The frame is placed under its own weight on the copper shuttle, as gluing or clamping can reduce the resonators quality factor.
The measured mode spectrum of our resonator is depicted in figure 2.12 and corresponds

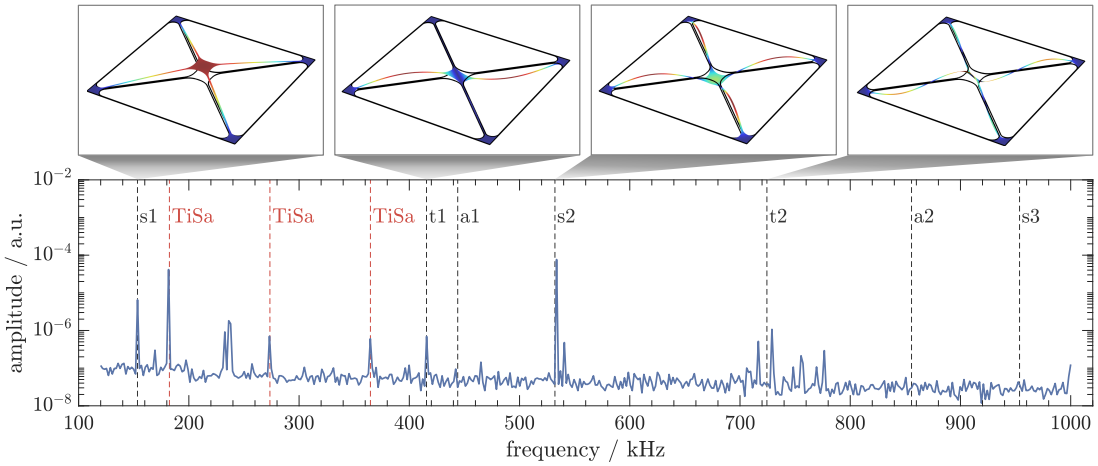

Figure 2.12: Mode spectrum of the trampoline resonator. The blue line shows a measurement of the mode spectrum of the in-house designed trampoline resonator recorded with a spectrum analyzer (FSP from *Rohde & Schwarz*), RBW: 100 Hz, VBW: 300 Hz. The black dashed lines depict the first seven resonances (s - symmetric, t - torsional, a - asymmetric), that were calculated in COMSOL during the design of the resonator. Above the plot the simulated displacement profiles for the modes that appear in the recorded spectrum are shown. Our work is concentrated mainly on the first symmetric mode that appears around 154 kHz. The red dashed lines depict parasitic noise in the spectrum that originates from the etalon modulation of the TiSa laser.

well to the calculated fundamental modes (black dashed lines). From the simulation the effective mass $m_{\text{eff}} = 3\,\text{ng}$ of the lowest mode that we focus on in our experiments, can be extracted. It has a mode frequency of $\omega_m \approx 2\pi \cdot 154\,\text{kHz}$. The quality factor, the mode frequency and hence the mechanical linewidth change with the temperature of the surrounding cryogenic environment. Therefore, we measured the quality factor in all used configurations by ringdown measurements and determined the respective mechanical linewidth from the measured mode frequency. The resulting numbers are stated in table 2.1. As one can see the quality factor of our resonator does not suffice to enter the quantum regime at room temperature.

Table 2.1: Properties of the MiM device that change with the environment temperature. The values for 0.5 K are taken from [77], all other values are determined within this work. The quality factor was calculated from ringdown measurements on the cooling (Q_{cool}) and heating side (Q_{heat}) of the cavity resonance (that will be introduced in section 2.3.2), respectively. The stated values are calculated by the harmonic mean $Q = 2Q_{\text{cool}}Q_{\text{heat}}/(Q_{\text{cool}} + Q_{\text{heat}})$.

Temperature-dependent MiM parameters				
T	ω_{m}	Q	Γ_{m}	N_{osc}
0.5 K	$2\pi \cdot 153.98\,\text{kHz}$	$(8.987 \pm 0.001) \cdot 10^7$	$2\pi \cdot (1.7 \pm 0.4)\,\text{mHz}$	1329
10 K	$2\pi \cdot 152.36\,\text{kHz}$	$(6.832 \pm 0.001) \cdot 10^7$	$2\pi \cdot (2.2 \pm 0.5)\,\text{mHz}$	50
293 K	$2\pi \cdot 154.42\,\text{kHz}$	$(6.662 \pm 0.004) \cdot 10^6$	$2\pi \cdot (23.2 \pm 0.8)\,\text{mHz}$	< 1

Optomechanical interaction

As already mentioned earlier the optical (ω_{cav}) and mechanical (ω_{m}) modes in an optomechanical system can be described as harmonic oscillators. For the small displacements that are typically created in the experiment this is an excellent approximation and leads to a Hamiltonian $\hat{H}_0$ of the form [24]

$$\hat{H}_0 = \hbar\omega_{\mathrm{cav}}\hat{a}^\dagger\hat{a} + \hbar\omega_{\mathrm{m}}\hat{b}^\dagger\hat{b}, \tag{2.41}$$

with the phononic (photonic) creation $\hat{b}^\dagger$ ($\hat{a}^\dagger$) and annihilation $\hat{b}$ ($\hat{a}$) operators. These are linked via $\hat{x} = x_{\mathrm{zpf}}(\hat{b}+\hat{b}^\dagger)$, $\hat{p} = -im_{\mathrm{eff}}\omega_{\mathrm{m}}x_{\mathrm{zpf}}(\hat{b}-\hat{b}^\dagger)$ to the position and momentum operators, where

$$x_{\mathrm{zpf}} = \sqrt{\frac{\hbar}{2m_{\mathrm{eff}}\omega_{\mathrm{m}}}} \tag{2.42}$$

is the zero-point fluctuation amplitude in the mechanical vacuum state $|0\rangle$. The quantity $\hat{b}^\dagger\hat{b}$ is the phonon number operator[8], whose average yields the phonon occupation of the mechanical mode: $\bar{n}_{\mathrm{m}} = \langle\hat{b}^\dagger\hat{b}\rangle$.
For the case of dispersive optomechanics the coupling of optical and mechanical modes leads to a modulation of the cavity resonance frequency by the mechanical amplitude:

$$\omega_{\mathrm{cav}}(x_{\mathrm{m}}) \approx \omega_{\mathrm{cav}} + x_{\mathrm{m}}\frac{\partial\omega_{\mathrm{cav}}}{\partial x_{\mathrm{m}}} + \cdots . \tag{2.43}$$

The frequency shift per displacement is called optomechanical coupling $G = -\partial\omega_{\mathrm{cav}}/\partial x_{\mathrm{m}}$. Rewriting $\hat{H}_0$ by using $\omega_{\mathrm{cav}}(x_{\mathrm{m}})$ up to first order and expressing x_{m} through x_{zpf} yields

$$\hat{H}_0 = \hbar\omega_{\mathrm{cav}}\hat{a}^\dagger\hat{a} + \hbar\omega_{\mathrm{m}}\hat{b}^\dagger\hat{b} - \hbar g_0\hat{a}^\dagger\hat{a}(\hat{b}+\hat{b}^\dagger). \tag{2.44}$$

The last term describes the interaction between the optics and the mechanics and $g_0 = Gx_{\mathrm{zpf}}$ denotes the single photon coupling strength.

The simplest realization of such a scheme is a Fabry-Pérot cavity with a mechanically compliant end mirror. For such cavities with resonance frequency $\omega_{\mathrm{cav}} = n\pi c/L$, where c denotes the speed of light, L the cavity length and $n \in \mathbb{N}$, the resonance condition is fulfilled if $n \cdot \lambda = 2L$. If the end mirror is displaced by x_{m} the cavity length is changed, which results in a position-dependent cavity frequency

$$\omega_{\mathrm{cav}}(x_{\mathrm{m}}) = \frac{n\pi c}{L + x_{\mathrm{m}}} \approx \omega_{\mathrm{cav}}\left(1 - \frac{x_{\mathrm{m}}}{L}\right) = \omega_{\mathrm{cav}} - x_{\mathrm{m}} \cdot \frac{\omega_{\mathrm{cav}}}{L}. \tag{2.45}$$

The frequency shift per displacement is therefore $G = -\omega_{\mathrm{cav}}/L$.

For a MiM system the optomechanical coupling $g_{\mathrm{m}} = -\partial\omega_{\mathrm{cav}}/\partial x_{\mathrm{m}}$ has a more complicated form and depends on many more parameters than just the cavity length. The resonators position x_{m} changes g_{m} periodically and therefore it must be placed pre-

[8] Equivalently $\hat{a}^\dagger\hat{a}$ is the photon number operator with the average photon occupation of the cavity field $\bar{n}_{\mathrm{cav}} = \langle\hat{a}^\dagger\hat{a}\rangle$.

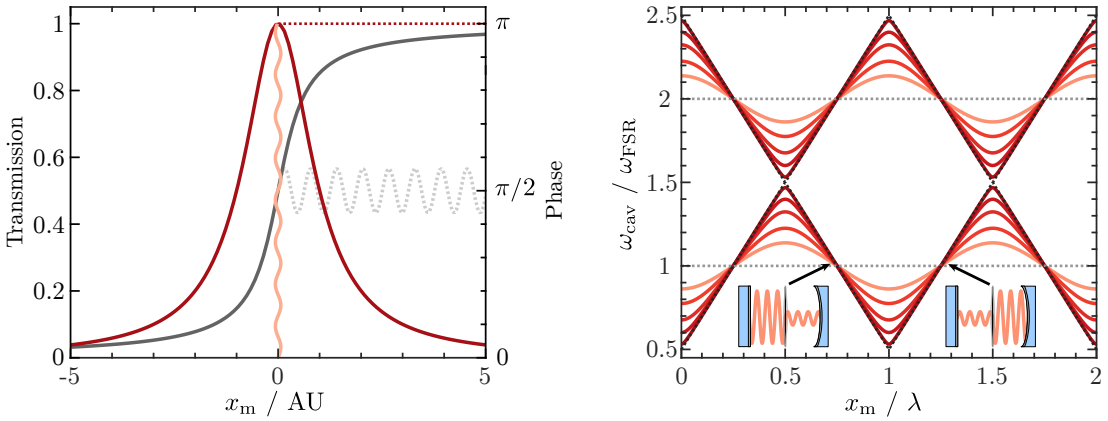

Figure 2.13: Cavity response to resonator displacement. Left panel: The solid lines show the cavity transmission (dark red), the phase of the transmitted light (grey) and modulation of the resonator position (light red). The effect of that modulation on the transmission and phase is plotted as a dotted line with the respective color. **Right panel:** Dependence of the cavity resonance frequency on the resonator displacement x_m from the cavity center normalized by the FSR, with r_m values (from light to dark) 0.42, 0.65, 0.85, 0.95 and 0.995. The horizontal dotted lines show the empty cavity resonant frequencies ($r_m = 0$) and the black dotted lines represent the left (negatively sloped) and right (positively sloped) sub-cavity resonances for $r_m = 1$.

cisely at the right point of the intra-cavity field to obtain the maximal linear coupling. This has been shown by modelling the resonator as a beam-splitter with a certain (amplitude) reflectivity r_m inside the cavity [123, 129]. By solving a set of coupled wave equations the cavity field amplitudes can be calculated and used to derive the cavity resonance frequency for a MiM system [130]

$$\omega_{MiM}(x_m) = N\omega_{FSR} + \frac{\omega_{cav}}{\pi}\left(\arccos[(-1)^{N+1}|r_m|\cos(2k_N x_m)] - \phi_r\right). \tag{2.46}$$

Here, $\omega_{FSR} = \pi c/L$ denotes the empty cavity FSR, ϕ_r is the phase change of the light reflected by the resonator and $k_N = \pi N/L$ is the N^{th} empty-cavity resonance. These frequencies are plotted in the right panel of figure 2.13 for the MiM system. The resonator divides the cavity into two sub-cavity modes that are coupled to each other via the resonator transmission. If the resonator position increases the left sub-cavity is elongated while the right one shortens, thus affecting their respective resonance frequencies (black dashed lines). The coupling of the sub-cavities leads to avoided crossings, which consequently result in a periodic modulation of the MiM systems resonance frequency. At the points where the cavity resonance changes linearly in x_m one sub-cavity is resonant with the light, while the other is anti-resonant as depicted by the insets. At these points also the optomechanical coupling g_m is linear. Since the reflectivities of the cavity end mirrors are unequal, also the linewidth of the cavity is modified by the redistribution of light between the sub-cavities [124, 129].

In our setup the resonator is not exactly in the middle of the cavity but closer to the planar cavity end mirror, leading to a slightly skewed shape of the cavity resonances ω_{cav}. This results in a steeper descending slope for the left sub-cavity and thus a larger

optomechanical coupling than for the moderate ascending slope of the right sub-cavity. In the extreme case where the resonator is placed very close to one end mirror the slope of the corresponding sub-cavity resonance gets so steep that the optomechanical coupling g_m at this point can exceed the coupling G of the bare Fabry-Pérot cavity [129, 130]. Such a cavity configuration is then called membrane at the edge (MATE).

In order to determine the optomechanical coupling experimentally the cavity transmission has to be measured for different positions of the resonator within the intra-cavity field to obtain $\omega_\mathrm{cav}(x_\mathrm{m})$. Since it is not possible to move the resonator inside the cavity in our setup we emulate the effect of the displaced resonator on the cavity field by moving the whole cavity instead. With the knowledge of $G = -\omega_\mathrm{cav}/L = 102.6\,\mathrm{GHz/nm}$ for an empty cavity[9] the optomechanical coupling can be determined implicitly by measuring the ratio

$$\frac{g_\mathrm{m}}{G} = \frac{\partial L_\mathrm{res}}{\partial x_\mathrm{m}}, \tag{2.47}$$

where L_res is the resonant cavity length ($\omega_\mathrm{L} = \omega_\mathrm{cav}$). This is depicted in the left panel of figure 2.14. Both fibers are scanned simultaneously at different speeds over their whole scan range using high voltage at the piezo tubes (see figure 2.11). In this scenario the length of the left sub-cavity is scanned many times (ΔL_1 on the y-axis) during one length scan of the right sub-cavity (depicted by ΔL_2 on the x-axis). The blue line denotes the normalized cavity transmission and the red solid line shows the line of constant cavity length that corresponds to a simultaneous change of $L_1 \to L_1 \pm \Delta x_\mathrm{m}$ and $L_2 \to L_2 \mp \Delta x_\mathrm{m}$. The latter one is obtained by a linear fit to the transmission maxima of the plot, which are acquired by fitting the Lorentzian transmission features along each column. Using the fact that the transmission lines are one FSR ($\lambda/2$) apart the piezo tubes can be calibrated to scale the axes in units of the wavelength. In this case the measurement was performed at $T_\mathrm{bath} = 10\,\mathrm{K}$ and the scan range of both fibers was sufficiently large to resolve at least one FSR along each scan direction.[10] Due to the temperature-dependent piezo stroke this is not possible at lower temperatures. In that case only the lower cavity fiber has a sufficiently large scan range to resolve one FSR. One can then use the slope of the line of constant cavity length to calculate the piezo calibration for the upper fiber as well [74, 77].
From this measurement we find the piezo calibration $c_\mathrm{low} = (1.58 \pm 0.08)\,\mathrm{nm/V}$ for the lower and $c_\mathrm{up} = (0.88 \pm 0.01)\,\mathrm{nm/V}$ for the upper fiber. These calibration factors are also necessary to perform the homodyne calibration described in section 2.2.2.
The line of constant cavity length can also be used to rotate the central transmission line in the left panel of figure 2.14, such that the red line becomes the new x-axis and the resonant cavity length L_cav can be expressed as a function of the resonator position x_m (right panel in figure 2.14). To determine g_m one can now use equation (2.46) to fit the data with r_m as the only free fit parameter. From the fit we obtain $r_\mathrm{m} = 0.61$ and g_m/G is calculated by taking the derivative in equation (2.47): $g_\mathrm{m}^\mathrm{max} = 0.88G = 90.3\,\mathrm{GHz/nm}$.

[9] Calculated for the used wavelength of $\lambda = 780.24\,\mathrm{nm}$, $\omega_\mathrm{cav} = 2\pi \cdot 384\,\mathrm{THz}$ and a cavity length of $L = (23.53 \pm 0.13)\,\mu\mathrm{m}$.

[10] One can measure the distance between two resonance lines along the vertical and horizontal direction of the plot.

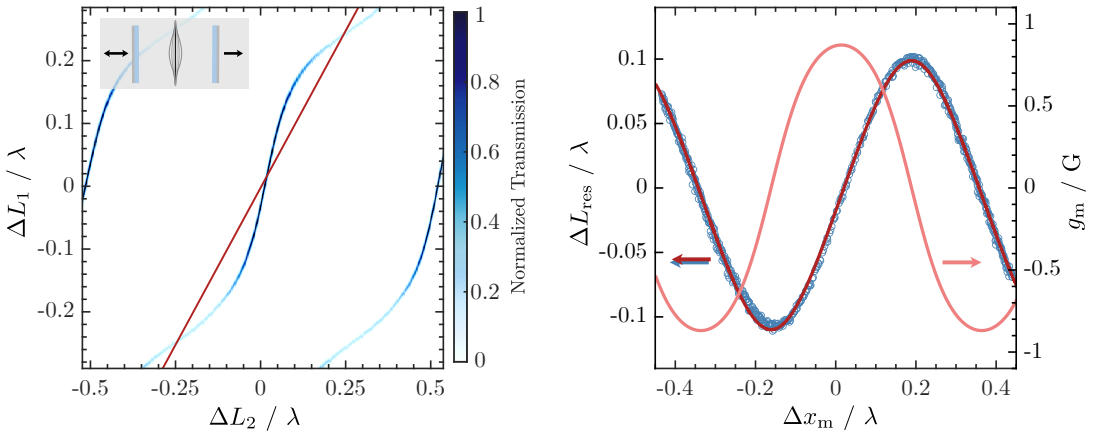

Figure 2.14: Optomechanical coupling. Left panel: Normalized transmission as a function of the resonator intra-cavity position, acquired by a fast scan (20 Hz) of the left sub-cavity during a slow scan (10 mHz) of the right sub-cavity. Red solid line denotes constant cavity length. Insert sketches the experimental realization. **Right panel:** Resonant cavity length ΔL_{res} as a function of resonator position x_{m} (blue circles), together with fit according to expression 2.46 (solid dark red line). By differentiating the fit result the optomechanical coupling g_{m}/G with $g_{\mathrm{m}}^{\mathrm{max}} = 0.88G$ is obtained (solid light red line).

2.3.2 Cavity locking using the optical spring effect

Until now, we considered the shift of the cavity resonance frequency $\Delta\omega_{\mathrm{cav}}$ as a consequence of the optomechanical coupling caused by a displacement of the resonators intra-cavity position x_{m}. However, the interaction can be exploited in the opposite direction as well, if the MiM system is pumped with a laser detuned by $\Delta = \omega_{\mathrm{cav}} - \omega_{\mathrm{L}}$ from the cavity resonance. In this scenario the cavity resonance frequency stays fixed, but the mechanical resonance frequency experiences a shift $\delta\omega_{\mathrm{m}}$. This can be explained by regarding the resonator position x_{m} as a dynamical quantity instead of a static one. As a consequence of the resonator motion the radiation pressure within the cavity is modulated via the optomechanical coupling g_{m}, which leads to a dynamical back-action that affects the resonator again [24, 131]. Mathematically, this is equivalent to the feedback cooling formalism presented in section 2.2.3. The radiation pressure force alters the response of the mechanical resonator, which can be viewed as a new effective susceptibility χ_{eff} again. This leads to a new effective spring constant $k_{\mathrm{m}}^{'} = m\omega_{\mathrm{m}}^{'2} = m(\omega_{\mathrm{m}} + \delta\omega_{\mathrm{m}})^2$ with the mechanical resonance frequency shift $\delta\omega_{\mathrm{m}}$ caused by the so-called optical spring effect. Likewise, a new effective mechanical damping rate $\Gamma_{\mathrm{m}}^{'} = \Gamma_{\mathrm{m}} + \Gamma_{\mathrm{opt}}$ is obtained, where Γ_{opt} is the optomechanical damping rate that can be positive or negative and thus lead to cooling or heating, respectively.

In order to measure this effect experimentally the cavity is pumped with a laser beam of constant power but variable detuning. The change of the resonator frequency $\delta\omega_{\mathrm{m}}$ and the cavity transmission are recorded as a function of the laser-cavity detuning $\Delta = \omega_{\mathrm{L}} - \omega_{\mathrm{cav}}$. To obtain the resonator frequency the light reflected from the cavity is analyzed by a lock-in amplifier. Figure 2.15 shows the measured data together with a Lorentzian fit to the transmitted power and a fit to the mechanical resonance frequency shift using equation (2.49). Utilizing the parameters from the fit the corresponding

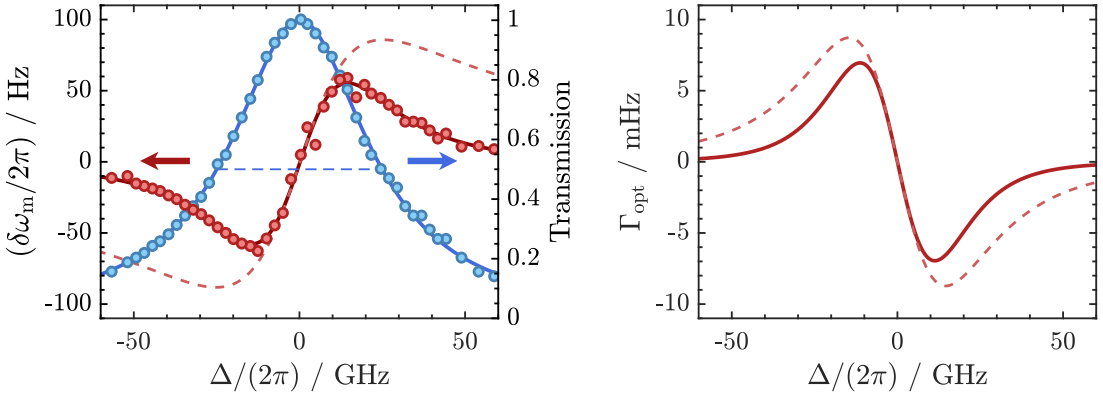

Figure 2.15: Optical spring effect. Left panel: Measured cavity transmission (blue circles) with Lorentzian fit (solid blue line) and measured mechanical frequency shift $\delta\omega_m$ (red circles) with fit according to equation (2.49) (solid red line) for varying laser-cavity detuning Δ and 23.9 µW cavity input power. The blue dashed line denotes the FWHM of the Lorentzian fit with $\kappa/2\pi = (49.95 \pm 0.19)$ GHz, which deviates 1 % from $\kappa/2\pi = (50.45 \pm 0.95)$ GHz obtained by the fit to $\delta\omega_m$. The data were acquired with the MiM system at room temperature, the cavity was not actively stabilized and the mechanical resonance frequency was $\omega_m = 2\pi \cdot 154.957$ kHz. **Right panel:** Optomechanical damping rate Γ_{opt} calculated using the fit results for $\delta\omega_m$ (left) in equation (2.50). In both panels the red dashed lines show the qualitative behaviour for a constant intra-cavity photon number $\bar{n}_{cav}(\Delta = 0)$.

optomechanical damping rate Γ_{opt} can be calculated according to equation (2.50), which is displayed in the right panel of the figure. Both $\delta\omega_m$ and Γ_{opt} are proportional to the intra-cavity photon number

$$\bar{n}_{cav}(x_m) = \frac{\bar{n}_{cav}^{max}}{1 + [2(Gx_m + \Delta)/\kappa]^2} \tag{2.48}$$

with $\bar{n}_{cav}^{max}$ the maximum number of circulating photons at resonance and the single photon coupling strength $g_0 = g_m^{max} \cdot x_{zpf}$ for a MiM system. They can be expressed by [24]

$$\delta\omega_m = \bar{n}_{cav} g_0^2 \left[\frac{\Delta + \omega_m}{(\Delta + \omega_m)^2 + \kappa^2/4} + \frac{\Delta - \omega_m}{(\Delta - \omega_m)^2 + \kappa^2/4} \right] \tag{2.49}$$

$$\Gamma_{opt} = \bar{n}_{cav} g_0^2 \left[\frac{\kappa}{(\Delta + \omega_m)^2 + \kappa^2/4} - \frac{\kappa}{(\Delta - \omega_m)^2 + \kappa^2/4} \right]. \tag{2.50}$$

Here, κ denotes the full width at half maximum (FWHM) linewidth of the cavity. With κ extracted from the fits the finesse $\mathcal{F}$ of the cavity for this specific alignment[11] can be calculated

$$\mathcal{F} = \frac{\omega_{FSR}}{\kappa} = \frac{\pi c}{\kappa L} = 138.2 \pm 9.5 \tag{2.51}$$

with the mean linewidth $\kappa/2\pi = (50.2 \pm 0.5)$ GHz and the measured cavity length at

[11] Similar to the optomechanical coupling also the finesse varies depending on the intra-cavity position of the resonator in the MiM system.

room temperature $L = (21.6 \pm 0.1)\,\mu\text{m}$. The maximal optomechanical damping rate extracted from this measurement is $\Gamma_{\text{opt}} = 2\pi \cdot 1.1\,\text{mHz}$ which is twenty times lower than the mechanical linewidth Γ_{m} at room temperature (see table 2.1).
As our system operates in the unresolved sideband regime ($\kappa \gg \omega_{\text{m}}$) equations (2.49) and (2.50) can be simplified to

$$\begin{aligned} \delta\omega_{\text{m}} &\approx \bar{n}_{\text{cav}} g_0^2 \frac{2\Delta}{\Delta^2 + \frac{\kappa^2}{4}} \\ \Gamma_{\text{opt}} &\approx -\bar{n}_{\text{cav}} g_0^2 \frac{4\kappa\omega_{\text{m}}\Delta}{\left(\frac{\kappa^2}{4} + \Delta^2\right)^2}. \end{aligned} \tag{2.52}$$

In the limit of small detunings ($\Delta \ll \kappa$), which is valid in our experiments these equations further simplify to

$$\begin{aligned} \delta\omega_{\text{m}} &\approx \bar{n}_{\text{cav}} g_0^2 \frac{8\Delta}{\kappa^2} \\ \Gamma_{\text{opt}} &\approx -\bar{n}_{\text{cav}} g_0^2 \frac{64\omega_{\text{m}}\Delta}{\kappa^3} \end{aligned} \tag{2.53}$$

and can be used to obtain the ratio

$$\frac{\Gamma_{\text{opt}}}{\delta\omega_{\text{m}}} = -\frac{8\omega_{\text{m}}}{\kappa}. \tag{2.54}$$

For a red-detuned laser drive $\Delta < 0$ we observe a frequency shift $\delta\omega_{\text{m}} < 0$ and an increased damping of the resonator by $\Gamma_{\text{opt}} > 0$, which results in a reduced resonator mode temperature

$$T_{\text{mode,opt}} = T_{\text{bath}} \frac{\Gamma_{\text{m}}}{\Gamma_{\text{m}} + \Gamma_{\text{opt}}}. \tag{2.55}$$

Here, T_{bath} denotes the effective bath temperature. For $k_B T \gg \hbar\omega_{\text{m}}$ the phonon occupation of the resonator mode is described by

$$\bar{n} = \frac{k_B T_{\text{mode}}}{\hbar\omega_{\text{m}}}. \tag{2.56}$$

In cryogenic environment the optomechanical damping rate Γ_{opt} can easily exceed the mechanical damping rate Γ_{m}, which makes it necessary to operate the cavity always on the cooling side of the resonance ($\Delta < 0$) as otherwise the negative optomechanical damping rate can destabilize the system and drive the resonator into limit cycle oscillations.

Active cavity length stabilization

As one can see in figure 2.15 the resonator frequency change $\delta\omega_{\text{m}}$ is centrally symmetric around the cavity resonance, which is a useful tool to adjust the laser-cavity

detuning around $\Delta = 0$. In practice, we work at a fixed wavelength[12] and adjust the cavity length to tune the MiM system on resonance. The optical spring effect, which is inherent in our system, translates even the smallest cavity length changes to a shift of the mechanical resonance frequency $\delta\omega_\mathrm{m}$. Around the cavity resonance this spring shift has an approximately linear dependence on the cavity length change ΔL of 26 kHz/nm per milliwatt pump power and therefore can be exploited as an error signal to stabilize the length of the cavity. Since our MiM system operates far in the sideband unresolved regime ($\kappa \gg \omega_\mathrm{m}$) the intra-cavity field (and correspondingly, the radiation pressure induced optical spring) follows the detuning adiabatically on all time scales relevant for the locking scheme. The functional principle and main characteristics of the optical spring effect based, optomechanical locking scheme are described in the following and were published in [132].

We employ an active feedback loop to stabilize the cavity length by using one of the cavity mirror piezos (see figure 2.11) as the feedback actuator. The piezo stroke generated by applying a control voltage V_c leads to a cavity length change, which in turn causes the resonator mode to experience a detuning-induced frequency shift $\delta\omega_\mathrm{m}(V_\mathrm{c})$ through the optical spring (see equation (2.49) and figure 2.15). Thus, the whole MiM system can be regarded as a voltage-controlled resonator (VCR). In the control loop (figure 2.16) the VCR is utilized to stabilize the resonator frequency ω_m, and hence the cavity detuning, to a digital local oscillator of frequency ω_set by use of a phase-locked loop (PLL). To obtain the resonator frequency its motion is continuously measured on a balanced homodyne detector (part of the VCR element in figure 2.16) and analyzed by a lock-in amplifier[13]. The detector signal is bandpass filtered[14] and dual-demodulated to access the amplitude and phase of the mechanical motion and thus the VCR. The latter is compared in the PLL to the phase of the set demodulator at frequency ω_set, which represents the setpoint of the lock. By adjusting the bandwidth of the demodulator to $B_\mathrm{d} = 10\,\mathrm{kHz}$, which is much larger than the locking bandwidth, we ensure that the gain and phase response of the detector are not limited by the demodulator. The demodulator phase output ϕ_err is fed as a voltage, scaled by 10 mV/deg, to a proportional integral differential (PID) controller. Here, the output from the phase detector ϕ_err is compared to the set phase $\phi_\mathrm{set} = 0$ and the output voltage V_c from the PID is lowpass filtered (bandwidth 5 kHz) to avoid unwanted excitations of the resonator before being applied to the MiM cavity piezo.

To characterize the performance of the control loop the response of the system to an external perturbation was investigated. By recording the gains and phases of all elements in the control loop using a network analyzer (NA) the so-called open loop response

$$G_0 = G_\mathrm{det} \cdot G_\mathrm{PID} \cdot G_\mathrm{lp} \cdot G_\mathrm{VCR} \cdot G_\mathrm{bp} \tag{2.57}$$

[12] For most experiments (e.g. coupling of the optomechanical to the atomic system) the wavelength is chosen to provide a certain detuning with respect to the atoms.

[13] HF2LI from *Zurich Instruments* with 50 MHz bandwidth - all operations regarding the optical spring lock e.g. demodulation, PID control, loop analysis, etc. are performed with this device.

[14] 2994-150-BNC from *KR Electronics*, center frequency $f_\mathrm{m} = 150\,\mathrm{kHz}$, 3 dB width of 50 kHz.

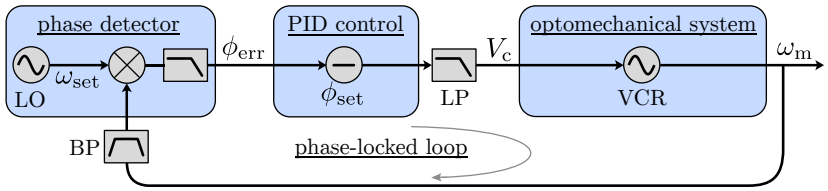

Figure 2.16: Sketch of the phase locked loop. Figure adapted from [132].

is obtained, which can be expressed as the product of the individual open loop transfer functions of all involved elements. G_{det} denotes the transfer function of the phase detector, G_{PID} of the PID controller, G_{VCR} of the optomechanical cavity and G_{lp} (G_{bp}) of the passive lowpass (bandpass) filter, respectively. From the individual transfer functions $G_{\mathrm{i}}(f)$ the frequency dependent gains $|G_{\mathrm{i}}(f)|$ and phase delays $\arg[G_{\mathrm{i}}(f)]$ of the corresponding loop elements can be determined. With the knowledge of the open loop response G_0, the closed loop response

$$G_{\mathrm{cl}}(f) = \frac{V_{\mathrm{c}}(f)}{V_{\mathrm{mod}}(f)} = \frac{G_0(f)}{1 + G_0(f)} \tag{2.58}$$

can be derived that characterizes the response of the whole system. For that we generate a phase modulation by applying a modulation voltage V_{mod} to one cavity piezo and measure the controller output voltage V_{c}.

A sketch of the measurement setup is presented in figure 2.17. The MiM system is stabilized at a red detuning $\Delta < 0$, by locking the resonator frequency to $\omega_{\mathrm{m}} = 2\pi \cdot 154.2\,\mathrm{kHz}$ using the spring-control PLL. While the lock is active, the stabilized cavity length is perturbed by the modulation voltage V_{mod} applied by the NA to the other cavity piezo, which is not part of the control loop. The output control voltage V_{c} of the loop is picked off and connected as an input to the NA. The measured open loop transfer functions of the individual loop elements G_{i} and the resulting closed loop response G_{cl} are depicted in figure 2.18. Since the optomechanical VCR has a bandwidth $B_{\mathrm{VCR}} \gg 10\,\mathrm{kHz}$ it can be regarded as a constant prefactor $G_{\mathrm{VCR}} \in \mathbb{R}$ and is therefore used as the only free fit parameter in the loop analysis. By multiplying all measured gains $|G_{\mathrm{i}}|$ and adding the measured phases $\arg(G_{\mathrm{i}})$ one arrives at the full open-loop gain G_0. The measured closed-loop gain $|G_{\mathrm{cl}}|$ and phase $\arg(G_{\mathrm{cl}})$ match the expected characteristics, calculated

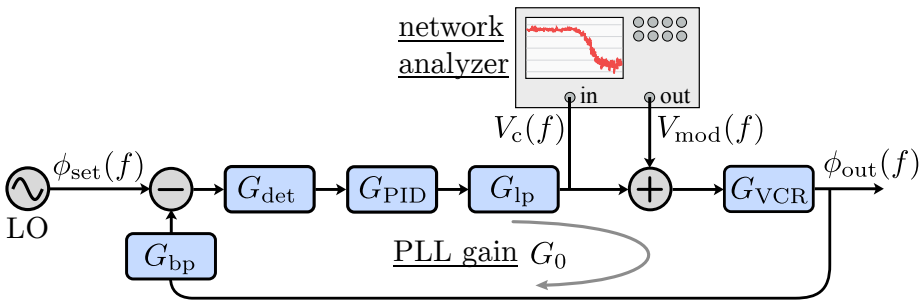

Figure 2.17: Sketch of the loop analysis measurement setup. Figure adapted from [132].

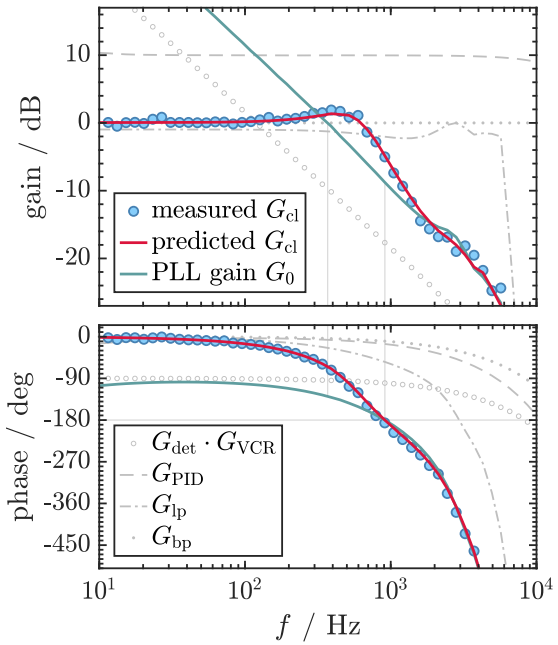

Figure 2.18: Loop response analysis. Direct measurement of the closed-loop response G_{cl} and indirect measurement of the open-loop response G_0 through measurement of the individual transfer functions G_i of the PLL elements. Top panel shows the gain $|G|$ and bottom panel shows the phase $\arg(G)$ of the measured G_{cl} (blue circles) and the predicted response (red solid line) calculated by equation (2.58) using the measured G_0 (green solid line). G_0 is derived from separate response measurements of the phase detector G_{det}, the PID controller G_{PID} and the passive lowpass (bandpass) filter G_{lp} (G_{bp}). $G_{VCR} \in \mathbb{R}$ is the only free parameter in G_0 to fit G_{cl}. The unity gain frequency $f_0 = 370\,\mathrm{Hz}$ (logarithmic zero-crossing at $|G_0| = 1$) and $f_\pi = 910\,\mathrm{Hz}$ for positive feedback [$\arg(G_0) = -180°$] are indicated by vertical lines. Figure adapted from [132].

using G_0 in equation (2.58), very well. We define the locking bandwidth of the spring control through the unity gain bandwidth (zero-crossing of the logarithmic scale) of the open loop transfer function $|G_0| = 1$, which corresponds to a frequency of $f_0 = 370\,\mathrm{Hz}$. The lock is stable with a phase margin of $\arg[G_0(f_0)] + 180° = 51°$ that is defined by the frequency difference of f_0 to the point $f_\pi = 910\,\mathrm{Hz}$ where the open-loop phase becomes $\arg(G_0) = -180°$. In consequence, this point allows to read of the gain margin $-|G(f_\pi)| = 8.8\,\mathrm{dB}$ of the lock, which indicates a good stability.

This locking scheme can be implemented in a variety of optomechanical systems, operating in the unresolved sideband regime, where the optical spring produces an asymmetric, dispersive feature around the cavity resonance. For the lock any mechanical mode, whose Q-factor and optomechanical coupling are sufficiently large, can be used. Strictly speaking, the linewidth Γ_m of the used resonator mode has to be narrow, compared to the width of the dispersive feature $\delta\omega_m^{max} - \delta\omega_m^{min}$, to allow for a reliable cavity length discriminating measurement. However, the shape of the error signal $\delta\omega_m(\Delta)$ is governed by the linewidth of the cavity κ and the mechanical frequency ω_m only (see equation (2.49)) and can not be tuned in general.

For our experimental setup, this locking scheme is superior to other locking schemes, as it does not require additional modulation of neither the used light[15], nor the cavity and it allows to stabilize the cavity on - or close to - resonance. Especially the latter is strictly required in order to perform coupling experiments between cold atoms and a mechanical resonator.

[15] Pound-Drever-Hall locking is unfavourable in our case, as the magnitude of the error signal scales with Ω_{mod}/κ. Since our cavity linewidth exceeds technically feasible modulation frequencies Ω_{mod} by far, the achievable signal to noise ratio is inapplicable for locking.

2.4 Preparation and measurement of atomic spin states

An alternative way of realizing a hybrid atom-mechanical system is to address the coupling of the resonator motion to internal atomic states instead of their center of mass motion. This approach is no longer limited by trapping frequencies in the sub-MHz range that are realizable in optical lattices in order to establish resonant coupling. Thus, it benefits from much higher employable resonator frequencies in the MHz or GHz range, depending on the choice of internal states i.e. Zeeman or hyperfine states. With increasing mechanical resonance frequency the thermal phonon occupation at a given bath temperature is reduced, which results in a decreased thermal decoherence rate and relaxes the requirements for the coupling strength to reach the strong coupling regime. Moreover, high frequency resonators are less susceptible to other decoherence sources like vibrational and laser noise.
The proposed schemes for long-distance coupling [42, 48] make use of the Faraday effect [133] that causes a polarization rotation of the light that traverses the atomic sample. This change in polarization can be utilized to transform spin oscillations, for example originating from Larmor precession of the atomic total angular momentum, into intensity modulations that enable radiation pressure coupling to the resonator. In this scenario the spin oscillation frequency can be easily tuned into resonance with the mechanical oscillation by variation of the magnetic field that provides the quantisation axis.
In order to enable internal state coupling in our hybrid system the preparation of the atomic sample in different m_F states of the $\mathrm{F} = 2$ manifold via radio frequency driven Rabi oscillations was implemented by C. Schellong [134]. During the course of this thesis the feasibility of the readout of these states via Faraday rotation was investigated together with J. Hahne [135].

2.4.1 m_F - state preparation

In order to achieve a clean and reproducible initialization of the atoms in one highly polarized spin state a stable magnetic offset field $\mathbf{B}_0$ that defines the quantization axis is needed. Furthermore, a thorough compensation of magnetic stray fields as well as the earth's magnetic field is mandatory. We use three pairs of compensation coils (see figure 2.21 and refer to [96] for details) to neutralize the stray fields in each spatial direction and employ the atoms as highly sensitive magnetic field sensors for the adjustment of the needed compensation currents[16]. A prerequisite for this procedure is a working BEC machine with condensates produced in an optical dipole trap, whose spin composition is analysed by Stern-Gerlach separation (SGS). A detailed description of the procedure can be found in [134].
The spin state preparation begins in the magnetic trap phase of the experimental cycle. In the MOT and molasses phases the atoms occupy all m_F states of the $\mathrm{F} = 2$ manifold. However, in the magnetic trap only atoms with $m_\mathrm{F} = +1, +2$ can be trapped. After rf-evaporation in the magnetic trap we obtain a spin polarized BEC in the stretched

[16] The residual magnetic stray fields after the compensation procedure were measured to be smaller than $B_\mathrm{res} = 3\,\mathrm{mG}$. The compensation has to be checked daily when working with spin states, since the magnetic stray fields in the lab can change over time due to experiments with strong magnetic fields ($>1\,\mathrm{T}$) in the neighbouring laboratories.

state $|\mathrm{F}=2, m_\mathrm{F}=+2\rangle$. An offset field generated by the Helmholtz coils, previously used for the MOT fields, provides a non-vanishing magnetic field at the trap center to minimize Majorana spin-flips and serves as the quantization field. The field is oriented along the z-axis in axial direction of the MOT coils and is parallel to the co-propagating dipole trap (DT1) and coupling lattice beams. We use one of the MOT coils to produce a gradient field for the SGS during time-of-flight at the end of the experiment cycle. Therefore, we ramp up another homogeneous offset field along the axial direction using one layer of the compensation coils to maintain the quantization axis before the magnetic trap is switched off and the atoms are transferred to the optical dipole trap.
For the preparation of distinct m_F-state distributions rf-pulses can be used to drive Rabi oscillations between the m_F states (see figure 2.24) and rf-sweeps can be applied to address specific m_F levels. If the offset field $\mathbf{B}_0$ is small the Zeeman splitting of hyperfine levels is linear and all transitions between adjacent m_F levels are equidistant. By applying a π-pulse[17] with an rf-frequency that matches the level splitting caused by the offset field the population of the initial m_F state distribution can be inverted. In our case this leads to the stretched state $|2,-2\rangle$. For larger offset fields the quadratic Zeeman effect lifts the degeneracy of the energy spacing and leads to avoided crossings of the energy levels. This enables to selectively address transitions between specific m_F-levels by tuning the rf-frequency. Using rf-sweeps the population can be adiabatically transferred to any m_F-state enabling access also to fully spin polarized but non-stretched states, e.g. $|2,+2\rangle \rightarrow |2,-1\rangle$ [136].

2.4.2 Spin state detection in a BEC via Faraday rotation

In this section we study interaction of a single, free propagating light beam with a spin polarized BEC that is held in an optical dipole trap. The atoms are prepared in the $|2,+2\rangle$ state as described in the previous section and are illuminated with a light pulse of duration τ detuned by $\Delta_{2,3}$ from the $\mathrm{F}=2 \rightarrow \mathrm{F}'=3$ transition of the D_2 line. The probe beam is traveling along the orientation of the bias field $\mathbf{B}_0$ in z-direction (see figure 2.19) and is polarized in the horizontal plane along x. In this configuration dispersive measurements of the atomic spin polarization can be performed.

The polarization state of the probe field can be described by the *Stokes operators* [137]:

$$\begin{aligned} \hat{S}_0 &= \frac{1}{2}\left(\hat{a}_+^\dagger \hat{a}_+ + \hat{a}_-^\dagger \hat{a}_-\right), \qquad \hat{S}_1 = \frac{1}{2}\left(\hat{a}_-^\dagger \hat{a}_+ + \hat{a}_+^\dagger \hat{a}_-\right), \\ \hat{S}_2 &= \frac{i}{2}\left(\hat{a}_-^\dagger \hat{a}_+ - \hat{a}_+^\dagger \hat{a}_-\right), \qquad \hat{S}_3 = \frac{1}{2}\left(\hat{a}_+^\dagger \hat{a}_+ - \hat{a}_-^\dagger \hat{a}_-\right). \end{aligned} \tag{2.59}$$

where $\hat{a}_\pm^\dagger(\hat{a}_\pm)$ are the creation (annihilation) operators of the $\sigma^\pm$ modes of the field[18] and $\hat{S}_0$ denotes the total intensity of the field. $\hat{S}_1$ can be understood as the imbalance between horizontal and vertical polarization, $\hat{S}_2$ as the imbalance between $\pm 45°$

[17] The spin state vector is rotated by π to the adjacent side of the Bloch sphere. The pulse duration depends on the applied rf-power.

[18] since the linear polarization of the probe field can be expressed as a superposition of two equally strong circular polarized fields, see figure 2.19

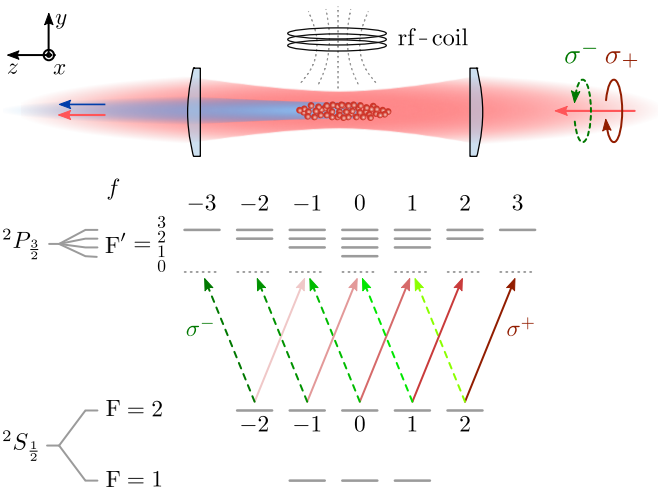

Figure 2.19: Faraday interaction scheme. The atomic sample is irradiated with a linearly polarized beam from the right and causes forward scattering of the Faraday-rotated light. The linear polarization can be decomposed to equal parts in circularly polarized light $\sigma^{\pm}$ whose interaction strength (indicated by the color brightness of the transitions) with the atomic cloud depends on the m_{F}-state of the atoms. The σ^{+} transitions for the $|2,+2\rangle$ state is enhanced by a factor of 15 over the σ^{-} transition [98].

polarization and $\hat{S}_3$ as the imbalance between σ^+ and σ^- [127]. Furthermore, the Stokes operators $\hat{S}_{\mathrm{i}}$, $\mathrm{i} = 1,2,3$ fulfill the angular momentum commutation relation $[\hat{S}_{\mathrm{i}}, \hat{S}_{\mathrm{j}}] = i\hbar\epsilon_{\mathrm{ijk}}\hat{S}_{\mathrm{k}}$ and thus are a convenient choice computationally as well as conceptually, since their dynamics can be understood as rotations on the Poincaré sphere (see figure 2.20).

The atom-light interaction is determined by the dynamics of the magnetic sublevels in the electronic ground-state manifold that couple to the polarization modes of the field. The dynamics in turn, affect the field through the spin-dependent refractive index of the atoms and change the atomic state through the polarization-dependent light-shift [138]. The interaction Hamiltonian can be expressed as

$$\hat{H}_I \;=\; -\sum_{F,F'} \hat{\mathbf{E}}^{(-)} \cdot \hat{\boldsymbol{\alpha}}_{F,F'} \cdot \hat{\mathbf{E}}^{(+)}, \tag{2.60}$$

where $\hat{\mathbf{E}}^{(+)}$ ($\hat{\mathbf{E}}^{(-)}$) is the rotating (counter-rotating) term of the probe electric field operator and $\hat{\boldsymbol{\alpha}}_{F,F'}$ is the atomic polarizability between the hyperfine ground and excited states F and F', respectively. Since the atomic polarizability is a rank-2 spherical tensor operator it can be decomposed into three irreducible components [139]

$$\hat{\boldsymbol{\alpha}}_{F,F'} \;=\; \hat{\boldsymbol{\alpha}}^{(0)}_{F,F'} \;\oplus\; \hat{\boldsymbol{\alpha}}^{(1)}_{F,F'} \;\oplus\; \hat{\boldsymbol{\alpha}}^{(2)}_{F,F'}. \tag{2.61}$$

Following [138, 140] the Hamiltonian can be written as

$$\hat{H}_I \;=\; \hat{S}_0\hat{A}_0 + \hat{S}_1\hat{A}_1 + \hat{S}_2\hat{A}_2 + \hat{S}_3\hat{A}_3 \tag{2.62}$$

with the operators $\hat{A}_k$ representing the atomic observables

$$\hat{A}_0 \;=\; g\left(\frac{2}{3}\alpha^{(0)}\hat{\mathbb{I}}_F + \alpha^{(2)}\left(\sum_{\mathrm{i}}^{N_{\mathrm{at}}} \hat{f}_z^{(\mathrm{i})} - \frac{1}{3}F(F+1)\hat{\mathbb{I}}_F\right)\right), \tag{2.63}$$

$$\hat{A}_1 = g\alpha^{(2)} \sum_{\mathrm{i}}^{N_{\mathrm{at}}} \left(\hat{f}_x^{(\mathrm{i})} \hat{f}_x^{(\mathrm{i})} - \hat{f}_y^{(\mathrm{i})} \hat{f}_y^{(\mathrm{i})} \right), \tag{2.64}$$

$$\hat{A}_2 = g\alpha^{(2)} \sum_{\mathrm{i}}^{N_{\mathrm{at}}} \left(\hat{f}_x^{(\mathrm{i})} \hat{f}_y^{(\mathrm{i})} + \hat{f}_y^{(\mathrm{i})} \hat{f}_x^{(\mathrm{i})} \right), \tag{2.65}$$

$$\hat{A}_3 = g\alpha^{(1)} \sum_{\mathrm{i}}^{N_{\mathrm{at}}} \hat{f}_z^{(\mathrm{i})}. \tag{2.66}$$

Here, $\alpha^{(0)}$ denotes the scalar, $\alpha^{(1)}$ the vector and $\alpha^{(2)}$ the tensor component of the polarizability [139, 141], $\hat{\mathbb{I}}_F$ is the identity operator on a space of dimension $2F+1$ and $g = \omega_L/(2\epsilon_0 V)$ is a constant that contains the interaction volume V. Finally, the sums over $\hat{f}_{\mathrm{k}}^{(\mathrm{i})}$ cover the per atom contributions to the total atomic angular momentum $\hat{F}_{\mathrm{k}}$.

The contributions of the individual terms in the scattering Hamiltonian from equation (2.62) can be interpreted as follows: The rank-0 term causes an atomic-state-independent light shift, which affects both circular polarization modes of the probe field in the same way and therefore will not influence our measurement process. It would be important if we intended to distinguish populations across different hyperfine states instead of sublevel populations within one hyperfine state, hence we can neglect it in the following. The other terms lead to a rotation of the Stokes vector on the Poincaré sphere (figure 2.20) about an axis and angle that depends on the moments of the atomic spin distribution. The rank-1 vector contribution causes a differential phase shift of the circular polarization modes that leads to a rotation around S_3, which precesses the Stokes vector S_{in} in the equatorial plane by an amount proportional to the magnetization along the probe propagation direction $\hat{F}_z \equiv \sum_{\mathrm{i}}^{N_{\mathrm{at}}} \hat{f}_z^{(\mathrm{i})}$. This is the origin of the *Faraday effect* that we want to exploit for the spin state detection. The rank-2 tensor contribution leads to rotations around S_1 or S_2 and couples spin coordinates to elliptical components of the probe field - a signature of birefringence. It can be used to measure the observables $\hat{F}_x^2 - \hat{F}_y^2 \equiv \sum_{\mathrm{i}}^{N_{\mathrm{at}}} \hat{f}_x^{(\mathrm{i})} \hat{f}_x^{(\mathrm{i})} - \hat{f}_y^{(\mathrm{i})} \hat{f}_y^{(\mathrm{i})}$ and $\hat{F}_x\hat{F}_y + \hat{F}_y\hat{F}_x \equiv \sum_{\mathrm{i}}^{N_{\mathrm{at}}} \hat{f}_x^{(\mathrm{i})} \hat{f}_y^{(\mathrm{i})} + \hat{f}_y^{(\mathrm{i})} \hat{f}_x^{(\mathrm{i})}$ and produces a second-order light shift proportional to the atomic quadrupole moment.

The final form of the interaction Hamiltonian is

$$\hat{H}_I = \frac{\hbar}{\tau} G_1 \hat{S}_3 \hat{F}_z + \frac{\hbar}{\tau} G_2 \left[\hat{S}_1 \left(\hat{F}_x^2 - \hat{F}_y^2 \right) + \hat{S}_2 \left(\hat{F}_x \hat{F}_y + \hat{F}_y \hat{F}_x \right) \right] \tag{2.67}$$

with the atom-light coupling constants G_1 and G_2 proportional to $\alpha^{(1)}$ and $\alpha^{(2)}$, respectively. They can be viewed as the per-atom rotation of the incoming light polarization and for atoms in $F = 2$ on the D_2 line amount to (see appendix A.1)

$$G_1 = \frac{\Gamma\lambda^2}{160\pi A} \left(3\mathcal{D}_{2,1} + 5\mathcal{D}_{2,2} - 28\mathcal{D}_{2,3} \right), \tag{2.68}$$

$$G_2 = \frac{\Gamma\lambda^2}{160\pi A} \left(-\mathcal{D}_{2,1} + 5\mathcal{D}_{2,2} - 4\mathcal{D}_{2,3} \right), \tag{2.69}$$

$$\text{with} \quad \mathcal{D}_{F,F'} = \frac{\Delta_{F,F'}}{\Delta_{F,F'}^2 + \Gamma^2/4}. \tag{2.70}$$

Here, Γ and λ denote the linewidth and wavelength of the D_2 tansition and $A = \pi R_{\mathrm{at}}^2$ is the effective interaction area[19]. In the experiment we choose a detuning $\Delta_{2,3}/2\pi = 5\,\mathrm{GHz}$ that is much larger than the excited state hyperfine splitting. Since $\Delta_{F,F'} \gg \Gamma$ we can assume $\mathcal{D}_{F,F'} \approx 1/\Delta_{F,F'}$ and with $\Delta_{2,3} \gg \Delta_{F,F'}$ for all F' we can set $\Delta_{2,1} \approx \Delta_{2,2} \approx \Delta_{2,3} \equiv \Delta_{\mathrm{eff}}$ which leads to

$$G_1 = -\frac{1}{8\pi}\frac{\Gamma\lambda^2}{A\Delta_{\mathrm{eff}}}, \quad \text{and} \quad G_2 = 0. \tag{2.71}$$

This is a remarkable result and tells us that for sufficiently large detunings (no matter if red or blue) the rank-2 component of the polarizability can be neglected. This is a consequence of the symmetry of the polarizability tensor and has nothing to do with the explicit dependence of the detuning of all three of its components (all scale in the same way with $1/\Delta$). By carefully adjusting the detuning the contributions of the polarizability tensor to the interaction can be tuned to engineer a Hamiltonian that can be used for different quantum-information applications [139].

In our case the Hamiltonian reduces to

$$\hat{H}_I = \hbar\frac{G_1}{\tau}\hat{S}_3\hat{F}_z \tag{2.72}$$

and the evolution of the vector operators $\hat{\mathbf{S}}$ and $\hat{\mathbf{F}}$ can be determined from the Heisenberg equation of motion [142]

$$\frac{\partial\hat{F}_{\mathrm{i}}}{\partial t} = \frac{1}{i\hbar}\left[\hat{F}_{\mathrm{i}}, \hat{H}_I\right], \tag{2.73}$$

with the angular momentum commutation relation $\left[\hat{F}_{\mathrm{i}}, \hat{F}_{\mathrm{j}}\right] = i\hbar\epsilon_{\mathrm{ijk}}\hat{F}_{\mathrm{k}}$. By inserting equation (2.72) into the commutator in (2.73) we obtain

$$\begin{aligned}
\frac{\partial\hat{F}_x}{\partial t} &= -\frac{\hbar}{\tau}G_1\hat{S}_3\hat{F}_y, & & \frac{\partial\hat{S}_1}{\partial t} = -\frac{\hbar}{\tau}G_1\hat{S}_2\hat{F}_z \\
\frac{\partial\hat{F}_y}{\partial t} &= \frac{\hbar}{\tau}G_1\hat{S}_3\hat{F}_x, & \text{and} \quad & \frac{\partial\hat{S}_2}{\partial t} = \frac{\hbar}{\tau}G_1\hat{S}_1\hat{F}_z, \\
\frac{\partial\hat{F}_z}{\partial t} &= 0, & & \frac{\partial\hat{S}_3}{\partial t} = 0.
\end{aligned} \tag{2.74}$$

With these equations we can formulate input/output relations for the components of $\hat{\mathbf{S}}$ and $\hat{\mathbf{F}}$ up to first order after the interaction time τ. With the atomic spin pointing

[19] Conventionally, the interaction area is chosen to be the probe beam cross section. However, since the BEC is much smaller than the beam in our case $R_{\mathrm{at}} \ll \mathrm{w}_{\mathrm{lat}}$ the cross section of the BEC is chosen in the following as the effective interaction area

along the z-direction and the probe polarization along the 1-direction we get

$$\begin{aligned}\hat{S}_2^{(\mathrm{out})} &= \hat{S}_2^{(\mathrm{in})} + \hbar G_1 \hat{S}_1 \hat{F}_z, \\ \hat{F}_z^{(\mathrm{out})} &= \hat{F}_z^{(\mathrm{in})}\end{aligned} \tag{2.75}$$

where $\hat{S}_1$ is rotated onto $\hat{S}_2$ by an amount that is proportional to $\hat{F}_z$. This is depicted on the Poincaré sphere in figure 2.20 by the angle φ_3, which is twice as large as the Faraday angle that is measured in the laboratory frame [137]

$$\theta_\mathrm{F} = \frac{|G_1| N_\mathrm{at}}{2} = \frac{1}{16\pi} \frac{\Gamma \lambda^2 N_\mathrm{at}}{\pi R_\mathrm{at}^2 \Delta_\mathrm{eff}} \tag{2.76}$$

that we expect to measure in our system. From the number of atoms $N_\mathrm{at} = 7 \cdot 10^4$ in our optical dipole trap and its trapping frequencies ω_i (see section 2.1) we can calculate the radii of the BEC using the Thomas-Fermi approximation [143]

$$R_i = \sqrt{\frac{2\mu}{m_\mathrm{Rb} \omega_i^2}}, \quad i = x, y, z \tag{2.77}$$

where μ is the chemical potential given by

$$\mu = \frac{\hbar \bar{\omega}}{2} \left(\frac{15 N_\mathrm{at} a}{a_\mathrm{HO}} \right)^{\frac{2}{5}} \tag{2.78}$$

with the scattering length a, $\bar{\omega} = (\omega_x \omega_y \omega_z)^{1/3}$ and $a_\mathrm{HO} = \sqrt{\hbar / (m_\mathrm{Rb} \bar{\omega})}$. In the plane perpendicular to the probe beam direction we arrive at a BEC radius of $R_\mathrm{at} = 3.7\,\mu\mathrm{m}$ which yields a maximal expected rotation angle of $\theta_\mathrm{F} = 24\,\mathrm{mrad} = 1.37°$.
Another measure for the strength of the atom-light interaction is the on-resonance optical depth [137]

$$d_0 = \frac{\sigma_0 N_\mathrm{at}}{A} = \frac{2\sigma_0 \theta_\mathrm{F}}{A G_1} \tag{2.79}$$

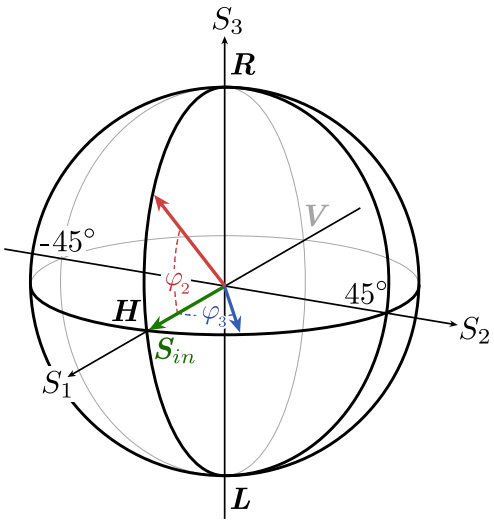

Figure 2.20: Transformation of the Stokes vector on the Poincaré sphere. For an initially linearly polarized beam S_{in} along S_1, a rotation on the sphere around S_3 by an angle $\varphi_3 \propto \langle \hat{F}_z \rangle$ corresponds to a rotation of the polarization vector proportional to the atomic magnetization (the Faraday effect). A rotation around S_2 by an angle $\varphi_2 \propto \langle \hat{F}_x \hat{F}_y + \hat{F}_y \hat{F}_x \rangle$ corresponds to a change in the ellipticity of the light (birefringence). These polarization changes can be detected as a difference in intensities of an appropriately configured polarimeter.

with the on-resonance scattering cross section $\sigma_0 = \lambda^2/\pi$ for π-polarized light. Here, equation (2.76) was used to arrive at an expression that can be used to determine d_0 from the Faraday rotation measurement. For the expected rotation angle this yields $d_0 = 315.4$.

Experimental realization of the spin state detection

Since we want to find out how well the atomic spin state can be read out via Faraday rotation in our current setup we use the coupling lattice beam as a probe beam, but insert an additional mirror in the beam path before the beam reaches the cryostat. It is already aligned with the dipole trap and can therefore be used almost right away. We had to take some additional precautions to make sure that absolutely no residual light is leaking through the coupling beam fiber when no probe pulse is applied. Due to a temporal jitter of the coupling beam shutter of $\tau_{\mathrm{on/off}} = 5\,\mathrm{ms}$ we observed severe atom loss in the BEC due to photon scattering before and after the application of a probe pulse. Details can be found in [135].
A sketch of the used setup is shown in figure 2.21. The coupling beam is collimated again before its polarization is rotated by 45° using a $\lambda/2$ plate for the analysis in a polarimeter that consists of a PBS and a balanced photodetector. Note, that the maximum sensitivity is achieved, when the polarimeter analyses the output along a direction perpendicular to the input. For the measurement of Faraday rotation the analyser needs to be oriented along the linear diagonal directions (±45°), whereas the usage of circularly polarized light for the analyses would perform a measurement of the second order atomic moment due to birefringence in the sample.

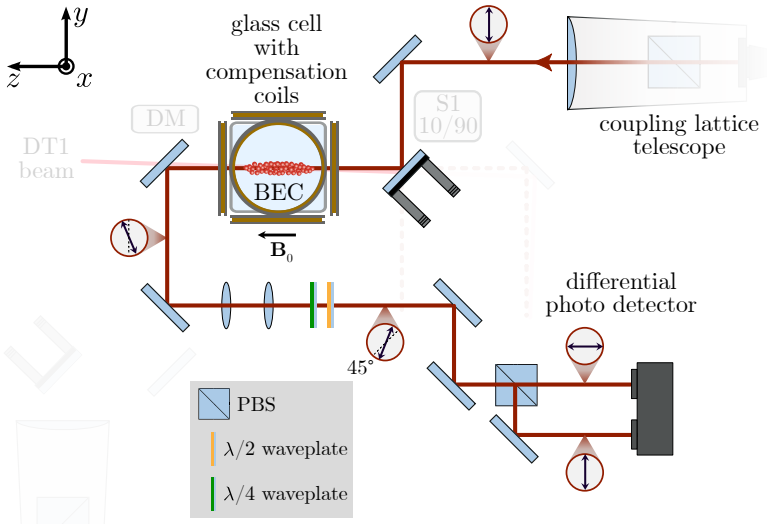

Figure 2.21: Experimental setup for the detection of Faraday rotation. The coupling beam is employed for the Faraday detection. Initially, it is p-polarized along the y-axis and after the interaction with the BEC it has acquired an s-polarized contribution. The beam is picked up with a mirror before it reaches the cryostat and is collimated and refocused on the photo detectors using two lenses. A $\lambda/4$ plate is used to compensate any unwanted ellipticity of the polarization and the subsequent $\lambda/2$ plate is used rotate the polarization by 45° to balance the signal on the differential detector (PDB210A from *Thorlabs* - DC to 1 MHz, CMRR > 40 dB).

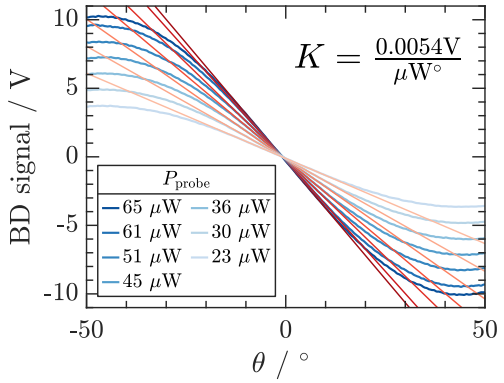

Figure 2.22: Calibration of the balanced detector. The signal produced by the balance detector for a known polarization modulation, applied with an EOM is recorded for different beam powers in front of the detector. The x-axis shows the angle by which the polarzation is rotated away from the 45° basis. Blue solid lines denote the detector signal and red solid lines are linear fits to extract the steepness of the slope.

Balanced detector calibration: In order to calibrate our polarimeter we place an EOM in the beam path of the probe beam to produce a well defined polarization rotation. The EOM is supplied with a triangular scan voltage and the resulting polarization modulation is measured on the balanced detector in the 45° basis. The intensity at the ports of the detector is described by *Malus law* and is given by $I_{\text{trans}} = I_0 \cos(\phi)^2$ and $I_{\text{refl}} = I_0(1 - \cos(\phi)^2)$, respectively. Therefore, the detector signal yields $S^{\text{BD}} = I_{\text{trans}} - I_{\text{ref}} = I_0(2\cos(\phi)^2 - 1) = I_0 \cos(2\phi)$, which allows us to assess a rotation angle of 90° between maximum and minimum intensity of the signal. Figure 2.22 shows the detector signal for different probe beam powers in front of the detector. Since the steepness of the slope increases linearly with the probe beam power we arrive at the calibration factor $K = 0.0054\,\text{V}/(\mu\text{W}\,^\circ)$.

Measurement of the BEC induced Faraday angle

As described earlier the atoms in the BEC are prepared in the $|2, +2\rangle$ state in the optical dipole trap. To measure the Faraday angle θ_{F} we apply probe pulses of $\tau = 300\,\mu\text{s}$ duration while the BEC is held in the dipole trap. In order to vary the atom number in the BEC we apply the probe pulses after a varying hold time in the dipole trap. Figure 2.23 shows the reduction of the total atom number in the BEC with increasing hold time in the DT (left panel), the Faraday angle as a function of time for exemplary atom numbers (central panel) and the Faraday angle per atom number in the BEC (right panel). In the central panel we can see that the Faraday angle decreases over the duration of the probe pulse. This can be attributed to atom loss due to photon scattering induced by the probe light. For the used parameters we can calculate the scattering rate according to [98, 144]

$$\gamma_{\text{sc}} = \frac{\Gamma}{2} \frac{2\Omega_\pi^2}{\Gamma^2 + 4\Delta_{2,3}^2 + 2\Omega_\pi^2} = 2870\,\text{Hz} \tag{2.80}$$

where $\Omega_\pi = 2\sqrt{2/3}\tilde{\Omega}_{jj'}\sqrt{\Phi_L}$ is the Rabi frequency for a laser beam with linear polarization and photon flux Φ_L [20]. This results on average in 0.86 scattering events per

[20] $\tilde{\Omega}_{jj'} = d_{jj'}\mathcal{E}_0/\hbar$ is the vacuum coupling strength, $d_{jj'}$ the reduced atomic dipole moment and $\mathcal{E}_0 = \sqrt{\hbar\omega_L/(2\epsilon_0 c A_p)}$ the vacuum electric field density with cross-sectional area A_p of the probe beam

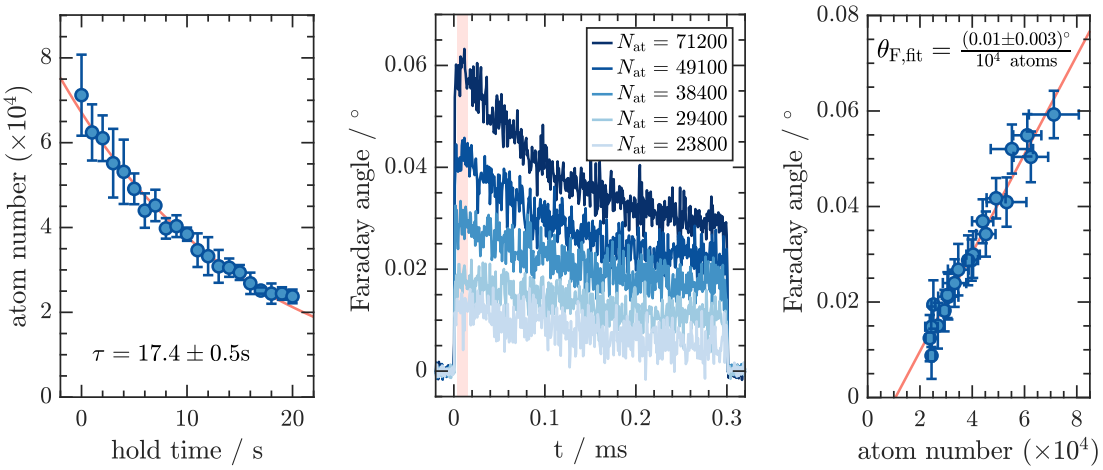

Figure 2.23: Characterization of the Faraday angle as a function of the atom number. Left panel: Atom number of the BEC in the optical dipole trap as a function of the hold time in the trap. **Central panel:** Measured Faraday angle θ_F for selected atom numbers in the ODT as a function of time. The atoms are prepared in the $|2,+2\rangle$ state and probed with a light pulse of 300 µs duration, $P_{\text{probe}} = 141\,\mu\text{W}$ power and a detuning $\Delta_{2,3}/2\pi = 5\,\text{GHz}$. θ_F is extracted from the amplitude of the signal in the first 20 µs (red shaded area). **Right panel:** Extracted Faraday angle (blue circles) as a function of the atom number in the BEC together with linear fit (red).

atom over the duration of the probe pulse.

The maximum Faraday rotation angle is extracted by averaging over the first 20 µs of the time traces. As expected θ_F increases linearly with the number of atoms but the measured rotation angle $\theta_{F,\text{max}} = (0.059 \pm 0.005)°$ is a factor of 21 smaller than calculated from equation (2.76). The same holds for the optical depth, which is calculated from equation (2.79) using the measured angle $d_{0,\text{max}} = 15.1$.

The most probable reason for that is the mode mismatch between the atomic sample and the probe beam mode (as indicated in figure 2.19). If an off-resonant laser beam is used to irradiate a large ensemble of atoms the scattered light interferes constructively in the forward direction of the incoming beam [145]. However, the efficiency of this process is determined by the geometry of the target and is maximized if the scattered light is well characterized by a single mode that overlaps with the input field. This overlap can be estimated by the Fresnel number

$$\mathsf{F} = \frac{\pi R_{\text{at}}^2}{\lambda L_{\text{at}}} \approx 1.7 \tag{2.81}$$

that compares the "atomic Rayleigh length" $\pi R_{\text{at}}^2/\lambda$ to the length of the atomic ensemble $L_{\text{at}} = 33.2\,\mu\text{m}$ and describes, whether the scattered light can be attributed to a single paraxial mode. For $\mathsf{F} \approx 1$ the single mode assumption is justified, but if $\mathsf{F} \gg 1$ for a wide sample, the emission can occur into a large number of modes, or if $\mathsf{F} \ll 1$ in the case of a very long sample, the light strongly diverges due to diffraction. For our BEC the single mode assumption is still applicable, yet it only accounts for the

geometry of the atomic ensemble. Additionally, the optical mode of the probe beam has to be matched to the scattered mode which in dipole trapped ensembles is approximately fulfilled if the waist of the probe beam matches the waist of the atomic ensemble [146, 147]. In our setup the probe beam waist is $w_{lat} \approx 20 R_{at}$ and therefore a deterioration in efficiency is expected.

Detection of Rabi oscillations via Faraday rotation

To demonstrate that the atomic spin state evolution can be observed in real-time using Faraday rotation we apply an rf-pulse simultaneously to the probe pulse to drive Rabi oscillations between the atomic m_F states. The rf-frequency is chosen to match the energy difference between the m_F states, which is determined by the applied bias field B_0.

The Rabi oscillations can be made visible in two ways: Either a destructive spin state measurement is performed, where the atoms are first prepared in a certain spin state, or mixture of spin states (depending on the duration of the rf-pulse), and subsequently

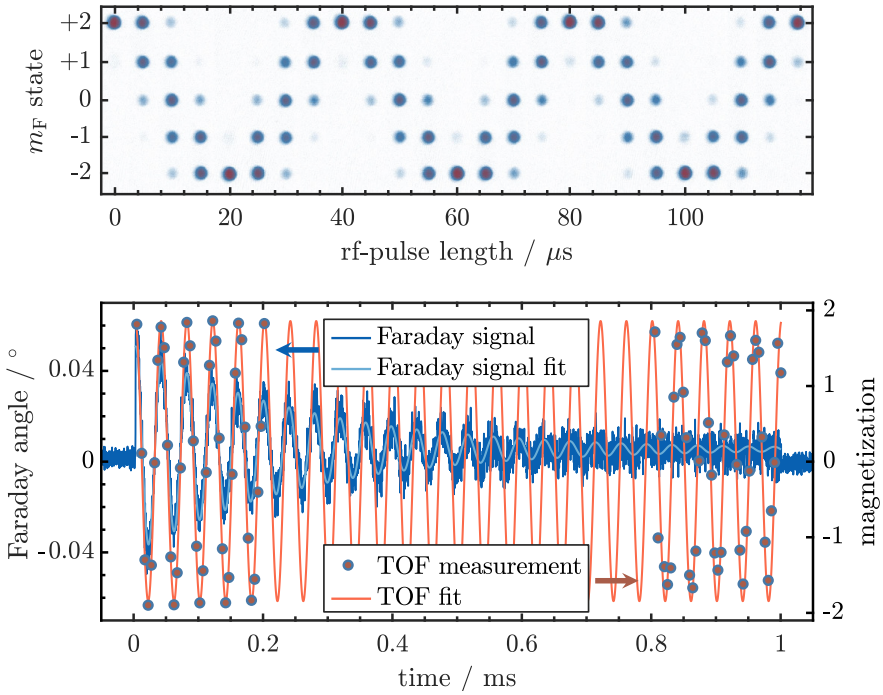

Figure 2.24: Measurement of Rabi oscillations via Faraday rotation vs. TOF. Top panel: Absorption images of the atomic ensemble after Stern-Gerlach separation during a time-of-flight measurement. The atoms are prepared in different m_F states by application of an rf-pulse of varying pulse length that leads to Rabi Oscillations between the states $m_F = +2$ and $m_F = -2$. **Bottom panel:** Comparison of a single-shot Rabi oscillation measurement via Faraday rotation (blue trace) with a Rabi oscillation measurement by mapping out the magnetization of the BEC via 80 TOF sequences (circles). The fits yield the Rabi frequencies $\Omega_{R,\mathrm{Fara}} = (25.281 \pm 0.007)\,\mathrm{kHz}$ and $\Omega_{R,\mathrm{TOF}} = (24.9752 \pm 0.0001)\,\mathrm{kHz}$. Parameters: $f_{\mathrm{RF}} = 906\,\mathrm{kHz}$, $B_0 = 1.32\,\mathrm{G}$, $P_{\mathrm{probe}} = 141\,\mu\mathrm{W}$, $\Delta_{2,3} = 5\,\mathrm{GHz}$. Note that on the time scale of $t \approx 1\,\mathrm{ms}$ the quadratic Zeeman effect is negligible for the applied magnetic field.

imaged by a standard absorption imaging sequence with an additional magnetic field gradient applied during the time-of-flight to separate the spin states (see top panel of figure 2.24). This technique requires a series of absorption images to map out the evolution of the spin state, since each image provides only a snapshot of the instantaneous spin state. At the same time it allows to determine the purity of the prepared atomic spin state.

The other way (presented in more detail in [135]) is to use a single light pulse of $\tau = 1\,\mathrm{ms}$ duration to make the evolution of the spins visible via Faraday rotation. In principle this method is capable to produce a quantum-non-demolition (QND) measurement of the atomic ensemble since the interaction entangles the atomic and light observables [137]. An exemplary measurement is presented in figure 2.24 (blue trace in bottom panel) where the Rabi oscillation can be observed in real-time. The oscillation is damped, which can be explained by the decrease in signal amplitude due to photon scattering from the probe beam that was already observed in figure 2.23. Nevertheless, the Rabi frequency $\Omega_{R,\mathrm{Fara}} = (25.281 \pm 0.007)\,\mathrm{kHz}$ can be extracted from a fit to the trace. It can be compared to the Rabi frequency determined from the fit of the magnetization of the sample that is obtained by summing over the relative atom numbers for all spin states in each TOF image (column in upper panel of figure 2.24). This fit yields a slightly lower Rabi frequency of $\Omega_{R,\mathrm{TOF}} = (24.9752 \pm 0.0001)\,\mathrm{kHz}$. The difference between the fitted Rabi frequencies is caused by the optical Stark effect [148] that leads to a detuning dependent light-shift of the atomic energy levels induced by the Faraday probe beam. For increasing detuning $\Delta_{2,3}$ we observe a decrease of $\Omega_{R,\mathrm{Fara}}$ that approaches $\Omega_{R,\mathrm{TOF}}$ asymptotically. At the same time the damping rate of the oscillation Γ_{osc}, which can be extracted from fits to data similar as depicted in figure 2.24, decreases with $1/(\Delta_{2,3})^2$, which confirms that the signal amplitude decreases due to photon scattering (see figure 2.25).

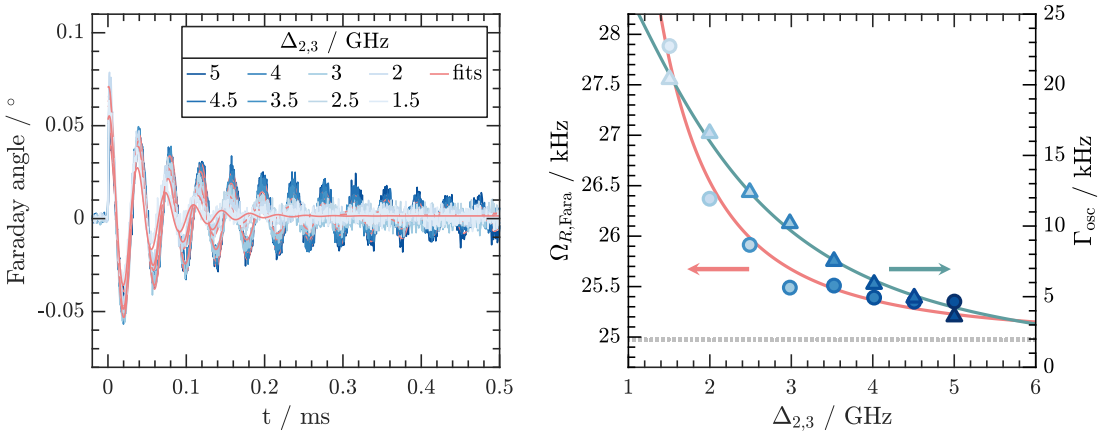

Figure 2.25: Rabi Oscillations via Faraday rotation for varying detuning. Left panel: Faraday signal of the spin state evolution for different probe beam detunings $\Delta_{2,3}$ between 1.5 GHz and 5 GHz at constant probe beam power $P_{\mathrm{probe}} = 141\,\mu\mathrm{W}$. For each detuning a fit (red lines) is used to extract the Rabi frequency $\Omega_{R,\mathrm{Fara}}$ and the damping rate Γ_{osc}. **Right panel:** Extracted Rabi frequencies $\Omega_{R,\mathrm{Fara}}$ (circles) with fit (red) and damping rates Γ_{osc} (triangles) with fit (blue) as a function of the probe beam detuning $\Delta_{2,3}$. The dotted line denotes $\Omega_{R,\mathrm{TOF}}$.

Larmor precession measurement

For an application in the sense of coupling to a mechanical resonator higher spin precession frequencies and much likely a larger signal amplitude are required. As for the frequency, the Larmor precession of the atomic spins can be utilized. Its frequency is dependent on the strength of the magnetic offset field, which defines the quantization axis:

$$f_{\mathrm{L}} = g_{\mathrm{F}} \frac{e}{4\pi m_e} B_0 \tag{2.82}$$

with the Landé-factor $g_{\mathrm{F}} = 1/2$ (for $F = 2$ in ^{87}Rb), as well as the charge e and the mass m_e of an electron. The offset field has to be adiabatically rotated into an axis perpendicular to the propagation axis of the light, such that the offset field lies in the oscillation plane of the probe beam's B-field component. Regarding the signal strength it turned out that a BEC is not the best choice. Although it has a much higher atomic density than for example atoms in a vapour cell, or confined in an optical dipole trap, it contributes with a considerably lower atom number to the overall signal. Since we could not observe any Larmor precession on our BEC sample we tested the Faraday measurement scheme on an ensemble of ultracold atoms released from the magnetic trap [135].
The atoms are prepared in the magnetic trap as described in section 2.1, except that the rf-evaporation is stopped before a BEC is produced. We obtain a thermal cloud of $N_{\mathrm{at}} \approx 1.1 \cdot 10^6$ atoms that we release from the magnetic trap. After 1 ms of free fall the probe pulse is applied to make sure that the atoms are still in the interaction region of the beam.

This measurement should rather be regarded as a proof-of-principle attempt since there are a few uncertainties in the measurement procedure. The offset field needs to be oriented along the y-axis of the experimental setup to observe Larmor precession. Since the magnetic fields in the MT are much larger than the offset field we have to switch the MT off to allow for observation. Moreover, we probe the atoms very shortly after release from the magnetic trap such that we can not rotate the offset field adiabatically into the y-direction, but have to switch it on already before we release the atoms from

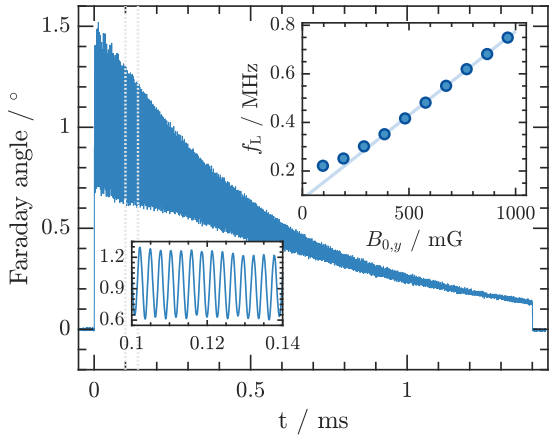

Figure 2.26: Larmor precession measurement. Exemplary trace of the Larmor precession measured in an ensemble released from the magnetic trap. Inserts show a zoom into the area between the dotted lines and the dependence of the Larmor frequency f_{Larmor} on the offset field $B_{0,y}$ in y-direction. The frequencies were extracted by Fourier analysis of traces similar to the depicted one, for different settings of $B_{0,y}$. For the plotted trace $f_{\mathrm{L}} = 0.351\,\mathrm{MHz}$. Parameters: $P_{\mathrm{probe}} = 100\,\mu\mathrm{W}$, $\Delta_{2,3} = 5\,\mathrm{GHz}$, $B_{0,y} = 385\,\mathrm{mG}$.

the trap. It is likely that this influences the atomic spin states in an unpredictable way. Nevertheless, we were able to detect the Larmor precession with this approach and the results are summarized in figure 2.26. Due to the increased atom number we observe much larger rotation angles with Larmor frequencies up to $f_{\mathrm{L}} = 0.75\,\mathrm{MHz}$. These were only limited by the available current source that produces the offset field $B_{0,y}$ at the time of the measurement[21]. As expected the Larmor frequency increases linearly with the applied offset field. The deviation of the data points for $B_{0,y} < 400\,\mathrm{mG}$ from the linear fit can be explained by residual magnetic field components in other spatial directions that were not well compensated. From the measured angle $\theta_{\mathrm{F,max}} = 1.49°$ we can calculate an optical depth of $d_{0,max} = 381$. Subsequent experiments should be performed in a far detuned, large volume optical dipole trap, which would allow for much better control over magnetic fields and longer interaction times.

Conclusion

In the previous sections the feasibility to detect the atomic spin states via a polarization measurement based on the Faraday effect was demonstrated. The presented method is capable of detecting polarization rotations by angles as small as $\theta_{\mathrm{F}} = 0.01°$ even in samples much smaller than the probe beam and to resolve Rabi oscillations and Larmor precession in real-time. However, for further application we note that the signal strength, characterized by the optical density d_0 that we obtain from a BEC, is likely too small to be useful for coupling experiments that involve a mechanical resonator. Larger signals can be obtained using samples with a higher atom number. A common approach is to employ cold atoms confined in an elongated dipole trap and to probe the sample along its long axis to maximize the number of atoms that contribute to the signal [127, 137]. This allows at the same time for long hold times and precise control of the quantization axis, given by an offset magnetic field. Additionally, the interaction strength can be maximized by matching the mode of the probe beam to the cloud size of the atomic ensemble.

We were preparing to implement the aforementioned changes in order to achieve stronger spin-light coupling and planned to utilize the described interaction scheme for coupling to a mechanical resonator. This also involved the design of a higher frequency mechanical resonator in the MHz range that would be less susceptible to low frequency noise and would benefit from a lower thermal phonon occupation. The resonator was simulated and designed in *COMSOL* by C. Friesen based on the findings in [90, 149] and fabricated by *Norcada*. It is made from a Si_3N_4 film that is patterned with a honeycomb structure of air holes resembling a crystalline structure. In the center of the material a few holes are displaced from the periodic arrangement and form a defect mode, which serves as the mechanical resonator. This allows to decouple the resonator from the acoustic noise of its support structure and lets the resonator mode decay evanescently into a "soft" clamping region [150]. In contrast to the usual "rigid" clamping the resonator experiences reduced noise from the frame modes and radiates less energy into the substrate, which leads to further increased Q-factors (values of $Q > 10^8$ at room temperature were reported [90]). Since this structure provides a region that can filter

[21] All traces and the corresponding Fourier transforms can be found in appendix A.2

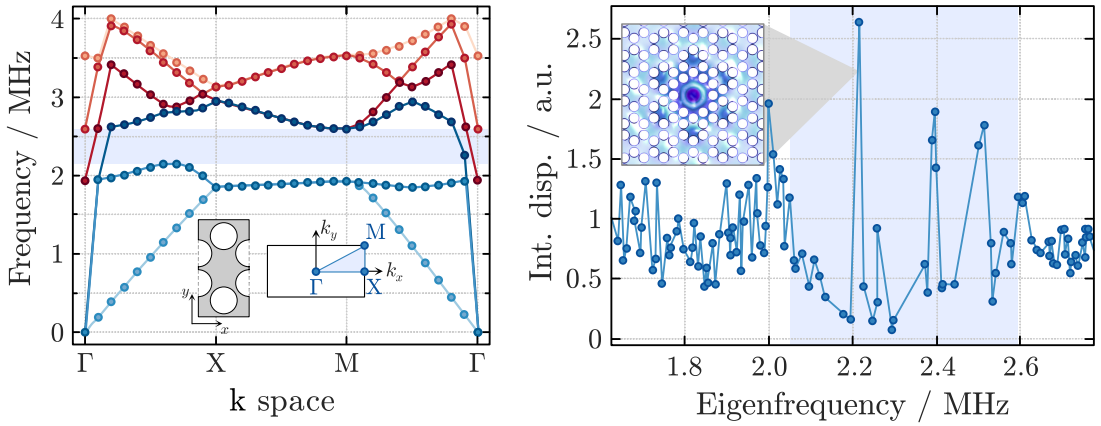

Figure 2.27: Mechanical response for our phononic shield resonator. Left panel: Simulated band diagram for a large number of unit cells. The inset shows one unit cell of the honeycomb lattice in real space and the corresponding first Brillouin zone in k space. The wave vector k is swept along the blue line within the Brillouin zone to map out the bands. The shaded blue region denotes the emerging band gap. **Right Panel:** Simulated integrated displacement spectrum of the mechanical mode. The large peak within the band gap at $f_\mathrm{m} = 2.215\,\mathrm{MHz}$ denotes the central resonance frequency of the mode. The inset shows the out-of plane displacement pattern of the mode of interest.

and confine acoustic waves it can be understood as a band gap. Therefore, this kind of resonator is often referred to as a phononic crystal or phononic shield resonator. Figure 2.27 shows the simulation data for our device. The blue shaded areas depict the band gap within which we expect the central resonator mode at a frequency of $f_\mathrm{m} = 2.215\,\mathrm{MHz}$. To produce a corresponding Larmor frequency we would need to apply a bias field of $B_0 = 3\,\mathrm{G}$ which is easily done experimentally. We have ordered 8 devices, which we still have to characterize experimentally.

However, shortly after the outbreak of the Corona pandemic a paper on light-mediated strong coupling of atomic spins to a mechanical resonator was published by T. Karg *et al.* [127]. It presented a comprehensive study of the spin-mechanical interaction, covering normal-mode splitting, coherent energy exchange, thermal noise squeezing and dissipative coupling in their hybrid atom-mechanical system. Thus, we had to acknowledge that this group was too far ahead of us and therefore we decided to cease our internal-state coupling efforts.

Chapter 3

Coupling experiments in a pump asymmetry compensated lattice

In this chapter the effect of the pump asymmetry on the coupling in the hybrid atom-mechanical system is studied by means of a numerical simulation as well as experimentally. An approach to compensate the asymmetry, suited to alleviate its undesirable consequences, is presented and the performance of the compensated coupling lattice is characterized. The utilized scheme allows to enter a previously inaccessible regime for sympathetic cooling of mechanical motion, albeit performing different than expected.

Hybrid atom-mechanical systems are a prominent subject of many proposals in fundamental research and may open the door to novel quantum technologies. Possible applications range from ground state cooling of mechanical motion [45–47, 68, 70, 151, 152], coherent quantum state transfer [43, 127, 144, 153], teleportation and entanglement [42, 151] to quantum backaction evading measurements of mechanical motion [64]. Moreover, schemes for improved precision force sensing [154] or the engineering of phase transitions in atomic clouds by coupling atoms to mechanical resonators were suggested [155–157]. Yet, many of those still remain to be demonstrated.

In our hybrid system consisting of cold ^{87}Rb atoms in an optical lattice and a mechanical resonator in a MiM system we want to bring both constituents together after initializing them in their respective ground states to study their coherent dynamics. For the mechanical resonator this can be achieved by cryogenic pre-cooling and subsequent feedback or sympathetic cooling. Both cooling mechanisms are, in principle, capable of ground state cooling the mechanical resonator even in the bad cavity regime ($\omega_\mathrm{m} \ll \kappa$) [45, 62, 70] and the latter can be employed to characterize the hybrid coupling mechanism.

One significant challenge in the realization of strong coupling to the center of mass motion of atoms in an optical lattice, is the occurrence of an instability that arises at high atomic densities in the hybrid atom-mechanical system [72–74]. Its origin is the asymmetric pumping in the coupling lattice, which is intrinsic in these systems and results in disruptive collective atomic motion in the lattice [75, 76]. The instability leads to excessive heating of the mechanical resonator and ensues predominantly in near detuned red lattices (see section 3.2).

On the atomic side, we can routinely produce Bose-Einstein condensates, but coupling them to the resonator was elusive in the past. To avoid excessive resonator heating at high atomic densities in a red detuned coupling lattice a blue detuned lattice was used for the coupling attempt. In this configuration however, the repulsive interaction with the lattice potential leads to anti-trapping and expells the atoms from the dipole trap. To counteract this, we utilized an additional (far) red detuned 2D lattice perpendicular to the coupling lattice, which provided increased confinement and enabled to observe the signature of atomic excitations to higher lattice bands at the mechanical resonance frequency [77].
Motivated by the prospect of surpassing the hitherto existing limitations, induced by asymmetric lattice pumping, we started to elaborate a scheme to compensate the asymmetry. This chapter describes our approach to realize a balanced coupling lattice that shall facilitate hybrid coupling in a so far inaccessible regime and might be suited to enable coupling of a BEC to a mechanical resonator.
Due to technical problems with our cryostat we were not able to run it at its base temperature of $T_{\mathrm{base}} = 500\,\mathrm{mK}$ over an extended period of time and had to warm it up several times to find the cause of the malfunction. Therefore, the measurements presented in this chapter were conducted at room temperature and the performance of the pump asymmetry compensated (PAC) lattice will be gauged against the uncompensated lattice.

3.1 Sympathetic cooling

Commonly, sympathetic cooling is known as a technique applied to microscopic particles of different species, where energy exchange between the species is mediated through inter-particle collisions. One species that can be effectively cooled, for example by laser or evaporative cooling, is used as the coolant for the other, which on its own can not be further cooled directly. In this way it is possible to cool ions with other ions [158] or neutral atoms [159], or to produce quantum degenerate Fermi gases of neutral atoms by cooling fermionic atoms through collisions with bosonic ones [160].
However, the energy can also be transferred indirectly by coupling two systems via a mediating link. Recently, this has been demonstrated by confining a single proton and a sample of laser cooled Be^+ ions in two spatially separated Penning traps, that were connected by the particle induced image currents transmitted through a superconducting LC-circuit [161].
In the realm of optomechanics we can also achieve collectively enhanced, long-range sympathetic cooling of a macroscopic mechanical resonator by utilizing laser cooled atoms confined in an optical lattice as the coolant [62, 65]. Interestingly, for the long-range interaction schemes cooling is possible despite the large mass ratio of $\approx 2 \cdot 10^6$ between the resonator and the atoms[22], in contrast to $\lesssim 100$ for the collision mediated sympathetic cooling schemes. In our case, the efficiency of the cooling effect depends on the coupling strength between the two subsystems, which can in return be inferred from sympathetic cooling measurements.

[22] Here, an effective mass $m_{\mathrm{eff}} = 3\,\mathrm{ng}$ of the resonator mode and $N_{\mathrm{at}} = 10^7$ Rb atoms are assumed.

In this section the theoretical principles of sympathetic cooling will be reviewed. Experimental results will be presented in section 3.5.

3.1.1 Principles of sympathetic cooling

In the following, the mechanical resonator mode and the motion of the atoms inside the lattice wells will be treated as harmonic oscillators that are coupled by a spring, which is given by the coupling light field. This hybrid coupling scheme for long-distance interaction is depicted in figure 3.1 and can be understood as follows [74, 162]. A displacement x_m of the mechanical resonator changes the cavity resonance frequency ω_cav of the MiM cavity (see section 2.3.1 and figure 2.13) and correspondingly the phase ϕ_r of the reflected light that creates the optical lattice. The phase shift with respect to the incoming beam is [24]

$$\phi_\mathrm{r} = \arctan\left(\frac{\Delta\kappa}{(\kappa/2)^2 - \Delta^2}\right) \overset{|\Delta|\ll\kappa}{\simeq} 0, \tag{3.1}$$

and accordingly its derivative with respect to the detuning yields

$$\frac{\mathrm{d}\phi_\mathrm{r}}{\mathrm{d}\Delta} = \frac{\kappa}{(\kappa/2)^2 + \Delta^2} \overset{|\Delta|\ll\kappa}{\simeq} \frac{4}{\kappa}. \tag{3.2}$$

As described in section 2.3.1 a small resonator displacement x_m causes a cavity frequency shift $\delta\omega_\mathrm{cav} = -g_\mathrm{m}x_\mathrm{m}$ and thus a phase shift $\delta\phi_\mathrm{r} = -(\mathrm{d}\phi_\mathrm{r}/\mathrm{d}\Delta)\delta\omega_\mathrm{cav} = 4g_\mathrm{m}x_\mathrm{m}/\kappa$. Hence, the minima of the optical lattice potential are displaced by $\delta x_\mathrm{lat} = -\delta\phi_\mathrm{r}/(2k_\mathrm{lat}) = -2g_\mathrm{m}x_\mathrm{m}/(\kappa k_\mathrm{lat})$, which leads to a force

$$F_\mathrm{at} = Nm_\mathrm{at}\delta x_\mathrm{lat}\omega_\mathrm{at}^2 = -\frac{2g_\mathrm{m}}{\kappa k_\mathrm{lat}}Nm_\mathrm{at}x_\mathrm{m}\omega_\mathrm{at}^2 = -Kx_\mathrm{m}, \tag{3.3}$$

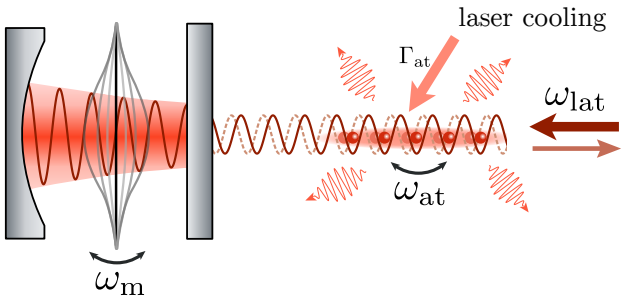

Figure 3.1: Coupling of a MiM system to atomic center of mass motion in an optical lattice. The mechanical resonator in the MiM system (see section 2.3) is coupled to ^{87}Rb atoms in an optical lattice of frequency ω_lat (see (2.6)), which is created by the reflected light from the MiM cavity. Due to the resonator motion with frequency ω_m the the confining optical potential for the atoms is periodically shifted. At the same time the atomic center of mass motion inside the potential modulates the radiation pressure on the resonator with frequency ω_at. By means of laser cooling the atoms, energy is dissipated from the system, which allows to sympathetically cool the resonator inside the cavity.

with the spring constant K on the ensemble of N atoms. Conversely, an atom displaced by x_{at} from the center of a harmonic optical potential experiences a restoring dipole force $F_{\mathrm{d}} = -m_{\mathrm{at}} x_{\mathrm{at}} \omega_{\mathrm{at}}^2$. This force arises from an imbalance of absorption and stimulated emission processes of photons from the counter propagating lattice beams. The displaced atoms preferably absorb photons from one lattice beam and re-emit them into the opposite beam. Due to the conservation of momentum each redistribution process alters the momentum of an atom by $2\hbar k_{\mathrm{lat}}$.
Consequently, we find the photon redistribution rate $\dot{n}_{\mathrm{ph}} = NF_{\mathrm{d}}/(2\hbar k_{\mathrm{lat}})$ that results in a power modulation $\delta P_{\mathrm{lat}} = \dot{n}_{\mathrm{ph}} \hbar \omega_{\mathrm{lat}}$ incident on the MiM cavity. The variation of the mean intra-cavity photon number $\delta \bar{n}_{\mathrm{cav}} \approx 4\beta t^2 \delta P_{\mathrm{lat}}/(\kappa \hbar \omega_{\mathrm{cav}})$ is directly proportional to the variation of the cavity incident power and can be used to describe the radiation pressure force $F_{\mathrm{rad}} = \hbar g_{\mathrm{m}} \bar{n}_{\mathrm{cav}}$ that acts on the mechanical resonator in the MiM system. With the reduced incoupling efficiency into the MiM system due to imperfect mode match β and the power transmittance t^2 of the optical path between the atoms and the MiM cavity we arrive at the variation of the radiation pressure force at the resonator, caused by a displacement of the atoms in the lattice

$$\delta F_{\mathrm{rad}} = -\frac{2g_{\mathrm{m}}}{\kappa k_{\mathrm{lat}}} \beta t^2 N m_{\mathrm{at}} x_{\mathrm{at}} \omega_{\mathrm{cav}}^2 = -\beta t^2 K x_{\mathrm{at}} \tag{3.4}$$

When comparing equations (3.3) and (3.4) it becomes clear that the force exerted on the resonator is reduced by the factor βt^2 compared to the force , which acts on the atoms. In our system the incoupling mode match is $\beta > 0.95$ [74] and the power transmittance of the optical path is $t^2 = 0.63(5)$ (see appendix B.1). This already makes the coupling of the atoms to the resonator asymmetric. Additionally, the optical losses and the finite reflectivity on resonance $\sigma_{\mathrm{cav}} = 0.53(1)$ cause a power imbalance of the counter propagating lattice beams which can lead to collective atomic oscillations [75, 76] and result in instabilities in the hybrid system [72, 73] as discussed later in section 3.1.2.

Equations of motion in the hybrid system

With the forces defined in equations (3.3) and (3.4) the coupled equations of motion for the two subsystems are [70, 162]

$$N m_{\mathrm{at}} \ddot{x}_{\mathrm{at}} = -\Gamma_{\mathrm{at}} N m_{\mathrm{at}} \dot{x}_{\mathrm{at}} - N m_{\mathrm{at}} x_{\mathrm{at}} \omega_{\mathrm{at}}^2 - K x_{\mathrm{m}} \tag{3.5a}$$

$$m_{\mathrm{eff}} \ddot{x}_{\mathrm{m}} = -\Gamma_{\mathrm{m}} m_{\mathrm{eff}} \dot{x}_{\mathrm{m}} - m_{\mathrm{eff}} x_{\mathrm{m}} \omega_{\mathrm{m}}^2 - \beta t^2 K x_{\mathrm{at}} + F_{\mathrm{th}}, \tag{3.5b}$$

with the atomic (and mechanical) damping rate Γ_{at} (Γ_{m}) and the thermal Langevin force F_{th} acting on the resonator (see section 2.2.3). Similar to section 2.2.3 the equations of motion can be Fourier transformed

$$\tilde{x}_{\mathrm{at}}(\omega) \chi_{\mathrm{at}}^{-1}(\omega) = -K \tilde{x}_{\mathrm{m}}(\omega) \tag{3.6a}$$

$$\tilde{x}_{\mathrm{m}}(\omega) \chi_{\mathrm{m}}^{-1}(\omega) = \tilde{F}_{\mathrm{th}} - \beta t^2 K \tilde{x}_{\mathrm{at}}(\omega) \tag{3.6b}$$

and are expressed through the susceptibilities

$$\chi_{\mathrm{at}}^{-1}(\omega) = N m_{\mathrm{at}} \left(\omega_{\mathrm{at}}^2 - \omega^2 - i\omega\Gamma_{\mathrm{at}}\right) \approx 2N m_{\mathrm{at}}\omega_{\mathrm{at}}(\omega_{\mathrm{at}} - \omega - i\Gamma_{\mathrm{at}}/2) \tag{3.7a}$$

$$\chi_{\mathrm{m}}^{-1}(\omega) = m_{\mathrm{eff}} \left(\omega_{\mathrm{m}}^2 - \omega^2 - i\omega\Gamma_{\mathrm{m}}\right) \approx 2m_{\mathrm{eff}}\omega_{\mathrm{m}}(\omega_{\mathrm{m}} - \omega - i\Gamma_{\mathrm{m}}/2), \tag{3.7b}$$

where a Taylor expansion around $\omega_{\mathrm{at/m}}$ was used to get to the approximation on the right side of the equations. By inserting equation (3.6a) into (3.6b) $\tilde{x}_{\mathrm{at}}$ can be eliminated and the response of the resonator motion $\tilde{x}_{\mathrm{m}}$ to the driving force in the coupled system is obtained:

$$\tilde{x}_{\mathrm{m}}(\omega)[\chi_{\mathrm{m}}^{-1} - \underbrace{\beta t^2 K^2 \chi_{\mathrm{at}}(\omega)}_{\chi_{\mathrm{sym}}^{-1}(\omega)}] \equiv \tilde{x}_{\mathrm{m}}\chi_{\mathrm{eff,s}}^{-1}(\omega) = F_{\mathrm{th}} \tag{3.8}$$

with the new effective susceptibility $\chi_{\mathrm{eff,s}}$ of the mechanical resonator. The formalism to describe sympathetic cooling is very similar to active feedback cooling (compare section 2.2.3) as both methods lead to cold damping due to an increased effective mechanical damping rate of the resonator caused by the imaginary part of χ_{sym}. Thus, sympathetic cooling can be regarded as a coherent feedback scheme [70]. Explicitly, we have

$$\chi_{\mathrm{sym}}^{-1}(\omega) = -\beta t^2 K^2 \chi_{\mathrm{at}}(\omega) = -\beta t^2 K^2 \frac{(\omega_{\mathrm{at}} - \omega) + i\Gamma_{\mathrm{at}}/2}{2N m_{\mathrm{at}}\omega_{\mathrm{at}}\left[(\omega_{\mathrm{at}} - \omega)^2 + (\Gamma_{\mathrm{at}}/2)^2\right]}, \tag{3.9}$$

which can be used to arrive at the new effective susceptibility $\chi_{\mathrm{eff,s}}$ of the sympathetically cooled mechanical resonator (assuming $\omega \approx \omega_{\mathrm{at}}$)

$$\chi_{\mathrm{eff,s}}^{-1}(\omega) = 2m_{\mathrm{eff}}\omega_{\mathrm{m}}\left(\omega'_{\mathrm{m}} - \omega - i\Gamma'_{\mathrm{m}}/2\right) \tag{3.10}$$

$$\text{with} \qquad \omega'_{\mathrm{m}} = \omega_{\mathrm{m}} + (\omega_{\mathrm{m}} - \omega_{\mathrm{at}})\frac{\Gamma_{\mathrm{sym}}}{\Gamma_{\mathrm{at}}} \tag{3.11}$$

$$\text{and} \qquad \Gamma'_{\mathrm{m}} = \Gamma_{\mathrm{m}}\left(1 + \frac{\Gamma_{\mathrm{sym}}}{\Gamma_{\mathrm{m}}}\right) \equiv \Gamma_{\mathrm{m}}(1 + g_{\mathrm{sym}}), \tag{3.12}$$

where the sympathetic cooling rate

$$\Gamma_{\mathrm{sym}}(N, \omega_{\mathrm{at}}) = \frac{g_N^2 \beta t^2 \Gamma_{\mathrm{at}}}{(\omega_{\mathrm{at}} - \omega_{\mathrm{m}})^2 + (\Gamma_{\mathrm{at}}/2)^2} \tag{3.13}$$

was introduced. It contains the single-phonon coupling rate [62, 70]

$$g_N = K x_{\mathrm{zpf}}^{\mathrm{m}} x_{\mathrm{zpf}}^{\mathrm{at}}/\hbar = |r_{\mathrm{m}}|\omega_{\mathrm{at}}\sqrt{\frac{N m_{\mathrm{at}}\omega_{\mathrm{at}}}{m_{\mathrm{eff}}\omega_{\mathrm{m}}}}\frac{2\mathcal{F}}{\pi} \tag{3.14}$$

with the mechanical and atomic quantum zero point fluctuations $x_{\mathrm{zpf}}^{\mathrm{m}} = \sqrt{\hbar/(2m_{\mathrm{eff}}\omega_{\mathrm{m}})}$ and $x_{\mathrm{zpf}}^{\mathrm{at}} = \sqrt{\hbar/(2m_{\mathrm{at}}\omega_{\mathrm{at}})}$ and the field reflectivity of the mechanical resonator r_{m}. In equation (3.12) the sympathetic cooling gain g_{sym} was introduced. Similar to the case of velocity-dependent feedback in section 2.2.3 it describes the cold damping effect due to the effectively increased damping rate Γ'_{m}. Also the reduced mode temperature of

the resonator can be described similarly [62]

$$T_{\mathrm{mode}} = \frac{T_{\mathrm{bath}}}{1+g_{\mathrm{sym}}} = T_{\mathrm{bath}}\frac{\Gamma_{\mathrm{m}}}{\Gamma_{\mathrm{m}}+\Gamma_{\mathrm{sym}}}. \tag{3.15}$$

Ensemble-integrated sympathetic cooling rate

When conducting a sympathetic cooling experiment the coupling beam is centred on a sample of atoms in a MOT, whose cloud radius R_{at} is much larger than the waist $\mathrm{w}_{\mathrm{lat}}$ of the coupling lattice beams. Therefore, it is reasonable to assume a constant atom number density n_{at} throughout the lattice volume. Moreover, previous experiments [73, 74] have shown that the density distribution is not changed significantly by the presence of the lattice. In the preceding passage the sympathetic cooling rate Γ_{sym} was calculated under the assumption that the atoms in the lattice are confined in identical potential wells with equal trapping frequency ω_{at}. This is only partially true. While the lattice intensity, and therefore also the lattice depth, along the axial direction of the trapping beams can safely be regarded as constant, since the Rayleigh range $z_{\mathrm{r}} = \pi {\mathrm{w}_{\mathrm{lat}}}^2/\lambda \approx 2\,\mathrm{cm} \gg R_{\mathrm{at}}$, the Gaussian intensity profile along the radial direction has to be considered. It leads to a radial dependency of the atomic trapping frequency $\omega_{\mathrm{at}}(r) = \omega_{\mathrm{at},0} e^{-r^2/{\mathrm{w}_{\mathrm{lat}}}^2}$ with the maximum trapping frequency $\omega_{\mathrm{at},0}$ in the center of the coupling lattice beams (note that outside this context, $\omega_{\mathrm{at},0}$ will simply be denoted by ω_{at}). Thus, in order to describe the experimental conditions more realistically Γ_{sym} in equation (3.13) has to be integrated over the radial beam profile. Following [162], the integral over the radial coordinate

$$\Gamma_{\mathrm{sym}}^{\mathrm{int}} = 2R_{\mathrm{at}} n_{\mathrm{at}} \int_0^{R_{\mathrm{at}}} \Gamma_{\mathrm{sym}}[N=1, \omega_{\mathrm{at}}(r)] 2\pi r \,\mathrm{d}r \tag{3.16}$$

can be converted into an integral over the frequency

$$\begin{aligned}\Gamma_{\mathrm{sym}}^{\mathrm{int}}(\omega_{\mathrm{at},0}) &= N_{\mathrm{lat}} \int_{\omega_{\mathrm{at}}(R_{\mathrm{at}})}^{\omega_{\mathrm{at},0}} \frac{\Gamma_{\mathrm{sym}}[N=1,\omega_{\mathrm{at}}]}{\omega_{\mathrm{at}}}\,\mathrm{d}\omega_{\mathrm{at}} \\ &= \frac{m_{\mathrm{at}} N_{\mathrm{lat}}}{m_{\mathrm{eff}}} |r_{\mathrm{m}}|^2 \beta t^2 \frac{\Gamma_{\mathrm{at}}}{\omega_{\mathrm{m}}} \left(\frac{2\mathcal{F}}{\pi}\right)^2 \int_{\omega_{\mathrm{at}}(R_{\mathrm{at}})}^{\omega_{\mathrm{at},0}} \frac{\omega_{\mathrm{at}}^2}{(\omega_{\mathrm{at}}-\omega_{\mathrm{m}})^2 + (\Gamma_{\mathrm{at}}/2)^2}\,\mathrm{d}\omega_{\mathrm{at}},\end{aligned}$$

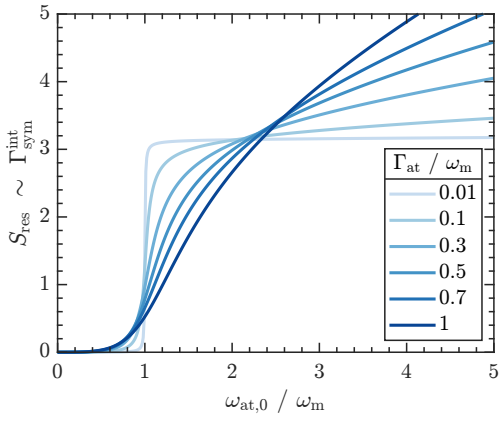

Figure 3.2: Ensemble-integrated sympathetic cooling rate $\Gamma_{\mathrm{sym}}^{\mathrm{int}}$ for different Γ_{at}. $\Gamma_{\mathrm{sym}}^{\mathrm{int}}$ is plotted as a function of the atomic trapping frequency $\omega_{\mathrm{at},0}$ for different Γ_{at} and is proportional to S_{res} in equation (3.18). For the model, constant atomic density in the lattice volume is assumed and both Γ_{at} and $\omega_{\mathrm{at},0}$ are in units of the mechanical resonator frequency ω_{m}.

where $N_{\mathrm{lat}} = 2R_{\mathrm{at}}\pi {w_{\mathrm{lat}}}^2 n_{\mathrm{at}}$ is the number of atoms in the lattice volume. Since $R_{\mathrm{at}} \gg w_{\mathrm{lat}}$ the lower integration limit can be set to $\omega_{\mathrm{at}}(R_{\mathrm{at}}) \to 0$ and the integral is solved to [74]

$$\Gamma_{\mathrm{sym}}^{\mathrm{int}}(\omega_{\mathrm{at},0}) = 2\frac{m_{\mathrm{at}}N_{\mathrm{lat}}}{m_{\mathrm{eff}}}|r_{\mathrm{m}}|^2\beta t^2\left(\frac{2\mathcal{F}}{\pi}\right)^2\omega_{\mathrm{m}}\cdot S_{\mathrm{res}}(\omega_{\mathrm{at},0}), \tag{3.17}$$

with the function

$$\begin{aligned} S_{\mathrm{res}}(\omega_{\mathrm{at},0}) \;:=\; & \left(1-\frac{\Gamma_{\mathrm{at}}^2}{4\omega_{\mathrm{m}}^2}\right)\left(\arctan\left[\frac{2\omega_{\mathrm{m}}}{\Gamma_{\mathrm{at}}}\right]+\arctan\left[\frac{2\left(\omega_{\mathrm{at},0}-\omega_{\mathrm{m}}\right)}{\Gamma_{\mathrm{at}}}\right]\right) \\ & +\frac{\Gamma_{\mathrm{at}}}{2\omega_{\mathrm{m}}^2}\left(\omega_{\mathrm{at},0}+\omega_{\mathrm{m}}\ln\left[\frac{\Gamma_{\mathrm{at}}^2+4\left(\omega_{\mathrm{at},0}-\omega_{\mathrm{m}}\right)^2}{\Gamma_{\mathrm{at}}^2+4\omega_{\mathrm{m}}^2}\right]\right) \end{aligned} \tag{3.18}$$

that shows step-like behaviour for a small atomic damping rate $\Gamma_{\mathrm{at}} \ll \omega_{\mathrm{m}}$ and grows smoothly as a function of the trapping frequency in the center of the beam until it diverges for $\Gamma_{\mathrm{at}} \to \omega_{\mathrm{m}}$ (see figure 3.2).

Quantized model of hybrid coupling and hybrid cooperativity

In the above treatment of sympathetic cooling the approach was purely classical and quantum noise processes that limit the minimum achievable temperature were neglected. Hence, for a realistic description the relevant dissipation processes in the system must be taken into account. A fully quantized model was introduced in [45] where the linearized effective interaction Hamiltonian

$$H_{\mathrm{int}} = \hbar g_N\left(\hat{a}_{\mathrm{m}}^\dagger\hat{a}_{\mathrm{at}} + \hat{a}_{\mathrm{at}}^\dagger\hat{a}_{\mathrm{m}}\right) \tag{3.19}$$

was found, which describes the coherent exchange between mechanical and atomic motional quanta through the annihilation and creation operators $\hat{a}_{\mathrm{m}}$ ($\hat{a}_{\mathrm{at}}$) and $\hat{a}_{\mathrm{m}}^\dagger$ ($\hat{a}_{\mathrm{at}}^\dagger$) for phonons of the mechanical resonators mode (motional quanta of the atomic mode). One of the most relevant consequences of this model is the introduction of additional contributions to the decoherence of the coupled system. Classically, arbitrarily low temperatures could be achieved with sufficiently high sympathetic cooling rates Γ_{sym} (see equation (3.15) and figure 3.2) by making the lattice very deep. The quantum model accounts for heating of the resonator by shot noise of the cavity photons via the mechanical momentum diffusion rate

$$\Gamma_{\mathrm{m}}^{\mathrm{diff}} = \frac{16P_{\mathrm{in}}\omega_{\mathrm{cav}}}{m_{\mathrm{eff}}c^2\omega_{\mathrm{m}}}|r_{\mathrm{m}}|^2\left(\frac{2\mathcal{F}}{\pi}\right)^2. \tag{3.20}$$

On the atomic side the decoherence is introduced by photon scattering Γ_{sc} and is described by the atomic momentum diffusion rate [96]

$$\Gamma_{\mathrm{at}}^{\mathrm{diff}} = \Gamma_{\mathrm{sc}}(k_{\mathrm{lat}}x_{\mathrm{lat}}^{\mathrm{at}})^2 = \frac{(k_{\mathrm{lat}}x_{\mathrm{zpf}}^{\mathrm{at}})^2\Gamma V_{\mathrm{lat}}}{\hbar\Delta_{\mathrm{at,L}}}. \tag{3.21}$$

In order to be able to observe the coherent transfer of single excitations expressed by equation (3.19), between the mechanical and the atomic system, their coupling has to exceed all decoherence rates in the system, which is fulfilled if the strong coupling condition [45]

$$g_N \gg \Gamma_\mathrm{m}^\mathrm{diff}, \Gamma_\mathrm{at}^\mathrm{diff}, \Gamma_\mathrm{m}^\mathrm{th} \tag{3.22}$$

is satisfied. Here, $\Gamma_\mathrm{m}^\mathrm{th} = \Gamma_\mathrm{m}\bar{n}_\mathrm{th}$ is the thermal decoherence rate due to the coupling to the thermal bath with the phononic mode occupation $\bar{n}_\mathrm{th} = k_\mathrm{B}T_\mathrm{bath}/(\hbar\omega_\mathrm{m})$. With all decoherence mechanisms considered one can find the equation for the steady state phonon occupation $\bar{n}_\mathrm{ss}$ of the mechanical resonator that can be reached by sympathetic cooling:

$$\bar{n}_\mathrm{ss} = \frac{\Gamma_\mathrm{m}^\mathrm{th}}{\Gamma_\mathrm{m}+\Gamma_\mathrm{sym}} + \frac{\Gamma_\mathrm{m}^\mathrm{diff}}{\Gamma_\mathrm{m}+\Gamma_\mathrm{sym}} + \frac{\Gamma_\mathrm{at}^\mathrm{diff}}{\Gamma_\mathrm{at}} + \left(\frac{\Gamma_\mathrm{at}}{4\omega_\mathrm{at}}\right)^2. \tag{3.23}$$

The last term originates from the counter-rotating terms in the Hamiltonian that become important for strong atomic damping due to a large cooling rate Γ_at.
For dominant thermal decoherence $\Gamma_\mathrm{m}^\mathrm{th} \gg \Gamma_\mathrm{m}^\mathrm{diff}$, large sympathetic cooling rates $\Gamma_\mathrm{sym} \gg \Gamma_\mathrm{m}$ and resonant coupling $\omega_\mathrm{at} \approx \omega_\mathrm{m}$ one can use equation (3.13) to summarize the first two terms in (3.23)

$$\frac{\Gamma_\mathrm{m}^\mathrm{th}+\Gamma_\mathrm{m}^\mathrm{diff}}{\Gamma_\mathrm{m}+\Gamma_\mathrm{sym}} \approx \frac{\Gamma_\mathrm{m}^\mathrm{th}}{\Gamma_\mathrm{sym}} = \frac{\bar{n}_\mathrm{th}}{C_\mathrm{hybrid}}. \tag{3.24}$$

Here, the hybrid cooperativity [70, 162]

$$C_\mathrm{hybrid} = \frac{4\beta t^2 g_N^2}{\Gamma_\mathrm{at}\Gamma_\mathrm{m}} = \frac{\Gamma_\mathrm{sym}}{\Gamma_\mathrm{m}} \tag{3.25}$$

was introduced, which is closely related to the strong coupling condition (3.22) and can be understood as a general indicator for coherent dynamics as it relates the strength of the hybrid coupling to the mechanical decoherence rate in a simple quantity. If $C_\mathrm{hybrid} \gg \bar{n}_\mathrm{th}$ is reached the mechanical resonator is cooled to its motional ground state ($\bar{n}_\mathrm{ss} < 1$) and coherent dynamics can be observed.

In order to reach the strong coupling regime the hybrid cooperativity C_hybrid and hence the single-phonon coupling strength g_N in equation (3.14), need to be increased as much as possible. This can be done in two ways: First, the experimental setup can be optimized. This includes the reduction of optical losses to reach values of β and t^2 close to unity, the use of a high-finesse cavity and a careful choice of the used mechanical resonator. Second, the number of atoms that participate in the coupling has to be maximized, as the coupling strength g_N scales with $\sqrt{N}$.
On the side of the experimental setup the optical losses were already minimized and the cavity is designed to provide a reflectivity on resonance as high as possible to realize the coupling lattice. However, this comes at the cost of a relatively low finesse such that we are limited to a value on the order of $\mathcal{F} \approx 140$. For the mechanical resonator three properties are relevant: a low effective mass m_eff of the mechanical mode employed

for the coupling, a narrow mechanical linewidth Γ_m and a high resonance frequency ω_m, as for resonant coupling ($\omega_\mathrm{m} \approx \omega_\mathrm{at}$) the coupling strength scales with ω_at. In this regard we also already optimized our setup by the choice of a trampoline resonator (see section 2.3) over a membrane [77], which has a lower linewidth by a factor of $\Gamma_\mathrm{m}^\mathrm{mem}/\Gamma_\mathrm{m}^\mathrm{tramp} = 14$ and a lower effective mass by a factor $m_\mathrm{eff}^\mathrm{mem}/m_\mathrm{eff}^\mathrm{tramp} = 23$ than the previously employed resonator [74]. Using the membrane resonator a maximum hybrid cooperativity of $C_\mathrm{hybrid} = 151 \pm 9$ [74] was achieved, which was much lower than the mode occupation $\bar{n}_\mathrm{th} = 3.95 \cdot 10^5$ at 5 K bath temperature. With the trampoline resonator much higher cooperativities are feasible and the only other parameter left to approach the strong coupling regime by sympathetic cooling is to increase the atom number.

3.1.2 Instability in the hybrid system

One of the main challenges in reaching a high number of atoms that participate in the coupling manifests in the occurrence of an instability in the hybrid system under certain experimental conditions. In this case sympathetic cooling can turn into heating that drives the resonator into large amplitude, limit-cycle oscillations. This effect has first been observed in the group of P. Treutlein in Basel and was studied by A. Vochezer *et al* (née Faber) [72, 73]. It sets in for small atom-light detuning $\Delta_\mathrm{at,L}$ of the coupling laser and large atom numbers. In fact, this instability turns out to be a general feature of atom-mechanical hybrid systems as we observe the same effect in our experiment as well [74].
An exemplary measurement is depicted in the left panel of figure 3.3. Here, atoms from a continuously loaded MOT were coupled to the mechanical resonator and the reduction of its mode temperature T_mode was measured as a function of the lattice depth for red and blue lattice detuning. The lattice depth is denoted in form of the atomic trapping frequency ω_at (see (2.3)), which is expressed in units of the mechanical resonance frequency ω_m. The experiment reveals that with increasing lattice depth, and thus increasing number of coupled atoms, the resonator mode temperature is reduced to a certain point ($\omega_\mathrm{at} \approx 1.25\,\omega_\mathrm{m}$). While for the blue detuned lattice the cooling efficiency further improves with increasing trapping frequency, the red detuned lattice leads to a rapid excitation of the resonator mode that results in large oscillation amplitudes, for which the mode temperature is not well defined any more.
This excitation induced instability can be explained by a delay in the coupling between the resonator and the atoms that is caused by an effective retardation of the atomic backaction onto the light field. Most likely this delay is produced by collective effects within the atomic ensemble that have been predicted by J. K. Asbóth *et al* [75, 76] to arise in asymmetrically pumped optical lattices. Since, we have an intrinsic asymmetry in our coupling lattice it is conceivable that collective atomic effects destabilize our coupling lattice. The influence of asymmetrical pumping will be discussed in detail in the next section 3.2.

The fact that we only observe the instability in the red detuned lattice can be explained by the attractive dipole potential at the intensity maxima of the trapping field. It gathers more atoms at the lattice sites than in the blue detuned case and thus exhibits

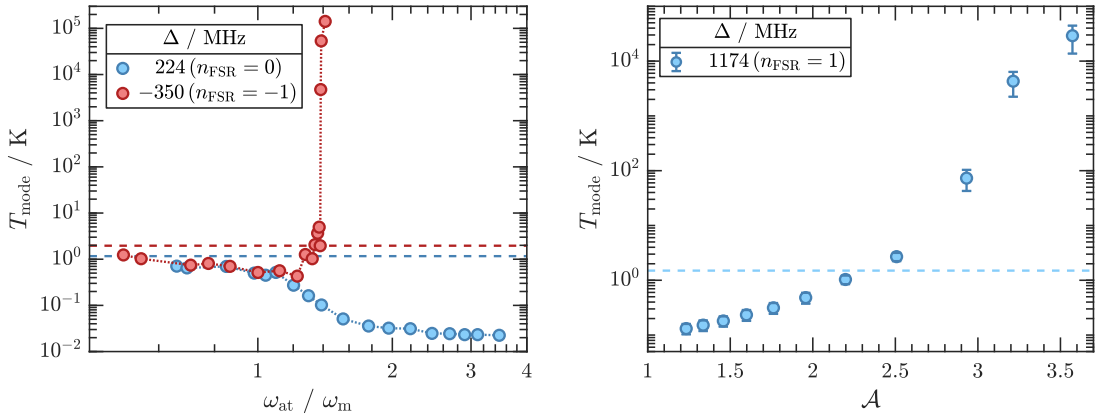

Figure 3.3: Instability in the hybrid coupling mechanism. Left panel: Resonator mode temperature T_{mode} for coupling to atoms in a continuously loaded MOT. For two different lattice detunings Δ the lattice depth is adjusted by varying the lattice power P_{lat} and is depicted by the trapping frequency ω_{at} in units of the resonator frequency ω_{m}. Blue detuning ($\Delta_{2,3} > 0$) refers to the $\mathrm{F}' = 3$ level of the D_2 line, red detuning ($\Delta_{2,1} < 0$) to the $\mathrm{F}' = 1$ level. For both detunings sympathetic cooling is visible, until in the red lattice the cooling turns into heating at $\omega_{\mathrm{at}} \approx 1.25\,\omega_{\mathrm{m}}$. The dashed lines denote the respective bath temperatures $T_{\mathrm{bath}} = T_{\mathrm{mode}}(P_{\mathrm{lat}} = 0)$. Note that in the case of heating, the resonator performs limit-cycle oscillations and T_{mode} is not well defined. Figure adapted from [74]. **Right panel:** Mode temperature T_{mode} for coupling to atoms in a high density MOT (see description in section 3.5) using a blue detuned lattice as a function of the pump asymmetry $\mathcal{A} = (I_{\mathrm{inc}} - I_{\mathrm{back}})/\sqrt{I_{\mathrm{inc}} I_{\mathrm{back}}}$. The dashed line denotes the feedback pre-cooled mode temperature without sympathetic cooling. The pump asymmetry is adjusted by introducing losses to the coupling beam after it has passed the atoms. The sympathetic cooling efficiency decreases with increasing asymmetry and finally turns into heating for $\mathcal{A} > 2.4$. Figure adapted from [77].

higher local atomic densities, which are predicted to further enhance the effect of the collective atomic backaction on the delay in the system due to the asymmetry. However, the theory predicts the instability to occur in blue detuned lattices as well. Its applicability to our system was proven in another experiment, where the pump asymmetry in the blue lattice was artificially increased [77]. By dumping a fraction of the incident beam power before it entered the MiM system, the losses in the optical path were increased, which resulted in a stronger asymmetry of the coupling lattice. Once the asymmetry exceeded a critical point, we observed similar heating effects in the blue detuned lattice as well (see right panel of figure 3.3). These measurements indicate that the instability of the hybrid system is indeed caused by the asymmetry in the pumping of our optical lattice and leads us to the conclusion that it can be overcome by reducing the asymmetry.

3.2 Influence of asymmetric pumping on an optical lattice

The previous section illustrated the occurrence of an instability in a hybrid system of cold atoms, whose motion is coupled to a mechanical resonator using an optical lattice. The experiments reported until now [65, 72] have two things in common: First, the employed coupling lattice is created by retro-reflection of the coupling beam from the

mechanical resonator, which is placed inside a cavity to enhance the optomechanical interaction. As a consequence the reflected beam carries only a fraction of the incident beam's power due to incoupling and mode matching losses and a finite reflectivity on resonance. Thus, the coupling lattices in these systems are intrinsically asymmetrically pumped. Second, the experiments aim at reducing the amplitude of mechanical motion of the resonator by interaction with a laser-cooled coupling partner. Therefore, the laser power used for the interaction mediating coupling light is restricted to relatively low values in order to prevent the resonator from heating, induced by absorption of the coupling light itself. This demands the use of near detuned light, with respect to the atomic transition, to produce the needed lattice depth for resonant coupling. In this regime however, the propagation of the trapping light is not unaffected by the presence of the atoms. Instead, it is substantially influenced by the atomic backaction, which can alter the equilibrium configuration and lead to collective motion in the system as derived by J. K. Asbóth *et al.* [75, 76]. Inspired by their findings A. Vochezer (neé Faber) studied the light-mediated interaction of atoms in different wells of an asymmetric lattice both theoretically and experimentally [73] in a system very similar to ours. She found that the atomic backaction can lead to large phase shifts of the lattice light that become relevant predominantly in regimes of high atom number or small detuning and are likely the origin of the aforementioned instability that occurs in hybrid atom-optomechanical systems. Her investigation motivated us to reproduce the simulation and to extend it by an additional beam that we want to use for the compensation of the asymmetry in our coupling lattice.

For the investigation of the dynamics in the lattice it is useful to establish a model that can be used to describe the system. We assume two counter-propagating lattice beams with equal beam shape but different intensities $I_{\mathrm{inc}} > I_{\mathrm{back}}$, where I_{inc} describes the intensity of the incident and I_{back} the intensity of the back-reflected lattice beam. Both are connected via the total reflectance of the MiM system on resonance R that

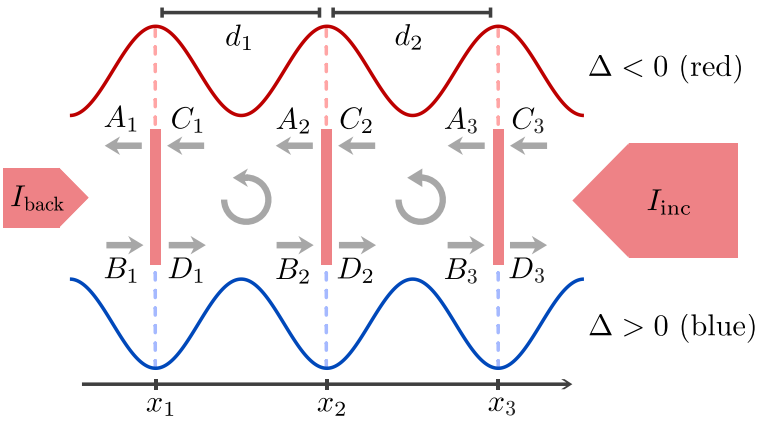

Figure 3.4: Illustration of the model to describe a 1D lattice. The atoms inside an optical 1D lattice can be described by an array of N beam splitters separated by the distance d_j with the field amplitudes A_j, B_j, C_j, D_j incident on the j-th beam splitter. For red detuning the atoms gather at the intensity maxima of the lattice, for blue detuning they localize at the intensity minima, whose positions are given by x_j. Figure adapted from [100].

includes all optical losses and the reflectivity of the resonator (see appendix B.1). For the reflected intensity $I_{\mathrm{back}} = R \cdot I_{\mathrm{inc}}$ holds. The atoms in the 1D lattice can be described as a periodic arrangement of thin, disk-shaped clouds at positions x_j that behave like beam splitters and are separated by a distance d_j (see figure 3.4). Each beam splitter is subject to dipole and radiation pressure forces that can be expressed through the in- and outgoing fields A_j, B_j, C_j, D_j at the j-th beam splitter. As our trapping beams have much larger waists than the lattice wavelength ($\mathrm{w}_{\mathrm{inc,ref}} \approx 69\,\mu\mathrm{m} \gg \lambda_{\mathrm{lat}} = 780\,\mathrm{nm}$) we can describe the incident fields through plane waves. The incident beam, propagating to the left, is then represented by $E_{\mathrm{left}}(x) = E_{\mathrm{inc}} \cdot e^{-ikx}$ and the reflected beam by $E_{\mathrm{right}}(x) = E_{\mathrm{back}} \cdot e^{ikx}$ with the corresponding intensities $I_{\mathrm{inc,ref}} = \frac{1}{2}\epsilon_0 c |E_{\mathrm{inc,ref}}|^2$. The intensity imbalance can be quantified by two alternative dimensionless quantities, the pump asymmetry, characterized by the normalized difference of the intensities [76]

$$\mathcal{A} = \frac{I_{\mathrm{inc}} - I_{\mathrm{back}}}{\sqrt{I_{\mathrm{inc}} I_{\mathrm{back}}}} = \left|\frac{E_{\mathrm{inc}}}{E_{\mathrm{back}}}\right| - \left|\frac{E_{\mathrm{back}}}{E_{\mathrm{inc}}}\right| > 0 \tag{3.26}$$

and the pump power ratio

$$\mathcal{P} = \frac{P_{\mathrm{inc}}}{P_{\mathrm{back}}} > 1. \tag{3.27}$$

For almost symmetric pumping ($\mathcal{A} \ll 1$), the two are related by $\mathcal{P} = 1 + \mathcal{A}$, whereas for highly asymmetric pumping ($\mathcal{A} \gg 1$), roughly $\mathcal{P} = \mathcal{A}^2$ holds.

3.2.1 Contraction of the lattice

For symmetric, red detuned optical lattices, where the counter-propagating beams have equal intensities, the backaction induced interaction leads to a moderate reduction of the lattice constant $d = \lambda_{\mathrm{lat}}/2$ as predicted in [163] and experimentally observed in [164, 165]. This can be intuitively understood by imagining the atoms at the intensity maxima as media with different refractive index than the surrounding environment, which leads to an alteration of the wavelength of the lattice light, as well as its phase. For blue lattice detuning, where the atoms effectively remain in the dark, the lattice constant remains unaffected. For an asymmetric lattice the situation changes, as in this case the beams can not interfere completely destructive any more and thus also atoms in a blue detuned lattice experience trapping at lattice sites with non-vanishing intensity. This leads to a reduction of the lattice constant in blue lattices as well and even further enhances the contraction in the case of red detuning as depicted in figure 3.5.

The effect can be quantified by utilizing the model. If we assume that the atoms are cold enough and the laser beams are intensive enough to provide deep trapping, the atoms form a stack of disk-shaped clouds. Each cloud then represents an infinitely thin plane of polarizable material, whose interaction strength depends on the complex linear polarizability α_{at} of the particles and their areal density $\eta = N_d/\sigma_L$. Here, N_d denotes the number of atoms in a disk-shaped cloud with area $\sigma_L = \pi {\mathrm{w}_{\mathrm{lat}}}^2/2$. These can be combined in a dimensionless coupling constant [73] that describes the (areal density of

the) polarizability of a cloud

$$\zeta \;=\; \frac{k\eta\alpha_{\mathrm{at}}}{2\epsilon_0} \;=\; -\frac{N_d\sigma_0\Gamma}{4\sigma_L\left(\Delta_{\mathrm{at,L}}+i\Gamma/2\right)} \tag{3.28}$$

with the resonant scattering cross-section $\sigma_0 = 3\lambda^2/2\pi$ and the atomic linewidth Γ. Its real part $\mathrm{Re}(\zeta)$ describes the dispersive atom-light interaction, while the imaginary part $\mathrm{Im}(\zeta)$ corresponds to dissipation via absorption and spontaneous emission. For us, $\Delta_{\mathrm{at,L}} \gg \Gamma$ in all experimentally relevant scenarios, hence we can neglect $\mathrm{Im}(\zeta)$.

Following [163] the propagation of the trap light through the atomic sample can be calculated using the 1D wave equation, where the N clouds are represented by Dirac-δ distributions of polarizable material

$$\left(\partial_x^2 + k^2\right) E(x) \;=\; -2E(x)\sum_{j=1}^{N}\zeta\delta(x-x_j). \tag{3.29}$$

The solution of (3.29) between two clouds is a superposition of plane waves

$$\begin{aligned} E(x_{j-1}<x<x_j) &= A_j e^{-ik(x-x_j)} + B_j e^{ik(x-x_j)} \\ &= C_{j-1}e^{-ik(x-x_{j-1})} + D_{j-1}e^{ik(x-x_{j-1})} \end{aligned} \tag{3.30}$$

with boundary conditions for the field, set by the clouds at positions $x = x_j$

$$E(x =_{\rightarrow} x_j) = E(x = x_{j\leftarrow}) \tag{3.31a}$$

$$\partial_x E(x =_{\rightarrow} x_j) - \partial_x E(x = x_{j\leftarrow}) = 2k\zeta E(x_j). \tag{3.31b}$$

When substituting the superposition ansatz (3.30) into the boundary conditions, we arrive at the equations for the mode amplitudes to the left and to the right of each atom cloud. These have the form of beam splitter relations [76]

$$A_j = \mathfrak{r}B_j + \mathfrak{t}C_j, \tag{3.32a}$$

$$D_j = \mathfrak{t}B_j + \mathfrak{r}C_j, \tag{3.32b}$$

with reflection and transmission coefficients

$$\mathfrak{r} = \frac{i\zeta}{1-i\zeta}, \quad \mathfrak{t} = \frac{1}{1-i\zeta}, \quad \text{and} \quad \zeta = -i\frac{\mathfrak{r}}{\mathfrak{t}}. \tag{3.33}$$

If the interaction is purely dispersive ($\zeta \in \mathbb{R}$) the photon number is conserved and $|\mathfrak{r}|^2 + |\mathfrak{t}|^2 = 1$ holds. Now, in order to specify the equilibrium positions of the clouds the optical force one each of them has to be considered. It can be derived by calculating the amount of momentum transferred to a cloud by the field via the surface integral of the Maxwell stress tensor over the volume $V = \sigma_L \mathrm{d}L$ that encloses the cloud [166] and yields the simple formula

$$F = \frac{\sigma_L\epsilon_0}{2}\left(|A|^2 + |B|^2 - |C|^2 - |D|^2\right). \tag{3.34}$$

Using the ingoing fields $B(x) = E_{\text{back}} \cdot e^{ikx}$ and $C(x) = E_{\text{inc}} \cdot e^{-ikx}$ and the relations (3.32) for the outgoing fields the position dependence of the force can be expressed explicitly [76]

$$\begin{aligned} F(x) &= \frac{2\sigma_L}{c|1-i\zeta|^2}\Big[(I_{\text{back}} - I_{\text{inc}})\text{Im}(\zeta) \\ &\quad - 2\sqrt{I_{\text{inc}} I_{\text{back}}}\text{Re}(\zeta)\sin(2kx+\Phi) + (I_{\text{back}} - I_{\text{inc}})|\zeta|^2\Big], \end{aligned} \tag{3.35}$$

where Φ is the relative phase of the two trapping beams. The first term describes the radiation pressure force on an atom due to absorption of light in the atomic ensemble, which is independent of the position and points in the direction of the weaker beam. The second term represents the dipole force that arises from absorption of light from one beam followed by stimulated emission into the other beam. If $|\zeta| \ll 1$ and $\Gamma \ll |\Delta_{\text{at,L}}|$, which is usually the case in our experiments, this term becomes the dominant one and $|1 - i\zeta|^2 \approx 1$. It produces a restoring force that generates a trap for the atoms. For red lattice detuning $\text{Re}(\zeta) > 0$ and the atoms are attracted towards areas of high intensity. Accordingly, in a blue detuned lattice $\text{Re}(\zeta) < 0$, thus the atoms are repelled. Additionally, if one beam carries a phase, it moves the position of the intensity maxima and hence the points to which the restoring force pulls the atoms. This can be used to couple the motion of the atoms to an external source that produces the phase shifts on the lattice light. The third term is generated by incoherent reflection at the atomic cloud and becomes important for high densities, where it can exceed the other two contributions. Note, that it also points towards the weaker beam. From the relative phase Φ a condition for the maximum asymmetry that still allows for trapping can be found [76]:

$$\mathcal{A}_{\text{max}} = 2\left|\frac{\text{Re}(\zeta)}{|\zeta|^2 + \text{Im}(\zeta)}\right|. \tag{3.36}$$

In the purely dispersive case ($\zeta \in \mathbb{R}$) the relation converts to the simple form

$$\mathcal{A}_{\text{max}} = \frac{2}{\zeta} \;\Leftrightarrow\; \zeta_{\text{max}} = \frac{2}{\mathcal{A}}. \tag{3.37}$$

If $I_{\text{back}} < I_{\text{inc}}$ more photons are on the left of the beam splitters than on the right, which exerts a force on them. If enough light is transmitted ($|\mathfrak{t}| > |\mathfrak{r}|\mathcal{A}/2$) and the beam splitter positions support interference, the number of outgoing photons is high enough to counteract the force and a steady state sets in. This steady state is characterized by a decreased lattice constant d that is given by

$$d_{\text{red}}(\zeta, \mathcal{A}) = \frac{\lambda}{2}\left(1 - \frac{\chi^+(\zeta, \mathcal{A})}{\pi}\right), \quad \zeta > 0 \tag{3.38a}$$

$$d_{\text{blue}}(\zeta, \mathcal{A}) = \frac{\lambda}{2}\left(1 - \left|\frac{\chi^-(\zeta, \mathcal{A})}{\pi}\right|\right), \quad \zeta < 0 \tag{3.38b}$$

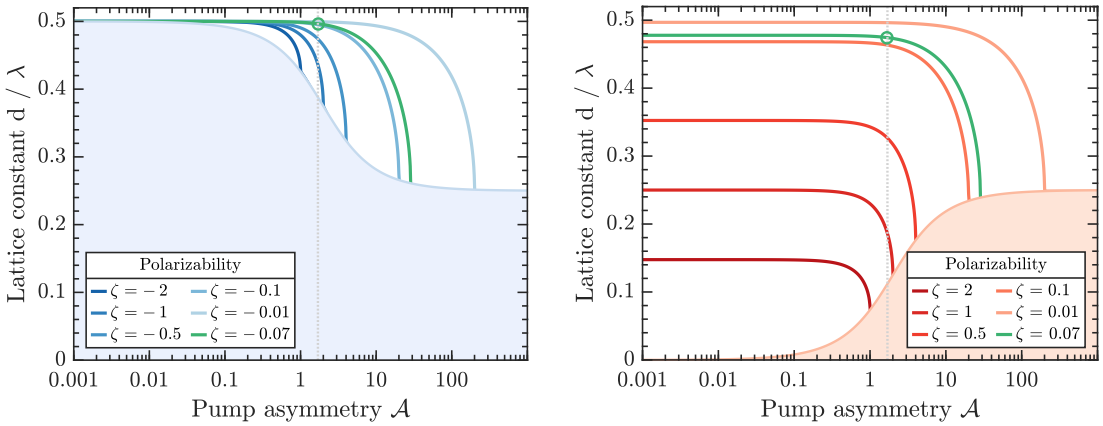

Figure 3.5: Pump asymmetry dependent lattice contraction. The plots show the contraction of the lattice constant d (solid lines) as a function of the pump asymmetry $\mathcal{A}$ for blue (left panel) and red (right panel) lattice detuning and different polarizabilities ζ. Regions where no stable operation of an optical lattice is possible ($\zeta\mathcal{A} < 2$) are denoted by the shaded areas. Our current pump asymmetry $\mathcal{A} = 1.7$ is indicated by the dotted line and the green circles show the calculated lattice constant for the case of $N_{\mathrm{at}} = 5.5 \times 10^7$ distributed over 10 beam splitters that is depicted in figure 3.6, where the phase shift becomes larger than 180° for the first time.

for red and blue lattice detuning respectively, with

$$\chi^{+} = \arccos\left(\frac{-\zeta^2\sqrt{4+\mathcal{A}^2}+\zeta\sqrt{4-\zeta^2\mathcal{A}^2}}{2\,(1+\zeta^2)}\right) \tag{3.39}$$

$$\chi^{-} = \arcsin\left(\frac{\zeta\sqrt{4+\mathcal{A}^2}-\zeta\sqrt{4-\zeta^2\mathcal{A}^2}}{2\,(1+\zeta^2)}\right). \tag{3.40}$$

The resulting contraction of the lattice constant is depicted in figure 3.5 for exemplary values of ζ. Note however, that the lattice contraction is a static effect, which is often masked by more dominant dynamic effects in the lattice. These can lead to the creation of density waves, which propagate in the direction of the weaker lattice beam and can eventually destroy the lattice. A thorough analytical treatment of this phenomenon can be found in [76]. On the other hand we know from active-feedback cooling experiments that an increasing phase lag between action and reaction can turn cooling of the resonator into heating. An evident question is therefore, whether an increasing optomechanical interaction between the atoms in the lattice can influence the aforementioned phase in a way that it can explain the observed heating.

3.3 Collective atomic effects in an asymmetric lattice

In order to study the dynamics that occurs in our atom-mechanical system we use a numerical simulation of the asymmetric coupling lattice that was initially set up by C. F. Klein during his Master thesis [100] and finalized in the course of this thesis. On the one hand it allows us to better understand the behaviour of the system and learn about its stability. On the other hand, we can use it to make predictions about the

behaviour when we add an auxiliary lattice beam to compensate for the intrinsic asymmetry. Asymmetrically pumped optical lattices were already studied using numerical simulations in [73, 76], and we use the same approach to set up the simulation for our system.

3.3.1 Modelling the system

As already described in section 3.2 we model the atomic clouds in the 1D lattice as an array of thin beam splitters as depicted in figure 3.4. To model the lattice we have to relate the light modes to the left of each atomic beam splitter to the modes to the right of them. Since we assume linear optics the relationship will be linear as well and can be expressed by a 2×2 matrix. The atomic clouds can be described by beam splitter matrices M_{BS} separated by the distance d_j. This allows us to use the transfer matrix formalism, which is an elegant tool to handle large composite systems (in our case consisting of travelling light fields and atomic beam splitters) by simple matrix multiplication. The transfer matrix of the system of interest is thus given by the product of the transfer matrices of all system components. In this way we only need to know the ingoing fields on both sides of the system to calculate the fields A_j, B_j, C_j and D_j at any position j in the lattice. Using the beam splitter relations from equation (3.32) we obtain the matrix for a single atomic cloud

$$M_{\mathrm{BS}} = \frac{1}{\mathfrak{t}} \begin{bmatrix} \mathfrak{t}^2 - \mathfrak{r}^2 & \mathfrak{r} \\ -\mathfrak{r} & 1 \end{bmatrix} \overset{(3.33)}{=} \begin{bmatrix} 1 + i\zeta & i\zeta \\ -i\zeta & 1 - i\zeta \end{bmatrix}. \tag{3.41}$$

Since we deal with coherent light fields we have to account for possible phase shifts between the beam splitters to cover interference effects between the superimposed beams. We do this by including the propagation of the light with the wave vector k between the beam splitters[23]

$$M_{\mathrm{prop},j} = \begin{bmatrix} e^{ikd_j} & 0 \\ 0 & e^{-ikd_j} \end{bmatrix}. \tag{3.42}$$

By multiplication of the matrices we can describe how an incident field evolves when passing a single lattice section consisting of two atomic clouds that are separated by a propagation distance d_1

$$\begin{bmatrix} A_1 \\ B_1 \end{bmatrix} = \underbrace{M_{\mathrm{BS}} \cdot M_{\mathrm{prop},1} \cdot M_{\mathrm{BS}}}_{:= M_{\mathrm{sys},1}} \begin{bmatrix} C_2 \\ D_2 \end{bmatrix}. \tag{3.43}$$

Here, the transfer matrix for the composite system $M_{\mathrm{sys},1}$ was introduced. This expression can be further generalized for a lattice of arbitrary size by multiplying with the

[23] The distance d_j between the beam splitters is calculated from adjacent beam splitter positions using equation (3.46).

corresponding transfer matrices for all N lattice sites:

$$\begin{bmatrix} A_j \\ B_j \end{bmatrix} = \underbrace{M_{\mathrm{BS}} \cdot \prod_{j}^{N} M_{\mathrm{prop},j} \cdot M_{\mathrm{BS}}}_{:=M_{\mathrm{sys},j}} \begin{bmatrix} C_N \\ D_N \end{bmatrix}, \tag{3.44}$$

Note, that C_N and D_N describe the fields to the right of the system, whereas A_j and B_j describe the fields to the left at any given beam splitter j. Using the symmetry of the beam splitter relations (3.32) we can see that a reflection along x corresponds to the simultaneous swapping of the amplitudes $A \leftrightarrow D$ and $B \leftrightarrow C$ and hence

$$\begin{bmatrix} A_j \\ B_j \end{bmatrix} = M_{\mathrm{BS}} \begin{bmatrix} C_j \\ D_j \end{bmatrix} \Leftrightarrow \begin{bmatrix} D_j \\ C_j \end{bmatrix} = M_{\mathrm{BS}} \begin{bmatrix} B_j \\ A_j \end{bmatrix}, \tag{3.45}$$

which can be used to calculate the fields to the right of the j-th beam splitter. With the knowledge of the ingoing left-propagating field $C_N = E_{\mathrm{inc}} \cdot e^{-ikx}$ and the right-propagating field $B_1 = E_{\mathrm{back}} \cdot e^{ikx}$ all fields at any position in the lattice can be calulated.

Now we have to add the mechanical resonator to the system. Since it can be represented by another beam splitter it seems straightforward to include it. However, its separation from the atomic beam splitters is much larger than d and cannot be precisely determined. Moreover, the fields that mediate the interaction travel through different media, such that an accurate description of the propagation matrix is difficult. Because the reflectivity of the resonator is implicitly included in the field amplitude E_{back}, we focus on the action of the resonator on the light field - a modulation of the phase. We account for the phase modulation by adding the phase term $\Phi(t) = \Phi_0 \cos(\omega t)$ to the ingoing field $B_1 = E_{\mathrm{back}} \cdot e^{ikx + i\Phi(t)}$. In a similar manner the cumulated effect of the collective optomechanical interaction in the optical lattice manifests itself in a phase shift of the amplitude modulation on the outgoing field A_1, i.e the atomic backaction on the resonator.

3.3.2 Numerical simulation and results

At the start of the simulation ($t = 0$) the positions of all atomic beam splitters are randomly shifted by a small displacement $\xi_j(t = 0)$ from their steady state positions x_j^{ss}, which are determined by the detuning dependent lattice constant introduced in (3.38) and the position offset x_{asym} caused by the asymmetric radiation pressure

$$x_j(t = 0) \;=\; x_j^{ss} + \xi_j(t = 0) \;=\; x_{\mathrm{asym}} + (j - 1)d_{\mathrm{red,blue}} + \xi_j(t = 0). \tag{3.46}$$

The random displacement $\xi_j(t = 0)$ is a uniformly distributed variable between ξ_{ini} and $-\xi_{\mathrm{ini}}$, with $\xi_{\mathrm{ini}} = 5 \times 10^{-4}\lambda$. In each time step the fields at all beam splitters are calculated and used to determine the force F_j on each beam splitter via (3.34). Next, all beam splitter positions for the following time step are calculated from the corresponding equation of motion

$$m_{\mathrm{BS}}\ddot{x}_j = -m_{\mathrm{BS}}\Gamma_{\mathrm{at}}\dot{x}_j + F_j(x_1, ..., x_N), \tag{3.47}$$

where $m_{\mathrm{BS}} = N_{\mathrm{at}} m_{\mathrm{Rb}}/N$ is the mass of a beam splitter and Γ_{at} is the laser-cooling induced atomic damping rate. From equation (3.47) we obtain a system of N differential equations that are coupled to each other via the force F_j. In order to solve the system of equations numerically we use the ordinary differential equation solver `ode45` in MATLAB. Since (3.47) represents differential equations of second order and the solver is only capable of solving a system of first order equations we have to reduce them to ordinary differential equations by making the subsitution $\dot{x}_j = X_j$, which leads to the first-order differential equations

$$\dot{x}_j = X_j \quad \text{and} \quad \dot{X}_j = -\Gamma_{\mathrm{at}} X_j + \frac{F_j}{m_{\mathrm{BS}}}. \tag{3.48}$$

They can now be solved by setting the initial conditions in form of initial positions x_j (equation (3.46)) and initial velocities $\dot{x}_j = \omega \xi_{\mathrm{ini}}$ for each beam splitter. We use the period of one oscillation $\tau_{\mathrm{osc}} = 2\pi/\omega$ to define the simulation time $t = 40\,\tau_{\mathrm{osc}}$. The system evolution is then solved incrementally by integrating the differential equations for each time step. After each iteration the the newly determined beam splitter displacements and velocities are used as the initial conditions for the following time step and the new distances d_j are calculated from the changed positions.

In order to determine the effect of the phase modulation at frequency ω carried by the beam coming from the mechanical resonator, the amplitude and phase of the resulting power modulation on the outgoing beam are evaluated after each simulation run. They can be interpreted as the atomic backaction on the lattice light and are imprinted on the beam that leaves the interaction region in the direction of the MiM system. The power modulation is described by $P_{\mathrm{left}} = \epsilon_0 c \pi {\mathrm{w_{lat}}}^2 |A_1|^2/4$. We only take it into account after an initial transient time $T_{\mathrm{damp}} = 1/\Gamma_{\mathrm{at}}$. To study the evolution of the amplitude and the phase, the modulation frequency is swept between 5 kHz and 500 kHz.

For parameters similar to the ones used in our sympathetic cooling experiments (see sections 3.1 and 3.5) we simulate the backaction of the atomic ensemble on the coupling lattice light. In order to keep the computing time low, we use only ten beam splitters in our simulation since, similar as in [72, 73], we find that the collective dynamics converge quickly for more than two beam splitters (see figure B.4). In figure 3.6 the situation in a balanced lattice ($R = 1$) is compared to an asymmetric lattice ($R = 0.22$) for varying atom numbers N_{at} in the lattice volume. We evaluate the relative amplitude of the power modulation $(P_{\mathrm{left}} - \langle P_{\mathrm{left}} \rangle)/\langle P_{\mathrm{left}} \rangle$ on the outgoing field propagating to the left, where the angled brackets denote the mean value. The phase of the power modulation is measured relative to the ingoing phase $\Phi(t)$.

In the balanced lattice we obtain the expected amplitude and phase response for a driven damped harmonic oscillator, where the position and width of the resonance depend sensitively on the set lattice power P_{inc} and detuning $\Delta_{\mathrm{at,L}}$, as well as the atomic damping rate Γ_{at}. Their shape obviously differs slightly from the textbook expectation, which can be attributed to the strong damping $\Gamma_{\mathrm{at}} = 0.3\,\omega_{\mathrm{m}}$ that was assumed for the

simulation, based on earlier experimental results [74, 77].
For comparison the inset shows the result of the simulation for low atomic damping and a single beam splitter. Here, the expected response is recovered. The phase modulation causes a displacement of the intensity maxima, which can be adiabatically followed by the atoms for low driving frequencies ω. Hence, the atoms barely oscillate in the trapping potential leading to a small power modulation. With increasing frequency the atoms can no longer follow the lattice motion and start to oscillate at larger amplitudes resulting in a stronger backaction. At resonance the driving is 90° ahead of the atomic motion and has the greatest impact. For further increased ω the atoms stay located at the minimum of the temporally averaged potential and do not react to the motion any more. Their phase lag approaches $\Delta\phi = -180°$. Under the effect of strong damping, as realized in the simulation, we observe a finite phase lag even at low driving frequencies and a negligible amplitude of the power modulation.

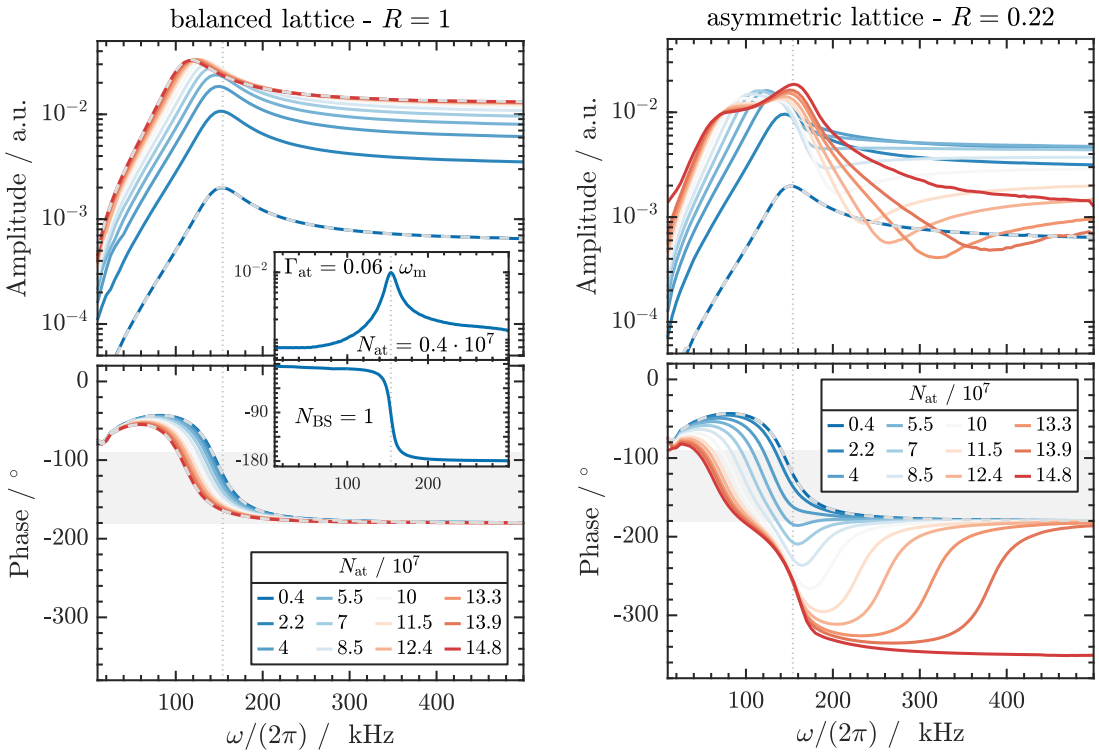

Figure 3.6: Simulated atomic response for variable atom number N_{at}. Amplitude and phase response of the relative power modulation $(P_{left} - \langle P_{left}\rangle)/\langle P_{left}\rangle$ of the outgoing beam as a function of the modulation frequency ω. The phase is referenced to the phase of the ingoing modulation. The vertical dotted lines mark the resonance frequency $\omega_{at} = \omega_m$ and the dashed grey lines denote the response of a single beam splitter. Grey areas denote the phase margin in which sympathetic cooling is expected to occur. **Inset:** Amplitude and phase response for a single beam splitter with $N_{at} = 0.4 \cdot 10^7$ and low damping $\Gamma_{at} = 0.06\,\omega_m$. For both, balanced and asymmetric lattice configurations the same simulation parameters were used except for the reflectivity R and the detuning $\Delta_{at,L}$. Parameters: ingoing power $P_{inc} = \pi w_{lat}^2 I_{inc}/2 = 100\,\mu W$, detuning $\Delta_{at,L}/(2\pi) = -9.6\,GHz$ ($R = 1$) and $\Delta_{at,L}/(2\pi) = -4.55\,GHz$ ($R = 0.22$), beam waist $w_{lat} = 70\,\mu m$, number of beam splitters $N_{BS} = 10$, atomic damping $\Gamma_{at} = 0.3\,\omega_m = 290\,kHz$ and driving amplitude $\Phi_0 = 2\pi \cdot 10^{-3}$.

The parameters for the simulation were chosen such that the atomic trapping frequency in the lattice ω_{at} coincides with the resonance frequency of our mechanical resonator ω_{m}. However, for increasing atom numbers the maximum of the amplitude at resonance is shifted to lower frequencies, which can be attributed to the increased inertia due to the higher atomic beam splitter masses. In the balanced lattice the atomic ensemble behaves like a single beam splitter and no intra beam splitter induced dynamics occur. This is indicated by the dashed lines in the left panel of figure 3.6 where the simulation was run exemplarily for the lowest and highest atom number under the assumption that all atoms are inside one beam splitter.

With regard to an asymmetric lattice the situation looks different. While at low atom numbers the ensemble still behaves like a single beam splitter, collective effects become increasingly important for larger systems with more atoms. This can be seen when comparing how the response of the system changes for different atom numbers and an increasing amount of beam splitters (figure B.4). From the right panel of figure 3.6 one can recognize that the amplitude response gets much more broadened than in the balanced lattice and separates into a double peaked feature. More importantly, the phase lag enlarges dramatically with increasing atom number and approaches $\Delta\phi = -360°$. This is a strong indicator for the hypothesis that the phase lag is responsible for the instability that occurs in the hybrid atom-mechanical system. It can be explained by revisiting the coupling mechanism:
The displacement x_m of the mechanical resonator from its equilibrium position produces a phase shift proportional to x_m on the reflected lattice light. This phase shift causes a displacement of the lattice sites and thus moves the atoms out of their equilibrium position inside the lattice potential. As a consequence the atoms redistribute the incoming lattice photons (see section 3.1.1), which results in a restoring force F_{d} acting in the opposite direction. Following the oscillation of the resonator the atoms also oscillate in their respective potential wells and thereby produce an intensity modulation at the oscillation frequency. This intensity modulation in turn exerts a time-dependent radiation pressure force F_{rad} on the resonator, which can influence its motion. If there is a phase lag $\Delta\phi$ between the motion of the resonator and the motion of the atoms, the resulting radiation pressure force can damp the resonator motion and lead to sympathetic cooling. The process is illustrated in figure 3.7, where the upper panel denotes the ideal case of a $\Delta\phi = -90°$ phase lag. The motion of the resonator is depicted by the sinusoidal line, where the differently coloured amplitudes show the direction of the displacement. The motion of the atoms is symbolized by the circles on the sinusoidal trajectory. Every time the resonator moves from the red to the blue position it is subject to F_{rad}, which counteracts the movement and leads to damping of the resonator. This is physically equivalent to the velocity dependent feedback cooling discussed in section 2.2.3. The lower panel illustrates the scenario for a phase lag of $\Delta\phi = -180°$. This is the tipping point, where damping turns into excitation, since F_{rad} acts on the resonator at the point of largest displacement (red) and in the direction of the resonator movement. Hence, for phase lags smaller than $\Delta\phi = -180°$ the resonator gets heated by the atomic motion and the maximum excitation appears at $\Delta_\phi = -270°$.

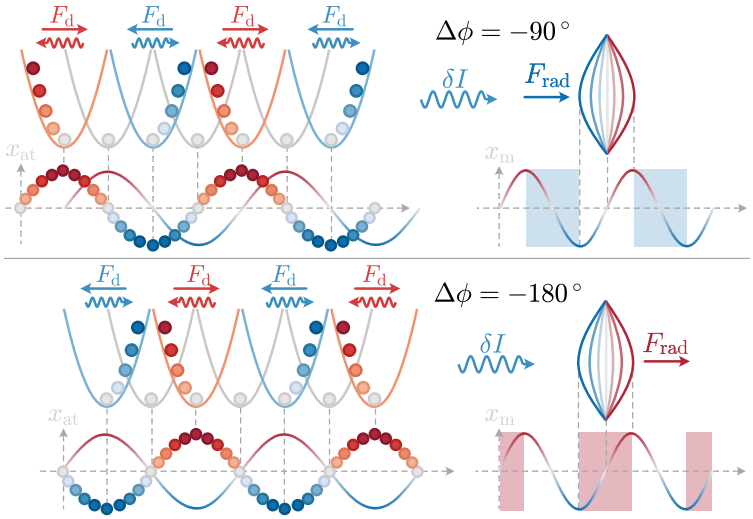

Figure 3.7: Effect of the phase lag on the atom-membrane interaction. The illustration shows how the atoms react to a displacement of the lattice potential that results from a phase modulation by the mechanical resonator. A lattice displacement to the left elevates the atoms to the right slope of the potential (blue) and a displacement to the right elevates the atoms to the left slope (red). When excited, the atoms experience the restoring force F_d and emit light preferably in the opposite direction. The oscillatory motion produces an intensity modulation δI that manifests as a radiation pressure force F_rad on the resonator. The resonator motion is depicted by the red and blue coloured sinusoidal line and the motion of the atoms is traced out by the circles on the sinusoidal trajectory. The shaded areas denote regions where F_rad leads to cooling (blue) - when the force acts in the opposite direction of the resonator motion - and heating (red) - when the force acts in the direction of the motion.

Qualitatively, the simulation reproduces the results obtained in [73] and gives a plausible explanation for the experimentally observed instability in the hybrid system. Motivated by this result, we can use the simulation to make a prediction about the system behaviour when an additional lattice beam is included in the simulation. This beam shall be used in the experiment to balance the pump power in the lattice and prevent the instability from occurring. The necessary properties to realize the scheme experimentally as well as the method to adjust the balancing of the resulting three beam coupling lattice are described in detail in the next sections. For now we only assume that the auxiliary lattice beam is co-propagating with the reflected beam in the right direction. To provide a balanced lattice the total reflected intensity has to be equal to the incident intensity $I_\mathrm{ref,tot} = I_\mathrm{inc}$. It is given by $I_\mathrm{ref,tot} = I_\mathrm{back} + I_\mathrm{aux} + 2\sqrt{I_\mathrm{back} I_\mathrm{aux}}\cos(\phi_\mathrm{aux,back})$. For simplicity we chose the relative phase between the auxiliary beam and the back-reflected beam to be $\phi_\mathrm{aux,back} = \pi/2$ such that $I_\mathrm{aux} = I_\mathrm{inc} - I_\mathrm{back}$ holds. To include the auxiliary beam into the simulation we simply add its contribution to the right propagating field: $B_1 = E_\mathrm{back} \cdot e^{i(kx+\Phi(t))} + E_\mathrm{aux} \cdot e^{i(kx+\phi_\mathrm{aux,back})}$, where $E_\mathrm{aux} = \sqrt{1-R}\cdot E_\mathrm{inc}$.

The simulation result for the PAC lattice is depicted in figure 3.8. As expected we recover similar results as for the balanced lattice with only two beams and no intra-beam splitter dynamics seem to occur. The only visible differences are that the amplitude is reduced, compared to the two beam balanced lattice, and does not monotonously

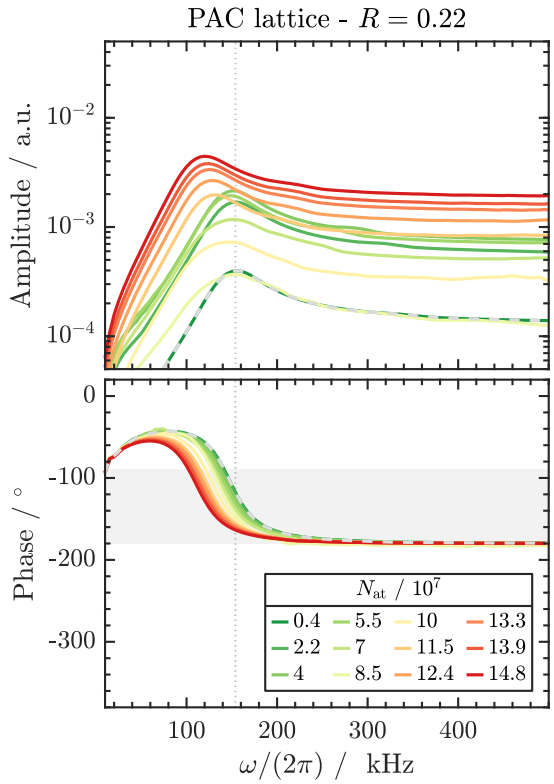

Figure 3.8: Simulated atomic response for variable atom number N_{at} with pump asymmetry compensation. Amplitude and phase response of the relative power modulation $(P_{left} - \langle P_{left}\rangle)/\langle P_{left}\rangle$ of the outgoing beam as a function of the modulation frequency ω. Here, a balanced optical lattice is simulated that is created by employing an auxiliary lattice beam, which is co-propagating with the back-reflected beam. The intensity $I_{aux} = 0.78\, I_{inc}$ and phase $\phi_{aux,back} = \pi/2$ are set to compensate the lacking intensity in the back-reflected beam, like described in section 3.5.2. The atomic backaction phase (lower panel) is referenced to the phase of the ingoing modulation. Again, the dashed lines denote the response of a single beam splitter and the dotted lines mark the resonance position. The grey shaded area denotes the phase margin where sympathetic cooling should occur.

grow with increasing atom number. The reduced amplitude can be explained by the fact that the modulation is carried by a much weaker beam with field amplitude E_{back} instead of E_{inc}. Hence, the resulting amplitude of the power modulation is expected to be lower than in the two beam balanced lattice. The non-monotonous behaviour of the amplitude response is an interesting yet not understood feature whose origin is left for future investigation. Potentially, interference effects between the unavoidable amplitude modulation of the combined auxiliary and back-reflected beam with the phase shifted amplitude modulation generated by the optical lattice play a role here. Remarkably, the frequency shift of the amplitude peak is equal in the PAC lattice and in the balanced two beam lattice, which can also be seen from the identical phase response. This result substantiates our conjecture that a compensation of the pump asymmetry in our lattice should enable us to increase the coupling strength trough a larger number of atoms that participate in the process.

Conclusion

The results of our numerical simulation show that light-induced interactions between atoms in different lattice wells occur in asymmetric lattices for regimes of high atomic polarizability ζ. When the atomic motion in the lattice is driven by a modulation of the phase of one ingoing beam, the atomic backaction on the light is completely different than in a balanced lattice, or for a single beam splitter. Most strikingly, the phase of the atomic backaction can be strongly delayed, which has a crucial effect if one considers closing the loop to act back on the source of the phase modulation. In this case for phase lags larger than $\Delta\phi = -180°$ the atomic backaction would resonantly enhance

the driving process and lead to instability of the system.
Experimentally, it is not feasible for us to determine the exact atom numbers in the lattice volume and thus precise modelling or a direct comparison with the experiment is difficult. Nevertheless, in a parameter regime similar to our experimental conditions the simulation shows atomic backaction effects that qualitatively agree with our measurements. The full range of parameter variations i.e. dependence on the detuning and its sign, atomic damping rate, lattice asymmetry and number of beam splitters in the simulation can be found in appendix B.2. The main observations are listed here in bullet points:

- Decreasing detuning $\Delta_{\mathrm{at,L}}$ leads to an increased atomic polarizability $\zeta \sim \frac{1}{\Delta_{\mathrm{at,L}}}$ and hence stronger backaction induced by collective effects.

- For increasing damping the initial phase lag is increased.

- For more than one beam splitter collective effects in the asymmetric lattice start to occur and saturate quickly for an increasing number of beam splitters.

- The larger the asymmetry the smaller the number of atoms at which collective effects start to play a role.

However, the simulation does not explicitly show different behaviour depending on the sign of the detuning. Although the configuration of the lattice changes, the effect on the backaction is seemingly the same. Thus the experimentally observed difference between red and blue lattice detuning can only be explained by an increased number of atoms that participate in the coupling in a red detuned lattice. Finally, we find that an auxiliary lattice beam that provides the lacking intensity to produce a balanced lattice can stabilize the system and suppress the collective atomic effects observed in an asymmetric two beam lattice. We conclude that a pump asymmetry compensated lattice should allow to involve more atoms in the coupling process, permit sympathetic cooling with dense atomic samples in a red detuned lattice and consequently increase the coupling strength.

3.4 Experimental design considerations

In the preceding sections the necessity to compensate the pump asymmetry in our setup was motivated. A suitable scheme to reach this goal is the use of an auxiliary lattice beam, which provides the power that is lacking in the back-reflected beam to produce a balanced coupling lattice. For that, the auxiliary beam has to be superimposed with the back-reflected beam from the cavity that carries the signal from the MiM system, such that they are indistinguishable at the site of the atoms. This requires identical frequency and polarization of the beams as well as ideal mode match. Moreover, the power of the auxiliary beam and its phase, relative to the back-reflected beam, must be independently adjustable. In the following the experiment specific demands will be regarded to determine the necessary properties for the auxiliary lattice beam.

Beam profile

The beam profile has to be mode matched to the coupling and back-reflected beam. This involves the waist size, focal position and divergence of the beam. Since the auxiliary beam will be focussed onto the atoms by a separate telescope it is essential to avoid astigmatisms and aberrations in the beam that would reduce the spatial coherence and lead to local intensity fluctuations in the lattice. Moreover, around the focal region Gaussian beams experience a phase advance, whose amount is described by the Gouy phase (see left panel in figure 3.9)

$$\varphi_{\text{gouy}} = \arctan\left(\frac{z}{z_0}\right) \tag{3.49}$$

where z is the position along the beam axis and $z_0 = \pi \mathrm{w_0}^2/\lambda$ is the Rayleigh range for a beam waist $\mathrm{w_0}$ and the wavelength λ. A mismatch in the waist size or displaced focal positions of the beams can lead to an additional relative phase $\Delta\varphi_{\text{gouy}}$ between the beams, which we have to avoid.
The influence of a waist mismatch on this phase is depicted in the central panel of figure 3.9. For a difference of 10 % in waist size a phase difference of $\Delta\varphi_{\text{gouy}} = 4°$ is acquired over the extent of the atomic cloud, which has a radius of $R_{\text{at}} \approx 2\,\text{mm} \approx 0.1 \cdot z_0$. Differing focal positions have an even stronger impact on $\Delta\varphi_{\text{gouy}}$ as is depicted in the right panel of figure 3.9. A position offset of $\Delta z = z_0/4 = 4.9\,\text{mm}$ already results in a relative phase difference of $|\Delta\varphi_{\text{gouy}}| = 14°$, which can have a significant impact on the combined lattice beam. In order to avoid these effects the setup must allow for positioning the auxiliary beam focus with sub-millimeter precision and the waists have to be matched up to a few micrometers.
In the realized setup the focal position can be adjusted with an accuracy of 0.1 mm

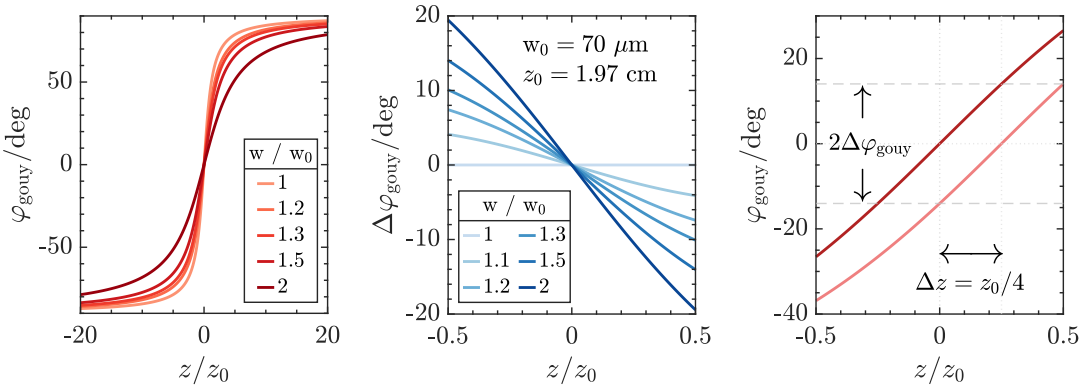

Figure 3.9: Gouy phase shift caused by different waist sizes and focal positions. For the calculations the waist size $\mathrm{w_0} = 70\,\mu\text{m}$ and Rayleigh range $z_0 = 1.97\,\text{mm}$ of our coupling lattice beam are assumed. **Left panel:** Gouy phase for different positions along the beam axis. Upon passage through the focal plane of a Gaussian beam φ_{gouy} leads to a phase shift of 180°. **Central panel:** Phase difference $\Delta\varphi_{\text{gouy}}$ introduced by deviant waist sizes of two beams for different ratios of the beam waists as a function of the position along the beam axis. **Right panel:** φ_{gouy} for two beams with equal waists that are $\Delta z = 4.9\,\text{mm}$ apart (dotted lines). The difference in focal position introduces a relative phase $\Delta\varphi_{\text{gouy}} = 14°$ (dashed lines).

and the waist sizes differ by 1.7 %, resulting in a maximum additional relative phase of $\Delta\varphi_{\mathrm{gouy}} = 0.5°$, whose effect should be negligible.

Relative phase and intensity

The auxiliary beam must have the same frequency and polarization as the coupling and back-reflected lattice beams in order to allow for maximal interference. Furthermore, in order to carefully balance the lattice, it must be possible to tune and fix the relative phase $\phi_{\mathrm{aux,back}}$ between the auxiliary and the back-reflected beams to arbitrary values. A convenient scheme for the stabilization of the relative phase of two beams is the so-called *side-of-fringe* lock. In our case, the fringe is a slope of the sinusoidal interference signal obtained by sweeping the relative phase ϕ_{rel} between two beams. A reference phase ϕ_{ref}, represented by a point on that slope, can be chosen to lock the actual phase ϕ_{act} to that reference phase using an actuator that is able to adjust the relative phase. Since the reference phase lies on a slope, a controller can discriminate the direction in which the actuator needs to shift the actual phase in order to coincide with the reference phase ($\phi_{\mathrm{rel}} = |\phi_{\mathrm{act}} - \phi_{\mathrm{ref}}| \to 0$). Typically, the reference phase ϕ_{ref} is chosen to be at the steepest point on the slope, which is exactly centred between the turning points of the signal and thus allows for the best locking stability. For our use-case the locking bandwidth should stay far below the mechanical resonance frequency ω_{m} as otherwise the lock could erase the resonators phase information from the signal. We anticipate the required locking bandwidth to be on the order of 5-10 kHz, since the planned interferometer is set up on a vibration isolated, temperature stabilized optical table with high stability optics mounts.

It is important to consider whether the combined back-reflected beam will be able to produce a balanced optical lattice. For that we first calculate the expected intensity I_{lat} of a regular 1D optical lattice

$$I_{\mathrm{lat}} = \frac{c\epsilon_0}{2}|\bar{E}_{\mathrm{inc}} + \bar{E}_{\mathrm{back}}|^2 = \frac{c\epsilon_0}{2}\left[|E_{\mathrm{inc}}|^2 + |E_{\mathrm{back}}|^2 + 2E_{\mathrm{inc}}E_{\mathrm{back}}\cos(2kx - \phi_{\mathrm{inc,back}})\right]. \tag{3.50}$$

where E_{inc} and E_{back} are the electric field amplitudes of the incident and back-reflected beam respectively and $\phi_{\mathrm{inc,back}}$ is relative phase between the beams. Since the lattice is produced by reflection from the MiM system the relative phase is fixed to $\phi_{\mathrm{inc,back}} = \pi$. We normalize the incident beam intensity to $I_{\mathrm{inc}} = 1$ and distinguish the case of a balanced lattice with $I_{\mathrm{back}} = I_{\mathrm{inc}}$ from an asymmetric lattice with $I_{\mathrm{back}} = 0.3I_{\mathrm{inc}}$ like it is present in our experiment. Both configurations are depicted in the left panel of figure 3.10. For a balanced lattice (red dashed line) the maximum lattice depth is $V_{\mathrm{lat,bal}} \propto 4I_{\mathrm{inc}}$ and the intensity completely vanishes at the minima. In our actual lattice (blue dashed line) the maximum lattice depth is reduced to $V_{\mathrm{lat,act}} \propto 4\sqrt{I_{\mathrm{inc}}I_{\mathrm{back}}}$ due to the asymmetry in the pumping which leads also to non-vanishing intensity at the lattice minima.

When the additional auxiliary beam is taken into account, equation (3.50) is extended by additional interference terms with the auxiliary beam

$$\begin{aligned} I_{\mathrm{lat}} &= \frac{c\epsilon_0}{2}|\bar{E}_{\mathrm{inc}} + \bar{E}_{\mathrm{back}} + \bar{E}_{\mathrm{aux}}|^2 \\ &= \frac{c\epsilon_0}{2}\Big[|E_{\mathrm{inc}}|^2 + |E_{\mathrm{back}}|^2 + |E_{\mathrm{aux}}|^2 + 2E_{\mathrm{inc}}E_{\mathrm{back}}\cos(2kx - \phi_{\mathrm{inc,back}}) \\ &+ 2E_{\mathrm{inc}}E_{\mathrm{aux}}\cos(2kx - \phi_{\mathrm{aux,back}}) + 2E_{\mathrm{back}}E_{\mathrm{aux}}\cos(\phi_{\mathrm{inc,back}} - \phi_{\mathrm{aux,back}})\Big]. \end{aligned} \tag{3.51}$$

Here, $\phi_{\mathrm{aux,back}}$ denotes the relative phase between the auxiliary and the back-reflected beam and the fields are defined in a similar way[24] as in section 3.2. Now, a lattice depth $V_{\mathrm{lat}} \propto 4I_{\mathrm{lat}}$ equal to the one in the balanced lattice can be obtained by different combinations of the auxiliary beam intensity I_{aux} and the relative phase $\phi_{\mathrm{aux,back}}$. This is depicted by the solid blue lines in the left panel of figure 3.10. Each shade represents a different set auxiliary beam intensity, which produces the same lattice depth as in a balanced two beam lattice for an appropriately set relative phase $\phi_{\mathrm{aux,back}}$. The right panel of figure 3.10 shows the normalized intensity $I_{\mathrm{aux,back}}$ resulting from the interference of the auxiliary and the back-reflected beam, depending on their relative phase. The circles denote the relative phase that has to be adjusted in order to produce a balanced lattice with three beams. Once the relative phase between the auxiliary and

[24] i.e. $\bar{E}_{\mathrm{inc}} = E_{\mathrm{inc}}e^{ikx}$, $\bar{E}_{\mathrm{back}} = E_{\mathrm{back}}e^{-i(kx-\phi_{\mathrm{inc,back}})}$ and $\bar{E}_{\mathrm{aux}} = E_{\mathrm{aux}}e^{-i(kx-\phi_{\mathrm{aux,back}})}$

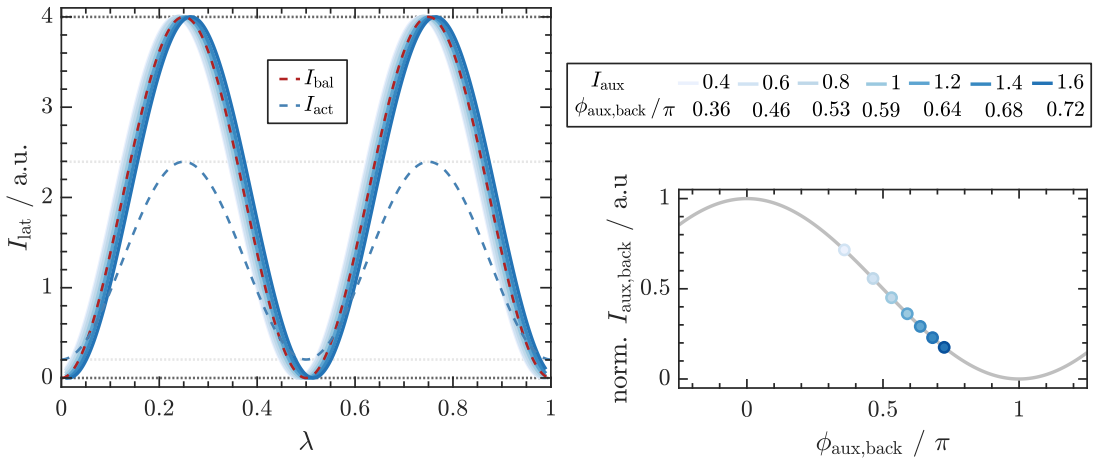

Figure 3.10: Intensity I_{lat} in the coupling lattice for different lock-points of the relative phase $\phi_{\mathrm{aux,back}}$. Left panel: Lattice intensity I_{lat} for a two beam lattice (dashed lines, equation (3.50)) in our actual configuration (blue) and a balanced one (red) compared to a three beam lattice with added auxiliary beam (solid blue shaded lines, equation (3.51)). Each shade represents a different set auxiliary beam intensity I_{aux} and the specific lattice depth that corresponds to the balanced two beam lattice is produced by an appropriate choice of the relative phase $\phi_{\mathrm{aux,back}}$. **Right panel:** Normalized intensity $I_{\mathrm{aux,back}} = I_{\mathrm{aux}} + I_{\mathrm{back}} + 2\sqrt{I_{\mathrm{aux}}I_{\mathrm{back}}}\cos(\phi_{\mathrm{aux,back}})$ obtained by interference of the auxiliary and back-reflected beam as a function of their relative phase $\phi_{\mathrm{aux,back}}$. The blue shaded circles denote the phase that has to be adjusted to produce a balanced lattice at the corresponding auxiliary beam intensity I_{aux}.

the back-reflected beam is fixed they can be regarded as one beam and we recover an ordinary 1D optical lattice with two counter-propagating beams.

Due to the fact, that we have to superimpose the auxiliary beam with the back-reflected beam on an optical element the losses in the back-reflected beam will further increase, leading to an even stronger initial pump-asymmetry. At the same time this means that only a small fraction of the auxiliary beam intensity will be co-propagating with the back-reflected beam after that element. To keep the additional losses in the back-reflected beam low and simultaneously be able to use a sufficient amount of the auxiliary beam we employ a substrate with a reflectivity of 92.8 % at 780 nm (see section 3.4.1). Together with other modifications to the setup this results in an intensity of the back-reflected beam of $I_{\mathrm{back}} \approx 0.235\, I_{\mathrm{inc}}$ [25]. From equation (3.50) the condition for a balanced lattice becomes apparent[26]

$$E_{\mathrm{inc}} = E_{\mathrm{back}} + E_{\mathrm{aux}} \tag{3.52}$$

and we find a range of auxiliary beam intensities that allow for balancing the three beam lattice for an appropriate relative phase setting:

$$I_{\mathrm{aux}}^{\mathrm{max,min}} = (\sqrt{I_{\mathrm{inc}}} \pm \sqrt{I_{\mathrm{back}}})^2 = (\sqrt{I_{\mathrm{inc}}} \pm \sqrt{0.235 I_{\mathrm{inc}}})^2 = \begin{cases} 2.2 I_{\mathrm{inc}} \\ 0.265 I_{\mathrm{inc}} \end{cases} \tag{3.53}$$

Note, that these two values are the extrema of the range of auxiliary beam intensities and require complete constructive or destructive interference to produce a balanced three beam lattice. Hence, they are not experimentally feasible with a setup that requires a finite slope of the interference signal to lock the phase. Nevertheless, the auxiliary beam setup is planned to provide intensities in this range.

3.4.1 The pump asymmetry compensation setup

In the following section the realized experimental setup for the compensation of the pump asymmetry in our coupling lattice is discussed. This setup was used to conduct the experiments that are presented later in section 3.5 and was set up together with C. F. Klein.

Optical setup

For the compensation of the pump asymmetry in our experiment we set up a dedicated auxiliary lattice beam that we employ to provide the lacking intensity in the back-reflected beam. The coupling lattice setup (discussed in section 2.2.1) was refined and is supplemented by the additional auxiliary beam. A detailed sketch with all relevant components is depicted in figure 3.11.
In order to ensure identical frequency, the auxiliary lattice beam is derived from the same beam as the coupling lattice incident beam. We exchanged the polarization maintaining fiber, which guides the lattice light from the laser system to the experiment by

[25] A detailed overview of all relevant optical losses in the setup can be found in figure B.1
[26] Assuming a fixed relative phase $\phi_{\mathrm{aux,back}}$ such that the two beams can be treated as one.

a single mode fiber, equipped with a fiber polarization controller (FPC). This allows to split the incident lattice beam conveniently at the PBS inside the coupling lattice telescope and to quickly change the splitting ratio if needed. At the outputs of the PBS the beam is collimated and has a waist of $w_{col} = 1.8\,mm$. The transmitted beam is focused onto the atoms by a $f = 500\,mm$ lens and produces a waist $w_{inc} = (69.8 \pm 0.8)\,\mu m$ at the site of the atoms in a working distance of $(505 \pm 2)\,mm$ [27]. Since only 20 % of the incident light are transmitted into the coupling beam branch we exchanged the substrate S1 in the differential mirror mount for a higher reflective one to provide sufficient intensity at the atomic site. After the beam has passed the atoms it is reflected from substrate S2 with a reflectivity of $R_{780} = 92.8\,\%$ and coupled into the cryostat. The cryostat telescope was rebuilt to produce an exact copy of the incident beam telescope and we exchanged also the PM fiber for an anti-reflection coated single mode fiber[28] with FPC to adjust the polarization of the back-reflected light from the cavity. This allows for fiber coupling efficiencies into the cryostat of up to 90 % for coupling lattice and homodyne light. We measured the waist of the back-reflected lattice beam to be $w_{back} = (69.7 \pm 0.1)\,\mu m$, which matches the incident beam waist very well within the error. Also the measured working distance of $(504 \pm 2)\,mm$ is nearly equal to the one of the coupling lattice telescope. Both telescopes are mounted on translation stages that allow to move the focal position along the beam propagation axis and align it with respect to the atoms in the glass cell.

The auxiliary beam (light red line in figure 3.11) leaves the coupling lattice telescope through the reflection port of the PBS and passes a combination of $\lambda/2$ waveplate and PBS that are used to adjust the auxiliary beam power independently from the incident beam power. Additionally, the auxiliary beam is p-polarized after the PBS and thus matched to the polarization of the other two lattice beams. Subsequently, the auxiliary beam diameter is reduced using telescope T_2 to fit through the EOM that we employ as a fast phase shifter. Telescope T_3 is an inverted version of T_2 and expands the beam back to its original diameter. Additional to the EOM, which has a large bandwidth but small phase stroke, we use a piezo mounted mirror, whose travel of 3.3 µm allows for larger phase shifts at the cost of a reduced bandwidth. Finally, the auxiliary beam passes telescope T_1 that is used to mode match it to the back-reflected lattice beam from the cavity. This telescope has a working distance of $(590 \pm 5)\,mm$ and is also positioned on a translation stage to position its focal plane with respect to the back-reflected beam. It produces a waist of $w_{aux} = (68.5 \pm 0.5)\,\mu m$ at the site of the atoms, which deviates by only 1.7 % from the waist of the back-reflected beam w_{back} (see figure 3.12). The auxiliary beam is superimposed with the back-reflected beam on substrate S2, where only 7.2 % of the auxiliary beam power are transmitted and the rest is dumped. For the alignment with respect to the back-reflected beam we installed two pellicle beam splitters in the common beam path of the back-reflected and auxiliary beam. Their reflectivity is strongly dependent on the tilt angle with respect to the beam axis and we measured it to be $(94 \pm 2)\,\%$ in their final position. One of them is placed right after substrate S2 and allows to view and overlap the beams at their focal

[27] Due to the slightly different mode field diameter of the new fiber the waist w_{inc} is decreased by 6 µm with respect to the previous lattice beam.

[28] We used the same fiber type as on the lattice incident telescope - *Nufern* 780-HP single mode fiber with 5 µm mode field diameter.

position using a beam profiling camera. After the alignment is finished the camera is replaced by a photo detector, which is positioned in the focal plane of the beams to derive the signal for the phase-lock. The second pellicle beam splitter is placed in front of the coupling lattice telescope and allows to monitor and align the beams in the far field. The alignment strategy will be outlined in the next paragraph.

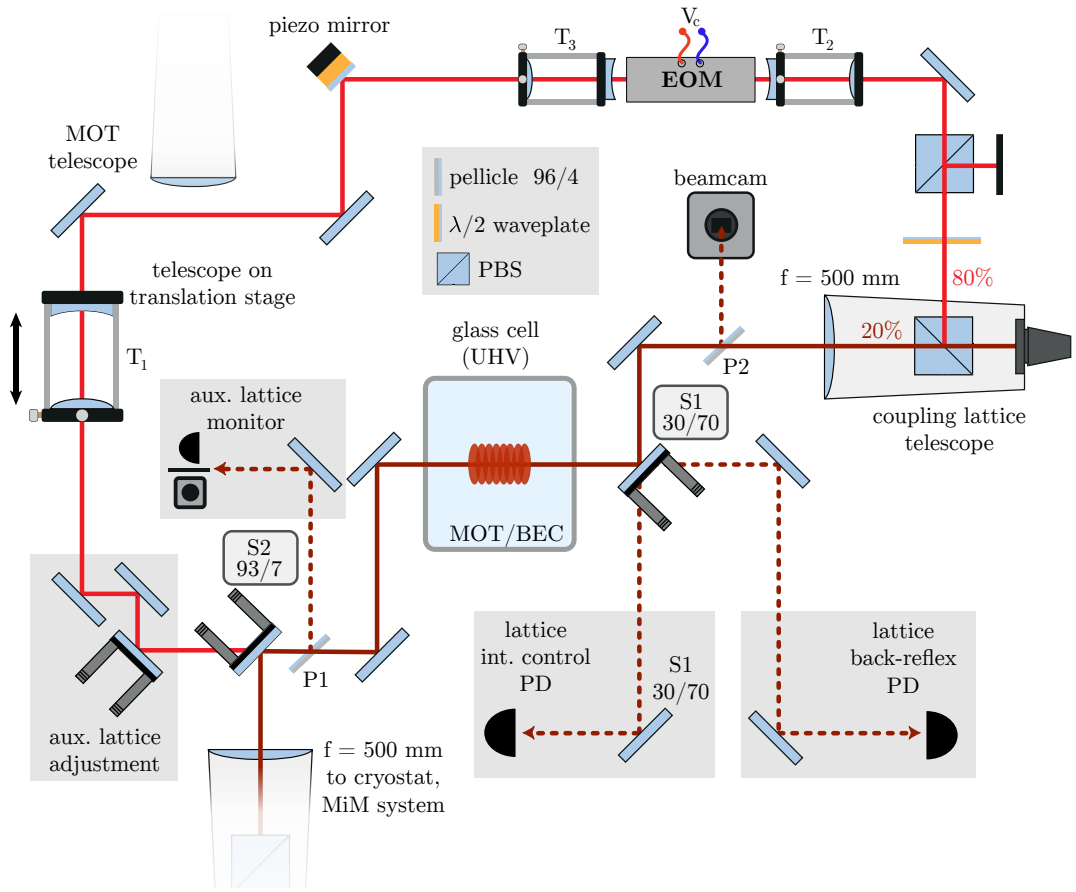

Figure 3.11: Realized optical setup for the auxiliary lattice beam. Modified setup of the coupling lattice (see figure 2.5) including the auxiliary beam path. The auxiliary beam is derived from the incident lattice light in the coupling lattice telescope (light red line). Its power can be adjusted independently using a $\lambda/2$ waveplate and a PBS. Telescope T_2 is used to reduce the beam diameter for passage through the EOM and T_3 restores the former beam size. The EOM (LM0202 0.1W KD*P 3x3 400-850 nm from *Linos*) is used together with the piezo mirror (ring actuator NAC2121 from *Noliac*) to shift the phase of the auxiliary beam with respect to the back-reflected beam from the cavity. Telescope T_1 is used to reproduce the beam shape of the back-reflected beam as good as possible and is placed on a translation stage to align the focus with respect to the atoms. The auxiliary and back-reflected beam are superimposed on the substrate S2 and their interference can be monitored in the focal plane (using a pellicle beam splitter on the left of the glass cell) or in the far field (using a pellicle on the right of the glass cell). Figure adapted from [100].

Auxiliary beam alignment

Along the beam path of the auxiliary beam we use different telescopes to shape the beam to our needs. First, the beam diameter has to be reduced in order to fit trough the aperture of the EOM (3x3 mm) without clipping. For that we use telescope T_2 which consists of two lenses with focal lengths $f_1 = 125\,\text{mm}$ and $f_2 = -20\,\text{mm}$ separated by a distance $d_{f_1,f_2} = 10.8\,\text{mm}$ that reduce the collimated beam waist to $w_{col} = 460\,\mu\text{m}$. After the beam has traversed the EOM it is expanded again to its original size by T_3, which is an inverted version of T_2. In front of the last beam shaping telescope T_1 we measure a waist of the collimated beam of $w_{col} = 1.89\,\text{mm}$. T_1 consists of two lenses with focal lengths $f_1 = -200\,\text{mm}$ and $f_2 = 200\,\text{mm}$ separated by a distance $d_{f_1,f_2} = 7.6\,\text{mm}$. The lenses are chosen to produce a beam waist as close as possible to the waist of the back-reflected beam, while at the same time providing a slightly larger working distance then the other two lattice telescopes. Of course with this setup the auxiliary beam cannot be perfectly mode matched, but we find reasonable mode overlap with the back-reflected beam along the whole common beam path (see figure 3.13).
All three telescopes have two main features in common: One of the lenses is fixed in a lens tube, which is mounted in a v-groove. The other lens is held by a moveable lens mount that allows for translation in the directions perpendicular to the beam axis. For the alignment the transmitted beam is viewed on a beam profiling camera and iteratively adjusted onto the center of the lenses using a beam walk and and the translation of the lens. The quality of the alignment is indicated by the beam shape and its susceptibility to move upon rotation of the telescope. Once no movement of the beam spot during rotation is visible the beam is properly aligned.
In order to measure the waist size of the auxiliary beam and its relative position with respect to the waist of the back-reflected beam we superimpose the beams roughly and use pellicle P1 to reflect a fraction of the light intensity onto a beam profiling camera. The beam camera is placed close to the focal position of the beams and moved along the beam propagation axis to record the beam size at different positions along the beam (see figure 3.12). The measured beam sizes are fitted using the formula for the evolving Gaussian beam width

$$w(z) = w_0\sqrt{1 + \left(\frac{z}{z_0}\right)^2} \tag{3.54}$$

to obtain the beam waists $w_{aux,back}$ and the corresponding waist positions. Using the translation stage of T_1 the focal position of the auxiliary beam can adjusted by the waist separation obtained from the fit (indicated by the two dotted lines in figure 3.12) and overlapped with the focal position of the back-reflected beam. For the final fine alignment of the auxiliary beam one can use Kapitza-Dirac diffraction as described in section 2.2.1 again. If the lattice backreflex is already well aligned onto the atoms a more convenient method for the alignment of the auxiliary beam can be used that leads to the same result. By maximizing the interference contrast between the auxiliary and back-reflected beam the auxiliary beam can be aligned onto the atoms. We do this by iteratively overlapping the beams at their focal position (using pellice P1) and in the far field (using pellicle P2) on the beam profiling camera until we observe only one global

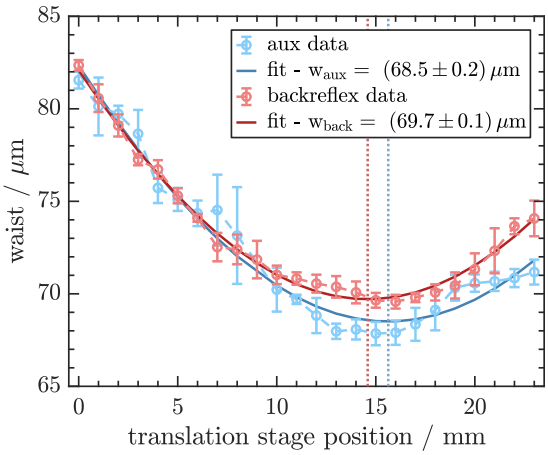

Figure 3.12: Measurement of the waist sizes w_{aux} and w_{back} back to back. After the auxiliary beam and the back-reflected beam are roughly overlapped we record the spot size of the beams at different positions along the beam axis using a beam profiling camera on a translation stage. Each data point is averaged over 20 shots. The dotted lines depict the waist positions obtained from the fit. The auxiliary beam telescope is moved by the distance of the waists after the measurement, to overlap the foci of the beams. Here the separation is (1.0±0.2) mm.

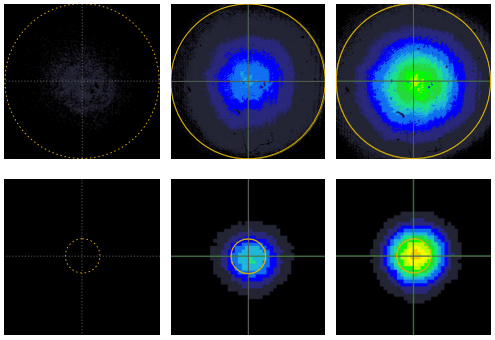

Figure 3.13: Interference between equally strong auxiliary and coupling lattice beam. The top row shows the time dependent interference in the far field (≈ 50 cm) behind the glass cell. The bottom row depicts the time dependent signal in the focal plane (zoomed 8x). From left to right the intensity increases from minimum to maximum.

interference fringe. This is depicted in figure 3.13, where the resulting interference at three instants in time is presented. When the beam powers are matched one observes complete destructive interference, which results in "blinking" of the beam spot on the beam profiling camera. In the far field the beams do not completely annihilate each other. This can be attributed to an imperfection in the mode match, since we can not reproduce the back-reflected beam over the whole beam path with a different set of optics. We concentrated our beam shaping effort mainly on the focal region, where the beams interact with the atoms, and find that the modes are matched sufficiently well.

Realized phase-locking scheme

During the master thesis of C. F. Klein [100] a first version of the auxiliary lattice beam setup was realized. At that time we used a mirror mounted on a piezo ring stack[29] to stabilize the relative phase between back-reflected and auxiliary beam. The choice of the actuator was based on our well working homodyne phase-lock, where we use the same actuator. We expected the relative phase drifts between the auxiliary and back-reflected lattice beam to be the same as between the local oscillator and the signal beam since they are mainly introduced by the cryostat fiber, which is traversed by the light in both cases. However, for the auxiliary lattice phase lock this actuator turned out to be not fast enough. A probable reason can be the better passive stability of the compact homodyne setup, where all optics are mounted on short posts resulting in a beam height of 50 mm over the optical table. In contrast, the beam height of the lattice

[29] HPSt 150/14-10/12 from *Piezomechanik* with 16 µm maximum stroke.

beams (120 mm) is predetermined by the position of the atoms in the glass cell. Additionally, the auxiliary beam has to be guided around the whole experimental setup[30] to be irradiated along the back-reflected beam.
For this reason we decided to implement a two-stage phase-lock that enables to stabilize slow frequency drifts using a piezo and is capable to handle the remaining higher frequency phase drifts with a fast EOM.

In the realized setup we use a pellicle in the common beam path of the back-reflected and the auxiliary beam to reflect a small fraction of the intensity onto a photo detector that we place in the focal plane of both beams. In this way we make sure that we can stabilize the intensity at the site of the atoms by adjusting the relative phase $\phi_{\mathrm{aux,back}}$. The signal from the photo detector is low-pass filtered at 60 kHz [31] and fed to a fast servo controller[32]. Its output is connected to a high voltage amplifier[33] that drives the EOM. The error signal from the servo controller is fed to a second, identical controller and its output is connected to another high voltage amplifier[34] that drives the piezo actuator. In this configuration the EOM is used as a fast proportional regulator and the piezo is configured as a pure integrator, which allows for the best locking performance due to the separation of time scales.
The nominal bandwidths of the phase shifting elements are 1 MHz for the EOM and 490 kHz for the unloaded piezo actuator. However, there are several factors that limit the achievable bandwidth in the experiment. The EOM has a half wave voltage of $U_\pi = 2 \cdot 259\,\mathrm{V}$ at 780 nm [35], thus the large bandwidth will be limited by the high voltage amplifier that drives the EOM. On the other hand the piezo actuator is glued between a 6 mm thick half-inch mirror and a one inch substrate, which is mounted in a standard mirror mount. The load of the small mirror drastically reduces the bandwidth of the actuator.
In order to estimate the achievable bandwidth of the components a test Mach-Zehnder interferometer was set up with both actuators placed in one interferometer arm. To characterize the piezo mirror bandwidth the intensity at the interferometer outputs is stabilized by locking the phase between both interferometer arms to the side of an interference fringe (as described in section 3.5.2). Next the setpoint of the lock is modulated with an amplitude that corresponds to 10 % of the intensity modulation depth due to interference and the modulation frequency is varied over a range of 10 Hz to 30 kHz. We are interested in the frequency range over which the piezo can follow the modulation and maintain the lock. Therefore, we measure the in-lock amplitude of the modulated intensity in the interferometer. Figure 3.14 shows the resulting amplitude and phase response. The in-lock frequency modulation can be followed up to a frequency of 2.5 kHz before a resonance at 3.4 kHz appears that significantly distorts the amplitude of the

[30] resulting in a 310 cm long beam path from PBS to photo detector see figure 3.11.
[31] This is done to make sure that the locking electronics do not see any frequency components from the mechanical resonator. Used SIM 965 analog filter from *Stanford Research Systems*.
[32] LB1005 from *New Focus* with 10 MHz bandwidth.
[33] HA51U-0.5B20 from *hivolt* with $U_\mathrm{d} = \pm 500\,\mathrm{V}$ output voltage and 30 kHz bandwidth.
[34] A-301 HS from *A.A. Lab Systems Ldt.* with $U_\mathrm{d} = \pm 200\,\mathrm{V}$ output voltage and 250 kHz bandwidth.
[35] The used EOM can rotate the polarization of a laser beam or retard the beams phase, depending on its orientation. Compared to the polarization rotation a phase retardation by π requires twice the voltage.

signal. If the EOM is included into the lock the amplitude of this resonance is reduced, which increases the overall bandwidth to $\approx 16\,\mathrm{kHz}$ before the next resonance appears. For reference the modulation bandwidth of the EOM alone is also measured. In this case the EOM is used to rotate the light polarization and a PBS is placed after the EOM to measure the amplitude and phase of the resulting intensity modulation. The measurement confirms that the bandwidth of the EOM is limited by the driving high voltage amplifier. At 30 kHz the amplitude response drops to $-1.6\,\mathrm{dB}$ in accordance with the specifications by the manufacturer.
From the half-wave voltage U_π of the EOM its maximum phase shift at the full modulation depth can be determined to $\Delta\phi_{\mathrm{EOM}} = \pi \cdot \frac{U_\mathrm{d}}{U_\pi} = 1.93\pi = 6.06\,\mathrm{rad}$. The piezo has a free stroke of 3.3 µm at a maximal drive voltage of $U_\mathrm{d} = 200\,\mathrm{V}$ and thus can produce a phase shift of $\Delta\phi_{\mathrm{piezo}} = 8.46\pi = 26.58\,\mathrm{rad}$.
Using the lock points and the corresponding photo detector signal from the measurements presented in sections 3.5.2 and 3.5.3 the residual in-lock phase noise can be determined. For a shift of the relative phase $\phi_{\mathrm{aux,back}} = \pi$ the interference signal changes from maximum to minimum, thus the peak to peak voltage U_{pp} of the photo detector signal can be assigned to this phase shift. The residual root-mean-square (rms) phase noise in the phase locked beam can then be calculated from the in-lock signal $U_{\mathrm{rms}}^{\mathrm{in-lock}}$ by

$$\phi_{\mathrm{rms}} = \frac{\pi}{U_{\mathrm{pp}}} U_{\mathrm{rms}}^{\mathrm{in-lock}}. \tag{3.55}$$

Note, that the residual phase noise depends on the lock point, as it increases with higher intensities. For typical lock settings in the experiments we obtain a residual phase noise between $\phi_{\mathrm{rms}}^{\mathrm{bof}} = 0.038\,\pi = 119\,\mathrm{mrad}$ and $\phi_{\mathrm{rms}}^{\mathrm{sof}} = 0.061\,\pi = 192\,\mathrm{mrad}$, where *bof* denotes the lowest used lock point at the bottom of the fringe and *sof* denotes a lock point close to the side of the fringe.

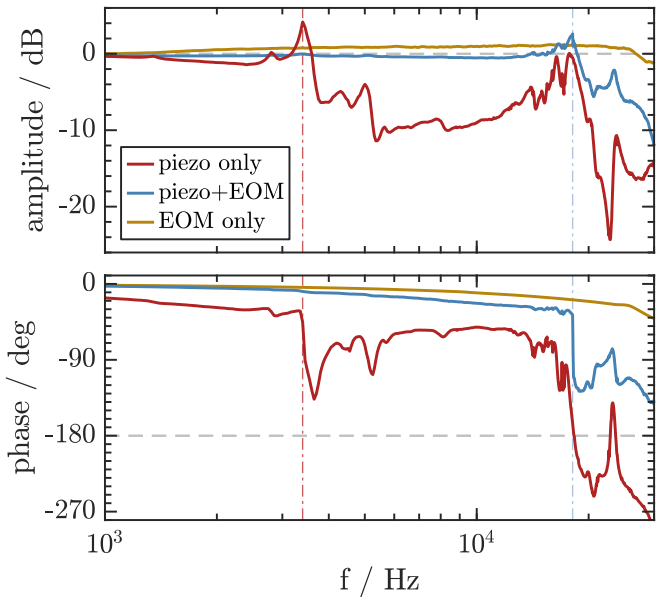

Figure 3.14: Bandwidth estimation of the used phase-shifting components. Measured amplitude and phase response of the used components for varying modulation frequency. The amplitude response is normalized to the measured modulation amplitude at 10 Hz and is flat below 1 kHz, thus the plot sows only higher frequencies. The dashed-dotted lines mark the most pronounced resonances of the piezo actuator at $f_1 = 3.4\,\mathrm{kHz}$ and $f_2 = 18.1\,\mathrm{kHz}$. It is clearly visible that the bandwidth of the combined lock is increased by more than 10 kHz. The modulation bandwidth of the EOM is measured at full modulation depth of ±500 V.

3.5 Sympathetic cooling in a pump asymmetry compensated lattice

In this section the conducted experiments to compensate the pump asymmetry in our system are presented. The goal is to investigate, whether the coupling strength between the two hybrid partners can be enhanced by alleviating the pump asymmetry. As described earlier in section 3.1.1 the sympathetic cooling mechanism is based on the resonance between the atomic oscillations in the coupling lattice with frequency ω_{at} and the oscillations of the mechanical resonator with frequency ω_{m}. The resulting sympathetic cooling rate Γ_{sym} follows a specific resonance behaviour depending on the maximum atomic trapping frequency ω_{at} on the beam axis (see figure 3.2). We studied this resonance behaviour of $\Gamma_{\mathrm{sym}}(\omega_{\mathrm{at}})$ in detail by sweeping the lattice depth in lattices with different pump asymmetries. From the sympathetic cooling rate the hybrid cooperativity C_{hybrid} (equation (3.25)) can be derived to gauge the strength of the hybrid coupling.
The lattice depth can be varied either by changing the lattice power P_{lat} or the lattice detuning $\Delta_{\mathrm{at,L}}$. For the coupling mechanism both methods are equivalent, but they lead to different parasitic effects. For example, when sweeping the detuning close to the atomic resonance the atomic scattering rate increases, the atoms are expelled from the trapping potential of the lattice and the sympathetic cooling rate is drastically reduced. On the other hand large coupling lattice powers lead to heating of the MiM system and thermal drifts of the cavity which can distort the measurement. We decided to sweep the lattice detuning at a fixed lattice power, as this allows to reliably stabilize the cavity length, avoids parasitic heating effects and is much more convenient for the adjustment of the balancing of the coupling lattice.

The presented measurements were performed with the MiM system at room temperature due to maintenance work on the cryostat. Qualitatively, this does not affect the experiments, as we primarily intended to investigate the influence of the pump asymmetry and its reduction on the atom-resonator coupling in our system. A decreased initial bath temperature mainly leads to lower final mode temperatures that can be reached with sympathetic cooling. The only concern we faced before doing the experiments at room temperature was the stability of the cavity length. With the MiM system at 500 mK we observed an excellent passive stability of the cavity in the past [74], such that no additional active cavity length stabilization was required. However, after the exchange of the mechanical resonator the cavity stability was seemingly reduced. This can be explained by the 20 times lower mechanical damping rate Γ_{m} of the trampoline resonator compared to the former membrane resonator. A reduced mechanical damping rate makes the resonator more susceptible to optomechanical heating close to resonance, and hence to shifts of the mechanical resonance frequency due to the optical spring effect (see section 2.3.2). These frequency shifts lead to a detuning from the cavity resonance and can not be distinguished from real cavity length changes. To circumvent this effect, moderate feedback cooling of the resonator was applied to suppress possible instabilities caused by optomechanical heating [77]. For the experiments presented here we chose a different approach and stabilized the cavity length using the

optical spring lock described in section 2.3.2.
In the following, the used experimental sequence and the evaluation method are described. Subsequently, the experimental results are presented and discussed and relevant parameters such as realized cooling rates and obtained hybrid cooperativities will be derived. The presented measurements were conducted together with C. F. Klein.

3.5.1 Experimental sequence

All coupling experiments presented in this section were performed with atoms confined in a compressed high optical density magneto optical trap (in the following denoted by high OD MOT). To realize this configuration the atoms are loaded for 5 s from the 2D-MOT into the 3D-MOT using a pushing beam and optimized MOT parameters for efficient loading. Subsequently, the pushing beam is switched off and the parameters are linearly ramped within 500 ms to a new set of MOT parameters optimized for high atomic density: cooling light intensity $I_0 = 31.5 I_{\mathrm{sat}} = 52.6\,\mathrm{mW/cm^2} \Rightarrow 2.25 I_{\mathrm{sat}} = 3.8\,\mathrm{mW/cm^2}$, magnetic field gradient $5\,\mathrm{G/cm} \Rightarrow 45\,\mathrm{G/cm}$ and cooling light detuning $\delta_{\mathrm{MOT}} = -2\pi \cdot 17.8\,\mathrm{MHz}\,(2.9\,\Gamma_{\mathrm{D_2}}) \Rightarrow -2\pi \cdot 37.8\,\mathrm{MHz}\,(6.2\,\Gamma_{\mathrm{D_2}})$. The final parameters were found to yield the highest sympathetic cooling rates in [74]. Next, the 2D-MOT is switched off and the coupling lattice is ramped to its final depth in 1 ms. In experiments that use the auxiliary lattice beam, the servo controllers stabilize the relative phase $\phi_{\mathrm{aux,back}}$ within 50 ms after the final lattice depth is reached. After 3 s of coupling the lattice is ramped down again in 10 ms and the resonator is allowed to rethermalize for 5 s, before the next sequence starts. A sketch of the experimental sequence is shown in figure 3.15.
In order to avoid unwanted optomechanical heating of the resonator during the measurements, the cavity is stabilized at moderate red detuning $\Delta_{\mathrm{cav}}/(2\pi) = -1\,\mathrm{GHz}$. This results in a measured optical spring shift of $\Delta\omega_{\mathrm{m}}/(2\pi) = 20\,\mathrm{Hz}$ and places the resonator on the optomechanical cooling side of the cavity resonance with a cooling rate of $\Gamma_{\mathrm{opt}} = 3.1\,\mathrm{mHz}$ that is negligible compared to the sympathetic cooling rate.
To quantify the sympathetic cooling effect we measure the mode temperature T_{mode} of the resonator during the coupling as a function of time using homodyne detection. The voltage signal from the photo detector is demodulated by a lock-in amplifier[36] to obtain

[36] HF2LI from *Zurich Instruments*

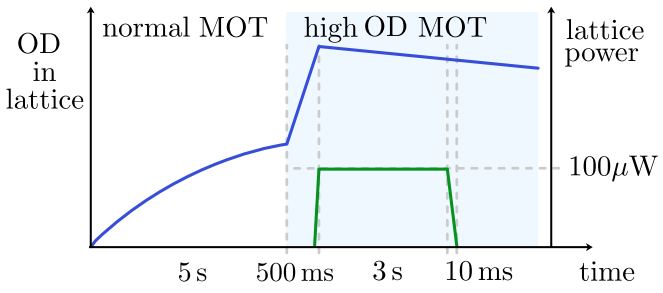

Figure 3.15: Experimental sequence for sympathetic cooling in the high OD MOT. The blue line denotes the optical density (OD) of the atoms and the green line shows the lattice power. After loading the MOT for 5 s the trap parameters are switched to produce a high OD MOT, while the lattice power is ramped up within 1 ms. The atoms are coupled to the mechanical resonator for 3 s before the lattice is ramped off again.

the PSD $S_y(\omega)$, which originates from a displacement of the mechanical mode at ω_m. The demodulator output voltage $V_d(t)$ is proportional to the integrated PSD $\langle x^2(t)\rangle$ and hence proportional to the mode temperature of the resonator (see equation (2.34)). This holds long as the demodulator bandwidth $B_d \gg \Gamma_m$ and $S_y \approx S_x$ (measured PSD corresponds to the real PSD), which is a good approximation if the thermal noise peak $S_x(\omega_m)$ is well above the noise floor S_x^{imp}. For the measurements at room temperature we determined the homodyne calibration factor to be $|\frac{\partial \phi_x}{\partial x_m}| = (0.738 \pm 0.006)\,\mathrm{rad/nm}$ (see section 2.2.2).

An exemplary trace of the time evolution of the resonators mode temperature is depicted in the left panel of figure 3.16. After the coupling lattice is ramped up ($t = 0\,\mathrm{s}$), the mode temperature reduces to the final sympathetically cooled temperature $T_{mode,min}$. We determine $T_{mode,min}$ by averaging the mode temperature over 1.4 s once a steady state after the initial cool-down is reached. The displayed trace (solid blue line) is an average of 15 measurements at equal parameters and the shaded region around the trace denotes the standard deviation. For the measurements where we used the auxiliary beam for the pump asymmetry compensation an additional evaluation step is needed. Simultaneous to the time evolution of the resonator mode temperature we record the cavity transmission and reflection signals as shown in the right panel of figure 3.16. The transmission signal (red lines) indicates the quality of the cavity lock, while the reflection signal (blue lines) lets us judge how well the auxiliary lattice lock worked. Since we permanently measure the resonator displacement, even when the coupling lattice is turned off, the optical spring lock is active all the time. However, when the lattice is ramped up the intra-cavity power rapidly increases and with it the

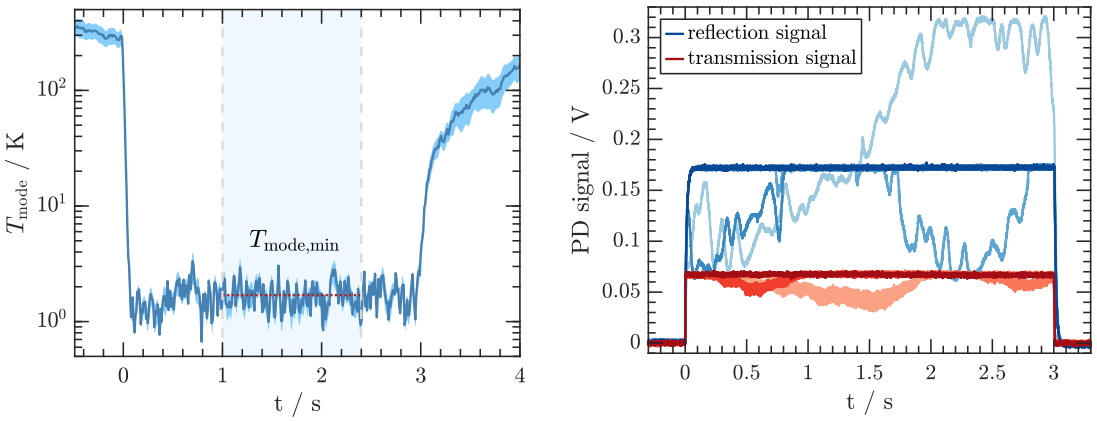

Figure 3.16: Sympathetic MOT cooling in the time domain. Left panel: Exemplary trace of the resonator mode temperature T_{mode} during sympathetic cooling in the high OD MOT. At $t = 0\,\mathrm{s}$ the lattice is ramped on and the mode temperature decreases due to the coupling to the atoms. The blue solid line is the average of 15 measurements and the shaded region around the trace denotes the standard deviation. The region between the dashed grey lines is used to determine $T_{mode,min}$ (red dotted line). Parameters: $P_{lat} = 100\,\mu\mathrm{W}$, $\Delta_{2,3} = 2\pi \cdot 361\,\mathrm{MHz}$, $\omega_{at} = 2.18\,\omega_m$. **Right panel:** Exemplary traces of the cavity reflection and transmission during a sympathetic cooling experiment. The dark red (blue) solid lines depict traces where both locks were stable. The lighter shades are examples for cases where the locks failed. In the latter case, corresponding time traces of the mode temperature evolution are excluded from further evaluation.

magnitude of the optical spring effect, resulting in a temporarily increased gain of the lock. In some cases this can destabilize or even break the lock, which can be observed on the cavity transmission signal. On the other hand it is possible that the auxiliary lattice lock can not stabilize the relative phase fast enough and the coupling takes place in a lattice with arbitrary lattice depth due to the random relative phase. For this reason we evaluate the corresponding transmission and reflection signals to each time trace of the resonator mode temperature evolution in order to determine if all locks were stable during the coupling. Only measurement runs where both locks were stable during the whole coupling time are regarded for further evaluation.

3.5.2 Blue detuned lattice

The first scenario we want to look at is sympathetic cooling in a blue detuned lattice. This configuration allows to investigate the hybrid coupling mechanism for high atomic densities even in a strongly asymmetric lattice. It is the ideal test bed to figure out if our approach to compensate the pump asymmetry in the coupling lattice works and how it performs in comparison to the asymmetric case.

Balancing of the lattice

We decided to work at a lattice power of 100 µW, which allows good control over the MiM cavity and does not lead to excessive heating when the lattice light is resonantly coupled to the cavity and no sympathetic or feedback cooling is applied. With the cavity on resonance (22 ± 1) % of the incident lattice light is reflected onto the atoms[37]. As illustrated in figure 3.10 balancing of the coupling lattice can be achieved with different combinations of the auxiliary beam power P_{aux} ($I_{\mathrm{aux}} \propto P_{\mathrm{aux}}$) and the relative phase $\phi_{\mathrm{aux,back}}$ between the auxiliary and the back-reflected beam. For a side of fringe lock the relative phase is $\phi_{\mathrm{aux,back}} = \pi/2$, the interference term vanishes and the beam powers P_{back} and P_{aux} simply add up to the total reflected power $P_{\mathrm{ref,tot}}$. Thus, we determine the needed auxiliary beam power to be $P_{\mathrm{aux}} = P_{\mathrm{inc}} - P_{\mathrm{back}}$ in this case. To find the exact needed powers we measure the incident beam power P_{inc} in front of the glass cell and calculate the power at the site of the atoms using the known transmission for a single surface of the glass cell (see figure B.1). The auxiliary beam power P_{aux} is measured at the same position (after the beam has traversed the glass cell) and the power of the back-reflected beam P_{back} is measured in front of the lattice back-reflex photo detector (see figure 3.11). Also the phase-locked total reflected power $P_{\mathrm{ref,tot}}$ of the combined back-reflex and auxiliary beam is measured in front of the photo detector. All values for the beam powers that are stated in the following are already converted to the power at the site of the atoms, using the transmission factors of the traversed optical elements.

[37] Due to the additional losses we had to introduce, in order to enable the use of the auxiliary lattice beam (see section 3.4.1).

Evidence for sympathetic cooling in a balanced lattice

With the auxiliary beam power set to $P_{\mathrm{aux}} = 0.78\,P_{\mathrm{inc}}$ sympathetic cooling measurements in a balanced lattice can be conducted. We use the experimental sequence described in section 3.5.1 and stabilize the relative phase to $\phi_{\mathrm{aux,back}} = \pi/2$ using the combined piezo and EOM lock. In this configuration the atoms experience equal intensities from both directions of the incoming lattice beams and hence the pump asymmetry in the lattice is compensated. In the following we will distinguish measurements where we employed the auxiliary lattice beam for pump asymmetry compensation (with PAC) from measurements without auxiliary beam (without PAC).

The lattice detuning is set to $\Delta_{2,3} = 2\pi\cdot 214\,\mathrm{MHz}$ [38] which leads to sympathetic cooling in our usual (asymmetric) lattice. Now the resonator mode temperature T_{mode} can be determined from the homodyne signal, which is demodulated at the resonator frequency ω_{m}. We slightly vary the lock-point of the relative phase around $\pi/2$ and measure the sympathetically cooled resonator mode temperature. The results are depicted in figure 3.17 and clearly show that sympathetic cooling in a balanced blue detuned lattice is possible. We observe a reduction of the mode temperature from room temperature to slightly below 3 K. In the left panel of figure 3.17 the measured mode temperature T_{mode} is plotted as a function of combined power of the back-reflected lattice beam P_{back}. The power is varied by changing the relative phase $\phi_{\mathrm{aux,back}}$, which is depicted in the right panel, where $P_{\mathrm{ref,tot}}$ is plotted as a function of $\phi_{\mathrm{aux,back}}$.

[38] In the following $\Delta_{2,3}$ denotes blue detuning relative to the atomic transition $|F = 2 \rightarrow F' = 3\rangle$, whereas $\Delta_{2,1}$ denotes red detuning relative to the $|F = 2 \rightarrow F' = 1\rangle$ transition.

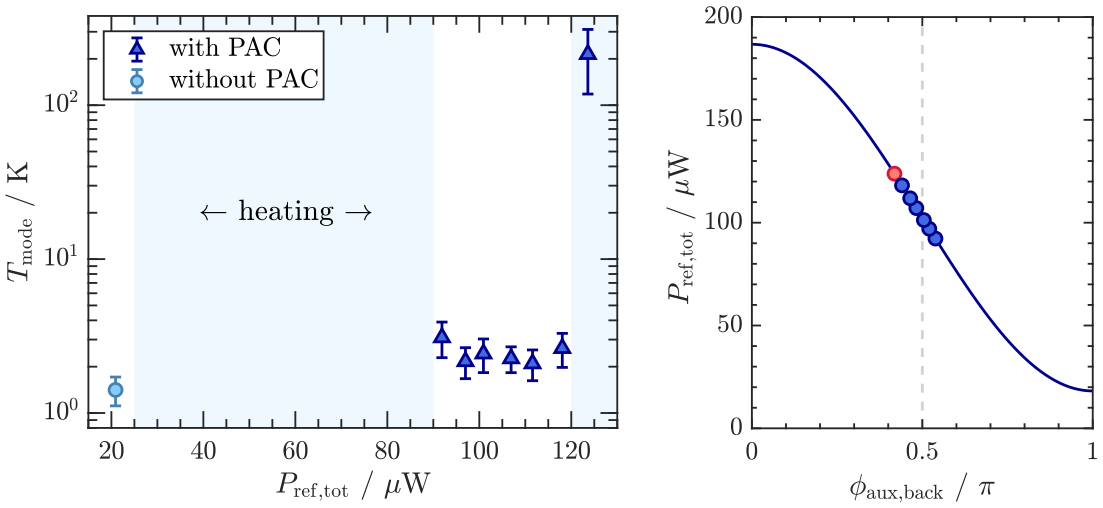

Figure 3.17: Variation of the lattice lock-point in blue detuned lattice. Left panel: Resonator mode temperature T_{mode} as a function of $P_{\mathrm{ref,tot}}$ resulting from different lock-points of the relative phase $\phi_{\mathrm{aux,back}}$. In the vicinity of $\phi_{\mathrm{aux,back}} \approx \pi/2$ the pump asymmetry is compensated and sympathetic cooling with the auxiliary lattice beam is possible. The shaded area denotes the range of $P_{\mathrm{ref,tot}}$ that is theoretically achievable by interference of both beams. **Right panel:** Total reflected power $P_{\mathrm{ref,tot}}$ of the interfering back-reflected and auxiliary beam as a function of their relative phase $\phi_{\mathrm{aux,back}}$. Blue circles show the lock-points at which sympathetic cooling in the PAC lattice occurred. Red circle denotes heating. Parameters: $P_{\mathrm{inc}} = 102.6\,\mu\mathrm{W}$, $P_{\mathrm{back}} = 22.1\,\mu\mathrm{W}$, $P_{\mathrm{aux}} = 80.4\,\mu\mathrm{W}$, $\Delta_{2,3} = 2\pi\cdot 214\,\mathrm{MHz}$.

For relative phases close to $\phi_{\mathrm{aux,back}} = \pi/2$ we measure a comparable sympathetic cooling effect, but if the relative phase is decreased (increased) towards 0 (π) the cooling turns into heating. This is illustrated by the red circle in the right panel of figure 3.17 that corresponds to the dark blue triangle in the left panel at $T_{\mathrm{mode}} = (214.4 \pm 96.2)\,\mathrm{K}$. For reference, also the mode temperature that is reached with sympathetic cooling at the set parameters in our asymmetric lattice without auxiliary beam is plotted (blue circle in the left panel). The measured mode temperature for the asymmetric lattice $T_{\mathrm{mode,noPAC}} = (1.4 \pm 0.3)\,\mathrm{K}$ is slightly lower than the mean mode temperature from the measurements around the balanced lattice configuration $\bar{T}_{\mathrm{mode,PAC}} = (2.5 \pm 0.6)\,\mathrm{K}$. This might be explained by the different resulting lattice depths that do not fulfil the resonance condition for hybrid coupling equally well. In order to evaluate this we have to compare the resonance behaviour of the sympathetic cooling in the balanced and the asymmetric lattice.

Resonance behaviour in a balanced lattice

In order to assess the strength of the hybrid coupling we have to investigate the evolution of the resonator mode temperature as a function of the coupling lattice depth. For atomic trapping frequencies $\omega_{\mathrm{at}} \approx \omega_{\mathrm{m}}$ close to the mechanical resonance frequency we expect to see resonant coupling behaviour and thus a reduction of the resonator mode temperature due to sympathetic cooling.

As described in the beginning of section 3.5 we vary the lattice depth by adjusting different lattice detunings within a range of several gigahertz around the atomic transition[39]. For each lattice detuning we measure the resonator mode temperature $T_{\mathrm{mode}}(t)$ and determine the minimum mode temperature $T_{\mathrm{mode,min}}$ after the initial cooldown as depicted in figure 3.16. We performed the measurement in our normal, asymmetric lattice and in the balanced, compensated lattice to compare the strength of the sympathetic cooling effect. The results are shown in figure 3.18 and one clearly observes the expected resonant behaviour for both lattice configurations. However, one also notices that the cooling behaviour is different for both lattices. In the balanced lattice the cooling effect is reduced compared to the asymmetric lattice for most trapping frequencies up to $\omega_{\mathrm{at}}/\omega_{\mathrm{m}} \approx 4.1$ where the minimum mode temperature $T_{\mathrm{min}}^{\mathrm{PAC}}$ is reached. Also the range of trapping frequencies that allows for efficient sympathetic cooling is broadened with respect to the asymmetric lattice. The fact that we observe sympathetic cooling at trapping frequencies of multiple ω_{m} can be understood by the influence of the Gaussian radial intensity profile of the trapping beams, which we did not include in our lattice depth calibration. Since the atomic cloud is much larger than the waists of the lattice beams there are atoms at all radii that contribute to the coupling with different sympathetic cooling rates due to their radius-dependent axial trapping frequencies. The decreased cooling performance can be attributed to the larger number of scattered photons in the balanced lattice due to the increased laser power at the site of the atoms. We observed qualitatively very similar effects in earlier experiments with a membrane resonator in which the detuning sweeps were performed at different laser powers [74].

[39] The lattice frequencies were adjusted manually with a precision of $\approx 5\,\mathrm{MHz}$ relative to a frequency f_0 which is determined with an absolute accuracy of 3 MHz using the transfer-lock (see section 2.2).

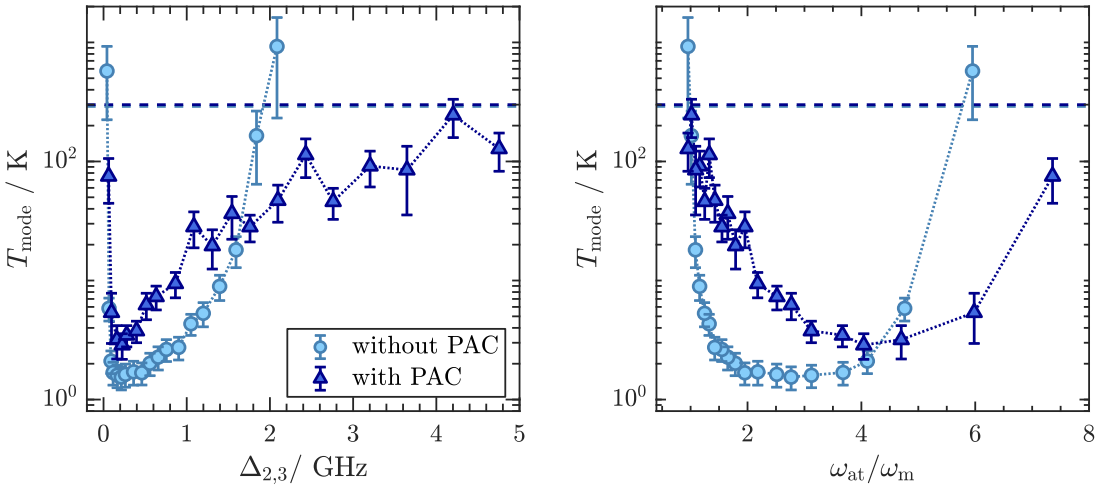

Figure 3.18: Sympathetic cooling with and without pump asymmetry compensation in blue detuned lattice. Minimum resonator mode temperature T_{mode} during sympathetic cooling with a high OD MOT as a function of the resonant lattice depth. **Left panel:** The lattice power is held constant and the detuning $\Delta_{2,3}$ is varied to tune the lattice depth. The circles show the resulting mode temperature $T_{\mathrm{min}} = (1.54 \pm 0.34)\,\mathrm{K}$ due to coupling mediated via an imbalanced lattice and the triangles denote the measured mode temperature $T_{\mathrm{min}}^{\mathrm{PAC}} = (2.87 \pm 0.69)\,\mathrm{K}$ in a balanced lattice. Dashed lines depict the bath temperature $T_{\mathrm{bath}} = 294\,\mathrm{K}$, which corresponds to the room temperature. **Right panel:** T_{mode} as a function of the (calibrated) atomic trapping frequency ω_{at} in units of the resonator frequency ω_{m}. Parameters: $P_{\mathrm{inc}} = 102\,\mu\mathrm{W}$, $P_{\mathrm{back}} = 20.5\,\mu\mathrm{W}$, $P_{\mathrm{aux}} = 102.2\,\mu\mathrm{W}$, $\phi_{\mathrm{aux,back}} = 0.57\,\pi$. Note that this measurement was performed after the parameter optimization in the red detuned lattice (section 3.5.3), where we found optimal sympathetic cooling for $P_{\mathrm{aux}} = P_{\mathrm{inc}}$.

There, the measured minimum mode temperature was 1.6 times higher when the lattice power was increased by a factor of 4. In our case the minimum mode temperature in the balanced lattice is 1.9 times higher than in the asymmetric lattice. Furthermore, residual phase noise in the combined back-reflected beam can lead to intensity noise that limits the performance of the PAC lattice. Nonetheless, this assumption could not be proven through independent measurements.

In order to obtain the sympathetic cooling rates for the coupling measurements in the balanced and asymmetric lattice we use the measured temperatures T_{mode}, T_{bath} and the mechanical linewidth Γ_{m} (from table 2.1) to calculate Γ_{sym} according to equation (3.15). The obtained cooling rates can be described by the theoretical model for the ensemble-integrated cooling rate (see equation (3.17) and figure 3.2) with the atomic cooling rate Γ_{at} and the single phonon coupling strength g_N as free fit parameters. The results are displayed in figure 3.19, where the atomic trapping frequencies are rescaled using the fit to account for the radial intensity distribution of the coupling lattice beams. Given that the same MOT parameters were used the extracted atomic cooling rates Γ_{at} should be equal. However, the PAC data can not be unambiguously fitted and therefore we retrieve an increased value for Γ_{at} from the fit. With the measured maximum sympathetic cooling rates the hybrid cooperativities can be calculated using

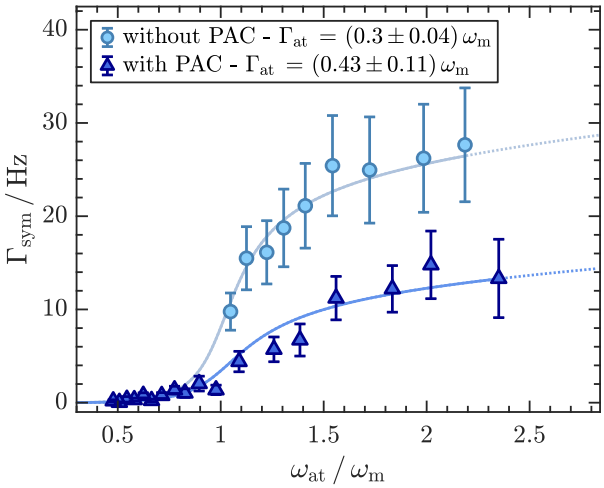

Figure 3.19: Resonance behaviour of $\Gamma_{sym}(\omega_{at})$ for MOT cooling in blue detuned lattice. Sympathetic cooling rate Γ_{sym} calculated with equation (3.15) using the temperatures T_{mode} and T_{bath} from figure 3.18. Data points with decreasing Γ_{sym} for large ω_{at} are omitted. The solid lines are fits according to equation (3.17), which are used to obtain the atomic cooling rate Γ_{at} and to rescale the x-axis. Maximum measured cooling rates: $\Gamma_{sym}^{max} = (27.7 \pm 6.1)\,\text{Hz}$ and $\Gamma_{sym,PAC}^{max} = (14.8 \pm 3.6)\,\text{Hz}$.

equation (3.25)

$$C_{hybrid} = (190 \pm 42) \qquad \text{and} \qquad C_{hybrid}^{PAC} = (102 \pm 25).$$

Evidently, although sympathetic cooling is possible in a blue detuned coupling lattice with compensated pump asymmetry the optomechanical coupling could not be enhanced in the balanced lattice.

3.5.3 Red detuned lattice

After we have observed that the pump asymmetry compensation works and that sympathetic cooling with our setup can be realized in a balanced blue detuned lattice we want to study the behaviour in the red detuned case. Until now, efficient sympathetic cooling in a red detuned lattice was only possible using atoms in an optical molasses, where the atomic density is reduced compared to a MOT [74]. In our hybrid experiment as well as in a similar one [72, 73] the attempt of sympathetic cooling with higher atomic densities in a red detuned lattice led to a dynamic instability that excited the mechanical resonator to limit-cycle oscillations instead of cooling it.

We repeat the measurements presented in section 3.5.2 with the same MOT parameters, leading to a high OD atomic sample, but change the detuning of the coupling lattice with respect to the atomic resonance from blue to red. Again we compare the scenario in our intrinsically asymmetric lattice to a lattice with additional auxiliary beam and study the resonant coupling behaviour as a function of the lattice depth by varying the lattice detuning $\Delta_{2,1}$. The auxiliary beam power is again set to the difference of P_{inc} and P_{back} to produce a balanced lattice when the relative phase is locked at the side of the fringe and the results are depicted in figure 3.20. The data without PAC reproduce the already known behaviour, where the resonator mode temperature is drastically increased as soon as the lattice detuning is small enough to approach the resonant lattice depth around $\omega_{at} \approx \omega_m$. In contrast, for the data where the auxiliary lattice beam is employed we observe a significant reduction of the mode temperature to a minimum value of $T_{min}^{PAC} = (8 \pm 2)\,\text{K}$ with the MiM-system at room temperature. Note

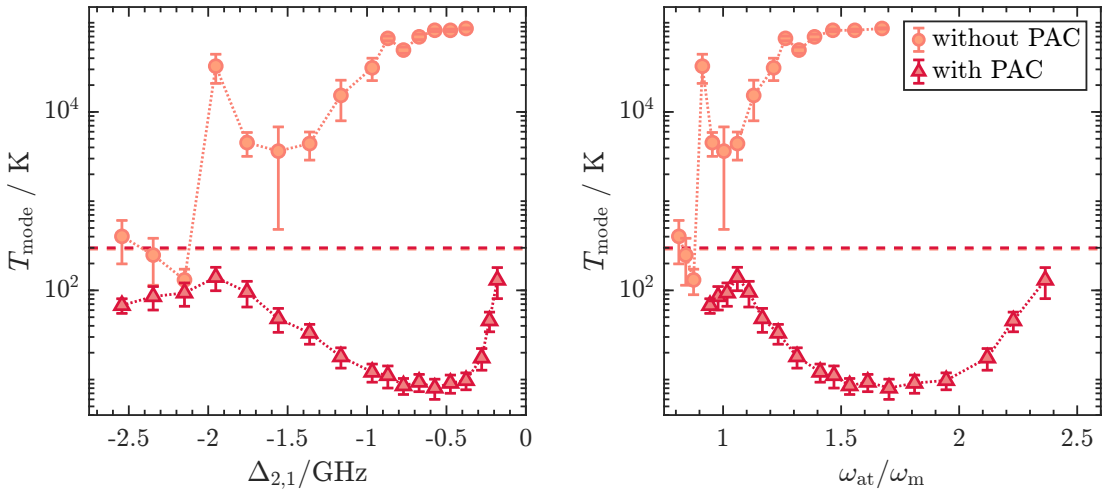

Figure 3.20: Sympathetic cooling with and without pump asymmetry compensation in red detuned lattice. Minimum resonator mode temperature T_{mode} during sympathetic cooling with a high OD MOT as a function of the resonant lattice depth. **Left panel:** The lattice power is held constant and the detuning $\Delta_{2,1}$ is varied to tune the lattice depth. The circles show the resulting mode temperature due to coupling mediated via an imbalanced lattice and the triangles denote the measured mode temperature $T_{\mathrm{min,PAC}} = (8 \pm 2)\,\mathrm{K}$ with applied auxiliary lattice beam. Dashed lines depict the bath temperature $T_{\mathrm{bath}} = 294\,\mathrm{K}$, which corresponds to the room temperature. **Right panel:** T_{mode} as a function of the (calibrated) atomic trapping frequency ω_{at} in units of the resonator frequency ω_{m}. Parameters: $P_{\mathrm{inc}} = 102.6\,\mu\mathrm{W}$, $P_{\mathrm{back}} = 21.2\,\mu\mathrm{W}$, $P_{\mathrm{aux}} = 81.4\,\mu\mathrm{W}$, $\phi_{\mathrm{aux,back}} = 0.78\,\pi$.

however, that the relative phase $\phi_{\mathrm{aux,back}} = 0.78\pi$ is set closer to the bottom of the fringe than to the side which results in a total reflected power of $P_{\mathrm{ref,tot}} = 38.5\,\mu\mathrm{W}$. Notably, cooling in a balanced lattice with this lattice configuration was not possible so we adjusted the relative phase at a fixed detuning until we observed a cooling effect and swept the detuning subsequently. The resulting lattice is still asymmetric but allows for sympathetic cooling. This unexpected result motivated a more detailed investigation of the lattice parameters that will be described in the following.

Parameter optimization

As already explained in section 3.4 a balanced lattice can be obtained from different combinations of the auxiliary beam intensity and the relative phase $\phi_{\mathrm{aux,back}}$. Therefore, we studied the sympathetic cooling behaviour for different ratios $P_{\mathrm{aux}}/P_{\mathrm{back}}$ from 1:1 to 7.4:1 of the auxiliary beam power with respect to the back-reflected power and varied the relative phase to tune the total reflected power $P_{\mathrm{ref,tot}}$. The incident power $P_{\mathrm{inc}} = 102.6\,\mu\mathrm{W}$ is held constant and we fix the detuning close to the point, where optimal sympathetic cooling occurred in the previous measurement (see figure 3.20). The results are shown in figure 3.21, where each color corresponds to one ratio $P_{\mathrm{aux}}/P_{\mathrm{back}}$ in all plots. For moderate auxiliary beam powers the data exhibit a minimum of the mode temperature when the power of the combined reflected beam is increased, which indicates the existence of an optimal relative phase (red, orange, yellow). The remaining power ratios lead to a monotonically increasing mode temperature with increasing $P_{\mathrm{ref,tot}}$. Each setting of the total reflected power corresponds to one value of $\phi_{\mathrm{aux,back}}$

as depicted in the top right panel. It stands out that all lock-points are situated on the lower half of the fringe. For every power ratio (>2:1) the point closest to the bottom of the fringe yields the lowest mode temperature. Moving the lock-point towards the side of the fringe, which results in a larger reflected power, leads to a higher T_{mode}. The lock-points were swept from the lowest possible value that allowed stable operation of the phase-lock to a setting were no cooling effect is visible any more. Clearly, the

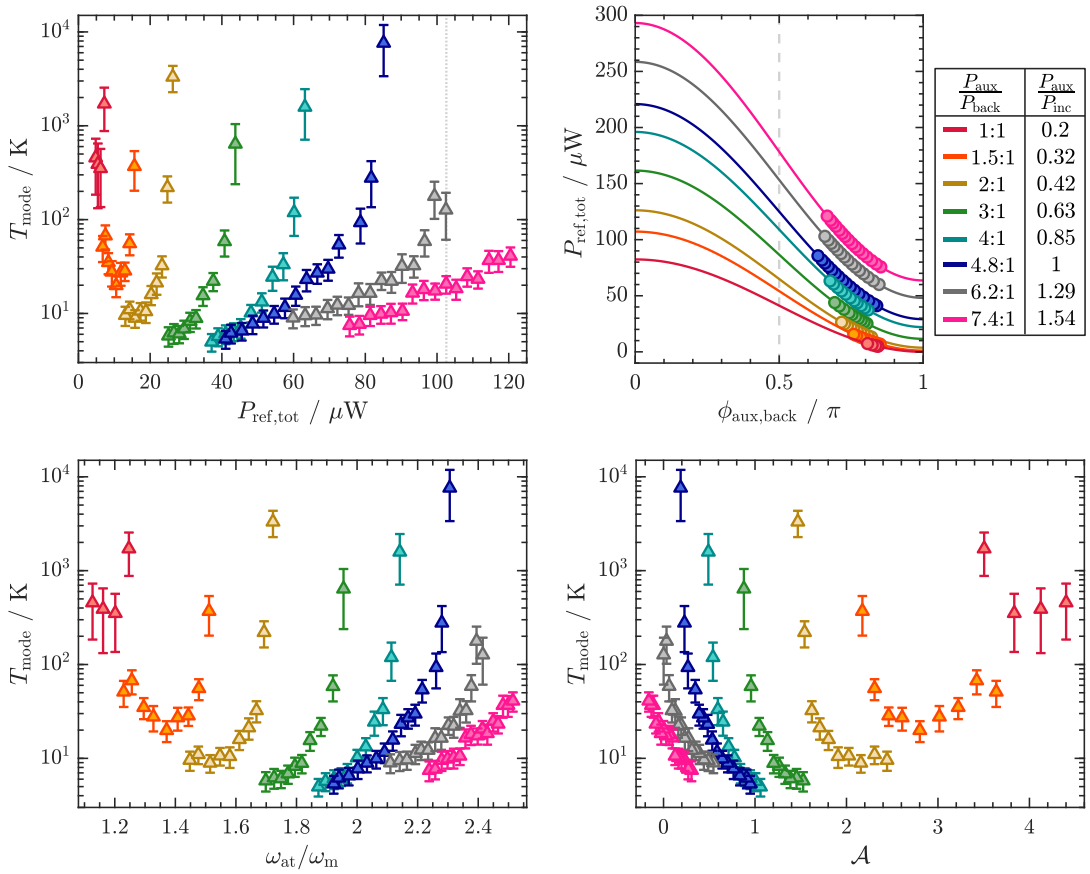

Figure 3.21: Sympathetic cooling efficiency in red detuned lattice for different pump asymmetries. To identify the parameters for the best sympathetic cooling efficiency in the high OD MOT P_{aux} is set to multiples of P_{back} (see left column in legend) and the resonator mode temperature T_{mode} is measured as a function of the total reflected power $P_{\mathrm{ref,tot}}$, which is varied by sweeping the relative phase $\phi_{\mathrm{aux,back}}$ between back-reflected and auxiliary beam. Corresponding $P_{\mathrm{ref,tot}}$ and $\phi_{\mathrm{aux,back}}$ are indicated by the same color. **Top left panel:** T_{mode} as a function of $P_{\mathrm{ref,tot}}$ resulting from varying the lock-point of the relative phase $\phi_{\mathrm{aux,back}}$ for different P_{aux}. The dotted line denotes a symmetric lattice, but clearly the cooling efficiency at this lattice configuration is inferior to other still asymmetric configurations. **Top right panel:** Total reflected power $P_{\mathrm{ref,tot}}$ of the phase-locked interfering beams as a function of their relative phase $\phi_{\mathrm{aux,back}}$ for different P_{aux}. The circles denote the lock-points at which T_{mode} is investigated. Interestingly, the lock-points corresponding to the lowest $P_{\mathrm{ref,tot}}$ and thus to the highest asymmetry in the resulting lattice, lead to the most efficient cooling. **Bottom left panel:** T_{mode} as a function of the (calibrated) atomic trapping frequency ω_{at} in units of the resonator frequency ω_{m}. **Bottom right panel:** T_{mode} as a function of the pump asymmetry $\mathcal{A}$ (see equation 3.26). Parameters: $P_{\mathrm{inc}} = 102.6\,\mu\mathrm{W}$, $P_{\mathrm{back}} = (21.4 \pm 0.5)\,\mu\mathrm{W}$, $\Delta_{2,1} = -475\,\mathrm{MHz}$.

most efficient cooling is achieved with the power ratios $P_{\mathrm{aux}}/P_{\mathrm{back}}$ 4:1 and 4.8:1 where the auxiliary beam power is close or equal to the incident beam power. We also find a configuration that allows for sympathetic cooling in a balanced red detuned lattice (denoted by the dotted line in the upper left panel of figure 3.21) but the cooling effect is less pronounced for this setting. Again, it seems likely that the resonance condition for the coupling is not equally well fulfilled here (compare bottom left panel), however this assumption could be ruled out by another detuning sweep for selected power ratios (see figure 3.22). Although we can not confirm our initial assumption, that sympathetic cooling works best in a balanced optical lattice we observe that the cooling efficiency improves with decreasing pump asymmetry according to our expectation. The optimal cooling is achieved at an asymmetry of $\mathcal{A} \approx 1$ and the performance deteriorates again towards the completely symmetric lattice at $\mathcal{A} = 0$ (compare bottom right panel in figure 3.21). For negative values of $\mathcal{A}$ the pump asymmetry is inverted and the combined reflected power exceeds the incident power.

In order to further characterize the sympathetic cooling in the red detuned lattice we study the resonant behaviour of the mode temperature as a function of the lattice depth by varying the detuning $\Delta_{2,1}$ again. We compare the power ratios $P_{\mathrm{aux}}/P_{\mathrm{back}} =$ 4:1 and 4.8:1, for which we obtained the lowest mode temperatures for the sweep of the relative phase and the ratio 7.4:1 at the setting of $\phi_{\mathrm{aux,back}}$ that resulted in the balanced lattice configuration. The results are shown in figure 3.22 and the individual

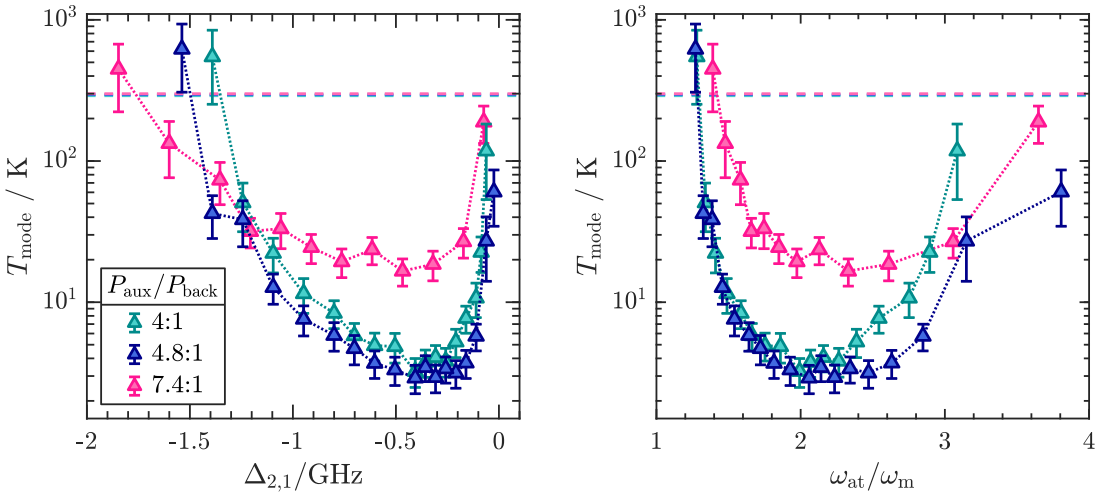

Figure 3.22: Sympathetic cooling in red detuned lattice for optimized parameters. Minimum resonator mode temperature T_{mode} as a function of the resonant lattice depth. **Left panel:** The lattice power is held constant and the detuning $\Delta_{2,1}$ is varied to tune the lattice depth. Comparison of the cooling efficiency of the two auxiliary beam powers P_{aux} that resulted in the lowest T_{mode} during the lock-point sweep (see figure 3.21) and a configuration that results in a balanced lattice (pink). Minimum reached temperatures are $T_{\mathrm{min,4:1}} = (3.24 \pm 0.75)\,\mathrm{K}$, $T_{\mathrm{min,4.8:1}} = (2.91 \pm 0.66)\,\mathrm{K}$ and $T_{\mathrm{min,7.4:1}} = (16.63 \pm 3.63)\,\mathrm{K}$. The dashed lines denote the bath temperatures $T_{\mathrm{bath}} = 294\,\mathrm{K}$, which corresponds to the room temperature. **Right panel:** T_{mode} as a function of the (calibrated) atomic trapping frequency ω_{at} in units of the resonator frequency ω_{m}. Parameters: $P_{\mathrm{inc}} = 102.6\,\mu\mathrm{W}$, $P_{\mathrm{back}} = 21.7\,\mu\mathrm{W}$, $\phi_{\mathrm{aux,back,4:1}} = 0.76\,\pi$, $\phi_{\mathrm{aux,back,4.8:1}} = 0.81\,\pi$, $\phi_{\mathrm{aux,back,7.4:1}} = 0.57\,\pi$.

power ratios are plotted in the same colours as in figure 3.21. Qualitatively, the trend of the blue data looks similar to sympathetic cooling in the blue detuned lattice without PAC, where the minimum mode temperature is also reached around $\omega_{at} \approx 2\omega_m$ at a detuning $|\Delta| < 0.5\,\mathrm{GHz}$. In the case of $P_{aux}/P_{back} = 7.4{:}1$ the minimal mode temperature is reached at a slightly higher lattice depth and the resonance feature is broadened similar to the blue lattice with PAC (compare figure 3.18). In this case however, the minimum mode temperature is also significantly higher than for the other two power ratios that yield equivalent minimum mode temperatures within the error.
A more quantitative analysis can be done by comparing the resulting sympathetic cooling rates Γ_{sym} and the deduced cooperativities. The calculation is equivalent to the one described in section 3.5.2 and the results are depicted in figure 3.23. Here, the extracted atomic cooling rates Γ_{at} are equal within the error for all three power ratios. From the measured sympathetic cooling rates we can calculate the hybrid cooperativities

$$C^{PAC}_{hyb,4:1} = (90 \pm 21) \quad , \; C^{PAC}_{hyb,4.8:1} = (100 \pm 23) \quad \text{and} \quad C^{PAC}_{hyb,7.4:1} = (17 \pm 4).$$

Another factor that influences the sympathetic cooling efficiency is the power in the coupling lattice. Therefore, we studied if the cooling effect in the PAC lattice can be further improved by changing the overall lattice power. We do this at the experimentally determined optimal power ratio of $P_{aux} = P_{inc}$ by varying the incident beam power. For each set incident power P_{inc} we fix the relative phase $\phi_{aux,back}$ at the lowest stable lock-point where the best cooling performance is observed (compare figure 3.21). Additionally, we adjust the detuning $\Delta_{2,1}$ for each power to maintain the same lattice depth for all measurements. The results are shown in figure 3.24. The measurement clearly indicates, that we did not operate at the optimal incident power. Compared to the power that we used in all our experiments presented before the mode temperature could be further reduced by a factor of 1.5 for an incident power of $P_{inc} = 65\,\mu\mathrm{W}$. Also the mode temperature increases for higher lattice powers at the same lattice depth as expected. Still, we do not exceed the cooling efficiency that we obtain in the blue detuned lattice without PAC.

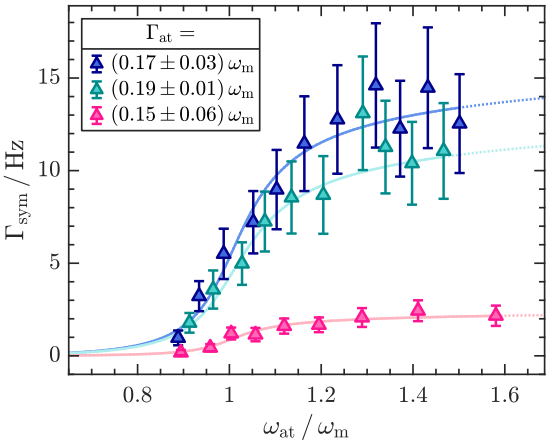

Figure 3.23: Resonance behaviour of $\Gamma_{sym}(\omega_{at})$ for MOT cooling in a red detuned lattice. Sympathetic cooling rate Γ_{sym} calculated with equation (3.15) using the temperatures T_{mode} and T_{bath} from figure 3.22. Data points with decreasing Γ_{sym} for large ω_{at} are omitted. The solid lines are fits according to equation (3.17), which are used to obtain the atomic cooling rate Γ_{at} and to rescale the x-axis. Maximum measured cooling rates: $\Gamma^{max}_{sym,4.8:1} = (14.6 \pm 3.4)\,\mathrm{Hz}$, $\Gamma^{max}_{sym,4:1} = (13.1 \pm 3.1)\,\mathrm{Hz}$ and $\Gamma^{max}_{sym,7.4:1} = (2.4 \pm 0.6)\,\mathrm{Hz}$.

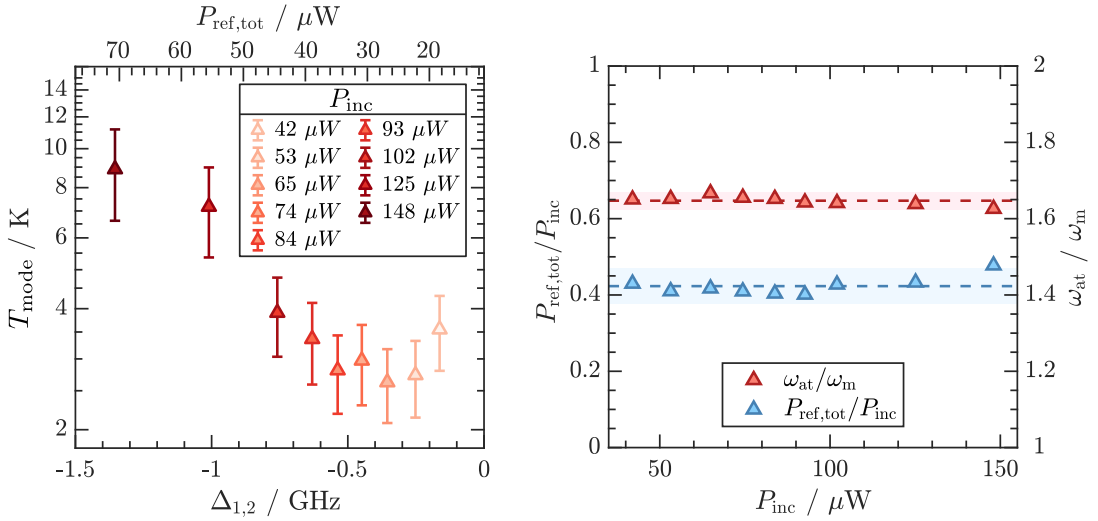

Figure 3.24: Sympathetic cooling as a function of the incident power in red detuned lattice. For the determined optimal ratio $P_{\mathrm{aux}} = P_{\mathrm{inc}}$ the influence of the incident power on the sympathetic cooling efficiency is investigated. At each set value of P_{inc} the relative phase $\phi_{\mathrm{aux,back}}$ is adjusted to the point where optimal cooling occurs and the lattice detuning $\Delta_{2,1}$ is chosen to produce the same lattice depth at the trapping frequency $\omega_{\mathrm{at}} = (1.65 \pm 0.01)\,\omega_{\mathrm{m}}$. **Left panel:** Resonator mode temperature T_{mode} for different set incident powers P_{inc} with the corresponding detuning (lower x-axis) and total reflected power $P_{\mathrm{ref,tot}}$ (upper x-axis) to produce constant lattice depth. **Right panel:** Power ratio $P_{\mathrm{ref,tot}}/P_{\mathrm{inc}}$ resulting from the choice of the relative phase $\phi_{\mathrm{aux,back}}$ (left y-axis) and lattice depth $\omega_{\mathrm{at}}/\omega_{\mathrm{m}}$ (right y-axis) as a function of the incident power P_{inc}. Shaded regions denote two times the standard deviation. All measurements were performed at $P_{\mathrm{aux}} = P_{\mathrm{inc}}$.

3.6 Conclusion

In this chapter we investigated the feasibility to improve the hybrid coupling between cold atoms and a mechanical resonator by alleviating the asymmetry in the coupling lattice. First, we convinced ourselves that the pump asymmetry in the coupling lattice is a reasonable cause for the arising instability that was observed in earlier experiments [74, 77]. This hypothesis was substantiated by a numerical simulation of an optical lattice, which is represented by a periodic array of thin beam splitters and is subject to a phase modulation, like it is caused by the mechanical resonator. We found that the system exhibits a phase lag that depends on the number of atoms in the system and the used lattice detuning. More importantly, for asymmetrically pumped optical lattices this phase lag can exceed $\Delta\phi = -180°$ which results in resonant driving of the phase modulation source (in our case the mechanical resonator) if the system is regarded as a closed feedback loop. The simulation also proved, that the build-up of large phase lags can be prevented by introducing an auxiliary lattice beam to compensate the pump asymmetry.

Consequently, we elaborated a scheme to prove this also experimentally. Indeed, we observed that it is possible to establish hybrid coupling between the atoms and the mechanical resonator in a balanced optical lattice, even at high atomic densities in a red detuned lattice, which was not possible before. Therefore, we can conclude that the

scheme is suited to stabilize the system and prevent it from exhibiting self-oscillations, which drive the resonator into limit-cycle oscillations.
However, the compensation of the pump asymmetry does not work as expected and behaves differently for red and blue lattice detuning. First of all, we observe that sympathetic cooling in the blue detuned PAC lattice is only possible when the lattice is properly balanced. For relative phases $\phi_{\mathrm{aux,back}}$ that result in a strongly asymmetric lattice no cooling effect is achieved. Moreover, the cooling effect for a well balanced lattice is inferior by roughly a factor of 2 to cooling in a blue detuned asymmetric lattice. This becomes clear by comparing the lowest achieved mode temperatures, the sympathetic cooling rates and the hybrid cooperativities:

blue lattice	$T_{\mathrm{mode}}^{\mathrm{min}}$	$\Gamma_{\mathrm{sym}}^{\mathrm{max}}$	C_{hybrid}
without PAC	$(1.50 \pm 0.34)\,\mathrm{K}$	$(27.7 \pm 6.1)\,\mathrm{Hz}$	(190 ± 42)
with PAC	$(2.87 \pm 0.69)\,\mathrm{K}$	$(14.8 \pm 3.6)\,\mathrm{Hz}$	(102 ± 25)

Interestingly, for red lattice detuning the PAC lattice behaves very different. The use of an additional lattice beam allows for sympathetic cooling in a high optical density MOT where cooling with our ordinary two beam lattice is not possible at all. Yet, the best cooling performance is not achieved in a balanced lattice configuration. Contrary to our expectation, the strongest cooling effect is obtained in a still asymmetric lattice. We find the optimal parameters for sympathetic cooling in the red detuned lattice by sweeping the relative phase $\phi_{\mathrm{aux,back}}$ between the auxiliary and the back-reflected beam for different power settings P_{aux} of the auxiliary beam. After the optimization we measure

red lattice	$T_{\mathrm{mode}}^{\mathrm{min}}$	$\Gamma_{\mathrm{sym}}^{\mathrm{max}}$	C_{hybrid}
with PAC	$(2.91 \pm 0.66)\,\mathrm{K}$	$(14.6 \pm 3.4)\,\mathrm{Hz}$	(100 ± 23)

for the optimal power ratio $P_{\mathrm{aux}} = P_{\mathrm{inc}}$. The obtained results indicate that the realized coupling in the PAC lattice is equally strong for red and blue lattice detuning, although the total reflected power is different ($P_{\mathrm{ref,tot}} = P_{\mathrm{inc}}$ for the blue lattice and $P_{\mathrm{ref,tot}} = 0.46\,P_{\mathrm{inc}}$ for the red lattice). This brings us to the conclusion that the coupling strength can not be enhanced by an additional lattice beam that does only interact with the atoms but not with the cavity. Also, this suggests that the improved stability of the red detuned lattice does not result in the participation of more atoms in the coupling process. To achieve stronger coupling it would be necessary to increase the lattice volume by using larger beam waists and enhance the reflectivity on resonance as well as the photon resonator coupling through an improved cavity finesse.
The difference in performance between the PAC lattice and the ordinary two beam lattice is probably caused by intensity noise introduced by the auxiliary beam phase lock or other mechanical jitter in the long optical path of the auxiliary beam setup that disturbs the lattice potential during the coupling. From the residual phase noise (see equation 3.55) we determine the relative in-lock intensity fluctuations to be on the order of 2 %. Beyond that we did not invest more time to explicitly identify the source of the performance deterioration.
Since our approach was not able to improve the coupling strength we also assess its

applicability to further BEC coupling experiments as low. We note, that the mechanical linewidth Γ_m of the trampoline resonator at room temperature is comparable to that of the previously employed square membrane at $T_\mathrm{base} = 500\,\mathrm{mK}$ ($\Gamma_\mathrm{m}^{\square} = 2\pi\cdot 24.5\,\mathrm{mHz}$) [74], which leads to an already increased hybrid cooperativity. For similar experiments at cryogenic temperatures we measured a maximum cooperativity of $C_\mathrm{hybrid} = (347 \pm 72)$. However, those experiments could not be performed at base temperature and were subject to a drifting bath temperature. Qualitatively, they show the same behaviour as the measurements presented in this chapter and can therefore be found in appendix B.3. Nevertheless, the hybrid cooperativity is orders of magnitude smaller than the residual phonon occupation of the resonator mode, which renders ground state cooling by means of sympathetic cooling impossible in our current setup. Therefore, we switch gears and follow a different approach to prepare our mechanical resonator in a quantum state, which will be described in the following chapter.

Chapter 4

From continuous to pulsed preparation and measurement

This chapter describes a novel detection method for high-sensitivity optomechnical displacement measurements at our experiment, which relies on a pulsed light-mechanics interaction and is capable of surpassing the standard quantum limit. The concept of conditional state preparation and tomography is introduced and the necessary experimental modifications for the application of the technique are presented. First experiments are performed to identify the capabilities of our system and to evaluate possible future enhancements.

Preparation and measurement of macroscopic objects in non-classical states is a long sought-after goal that promises insight into the quantum to classical transition [25, 167]. A well established platform to study the formation of such non-classical states of massive objects and their decoherence is posed by the field of cavity optomechanics [24]. It has already led to the demonstration of ground state cooling [56, 111, 112], entanglement [92, 168], quantum squeezing [91, 169, 170] and coherent state transfer [58, 127, 171, 172] of mechanical motion. Still, there is an ongoing pursuit to improve the sensitivity of the utilized measurement schemes to characterize the quantum states of motion. The ultimate goal is to be able to fully reconstruct these quantum states, which requires a resolution better than the width of the mechanical zero-point motion x_{zpf} [81].

Due to the intrinsic linkage between control and detection of motional states, each measurement process can be associated with a competition between the gain of information (measurement rate), noise added by the measurement (backaction) and decoherence. Full control over a system can be gained, if the measurement rate exceeds all deleterious effects allowing for feedback cooling to the ground state [113, 173, 174] and conditional preparation of pure quantum states [175, 176]. Typically, optomechanical detection schemes are based on displacement measurements that are long compared to the mechanical oscillation period, termed *continuous measurements*. Their sensitivity is bounded fundamentally by the Heisenberg uncertainty principle, which manifests in the standard quantum limit (see figure 2.7). The measurement imprecision due to quantum noise (e.g. photon shot noise) can be reduced by increasing the probe field strength,

but this comes at the cost of an increased measurement backaction due to radiation pressure noise. The point of minimum uncertainty is reached when both, the imprecision and backaction noise, add equal contributions to the overall measurement noise. In continuous measurements this corresponds to probing the non-commuting position and momentum variables simultaneously, limiting the sensitivity to the ground state size x_{zpf} of the probed object.
It is however possible, to circumvent the backaction by only partially measuring the state of the system. A measurement performed on a single quadrature variable can be in principle arbitrarily precise as long as only information about this quadrature is gathered. All the measurement imprecision is then transferred to the unmeasured quadrature [78].

4.1 Backaction evading measurements

The concept of backaction evading measurements was originally proposed by Braginsky and Vorontsov [177] and is often also termed *quantum nondemolition* measurement [78]. It is defined by a sequence of precise measurements of an observable A, whose results are exactly predictable from the outcome of the initial measurement of A. The measurement is only backaction free, if the system commutes with itself at different instants of time $t_j,\ t_k$ after it has evolved according to the Heisenberg equations of motion such that its commutator yields $[A(t_j), A(t_k)] = 0$. If this condition is satisfied at all times A is called a continuous quantum nondemolition (QND) variable.
Considering a harmonic oscillator, the position x and momentum p are subject to the commutation relations

$$\begin{aligned}[x(t), x(t+\tau)] &= \frac{i\hbar}{m\omega}\cos(\omega\tau) \\ [p(t), p(t+\tau)] &= i\hbar m\omega \sin(\omega\tau).\end{aligned} \tag{4.1}$$

Hence, they are not continuous QND observables. Due to the periodically vanishing commutators at integer multiples of half-periods these observables can however be measured without backaction and are therefore termed stroboscopic QND observables. Such well-timed measurements thus result in precise knowledge of x at instants $\tau = (n + 1/2)\pi/\omega$ and p at $\tau = n\pi/\omega$ (with $n \in \mathbb{N}_0$) but are uncertain at other times.
In quantum theory it is often useful to introduce the complex amplitude of an oscillator [178]

$$X + iY = \left(\frac{x + ip}{m\omega}\right) e^{i\omega t} \tag{4.2}$$

whose real and imaginary parts form QND observables at all times

$$X = x(t)\cos(\omega t) - \frac{p(t)}{m\omega}\sin(\omega t) \tag{4.3a}$$

$$Y = x(t)\sin(\omega t) + \frac{p(t)}{m\omega}\cos(\omega t). \tag{4.3b}$$

During a measurement a single observable can be measured with arbitrary precision at the cost of strongly increasing the uncertainty in the other observable while the fundamental precision limit

$$\Delta X \Delta Y \geq \frac{\hbar}{2m\omega} \;=\; x_{\mathrm{zpf}}^2 \tag{4.4}$$

is enforced by the commutation relation $[X, Y] = i\hbar/(m\omega)$, which follows from $[x, p] = i\hbar$ [78].

Numerous examples of such backaction evading measurements have been shown in different quantum systems including mechanical systems, optical fields and spin ensembles [64, 113, 179–182]. In the optomechanical realisations the backaction was avoided by only probing one of the motional quadratures while gaining no knowledge about the other orthogonal one. The applicable experimental schemes depend on the ratio between the mechanical resonance frequency ω_{m} and the cavity linewidth κ. Many systems operate in the sideband resolved regime ($\omega_{\mathrm{m}} \gg \kappa$), where a technique termed *two-tone driving* can be applied. It is based on a modulation of the optomechanical interaction by amplitude modulation of the drive at the mechanical frequency, which leads to effectively pumping the cavity at the upper and lower cavity sideband. In this way a time varying intra-cavity amplitude is obtained that accumulates a phase, proportional to the quadrature X in equation (4.3a), on time scales that are long compared to $1/\omega_{\mathrm{m}}$. Since only the quadrature X is probed, the measurement backaction is completely deposited in Y. Such measurements have been performed in microwave optomechanical systems [183, 184] and with photonic crystal nanobeams [185].
Another possibility is to use a *variational readout* scheme that employs a time or frequency dependent readout of the output field to cancel the backaction via correlations in the quantum fluctuations of the amplitude and phase quadrature [181, 182].
In systems where $\kappa \gg \omega_{\mathrm{m}}$ the optical mode decays much faster than a mechanical period. Therefore, this unresolved sideband regime allows to make snapshot-like measurements of the mechanical motion that only probe the instantaneous position of the resonator and do not acquire any information about its momentum. Such pulsed measurements where originally conceived in 1978 by Braginsky *et al.* [109] and described more recently under the name *pulsed quantum optomechanics* by M. Vanner *et al.* [79]. The latter outline a procedure that allows for *cooling by measurement*, which was realized in a simplified proof of principle experiment [80] and later refined by J. Muhonen *et al.* [186]. However, the achieved sensitivity was not good enough to resolve the mechanical ground-state width.

4.1.1 Pulsed backaction evasion

For instantaneous position measurements of a duration $\tau \ll 2\pi/\omega_{\mathrm{m}}$, the position can be determined with an imprecision that is limited by the shot noise arising from the number of photons in the probe pulse. If the pulses are sufficiently intense, this imprecision can become smaller than the width of the mechanical ground state x_{zpf} and surpass the standard quantum limit.

When the measurement process is considered in the time domain, it becomes apparent that the backaction can be avoided by appropriately timing the measurement sequence. The time dependent motion of a mechanical resonator can be described by recasting equations (4.3) in the familiar form

$$x(t) = X_{\mathrm{M}}(t)\cos(\omega_{\mathrm{m}}t) + P_{\mathrm{M}}(t)\sin(\omega_{\mathrm{m}}t) \tag{4.5a}$$

$$\frac{p(t)}{m_{\mathrm{eff}}\omega_{\mathrm{m}}} = -X_{\mathrm{M}}(t)\sin(\omega_{\mathrm{m}}t) + P_{\mathrm{M}}(t)\cos(\omega_{\mathrm{m}}t), \tag{4.5b}$$

where $X_{\mathrm{M}}(t)$ and $P_{\mathrm{M}}(t)$ are the position and momentum quadratures of the resonator. They vary slowly, on a time scale set by the inverse of the mechanical dissipation rate Γ_{m}, and are driven by the thermal occupation of the surrounding bath. This means that they diffuse randomly in phase space at the thermal decoherence rate Γ_{th}, or in other words remain unchanged within the thermal decoherence time $t_{\mathrm{th}} = 1/(\Gamma_{\mathrm{m}} n_{\mathrm{th}})$ [187].

A phase sensitive homodyne measurement of a short probe pulse at time $t = 0$ will yield a position measurement that is linearly proportional to the mechanical position quadrature X_{M} (see (4.6a)). Since no information about the momentum quadrature P_{M} is acquired we can not predict the trajectory of the motion from a single measurement. However, due to the periodicity of the motion we can anticipate to measure the same result (up to the measurement imprecision), if we apply a second pulse exactly one mechanical period T later and the thermal decoherence is negligible during that time. This is illustrated in figure 4.1. Since we probe the same quadrature, the first measurement allows us to predict the outcome of the second with an accuracy that can be better than the zero-point motion. The backaction from this measurement due to the radiation pressure force can be decomposed into two contributions: a stochastic one that depends on the photon shot noise in the pulse, proportional to $\sqrt{\bar{N}}$ and a coherent one, proportional to the mean photon number $\bar{N}$ that alters the resonator momentum p (see (4.6b)). It affects the position only at a later time t' such that $\omega_{\mathrm{m}}t' = \pi/2$. Hence, for the measurement at time $t = 0$ only the unmeasured quadrature P_{M} is subject to the backaction noise.

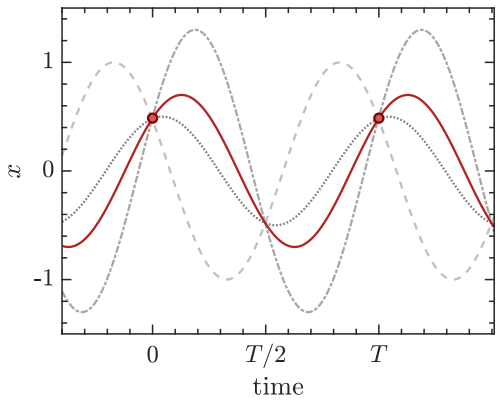

Figure 4.1: Illustration of instantaneous position measurement. Exemplary trajectories of the mechanical position for a fixed ω_{m}. Regardless of the amplitude or phase, measurements at time $t = 0$ and $t = T = 2\pi/\omega_{\mathrm{m}}$ have the same outcome. Hence, pulsed measurements allow to make predictions about the position at specific times without any knowledge about the momentum.

Quantitatively, this optomechanical interaction can be described by the following input-output relations [80, 188]

$$X_{\mathrm{L}}^{out} = X_{\mathrm{L}}^{in}, \quad P_{\mathrm{L}}^{out} = P_{\mathrm{L}}^{in} + \chi X_{\mathrm{M}}^{in}, \tag{4.6a}$$

$$X_{\mathrm{M}}^{out} = X_{\mathrm{M}}^{in}, \quad P_{\mathrm{M}}^{out} = P_{\mathrm{M}}^{in} + \chi X_{\mathrm{L}}^{in} + \Omega_{\mathrm{L}}. \tag{4.6b}$$

Here, X_{L} and P_{L} are the amplitude and phase quadratures of the probe field, the superscripts *in* (*out*) identify the operators prior to (after) the interaction and Ω_{L} denotes the momentum transferred by the probe pulse. The amount of exchanged quadrature information between light and mechanics is quantified by the measurement strength

$$\chi = \frac{8g_0\sqrt{\eta\bar{N}}}{\kappa}, \tag{4.7}$$

where the constant η denotes the measurement efficiency affected by optical losses and inefficient detection. The measurement strength can be understood as a figure of merit for the pulsed measurement protocol, as it can be used to determine the sensitivity of the measurement. Vice versa one can calculate the needed measurement strength to resolve the zero point motion. By recalling the phase shift $\delta\phi_{\mathrm{r}}$ produced by a resonator displacement x_{m} (see section 3.1.1) we find the variation of the optical phase due to a change of the displacement quadrature δX_{M} to be $\delta\phi_{\mathrm{r}} = 4g_{\mathrm{m}}\delta X_{\mathrm{M}}/\kappa$, since $x_{\mathrm{m}} \propto \delta X_{\mathrm{M}}$. Using the number-phase uncertainty relationship $\delta\phi\delta N \geq 1/2$ [189] the required number of photons per pulse to reach a minimum quadrature imprecision that corresponds to the zero-point motion ($\delta X_{\mathrm{M}} = x_{\mathrm{zpf}}$) can be estimated to [187]

$$\sqrt{\bar{N}} \geq \frac{\kappa}{8g_0}. \tag{4.8}$$

Here, $g_0 = g_{\mathrm{m}}x_{\mathrm{zpf}}$ and the photon number uncertainty given by the shot noise $\delta N = \sqrt{\bar{N}}$ [189] was used. By comparing equations (4.7) and (4.8) and assuming ideal measurement efficiency ($\eta = 1$) we arrive at the condition for the measurement strength that allows to resolve the width of the ground state

$$\chi \geq 1. \tag{4.9}$$

Fulfilling this requirement is a challenging task, as can be seen from the measurement strengths $\chi_{\mathrm{Vanner}} = 2.1 \cdot 10^{-4}$ [80] and $\chi_{\mathrm{Muhonen}} = 0.079$ [186][40] that were reported until now. With our current setup[41] we would need $\bar{N} \approx 12.7 \cdot 10^9$ photons per pulse which is not within reach for us at the moment. The present limitations regarding the measurement strength and possible experimental modifications to significantly improve it will be discussed in section 4.3.1.

[40] This value is corrected by a factor of $1/\sqrt{2}$ to provide comparability with Vanner *et al.*. It was omitted by authors in their publication and therefore they stated $\chi = 0.11$. We abide by the definition used by Vanner *et al.* see equation (4.17).

[41] This refers to the parameters of the optomechanical system that can be found in section 2.3.

4.1.2 Preparation and reconstruction of mechanical motional states

As already mentioned in the beginning of the chapter the preparation and manipulation of quantum states by means of quantum optics is a promising route to study non-classical behaviour of macroscopic objects. An important and yet to be experimentally demonstrated task is to perform a complete optomechanical reconstruction of a quantum state. A suitable technique for the reconstruction is to first transfer the mechanical quantum state onto a light field and then perform optical homodyne tomography [81, 190, 191]. Conveniently, the mechanical quadrature information is imprinted automatically during the pulsed light-mechanics interaction (see (4.6a)). Homodyne tomography is originally performed by measuring the quadrature amplitudes of the light field at various relative phases between the signal and LO beam for the characterization of its quantum state. In order to map out the state of the mechanics a conceptually similar scheme can be applied, which will be described further below.
The knowledge of the state of a system provides the ability to predict the outcome of future measurements on the system [175] - for quantum states based on a probability distribution. It is always defined with respect to a specific observer and due to its probabilistic description it is incomplete. By performing a measurement on the system the observers knowledge is increased and hence the state of the system is changed. Such transfer from an undefined superposition of possible configurations to a specific one is termed projective measurement in quantum measurement theory. The resulting a-posteriori state can then be called a *conditional state*; conditioned by the outcome of the measurement [175, 187].

In our case we want to describe the state of a mechanical resonator, which initially is found in a thermal state that is defined by its environmental temperature T. Due to its high Q-factor it can be approximated by a harmonic oscillator, whose position and momentum in a thermal state are described by a Gaussian distribution with the variances [192]

$$\sigma_x^2 = \frac{\hbar}{m_{\mathrm{eff}}\omega_{\mathrm{m}}}(n+\frac{1}{2}) = \frac{k_B T}{m_{\mathrm{eff}}\omega_{\mathrm{m}}^2} = 2n_{\mathrm{th}}x_{\mathrm{zpf}}^2 \tag{4.10a}$$

$$\sigma_p^2 = m_{\mathrm{eff}}\hbar\omega_{\mathrm{m}}(n+\frac{1}{2}) = m_{\mathrm{eff}}k_B T = \frac{\hbar^2 n_{\mathrm{th}}}{2x_{\mathrm{zpf}}^2}, \tag{4.10b}$$

where in the second step the equipartition theorem was used. If we now perform a measurement of this state the result will be a new state with a distribution that depends on the amount of information gained, i.e. the strength of the measurement. This new state is *prepared* by the measurement.

Assuming we make an ideal measurement of the position quadrature X_{M} at time $t = 0$ using a short light pulse, the best possible prediction for the position of the resonator at later times is given according to (4.5a) by $X_{\mathrm{M}}\cos(\theta)$ with $\theta = \omega_{\mathrm{m}}t$. It differs from the actual position by $x(t) - X_{\mathrm{M}}\cos(\theta) = P_{\mathrm{M}}\sin(\theta)$. This quantity vanishes periodically at $\theta = n\pi$ (with $n \in \mathbb{N}_0$), which shows that information about one quadrature allows to predict the mechanical position every half-period (see figure 4.1). The conditional

state is therefore a squeezed state of motion represented by an asymmetric Gaussian in phase-space with narrow position and large momentum width.

Based on this principle M. Vanner *et al.* proposed a protocol to produce a conditional mechanical state with reduced uncertainty [79], which is depicted in figure 4.2. One can perform a subsequent pulsed measurement of the position quadrature after a quarter-period of mechanical evolution. As a consequence of the first measurement, the measurement backaction was imparted on the momentum quadrature P_M. However, after a quarter-period of oscillation the former momentum quadrature has evolved and become the new position quadrature, with a large position uncertainty due to the backaction. The second measurement now allows to reduce this uncertainty again by an amount proportional to the measurement strength. Once more, the backaction of this second pulse does not affect the measurement of the position quadrature. Since we now im-

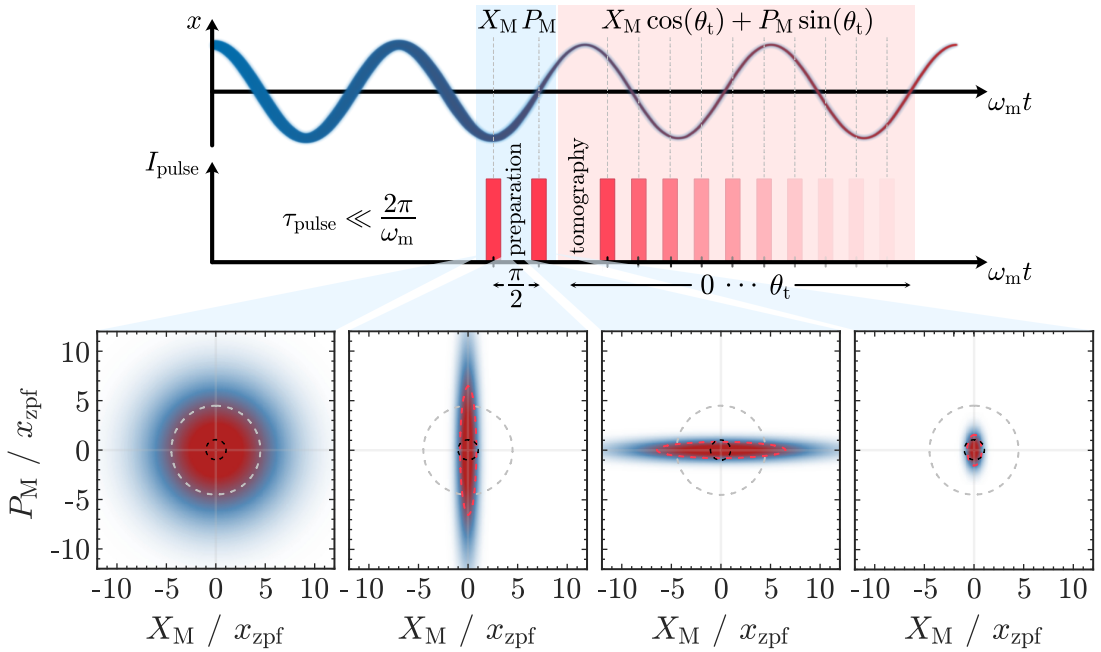

Figure 4.2: Pulsed preparation and state reconstruction scheme. Upper panel: The top graph shows the trajectory of the mechanical position according to equation (4.5a), whose uncertainty is reduced by the pulsed measurement. The lower graph shows the pulse sequence that is used for the preparation and tomography of the mechanical state (red bars). **Lower panel:** Phase-space distributions according to equation (4.12) of the mechanical state at different times during the pulse sequence (indicated by the blue shaded areas). The dashed lines depict the 2σ-widths of the initial (grey), squeezed (red) and ground state (black). Prior to the first pulse the system is in a thermal state with $n_\mathrm{th} = 40$ (chosen to ensure reasonable figure dimensions). After the pulsed measurement with measurement strength $\chi = 1$ the state is strongly squeezed in the X_M quadrature. During a quarter-period of mechanical oscillation the state evolves into a P_M quadrature squeezed state before the second pulse is applied that produces a high purity squeezed mechanical state. For $\chi \geq 1$ the width of the mechanical state can be reduced below x_zpf, regardless of the initial thermal occupation n_th as can be seen in (4.13b). Note, that the effect of the momentum transfer was omitted in these plots to illustrate the variances $\sigma^2_{\theta_\mathrm{t}}$ of the conditionally prepared state. The actual mechanical state is displaced after each pulse by the amount of transferred momentum Ω_L.

plicitly measure the momentum via a position measurement, the conditional state can be described by equation (4.5b) and yields $p(t)/(m_{\mathrm{eff}}\omega_{\mathrm{m}}) - P_{\mathrm{M}}\cos(\theta) + X_{\mathrm{M}}\sin(\theta) = 0$. This tells us that two subsequent ideal measurements of the position and the momentum provide us with perfect knowledge of the state. However, in reality a measurement is never ideal such that a residual uncertainty, given by the variances in equations (4.10) remains.
The result is therefore a conditional state with strongly reduced uncertainty, compared to the initial state. Due to the increased knowledge of the mechanical state its entropy is reduced, which can be expressed in terms of an effective thermal occupation and hence leads to „cooling by measurement" [80]. The method is rapid as the interaction takes place within one mechanical oscillation period and has a considerable tolerance to the initial thermal occupation as well as the surrounding thermal bath. Hence, it does not require cryogenic operation and allows in principle to generate high purity and quantum squeezed states of mechanical motion by measurement [80].

Note, that this cooling is only to be understood as a reduction of the size of the phase-space probability distribution due to increased knowledge of the state and does not decrease the real thermal phonon occupation of the resonator.

Finally, to measure the resulting conditional state its phase space probability distribution has to be mapped out by a tomographic measurement. This can be done by utilizing a third pulse after a variable wait time and requires many repetitions of the same preparation and measurement sequence to record the necessary statistics. In contrast to the classical homodyne tomography not the phase angle ϕ_{lo} between signal and LO beam is varied, but the rotation angle θ_{t} of the mechanical state in phase-space, which corresponds to different times of mechanical evolution after the preparation sequence. In this way, different quadrature contributions of the mechanical state are projected on the phase quadrature of the light and can be measured at the same homodyne angle. The homodyne detection is operated at $\phi_{\mathrm{lo}} = \pi/2$ to measure the optical phase quadrature P_{L}. After many repetitive measurements of P_{L} the measurement outcome is given by a probability distribution [80]

$$\Pr(P_{\mathrm{L}}) = \frac{1}{\sqrt{\pi}} \int \exp\left[-(P_{\mathrm{L}} - \chi X_{\mathrm{M}})^2\right] \Pr(X_{\mathrm{M}}, \theta_{\mathrm{t}})\, \mathrm{d}X_{\mathrm{M}}, \tag{4.11}$$

which is a convolution of the marginal distributions of the mechanical state $\Pr(X_{\mathrm{M}}, \theta_{\mathrm{t}}) = \langle X_{\mathrm{M}}|\rho_{\mathrm{M}}^{\mathrm{in}}(\theta_{\mathrm{t}})|X_{\mathrm{M}}\rangle$ and a kernel that depends on the shot noise and the measurement strength χ of the probe pulse. For small χ the convolution washes out the features of the marginal distribution, whereas for growing χ the optical phase quadrature probability $\Pr(P_{\mathrm{L}})$ approximates the marginals with increasing accuracy. The marginal distributions $\Pr(X_{\mathrm{M}}, \theta_{\mathrm{t}})$ can be viewed as projections of the phase-space probability distribution onto the X_{M} quadrature axis after different mechanical evolution angles θ_{t}. By measuring the optical phase quadrature distributions $\Pr(P_{\mathrm{L}})$ that approximate these marginals for a set of angles θ_{t}, the phase-space distribution can be reconstructed via a back-projection called inverse Radon transformation [191, 193].

In the original proposal [79] the light-mechanics interaction is described by means of nonunitary measurement operators [175, 194]. After action on an (in general) initially thermal mechanical state that can be described by a Gaussian distribution they produce the following dependence of the marginals

$$\langle X_{\mathrm{M}}|\rho_{\mathrm{M}}^{\mathrm{in}}(\theta_{\mathrm{t}})|X_{\mathrm{M}}\rangle \propto \exp\left[-\frac{(X_{\mathrm{M}}-\langle X_{\mathrm{M}}^{\theta_{\mathrm{t}}}\rangle)^2}{2\sigma_{\theta_{\mathrm{t}}}^2}\right], \tag{4.12}$$

where

$$\langle X_{\mathrm{M}}^{\theta_{\mathrm{t}}}\rangle = \frac{\chi P_{\mathrm{L}}}{\chi^2+\frac{1}{1+2n_{\mathrm{th}}}}\cos(\theta_{\mathrm{t}}) - \Omega_{\mathrm{L}}\sin(\theta_{\mathrm{t}}) \tag{4.13a}$$

$$\sigma_{\theta_{\mathrm{t}}}^2 = \frac{1}{2}\frac{\cos^2(\theta_{\mathrm{t}})}{\chi^2+\frac{1}{1+2n_{\mathrm{th}}}} + \frac{1}{2}\left(\chi^2+1+2n_{\mathrm{th}}\right)\sin^2(\theta_{\mathrm{t}}) \tag{4.13b}$$

are the mean and variance of the resulting conditional state, respectively. From equation (4.13b) the effect of squeezing one quadrature while anti-squeezing the other quadrature, depending on the evolution angle θ_{t} and the measurement strength χ, becomes evident. For large initial occupation $n_{\mathrm{th}} \gg 1$, which is always fulfilled in our experiment, we recover

$$(\text{for } \theta_{\mathrm{t}}=0) \quad \rightarrow \quad \langle X_{\mathrm{M}}^{\mathrm{out}}\rangle \simeq \frac{P_{\mathrm{L}}}{\chi}, \quad \sigma_{X_{\mathrm{M}}^{\mathrm{out}}}^2 \simeq \frac{1}{2\chi^2} \tag{4.14a}$$

$$(\text{for } \theta_{\mathrm{t}}=\frac{\pi}{2}) \quad \rightarrow \quad \langle P_{\mathrm{M}}^{\mathrm{out}}\rangle = \Omega_{\mathrm{L}}, \quad \sigma_{P_{\mathrm{M}}^{\mathrm{out}}}^2 = \frac{\left(\chi^2+1+2n_{\mathrm{th}}\right)}{2}. \tag{4.14b}$$

Consistently with equation (4.11) the mechanical position quadrature is reproduced by the optical phase quadrature for $\chi \to 1$. At the same time the width of the output state is reduced below the ground state width ($\sigma_{X_{\mathrm{M}}} < 1$), regardless of the initial thermal occupation n_{th}.

4.2 Experimental realization

Pulsed optomechanics experiments require fast and intense light-matter interactions on a time scale much shorter than the typical evolution time of the involved mechanical resonator. The interaction strength of the used light pulses can be enhanced by surrounding the investigated mechanical object with a cavity, forming a compound optomechanical system. To accommodate such short light pulses the linewidth of the cavity κ needs to exceed the mechanical angular frequency ω_{m} by orders of magnitude. In our system both requirements can easily be fulfilled as the cavity linewidth is much larger than the mechanical frequency $\omega_{\mathrm{m}}/\kappa \approx 10^{-6}$ and pulse lengths of several hundred nanoseconds are short compared to the oscillation period of the resonator $T_{\mathrm{m}} \approx 6.5\mu\mathrm{s}$.

In this section, the technical demands on pulsed preparation and measurement of mechanical motion will be discussed. Furthermore, these kinds of experiments require a modification to the homodyne detection setup that will be elaborated in the following.

Finally, first measurements of pulsed preparation and tomography in our setup will be presented. The changes to the experimental setup, programming of the measurement device, the first measurements as well as the writing of the evaluation code were carried out together with C. F. Klein.

4.2.1 Generation and detection of short pulses

During the interaction with the mechanical resonator its motional quadrature information is transferred onto the field quadratures of the optical mode. Consequently, the quadrature information of interest is encoded in the phase of the light. Therefore, a phase sensitive detection scheme is needed to read out this information. The standard phase sensitive measurement technique is balanced homodyne detection [103], which is capable of being quantum noise limited. Although it is commonly used in continuous detection schemes, it can equally well be applied for the detection of laser pulses. However in this case a few more things have to be taken into account: The mode match between the signal and the LO beam has not only to be regarded in the spatial but also in the temporal domain. Whereas the spatial mode match is equally important for an efficient detection in the continuous and pulsed case the temporal mode match needs to be considered carefully in the pulsed domain. It is of vital importance that the path lengths in the homodyne interferometer are equally long, as otherwise the signal and LO pulses disperse on their way through the detection setup and consequently reduce the detection efficiency due to lacking interference.

Short pulse generation

For the pulsed preparation and measurement scheme described in the previous section 4.1.2 pulse trains with arbitrary pulse spacing, pulse duration and potentially also pulse shape are needed. In order to produce such pulse trains two main ingredients are necessary: an actuator that modulates the desired intensity pattern onto the light and a suitable source to drive the actuator. As for the driving source arbitrary waveform generators are the devices of choice. They are in principle capable of producing any waveform with arbitrary complexity in a repetitive or single shot manner to probe or drive a device under test. The time scales and complexity of the generated waveform depend on the sampling rate as well as the available sample memory and vertical resolution of the device.
We use the UHF-AWG from *Zurich Instruments* with a sampling rate of 1.8GSa and 14bit vertical resolution, which gives us the flexibility to produce sufficiently short pulses even for higher frequency resonators in the MHz range (like the one shown and described in figure 2.27). The device also features an equally fast digitizer and a lock-in amplifier with 600 MHz bandwidth that we use for all recording and measurement applications in the continuous and the pulsed operation regime.
For the actuation only electro-optic modulators[42] (EOMs) can exploit the full capability of powerful waveform generators as their modulation bandwidths extend into the

[42] In principle also AOMs together with rf-switches can be considered but in order to reach fast actuation times very small beam diameters of $\approx 25\,\mu m$ are needed. Also they are rather suited for fast switching/production of rectangular pulses than arbitrary pulse shapes.

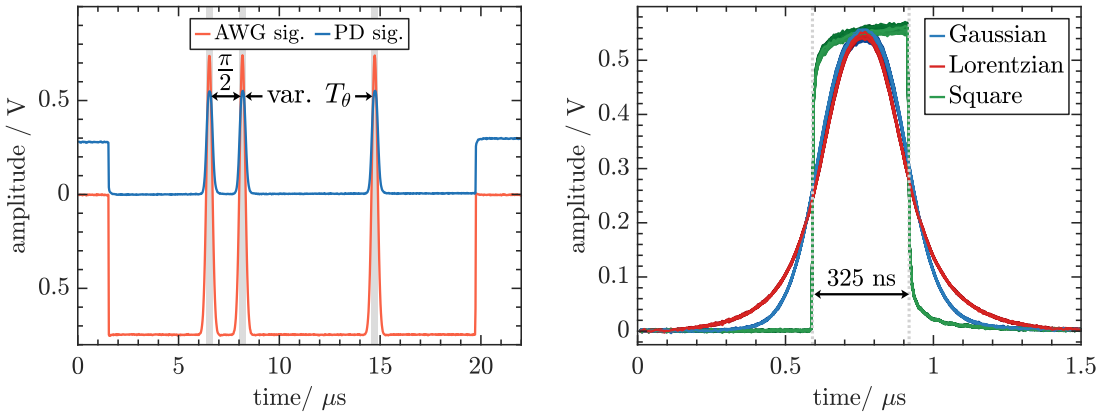

Figure 4.3: Pulse generation and reproducibility. Left panel: Exemplary pulse train like the ones used for pulsed preparation and tomography experiments. The first two pulses are separated by a quarter oscillation period (1.64 µs) of the trampoline resonator and the third pulse is applied after a variable wait time T_θ. The red line shows the waveform generated by the AWG that is employed to produce a pulse train with Gaussian shaped pulses of 325 ns duration using the amplitude modulator (blue line). **Right panel:** Exemplary pulses of different shapes are displayed. For each shape 30 time traces of the pulses are plotted. They nearly perfectly overlap with a timing jitter smaller than the resolution of the aquisition (2.2 ns) and a relative amplitude jitter of $\approx 1.5\,\%$. The used detector has a bandwidth of 500 MHz

gigahertz range. However, in general EOMs require high drive voltages on the order of hundreds of volts to reach their full modulation depth. Suitable electronic circuits can switch such large voltages within a few nanoseconds but for arbitrary signal modulation their bandwidth is not sufficient. The solution are fiber coupled waveguide modulators that feature small electrode distances and can therefore work with very low modulation voltages while still allowing for outstanding modulation frequencies. Their only downside is the low power transmission that is limited by the high insertion loss on the order of 4-7 dB. Depending on the used wavelength the maximum optical input power lies between 10 mW and 300 mW. For our setup we chose the fiber coupled amplitude modulator AM785b from *Jenoptik*, which has a very low half wave voltage $V_\pi = 1.83\,\mathrm{V}$, a minimum optical rise time of $\approx 500\,\mathrm{ps}$ and a maximum input power of 30 mW.
An exemplary pulse train produced with the amplitude modulator is depicted in the left panel of Fig. 4.3. The red trace is the waveform that is applied to the modulator and the blue trace shows the resulting pulse train recorded by the photodetector. The right panel shows a zoom into a single pulse of such a pulse train. For each pulse shape 30 time traces are plotted to highlight the nearly perfect reproducibility of the pulses. The reason for the distorted shape of the square pulse is the transient photocurrent response of the detector, which depends on the properties of the detector material.

Short pulse detection

In order to be able to read out the mechanical quadrature information carried by the light we employ the phase sensitive balanced homodyne measurement technique. The main requirement for the detection is to be able to observe quantum noise on the optical pulses in the time-domain under typical operating conditions.

For that a detector with a flat amplification profile over a large bandwidth is needed that provides sufficient time resolution to measure the optical pulses. The flat profile prevents ringing of the detector response after a short pulse, which would degrade the detection resolution and disturb the measurement. However, a high bandwidth comes at the cost of low gain which can negatively affect the signal to noise ratio. This can be overcome to some degree by using an increased detection power. Again, there is a restriction on doing that, which is given by the detectors saturation threshold and its capability to eliminate classical noise contributions [195]. The latter is called common mode rejection ratio (CMRR) and depends not only on the detector electronics but also on the careful alignment of the detection optics. In order to reach an optimal CMRR the path lengths in the interferometer as well as the optical modes of the interfering beams must be perfectly matched and their powers have to be optimally balanced on the photodetectors. If the pulses and hence the measurement outcome were dominated by classical noise it would not be possible to resolve the squeezing effect on the mechanical quadratures.

In our detection setup (see section 4.2.2) we use the commercially available balanced detector from *FEMTO*[43]. All measurement data presented in this chapter were recorded using this detector. To justify its suitability for pulsed optomechanics experiments a series of characterization measurements were performed. First the linear amplitude response of the detector was verified. For that each photodetector port was illuminated with increasing power up to 640 µW (saturation limit), while the other port was blocked and the differential signal was measured. For both photodetectors a linear response up to 560 µW[44] was measured. Higher powers resulted in a relative deviation of 3.5 % from linear response (see appendix C.1).

Next the frequency response of the detector setup was measured to determine its subtraction capability. For that the signal beam was blocked and the LO was set to a fixed power of 200 µW. Using the fiber EOM the light amplitude was slightly modulated at $V_\pi/20$ over a frequency range of 500 MHz[45]. The normalized results are shown in the left panel of Fig. 4.4. The amplitude response was recorded for each detector port individually (blue traces - PD^+/PD^-), for both ports at the same time (red trace - balanced) and without illumination of the detector (grey trace - dark). In the frequency range up to 10 MHz the average CMRR is better than 45 dB and then decreases due to the increase of electrical noise by 10 dB/decade for frequencies above 100 kHz and the roll-off of the detector response. The latter is most likely caused by a decreasing (optical) intensity modulation depth from the EOM at higher frequencies, rather than a limited bandwidth of the detector[46]. Nevertheless, this could not be verified by a separate measurement.
Finally, we measured the optical noise variance on the detection light in our setup

[43] HBPR-500M-10K-SI-FS(T): DC...500 MHz, gain 2.55-5.1 kV/W, $\mathrm{NEP}_{\max}$ 60 pW/$\sqrt{\mathrm{Hz}}$ @ 500 MHz

[44] The manufacturer specifies linear response for differential powers up to 400 µW.

[45] It was verified before the measurement that the voltage modulation amplitude is constant over the whole bandwidth

[46] After consultation with the manufacturer we found that they calibrate their spectrum analyser with a reference trace, recorded by a fast (GHz bandwidth) detector, to avoid this deleterious effect during the characterization procedure.

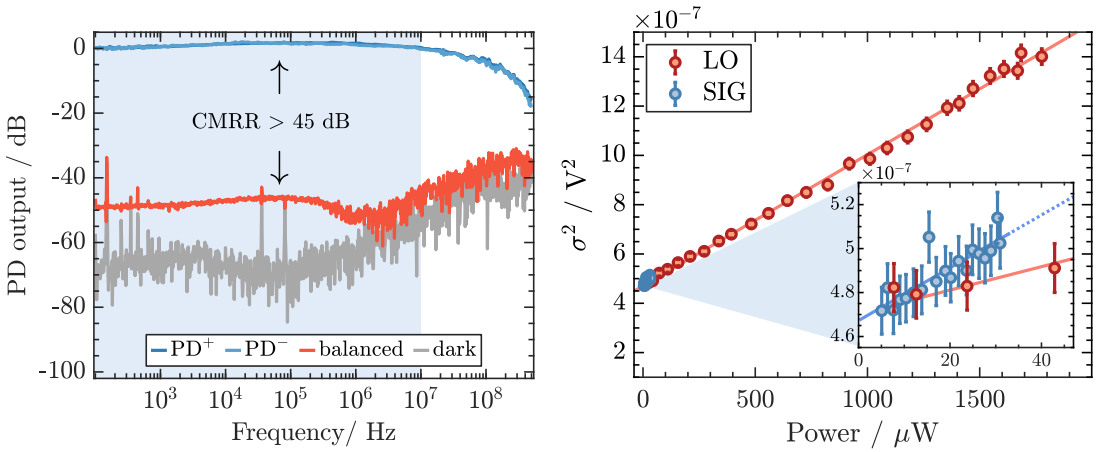

Figure 4.4: Characterization of the balanced detector setup. Left panel: Measured frequency response of the used detector. Up to 10 MHz the CMRR is better than 45 dB. For higher frequencies it decreases to a minimum value of 20 dB at 500 MHz due to the roll-off of the detector response. The average shot noise clearance is 19 dB up to 500 kHz and reduces to 6.9 dB with increasing frequency. **Right panel:** Measurement of the signal and LO noise variance for different powers at a signal/LO ratio of 1:50. The insert shows the zoomed signal data for low powers. For both, signal and LO the noise variance scales linearly in the range of applicable powers, which indicates shot noise limitation. The unequal slopes can be explained by a different setting of the input range of the data acquisition device for the signal beam measurement.

for increasing photon number. The measurement was performed with the homodyne detection in continuous and pulsed mode and in both cases yielded a linear increase of the noise variance with increasing laser power (right panel of figure 4.4). Since the photon statistics are described by a Poisson distribution the variance of the measured intensity is proportional to the mean photon number $\sigma^2 = \bar{N}$. From the observed linear behaviour we infer that the detection is shot noise limited in the range of applied powers, which are constrained by the optical losses in the setup. The stated signal and LO powers in this chapter are always measured behind PBS_3 in figure 4.6.

Temporal overlap: In our experimental setup the signal beam is coupled into an optical fiber that guides it to the optomechanical system inside the cryostat. Therefore, we have an intrinsic path length difference in our homodyne interferometer as the light travels slower through the fiber than through air. Since our homodyne detection setup was used only for continuous signals in the past the path lengths outside the cryostat were matched to ensure good spatial mode overlap. To characterize the effective path length difference in the interferometer the temporal mode overlap was measured using different pulse durations (see Fig. 4.5).
For the measurement the signal and LO beams were adjusted to be equally strong and their polarization was set with the $\lambda/2$-plate at the splitting PBS to guide only the signal or LO beam to either of the balanced photodiode ports. The resulting signal is shown in the left panel of Fig. 4.5. When the first pulse impinges on the differential photodetector it creates a spike in the signal until the second pulse arrives and their photocurrents are subtracted. The second spike is caused by the fraction of the delayed pulse that does not

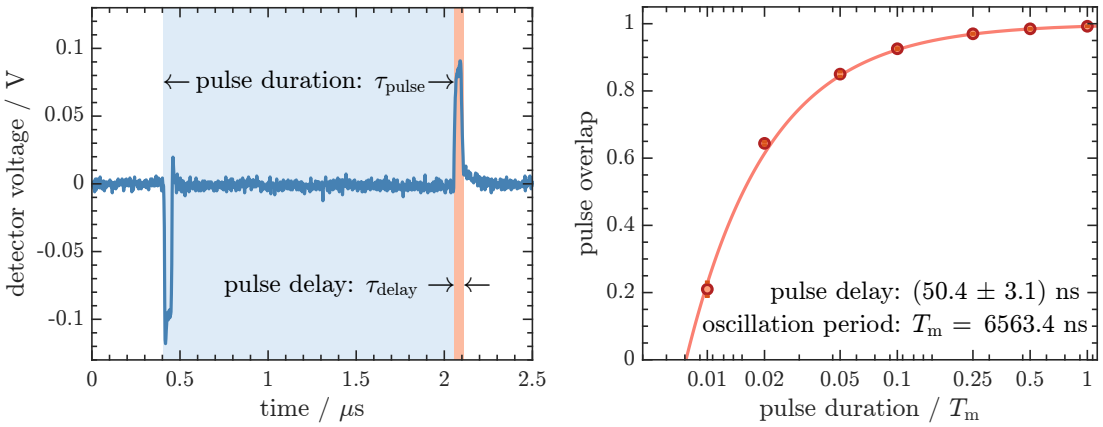

Figure 4.5: Measurement of the temporal pulse overlap. To characterize the delay between the arrival of the signal and LO pulses at the detector different pulse durations were adjusted to measure the temporal overlap. The overlap is defined as $(\tau_{\text{pulse}} - \tau_{\text{delay}})/\tau_{\text{pulse}}$. **Left panel:** Single exemplary pulse trace for $\tau_{\text{pulse}} = T_{\text{m}}/4$. The blue shaded area represents the pulse duration and the red shaded area represents the pulse delay. **Right panel:** Temporal pulse overlap versus applied pulse duration. The circles show the measured data whereas the solid line denotes the expected functional behaviour for the measured delay of $\tau_{\text{delay}} = (50.4 \pm 3.1)$ ns. Each data point is the average of 20 pulses.

arrive simultaneous with the first pulse on the photodetector. Hence, both spikes are equally wide and their width characterizes the delay τ_{delay} between the pulses caused by the effective path length difference. The blue shaded area depicts the applied pulse duration τ_{pulse}. The overlap is calculated from the ratio of the simultaneously arriving pulse fractions and the pulse duration $(\tau_{\text{pulse}} - \tau_{\text{delay}})/\tau_{\text{pulse}}$. This measurement scheme is well suited to optimize the temporal mode match by reducing the path length difference as will be described in section 4.2.2.

4.2.2 Modification of the homodyne detection setup

As mentioned earlier the transition from continuous to pulsed measurements requires some modifications in the detection setup that shall be discussed in this section. The modified setup is depicted in Fig. 4.6 and will be explained in the following.
The first major difference to the previously used detection setup (see figure 2.8) is the utilization of a fiber coupled waveguide EOM for the generation of the short pulses. The EOM is used in a hybrid continuous/pulsed mode as will be explained in section 4.2.3 and can therefore be applied to control the homodyne intensity as well. It guides the light from the laser system to the detection setup through a PM fiber. There is only one drawback to using a fiber EOM for the pulse generation and that is limited transmitted power. For our working wavelength the low damage threshold of the EOM leads to a maximally transmitted optical power of $P_{\text{trans}} \approx 5.5\,\text{mW}$ [47]. We are aware that this significantly restricts the achievable measurement strength but our focus lies first on the investigation of the applicability of the pulsed measurement scheme in our

[47] For 780 nm the specified maximum input power is 30 mW but due to an insertion loss of 5.6 dB only 7.5 mW can be transmitted. Additionally, the fiber coupling efficiency and losses due to a PM mating sleeve that is used to extend the fiber into the lower laboratory have to be regarded.

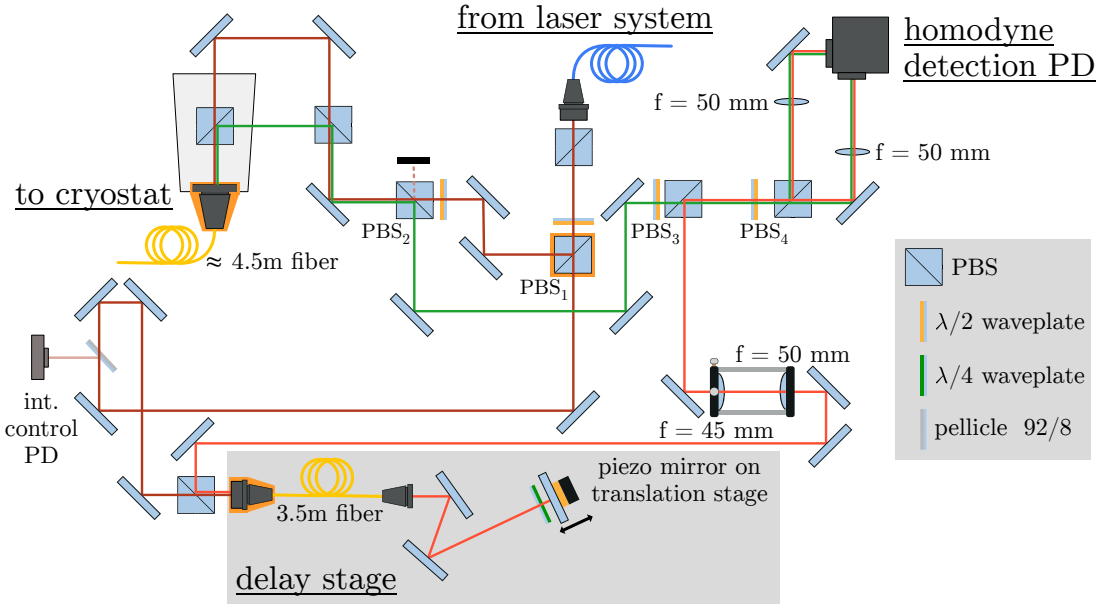

Figure 4.6: Modified homodyne setup for pulsed optomechanics. The detection light from the fiber EOM is split at PBS_1 into a signal and LO beam with an adjustable splitting ratio. Care is taken that both beams cover the same distance before they are coupled into the cryostat and the delay stage, respectively (dark red beam paths between the orange highlighted elements). A fraction of the LO beam is picked up for the intensity control of the detection light. After reflection from the MiM system and the piezo mirror the signal and LO beams are overlapped again at PBS_3 and again the green and light red beam paths are equally long. All stated signal and LO powers in this chapter are measured behind PBS_3. Finally, the polarizations of the superimposed beams are rotated by 45° and split with a 50/50 ratio at PBS_4, before being focused onto the differential detector.

system and the identification of possible pitfalls. Feasible measures to improve the measurement strength will be discussed in section 4.3.1.

Instead of a 50/50 beam splitter we now use a polarizing beam splitter (PBS_1 - shaded orange in Fig. 4.6) to be able to adjust variable splitting ratios between the signal and LO beam. The signal beam is reflected at PBS_1 and guided to the cryostat telescope where it is coupled into an SM fiber that leads the light to the MiM system. Fiber polarization controllers (FPCs) are employed to adjust the polarization of the backreflected signal beam. The LO beam is guided to to a delay stage composed of a 3.5 m long SM fiber embedded in FPCs as well and a ≈ 1.5 m free-space optical beam path. At its end the light is retroreflected from a piezo mirror that is mounted on a translation stage for fine tuning of the free space beam path. The piezo mirror is used to stabilize the phase between the signal and LO beam. To ensure optimal mode match all fiber couplers[48] used in the setup are identical and the beampaths of the dark red beams between the orange highlighted elements in Fig. 4.6 are equally long. For the delay stage we measure a round-trip efficiency of $\eta_{\text{delay}} = 63\,\%$, which could be improved in a future setup by cutting the fiber to the right length and applying a highly reflective coating to its end face.

[48] Except for the outcoupler in the delay stage as this one has nothing to do with the mode match between the signal and LO beam.

The reflected LO beam (light red) passes a beam shaping telescope that is used to optimize its waist size to match the signal beams shape and is spatially overlapped with the signal beam (green) on PBS_3. Again the beam paths of the reflected signal and LO beams are adjusted to be equally long for best spatial overlap. At PBS_4 both beams are in the same spatial mode but have perpendicular polarizations and can therefore be split exactly 50/50 by rotating their polarization by 45°. Finally, the combined beams are focused onto the photodiodes of the differential detector. Their alignment is checked before each measurement run and we observe interference visibilities of $\mathcal{V} = 95 - 99\,\%$. The delay stage is used to compensate for the path length difference introduced by the fiber that leads to the cryostat. Its length was not exactly known and had therefore to be estimated by the pulse delay measurement shown in Fig. 4.5. We decided to set up a combined fiber/free space delay stage as a purely free-space delay stage would require a path length of ∼15 m and would probably severely deteriorate the stability of the homodyne interferometer. The length of the free-space beam path can be adjusted using a similar measurement to the one shown in the left panel of Fig. 4.5. When the path length difference is consecutively reduced the spikes approach each other until they coincide and vanish completely.

4.2.3 Experimental sequence

The reconstruction of mechanical motional states requires many repeated measurements of the same, equally prepared state. Since every light pulse transfers momentum to the resonator the application of a pulse train can either lead to an excitation or damping of the mechanical motion, dependent on the timing of the pulses with respect to the mechanical oscillation period. If many pulse trains are applied in rapid succession this predominantly leads to an excitation of the mechanical motion and thus to heating. In order to provide similar starting conditions for each measurement one can either wait until the excitation has subsided or actively drive the resonator into the same initial state by active feedback cooling. Due to the high Q-factor of our resonator its damping rate on the order of a few mHz would require minutes of waiting between the measurements. Therefore, we decided to apply moderate feedback to deterministically prepare the initial state, prior to the pulsed measurement.
Another important aspect is the phase sensitive readout of the homodyne signal. The mechanical motion is encoded in the phase quadrature of the reflected light from the cavity and thus it is necessary to set the LO phase to $\phi_{\mathrm{lo}} = \pm\pi/2$. This results in a fluctuation of the differential homodyne signal around zero according to equation (2.13). During the experiment cycle we operate the homodyne detection in a hybrid continuous and pulsed manner. In order to apply feedback cooling the resonator displacement has to be tracked the whole time and the LO phase needs to be stabilized. During the a pulse train the detection light is switched off for a short period of time, between the pulses and subsequently switched on again. This is achieved by regulating the homodyne intensity with the EOM to a constant value at all times, except during the pulse train. Consequently, for the duration of a pulse train we must rely on the passive phase stability of the system. The measurement procedure can be understood by looking at figure 4.7, which illustrates the important time scales of the sequence.
The experiment is performed at a measurement rate of 800 mHz, which allows to record

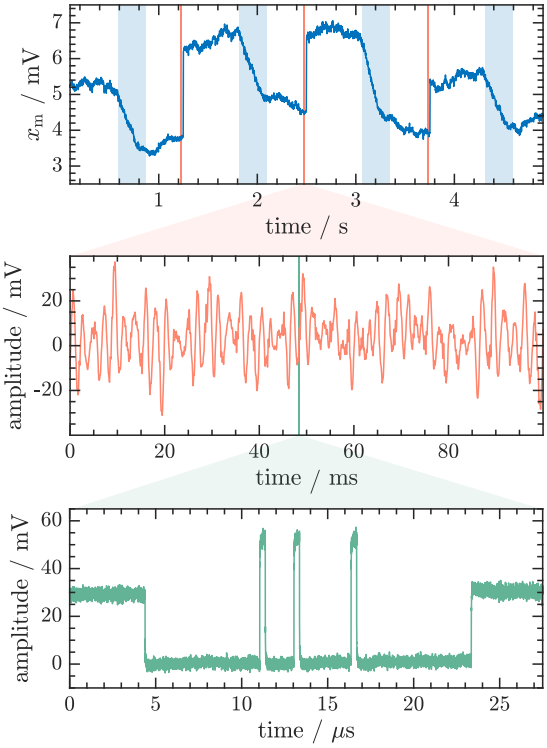

Figure 4.7: Dissection of time scales in the pulsed experiment protocol. Top panel: Zero-span measurement of the homodyne signal phase quadrature demodulated at the resonator frequency $\omega_m/(2\pi) = 152.3646\,\mathrm{kHz}$ with a demodulator bandwidth $B_d = 1.5\,\mathrm{kHz}$. The amplitude is directly proportional to the resonator displacement and shows its time evolution during a pulsed experiment sequence. The blue and red shaded areas denote the application of feedback cooling and measurement pulse trains, respectively. The measurement rate is 800 mHz. **Central panel:** Time trace of the phase-locked homodyne signal for an off-resonant cavity setting. The pulsed measurement is triggered on a zero-crossing of the phase-lock signal to measure at the most phase sensitive point. **Lower panel:** Exemplary pulse train recorded for an off-resonant cavity setting and the phase-lock slightly offset from zero.

the required statistics in relatively short time and enables reproducible initial state preparation. The top panel of figure 4.7 shows an exemplary section of the demodulated homodyne signal that represents the time evolution of the resonator displacement. The blue shaded areas show intervals of $\tau_{fb} = 250\,\mathrm{ms}$ duration (20 % duty cycle), where feedback cooling is applied. Subsequently, the resonator evolves freely for $\tau_{th} = 400\,\mathrm{ms}$ before a pulse train is applied (red shaded areas). After the pulse train another free evolution period of $\tau_{th} = 600\,\mathrm{ms}$ duration follows and then the cycle is repeated.
In order to ensure best phase sensitivity during the pulsed measurement the AWG, which generates the pulse train, is triggered on a zero-crossing of the phase-locked homodyne signal as depicted in the central panel of figure 4.7. The displayed homodyne signal carries low frequency noise with dominant contributions at 50 Hz, 150 Hz and 450 Hz[49] and has a noise amplitude of $V_{noise}^{rms} = 11.3\,\mathrm{mV}$. Thus, randomly timed pulse train application would result in larger scattering of the measurement outcomes. The transition from the continuous to the pulsed measurement can be seen in the bottom panel of figure 4.7. The trace shows a pulse train that was recorded for an off-resonant cavity setting, where the light does not carry any mechanical quadrature information. The LO phase is adjusted to deviate slightly from $\phi_{lo} = \pi/2$ on purpose. We use such traces for the pulse position localization in the data evaluation and therefore term them *calibration traces*. Furthermore, one can clearly identify the transition from the continuous measurement to the pulsed measurement. In continuous operation the intensity is regulated by operating the fiber EOM at the 50 % working point as described for the feedback beam in section 2.2. During the pulse train the EOM is switched between no

[49] Our detector is power supplied with batteries to avoid electrical noise contributions from the line voltage and electrically isolated from the optical table but still we see noise at multiples of 50 Hz, whose source is not identified yet.

transmission and full transmission to produce the pulses. Therefore, the pulse levels exceed the voltage level prior to and after the pulse train. The pulse trains are recorded with a sampling rate of 450 MSa/s and 12 bit vertical resolution using the digitizer functionality of our lock-in amplifier.

4.3 First experimental results

The results presented in this section show the feasibility of pulsed preparation and measurement of conditional mechanical states in our system. The experiment was performed at cryogenic temperatures of $T_{\mathrm{MiM}} = 10\,\mathrm{K}$ measured in proximity of the MiM system. The determined homodyne calibration was presented in section 2.2.2 and yields $\partial\phi_{\mathrm{x}}/\partial x_{\mathrm{m}} = (0.56 \pm 0.01)\,\mathrm{rad/nm}$. For the characteristic parameters of the resonator measured at this temperature refer to table 2.1.

When choosing the pulse length one has to make a trade-off regarding the used photon number. On the one hand, the best possible measurement strength is needed, which scales with the total number of photons (see equation (4.7)). On the other hand the pulses have to be short compared to the mechanical oscillation period, which limits the amount of photons per pulse. Therefore, we decided to use pulses of $\tau_{\mathrm{pulse}} = 325\,\mathrm{ns}$ duration, which corresponds to a fraction of the oscillation period of $T_{\mathrm{m}}/20$ and is comparable to the ratio between pulse length and oscillation period used in [186]. For the data presented here we use a ratio between the signal and LO power of 1/50 at a maximum LO power of $P_{\mathrm{lo}}^{\mathrm{cw}} = 1.5\,\mathrm{mW}$. The mechanical conditional state is prepared using two preparation pulses $P_{\mathrm{L}}^{(1)}$ and $P_{\mathrm{L}}^{(2)}$ separated by a quarter mechanical oscillation period $T_{\mathrm{m}}/4 = \pi/2$ and is subsequently measured with a third tomography pulse $P_{\mathrm{L}}^{(3)}$. For the tomography we record 10 marginal distributions separated by $\theta_{\mathrm{t}} = 0.1\,\pi$. Each marginal distribution is obtained by constructing a histogram from the measurement outcomes of 600 recorded pulse trains. As described in section 4.1.2 we can calculate the conditional state from the measurement outcomes by making the assignments $X_{\mathrm{M}} \rightarrow P_{\mathrm{L}}^{(1)}$ and $P_{\mathrm{M}} \rightarrow P_{\mathrm{L}}^{(2)}$ and hence obtain

$$C(\theta_{\mathrm{t}}) = P_{\mathrm{L}}^{(3)} - P_{\mathrm{L}}^{(2)}\cos(\theta_{\mathrm{t}}) + P_{\mathrm{L}}^{(1)}\sin(\theta_{\mathrm{t}}). \tag{4.15}$$

Phase noise elimination

In order to conveniently extract the mechanical information from the signal we have to process the data before final evaluation. This means that we have to separate the phase information that was imprinted on the light by a displacement of the resonator from the residual phase fluctuations, which appear on the detection light. Figure 4.8 illustrates the procedure.

In contrast to the pulse train depicted in figure 4.7 the pulse train in the top panel of figure 4.8 is applied on resonance with the cavity and for $\phi_{\mathrm{lo}} = \pi/2$. Ideally, the resulting signal should resemble a flat line with three pulses differing from zero by an amount proportional to the photon shot noise and the phase shift induced by the interaction with the resonator. Since we know that the pulses sample the harmonic oscillation of the resonator we fit the averaged pulse amplitudes with a sine at the

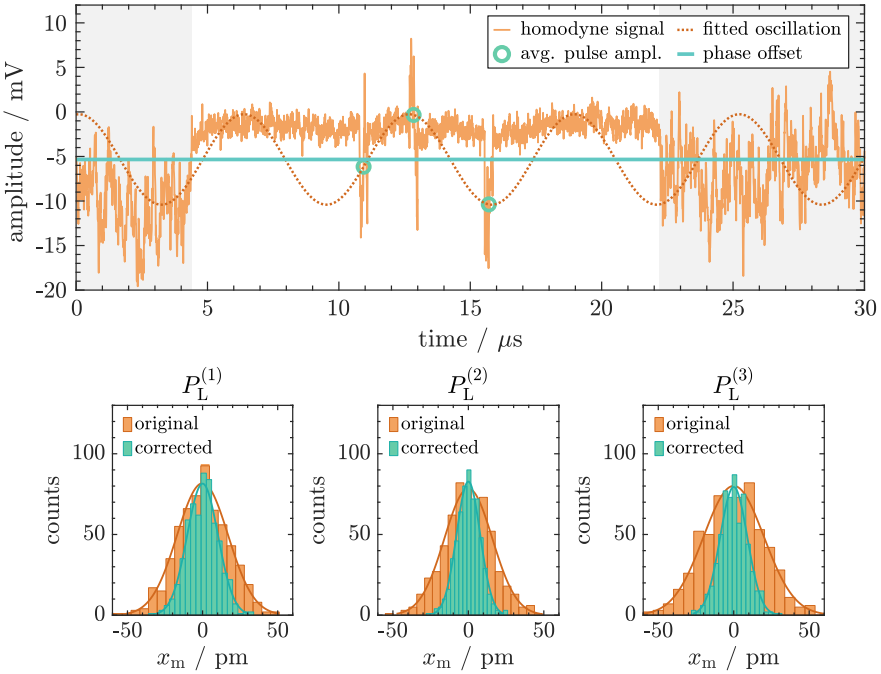

Figure 4.8: Residual phase noise subtraction scheme. Top panel: Exemplary pulse train for a resonant cavity setting during a pulsed measurement at $\theta_t = 0.9\,\pi$. Despite triggering on a zero-crossing of the phase-lock signal we observe disruptive phase noise on the signal that leads to an offset of the mechanical motion induced phase information. We fit a sine at the resonator frequency to the measured pulse levels with the amplitude, phase and offset as free fit parameters. The fitted offset is subtracted from the pulse levels to cancel the effect of the parasitic phase noise. **Lower panel:** Exemplary histograms for the measurement outcomes of the first, second and third pulse at $\theta_t = 0.9\,\pi$, showing how the phase noise broadens the pulse level distribution. The pulse levels are converted into resonator displacement using the homodyne calibration.

resonator frequency and the amplitude, phase and offset as free fit parameters. By subtracting the fitted offset from all pulse amplitudes we can eliminate the effect of the phase fluctuations and recover the undistorted phase information encoded in the pulse amplitudes, as their relative distances remain unchanged.

Pulse trains that probe the resonator in a more excited state exhibit clearly visible oscillations in the grey shaded regions whose amplitude and phase match the fitted sine curve very well and hence confirm the applicability of the fit (see appendix C.1). Note however, that this scheme works only well for tomography pulses in a distance of approximately one mechanical period from the second preparation pulse. For larger pulse separations the amplitudes can not be unambiguously fitted any more. The lower panel of figure 4.8 shows the effect of the phase noise elimination on the measurement outcomes of the first, second and third pulse for one exemplary tomography angle $\theta_t = 0.9\,\pi$. The average pulse amplitude is converted into a resonator displacement using our homodyne calibration.

Mechanical state reconstruction

Using the processed measurement outcomes the mechanical state can be reconstructed. First, by only regarding the first pulse $P_{\mathrm{L}}^{(1)}$ of each pulse train it is possible to map out the initial thermal state of the resonator. Since every pulse represents a measurement the first pulse samples the random thermal distribution prior to the interaction. Thus, comparing the measurement outcomes of the first pulse for all tomography angles should yield equally wide Gaussian distributions. A subset of histograms (blue) for various tomography angles is shown in figure 4.9. Indeed, we recover similarly broad normal distributions for the measurement outcomes of the first pulse at every tomography angle with a mean width of $\bar{\sigma}_{\mathrm{th}} = (11.01 \pm 1.57)\,\mathrm{pm} = (2568 \pm 367)\,x_{\mathrm{zpf}}$.

In contrast to the thermal state, the width of the conditional state (red) changes with the tomography angle and is strongly squeezed at $\theta_{\mathrm{t}} = \pi$, exactly as it is expected. Recalling the scheme presented in figure 4.2 the second pulse $P_{\mathrm{L}}^{(2)}$ produces a „double" squeezed state that is narrower in the X_{M} quadrature than in P_{M}. A measurement after free evolution of $\theta_{\mathrm{t}} = \pi$ results in a repeated probing of the X_{M} quadrature and hence should reproduce the semi-minor axis of the ellipse. Similarly, a measurement after $\theta_{\mathrm{t}} = \pi/2$ corresponds to probing of P_{M} and therefore samples the semi-major axis of the ellipse. For the conditional state we measure a minimum width of $\sigma_{\mathrm{cond}}^{(\theta_{\mathrm{t}}=\pi)} = (137 \pm 4)\,\mathrm{fm} = (32 \pm 0.9)\,x_{\mathrm{zpf}}$, which corresponds to 38 dB of thermal noise

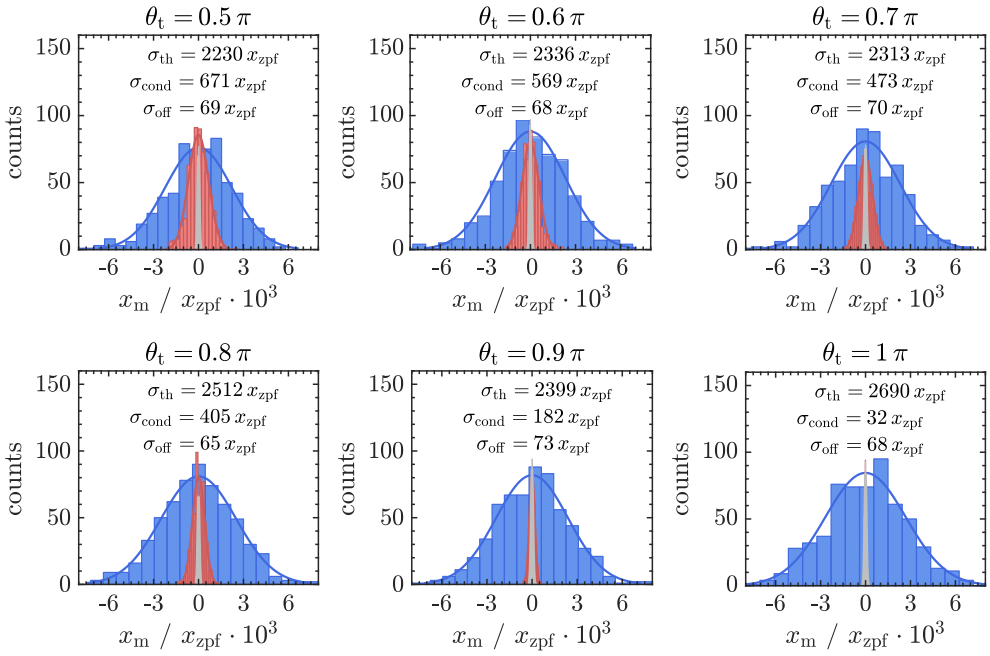

Figure 4.9: Measured marginal distributions for different tomography angles. The subset of histograms show the width of the thermal state (blue) corresponding to the measurement outcomes of the first pulse, the width of the conditionally prepared state (red) calculated from the measurement outcomes of all three pulses according to equation (4.15) and the width of the off-resonant measurement outcome distribution (grey). The corresponding widths for each tomography angle are specified above the respective histograms and are scaled in units of the resonator zero point motion $x_{\mathrm{zpf}} = 4.28\,\mathrm{fm}$.

squeezing in the position variance [81].

To reconstruct the phase-space distribution of the mechanical state an inverse Radon transformation[50] is performed on the measured mechanical marginals for all tomography angles θ_t. If the marginals are treated as projections of the phase-space distribution, the inverse Radon transformation can be regarded as a back-projection of the marginal distributions that restores the original phase-space distribution. The resulting reconstructed phase-space distributions are shown in figure 4.10. From the widths of the thermal and conditional state the effective temperature of the states can be determined according to equation (4.10):

$$T_\mathrm{eff}^\mathrm{th} = \frac{m_\mathrm{eff}\omega_\mathrm{m}^2\bar{\sigma}_\mathrm{th}^2}{k_\mathrm{B}} \quad \text{and} \quad T_\mathrm{eff}^\mathrm{cond} = \frac{m_\mathrm{eff}\omega_\mathrm{m}^2\sigma_\mathrm{cond}^{(\theta_\mathrm{t}=0)}\sigma_\mathrm{cond}^{(\theta_\mathrm{t}=\pi/2)}}{k_\mathrm{B}}. \tag{4.16}$$

The results show that the pulsed preparation and measurement scheme can be successfully applied in our setup and that we are able to detect squeezed conditional states of mechanical motion. However, there is a lot of room for improvement. In order to specify the requirements to resolve the mechanical zero-point motion we need to con-

[50] We use the MATLAB function `iradon` for the transformation and feed it with a kernel distribution fit of the histograms to reproduce their shape.

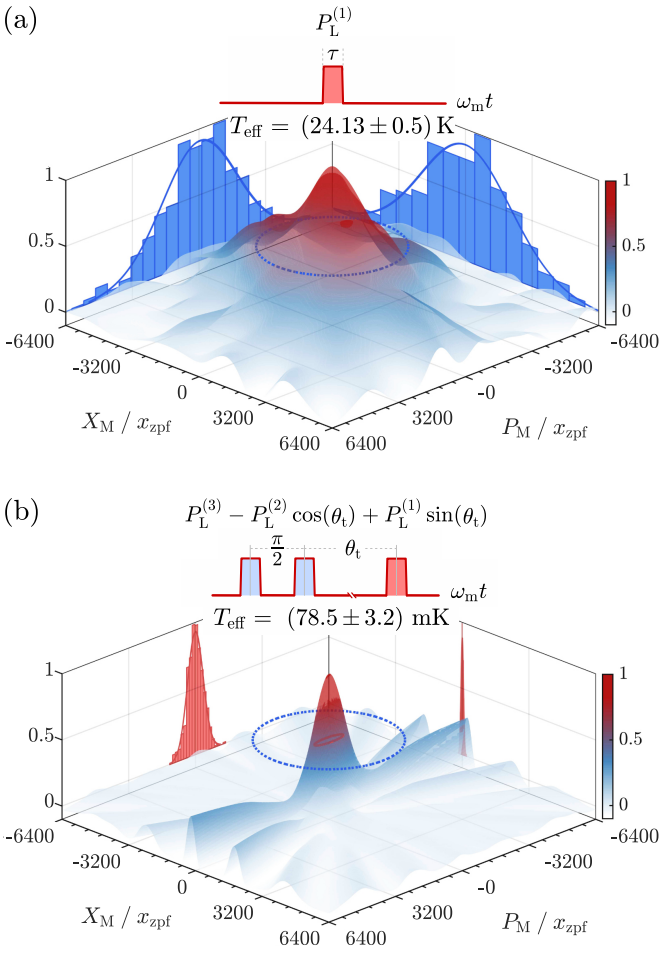

Figure 4.10: Preparation and state reconstruction of mechanical motion using pulsed measurement scheme. Pulse protocols (blue - preparation, red - tomography) and reconstructed phase-space distributions from the measured mechanical marginals. **(a):** Reconstruction of the initial thermal state driven by thermal noise. The blue dashed circle with radius σ denotes the width of the initial thermal state. **(b):** Reconstruction of the conditionally prepared mechanical state. Clearly a reduction of the state width as well as squeezing in the X_M quadrature is visible (indicated by the red ellipse). Both phase-space distributions are normalized for better visualization. The effective temperatures are calculated according to equation (4.16).

textualize the obtained results in terms of the measurement strength. To determine the measurement strength experimentally we need to measure the optical phase distribution without the contribution of mechanical position fluctuations. This can be done by applying identical pulses away from the cavity resonance and evaluating the distribution of the average pulse amplitudes again. The only difference is that we have to account for the higher reflectivity of the cavity away from resonance. We do this by reducing the signal power by the amount that corresponds to the cavity reflectivity on resonance. Also for the off-resonant data we have to eliminate the contribution from the fluctuating phase, which we do by subtraction of the mean of the pulse amplitudes. By this we cancel the random offset that is equal for all three pulses without affecting the relative scattering of the amplitudes within each pulse train. Exemplary histograms (grey) are depicted in figure 4.9 together with the marginals for the thermal and conditional state. Considering all off-resonantly measured distributions we obtain a mean width of $\bar{\sigma}_{\mathrm{off}} = (269.6 \pm 12.8)\,\mathrm{fm} = (63 \pm 3)\,x_{\mathrm{zpf}}$. Using this result we retrieve the measurement strength via equation (4.14b)

$$\chi \simeq \frac{1}{\sqrt{2}\sigma} = 0.011. \tag{4.17}$$

Hence, with the current measurement setup we achieve a measurement strength that is a factor of 7 lower than the one published by J. Muhonen *et al.* [186].

4.3.1 Conclusion

We have demonstrated the application of a pulsed preparation and measurement technique that allows to measure a single mechanical quadrature with a precision below the standard quantum limit in a first experiment with our setup. Although, we do not reach this precision yet we observe a significant reduction of the conditional state variance compared to the initial thermal state of the mechanical resonator. This is the first step towards the conditional preparation of non-classical states of mechanical motion at our experiment.

In order to achieve this, we have to increase the measurement strength $\chi = 8g_0\sqrt{\eta\bar{N}_p}/\kappa$, which is currently in progress. We are preparing for an exchange of the fiber cavity for another one with a higher finesse. At present, we have fiber cavities with a ten times higher finesse and a reflectivity on resonance of $\sigma_{\mathrm{ref}} = 0.83$ available[51]. Also, we are conferring with other manufacturers about achievable coating specifications to evaluate possible plano-concave cavity configurations with an even higher finesse. An increased finesse would lead to a reduction of the cavity linewidth and thus enhance the measurement strength. With the available cavities we could already improve the measurement strength by a factor of 10 without changing any other parameters.

A significant limitation of our current proof-of-principle setup are the optical losses in the LO delay branch, which we will have to eliminate. Furthermore, the available optical power in the signal beam will have to be increased by a factor of ∼100. A possible solution to achieve this is to use a pulsed signal beam and interfere it with a continuous LO. In this way all the transmitted power from the fiber EOM can be used for the probe

[51] They were in-house produced by C. F. Klein [196] and coated by *LASEROPTIK*

pulses which should suffice to reach $\chi \approx 1$. Furthermore, the detection efficiency can be improved by identification and elimination of the present electrical noise sources. For example the use of a line trigger can help to reduce the low frequency noise at 50 Hz and multiples thereof by synchronization of the experiment with the mains frequency. Another deleterious effect that adds to the phase noise is the excitation of the second symmetric mode s2 at $\omega_{\mathrm{m}}^{(\mathrm{s2})}/(2\pi) = 531.665\,\mathrm{kHz}$ (see figure 2.12) of the resonator, which we occasionally observe on the pulse trains (shown in figure C.1). Its occurrence will have to be studied more systematically and its effect could be omitted by data post-selection or the application of a Kalman filter [197, 198], which is a powerful tool for optimal state estimation.
An alternative, but related approach was proposed in [199] and relies on the study of conditional dynamics driven by stroboscopic pulse trains of equidistant pulses. These can realize conditional squeezing and quantum state preparation in a similar manner to the method with only few pulses, but in contrast alleviate the demanding requirement of a single pulse measurement strength of $\chi = 1$. The authors derive a condition for achieving ground state resolution with stroboscopic driving that depends on the mechanical Q-factor and the occupation of the thermal bath

$$\chi_{\mathrm{strobo}} > \sqrt{2\pi(\bar{n} + 1/2)/Q}. \tag{4.18}$$

At cryogenic conditions, assuming a bath temperature of $T_{\mathrm{bath}} = 5\,\mathrm{K}$ that is realistically achievable in our system and the measured Q-factor of $Q = 8.9 \cdot 10^7$ a measurement strength of $\chi_{\mathrm{strobo}} = 0.22$ would suffice for quantum state preparation.
In this respect, we are confident that the aforementioned actions will enable us to further increase our measurement strength and to observe non-classical mechanical states in the near future.

Appendix A

Atom-light interaction

A.1 Derivation of the atom-light coupling constants

Starting from equation (2.62) in chapter 2 the atom light coupling constants G_0, G_1 and G_2 shall be derived:

$$\hat{H}_I = \hat{S}_0\hat{A}_0 + \hat{S}_1\hat{A}_1 + \hat{S}_2\hat{A}_2 + \hat{S}_3\hat{A}_3 \tag{A.1}$$

with the operators $\hat{A}_k$ representing the atomic observables

$$\hat{A}_0 = g\left(\frac{2}{3}\alpha^{(0)}\hat{\mathbb{I}}_F + \alpha^{(2)}\left(\sum_{\mathrm{i}}^{N_{\mathrm{at}}}\hat{f}_z^{(\mathrm{i})} - \frac{1}{3}F(F+1)\hat{\mathbb{I}}_F\right)\right), \tag{A.2}$$

$$\hat{A}_1 = g\alpha^{(2)}\sum_{\mathrm{i}}^{N_{\mathrm{at}}}\left(\hat{f}_x^{(\mathrm{i})}\hat{f}_x^{(\mathrm{i})} - \hat{f}_y^{(\mathrm{i})}\hat{f}_y^{(\mathrm{i})}\right), \tag{A.3}$$

$$\hat{A}_2 = g\alpha^{(2)}\sum_{\mathrm{i}}^{N_{\mathrm{at}}}\left(f_x^{(\mathrm{i})}f_y^{(\mathrm{i})} + f_y^{(\mathrm{i})}f_x^{(\mathrm{i})}\right), \tag{A.4}$$

$$\hat{A}_3 = g\alpha^{(1)}\sum_{\mathrm{i}}^{N_{\mathrm{at}}}\hat{f}_z^{(\mathrm{i})}. \tag{A.5}$$

Using $\hat{F}_{\mathrm{k}} \equiv \sum_{\mathrm{i}}^{N_{\mathrm{at}}}\hat{f}_{\mathrm{k}}^{(\mathrm{i})}$ equation (A.1) can be recast in a from that represents the dependence on the atomic polarizabilities $\alpha^{(0)}$, $\alpha^{(1)}$ and $\alpha^{(3)}$

$$\begin{aligned}
\hat{H}_I^{(0)} &= \frac{2}{3}g\alpha^{(0)}\hat{S}_0\hat{\mathbb{I}}_F \\
\hat{H}_I^{(1)} &= g\alpha^{(1)}\hat{S}_3\hat{F}_z \\
\hat{H}_I^{(2)} &= g\alpha^{(2)}\left[\hat{S}_0\left(\hat{F}_z^2 - \frac{1}{3}F(F+1)\hat{\mathbb{I}}_F\right) + \hat{S}_1\left(\hat{F}_x^2 - \hat{F}_y^2\right) + \hat{S}_2\left(\hat{F}_x\hat{F}_y + \hat{F}_y\hat{F}_x\right)\right]
\end{aligned} \tag{A.6}$$

with

$$g = \frac{\omega_L}{2\epsilon_0 V} = \frac{\pi}{\epsilon_0\lambda}\frac{1}{A\tau} \quad \text{where} \quad V = A\tau c \tag{A.7}$$

The rank-0, rank-1 and rank-2 components of the polarizability tensor $\hat{\boldsymbol{\alpha}}$ are given by [142]

$$\alpha^{(0)} = (-1)^{(2F)} \sum_{F'} \alpha_F^{F'} \left((2F-1)\delta_{F-1}^{F'} + (2F+1)\delta_F^{F'} + (2F+3)\delta_{F+1}^{F'} \right) \tag{A.8}$$

$$\alpha^{(1)} = (-1)^{(2F)} \sum_{F'} \alpha_F^{F'} \left(-\frac{2F-1}{F}\delta_{F-1}^{F'} - \frac{2F+1}{F(F+1)}\delta_F^{F'} + \frac{2F+3}{F+1}\delta_{F+1}^{F'} \right) \tag{A.9}$$

$$\alpha^{(2)} = (-1)^{(2F)} \sum_{F'} \alpha_F^{F'} \left(\frac{1}{F}\delta_{F-1}^{F'} - \frac{2F+1}{F(F+1)}\delta_F^{F'} + \frac{1}{F+1}\delta_{F+1}^{F'} \right) \tag{A.10}$$

with the Kronecker-delta

$$\delta_i^j = \begin{cases} 1, & \text{if } i = j, \\ 0, & \text{if } i \neq j \end{cases} \quad \text{and} \quad \alpha_F^{F'} = \alpha_0 \mathcal{D}_{F,F'} (-1)^{J+J'+2I} (2J'+1) \begin{Bmatrix} J' & F' & I \\ F & J & 1 \end{Bmatrix}^2 \tag{A.11}$$

where

$$\alpha_0 = \frac{3\epsilon_0 \hbar \Gamma \lambda^3}{8\pi^2} \quad \text{and} \quad \mathcal{D}_{F,F'} = \frac{\Delta_{F,F'}}{\Delta_{F,F'}^2 + \Gamma^2/4}. \tag{A.12}$$

Setting the nuclear spin $I = 3/2$, $J = 1/2$, $J' = 3/2$ and $F = 2$ we get and hence A.8

F'	$\begin{Bmatrix} 3/2 & F' & 3/2 \\ 2 & 1/2 & 1 \end{Bmatrix}$	$\alpha_2^{F'}$
0	0	0
1	$\frac{1}{2}\sqrt{\frac{1}{30}}$	$-\frac{1}{30}\alpha_0 \mathcal{D}_{2,1}$
2	$-\frac{1}{2}\sqrt{\frac{1}{10}}$	$-\frac{1}{10}\alpha_0 \mathcal{D}_{2,2}$
3	$\frac{1}{2}\sqrt{\frac{1}{5}}$	$-\frac{1}{5}\alpha_0 \mathcal{D}_{2,3}$

become

$$\alpha^{(0)} = \alpha_0 \left(-\frac{1}{10}\mathcal{D}_{2,1} - \frac{1}{2}\mathcal{D}_{2,2} - \frac{7}{5}\mathcal{D}_{2,3} \right) \tag{A.13}$$

$$\alpha^{(1)} = \alpha_0 \left(\frac{1}{20}\mathcal{D}_{2,1} + \frac{1}{12}\mathcal{D}_{2,2} - \frac{7}{15}\mathcal{D}_{2,3} \right) \tag{A.14}$$

$$\alpha^{(2)} = \alpha_0 \left(-\frac{1}{60}\mathcal{D}_{2,1} + \frac{1}{12}\mathcal{D}_{2,2} - \frac{1}{15}\mathcal{D}_{2,3} \right). \tag{A.15}$$

Inserting equations (A.12) and (A.7) into (A.6) we obtain

$$\hat{H}_I^{(0)} = \frac{\hbar}{\tau} \underbrace{\frac{\Gamma\lambda^2}{40\pi A} \left(-\mathcal{D}_{2,1} - 5\mathcal{D}_{2,2} - 14\mathcal{D}_{2,3} \right)}_{:= G_0} \hat{S}_0 \hat{\mathbb{I}}_F \tag{A.16}$$

$$\hat{H}_I^{(1)} = \frac{\hbar}{\tau} \underbrace{\frac{\Gamma\lambda^2}{160\pi A}\left(3\mathcal{D}_{2,1} + 5\mathcal{D}_{2,2} - 28\mathcal{D}_{2,3}\right)}_{:= G_1} \hat{S}_3 \hat{F}_z \tag{A.17}$$

$$\hat{H}_I^{(2)} = \frac{\hbar}{\tau} \underbrace{\frac{\Gamma\lambda^2}{160\pi A}\left(-\mathcal{D}_{1,2} + 5\mathcal{D}_{2,2} - 4\mathcal{D}_{2,3}\right)}_{:= G_2} \cdot [\dots] \tag{A.18}$$

with

$$[\dots] = \left[\hat{S}_0\left(\hat{F}_z^2 - \frac{1}{3}F(F+1)\hat{\mathbb{I}}_F\right) + \hat{S}_1\left(\hat{F}_x^2 - \hat{F}_y^2\right) + \hat{S}_2\left(\hat{F}_x\hat{F}_y + \hat{F}_y\hat{F}_x\right)\right] \tag{A.19}$$

A.2 Larmor-precession data

For completeness all traces that were evaluated for the insert in figure 2.26 are presented here. In some traces we note a collapse and revival of the oscillation envelope that might be caused by the non-adiabatic magnetic field switching. However, its origin was not further investigated.

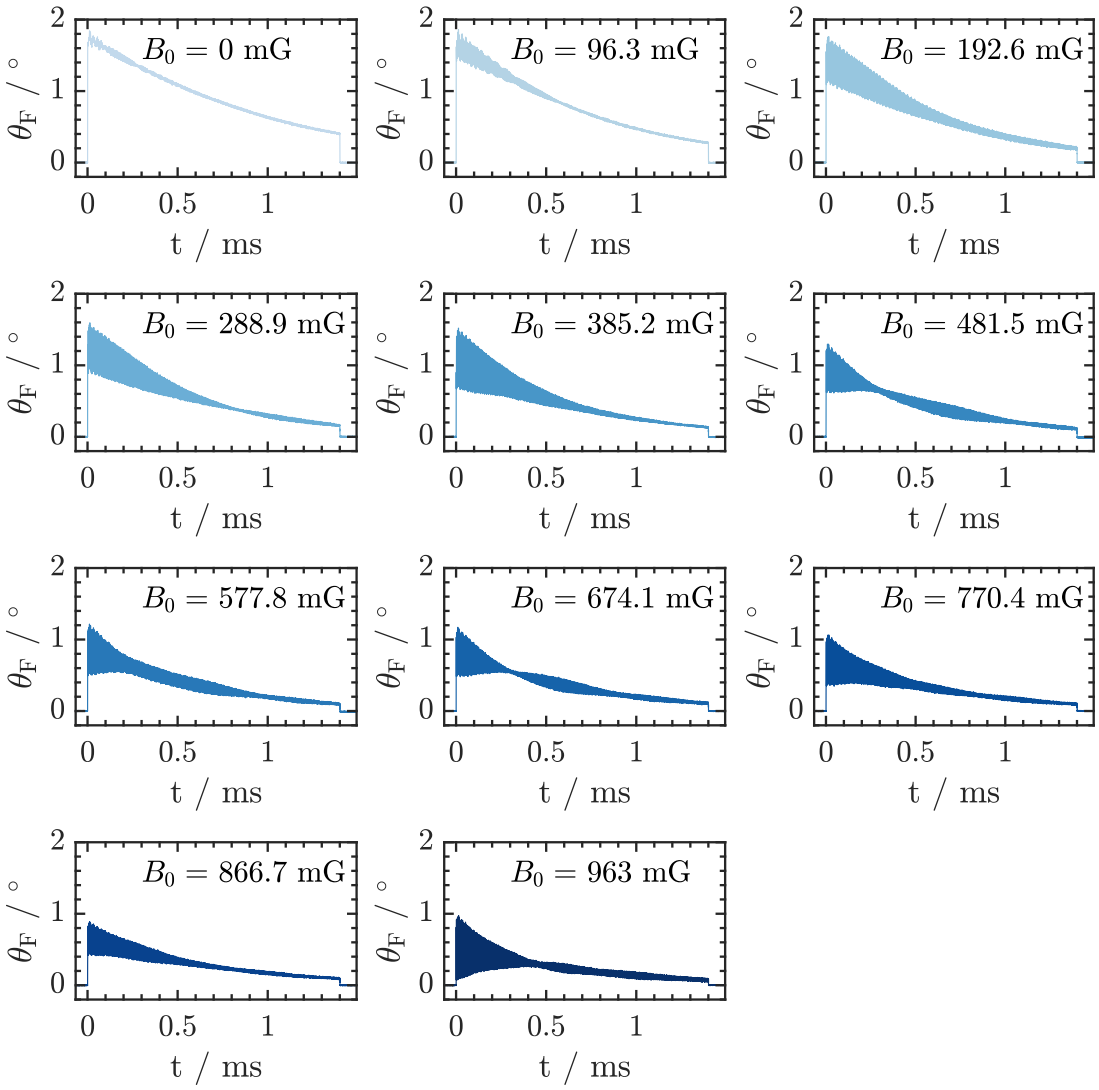

Figure A.1: Larmor-precession traces.

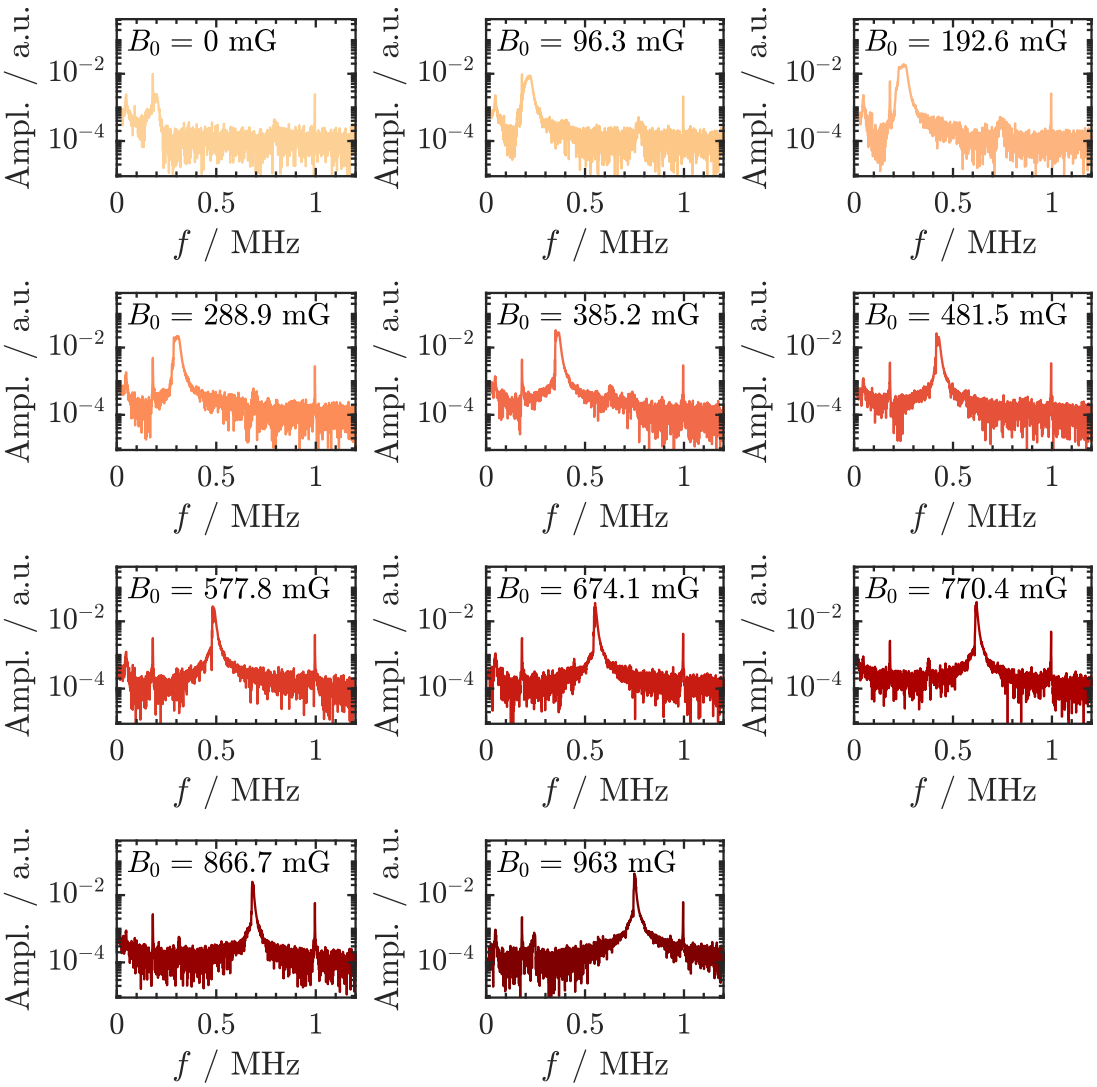

Figure A.2: Fourier transforms of the Larmor-precession traces. To evaluate the magnetic field dependence of the Larmor-frequency f_L the traces in figure A.2 were Fourier transformed and the resulting frequency spectra are depicted here. There are two magnetic field independent features in each spectrum, one at $f_1 = 182\,\mathrm{kHz}$ and the other at $f_2 = 1\,\mathrm{MHz}$. f_1 is the second harmonic of the etalon dithering frequency inside the TiSa laser cavity, which is used to stabilize the laser frequency, and should in normal operation be suppressed by a noise eater circuit. Yet, at the time of the Larmor-precession measurement this part of the Laser was not functional, which led to frequency components of 91 kHz and 182 kHz on the TiSa light. f_2 originates from the sampling rate of the oscilloscope in the measurement and is only an artefact.

Appendix B

Coupling lattice

B.1 Coupling lattice losses

The most relevant losses in the coupling lattice setup presented in figure 3.11 are depicted here in figure B.1. T_1 is the transmittance of the pellicle that we use for the alignment of the auxiliary beam with respect to the back-reflected beam and T_2 is the transmittance of the substrate S1, which is used for the intensity control of the lattice and to monitor the back-reflected beam from the cavity. T_3 is the total transmittance of the glass cell but for the daily power balancing in the experiment we use the more relevant single surface transmittance $\sqrt{T_3} \approx 0.95$ to calculate the power at the site of the atoms.

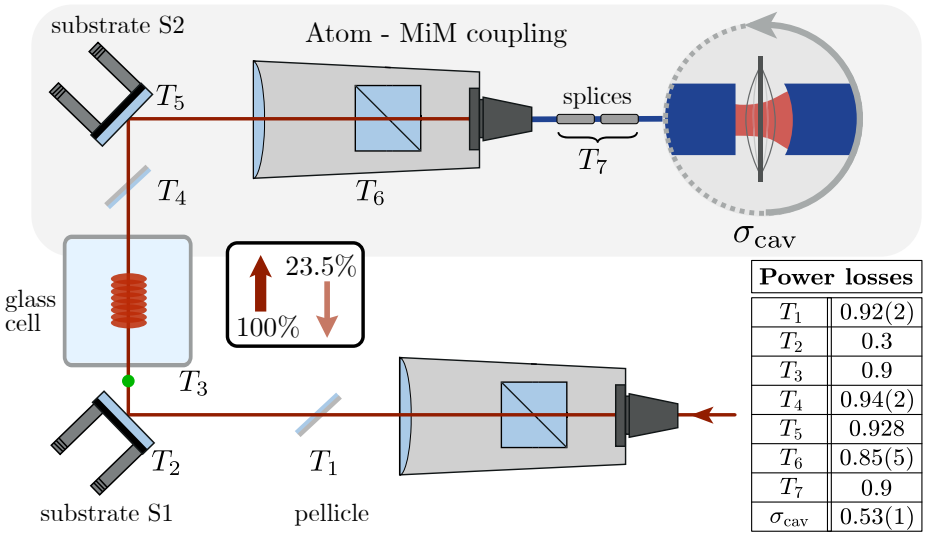

Power losses	
T_1	0.92(2)
T_2	0.3
T_3	0.9
T_4	0.94(2)
T_5	0.928
T_6	0.85(5)
T_7	0.9
σ_{cav}	0.53(1)

Figure B.1: Optical losses of the coupling lattice beam. Sketch of the most relevant optical losses measured in the coupling lattice setup depicted in figure 3.11. For a lattice incident power of 100 % at the site of the atoms approximately 23.5 % of the light is reflected from the MiM device (cavity on resonance). The exact value varies from day to day and depends on the alignment of the individual components. The measured power transmittances of each element are given in the table. For the elements where the losses have a strong dependency on the alignment the typical error margin is stated. For the atom-MiM coupling only the transmittances in the grey shaded area are relevant.

In practice we measure the power of the incident and auxiliary beam directly in front of the glass cell (at the position of the green dot after S1) and calculate the power at the position of the atoms using $\sqrt{T_3}$. The power of the back-reflected beam is measured behind substrate S1 and its amount at the atomic site is calculated using $\sqrt{T_3}$ and T_2. T_4 is the transmittance of the second pellicle and T_5 is the transmittance of substrate S2, which we use for the superposition of the auxiliary beam with the back-reflected beam. T_6 includes the fiber coupling losses and T_7 are the losses on a single pass through the fiber splices. The reflectivity of the cavity on resonance is denoted by σ_{cav} and its value for the off-resonant cavity corresponds to the reflectivity of the coating on the cavity incident fiber $\sigma_{\mathrm{cav,off}} = 0.92$.

B.2 Further simulation results

As described in section 3.3.2 a few additional results of the numerical simulation shall be presented here.

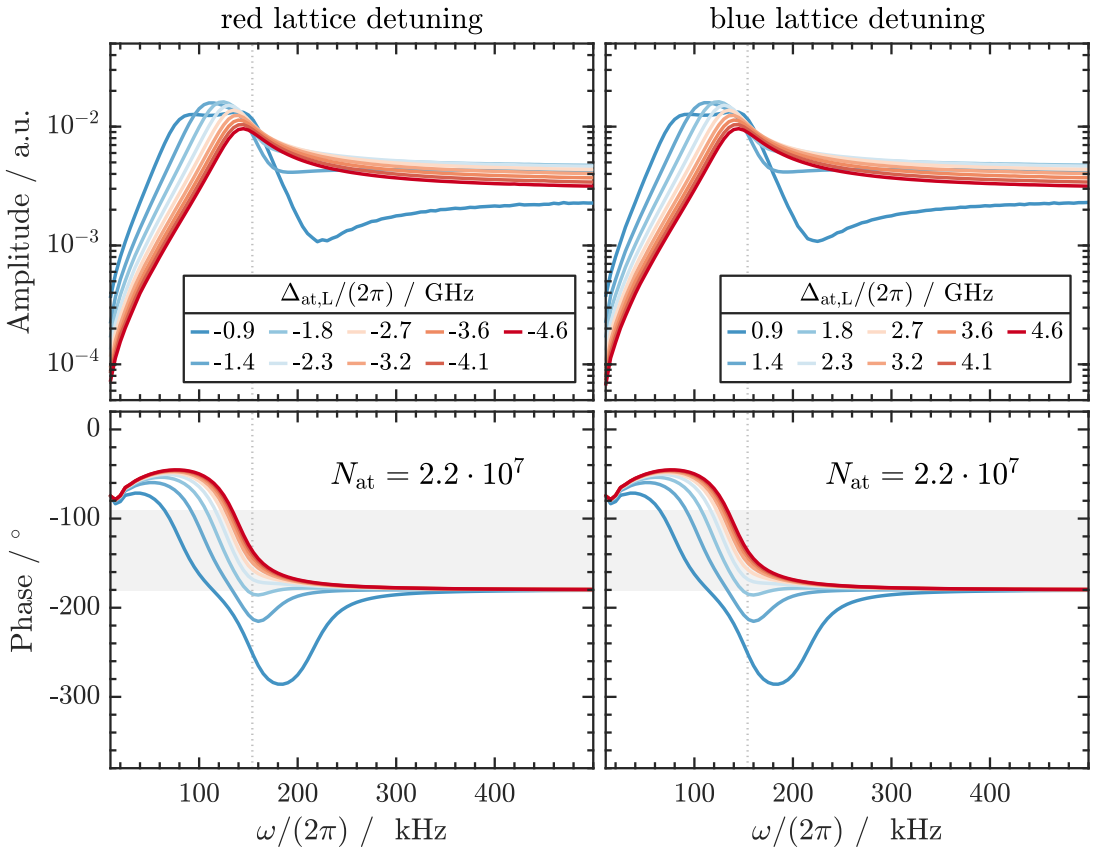

Figure B.2: Detuning sweep for red and blue lattice detuning $\Delta_{\mathrm{at,L}}$. Simulated atomic response for a variation of the lattice detuning. In order to keep the lattice depth constant the power P_{inc} is varied in proportion to $\Delta_{\mathrm{at,L}}$. The simulation result looks nearly identical for red and blue lattice detuning. Parameters: reflectivity $R = 0.22$, incident power $P_{\mathrm{inc}} = 10\,\mu\mathrm{W}$-$100\,\mu\mathrm{W}$, atomic damping rate $\Gamma_{\mathrm{at}} = 0.3\,\omega_{\mathrm{m}}$, atom number $N_{\mathrm{at}} = 2.2 \cdot 10^7$ and number of beam splitters $N_{\mathrm{BS}} = 10$.

For a better understanding of the collective behaviour we varied several other parameters in the simulation. Figure B.2 shows the atomic response for a variation of the lattice detuning $\Delta_{\mathrm{at,L}}$. The incident power P_{inc} was varied correspondingly to maintain the same lattice depth for every detuning. In the asymmetric lattice ($R = 0.22$) we recover the response of a single beam splitter for large enough detuning. With decreasing detuning the atomic polarizability increases as $\zeta \sim \frac{N_{\mathrm{at}}}{\Delta_{\mathrm{at,L}}}$ and thus collective effects start to occur below $|\Delta_{\mathrm{at,L}}/(2\pi)| = 2.7\,\mathrm{GHz}$ for the set atom number N_{at}. Notably, the simulation produces almost identical results for red and blue lattice detuning, indicating that the atomic backaction is independent of the sign of the detuning. Although the lattice configuration changes due to the contraction of the lattice constant the dynamic effects seem to play a more significant role. The experimentally observed, detuning dependent behaviour has most likely two reasons. First, the hyperfine structure of the excited state, which becomes relevant for red lattice detuning if $\Delta_{\mathrm{at,L}} < \Delta_{\mathrm{HFS}}$ is not included in the simulation. Furthermore, for these detunings the atomic polarizability can not be assumed purely dispersive any more and one has to take into account $\mathrm{Im}(\zeta)$ as well. Secondly, due to the attractive potential in the red detuned lattice higher

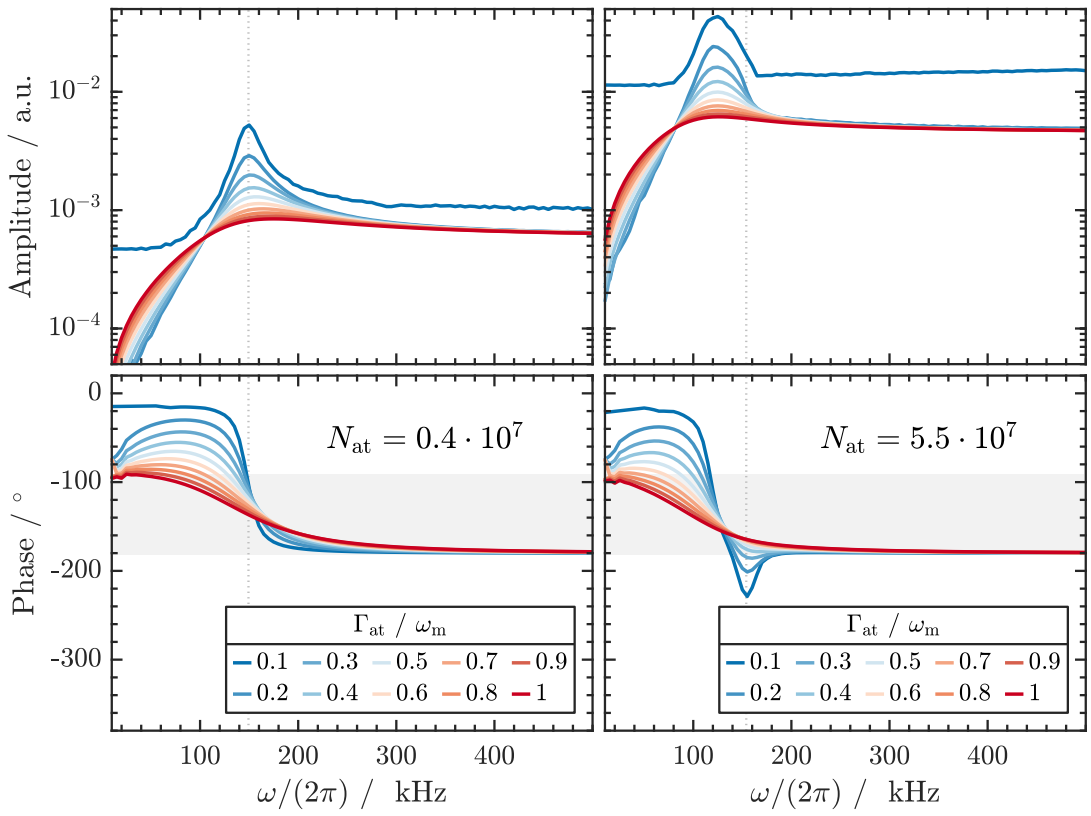

Figure B.3: Sweep of the atomic damping rate Γ_{at}. Simulated atomic response for a variation of the atomic damping rate at two different atom numbers $N_{\mathrm{at}} = 0.4 \cdot 10^7$ (left panel) and $N_{\mathrm{at}} = 5.5 \cdot 10^7$ (right panel). If the damping strong enough it can suppress the collective atomic dynamics that occur for large atom numbers. The position of the resonance is shifted towards lower frequencies due to the increased atom number (compare figure 3.6). Parameters: reflectivity $R = 0.22$, incident power $P_{\mathrm{inc}} = 100\,\mu\mathrm{W}$, detuning $\Delta_{\mathrm{at,L}}/(2\pi) = -4.55\,\mathrm{GHz}$ and number of beam splitters $N_{\mathrm{BS}} = 10$.

atomic densities occur at the intensity maxima in the red detuned lattice than at the intensity minima in the blue detuned lattice, which is also not included in the simulation. Therefore, one observes collective effects due to the increased atomic polarizablity ζ by the factor of N_{at} in the experiment.

Figure B.3 shows the atomic response for a variation of the atomic damping rate Γ_{at}. For low atom numbers and a moderate damping we recover a response very similar to the ideal damped driven harmonic oscillator like depicted in the left panel of figure 3.6. With increasing damping the resonant amplitude response is suppressed and the phase lag is increased. For larger atom numbers however, strong damping can even suppress the collective dynamics (right panel). Yet, this regime is experimentally not accessible.

In figure B.4 the number of beam splitters N_{BS} was varied between 1 and 15 for different atom numbers N_{at}. For only one beam splitter collective effects can not occur and the response is given by the single beam splitter model as expected. Already for two atomic beam beam splitters intra-beam splitter effects set in that lead to a deformation of the atomic response from the single beam splitter shape. For more than three beam splitters the response does not change any more. At large atom numbers exceeding $N_{\mathrm{at}} = 8 \cdot 10^7$ the simulation does not return a stable solution for a single beam splitter any longer. In the experiment the number of lattice sites amounts to $N_{\mathrm{BS}} = 2R_{\mathrm{at}}/(\lambda/2) \approx 10^4$. A simulation with this amount off lattice sites is not reasonable due to the extensive computing time.

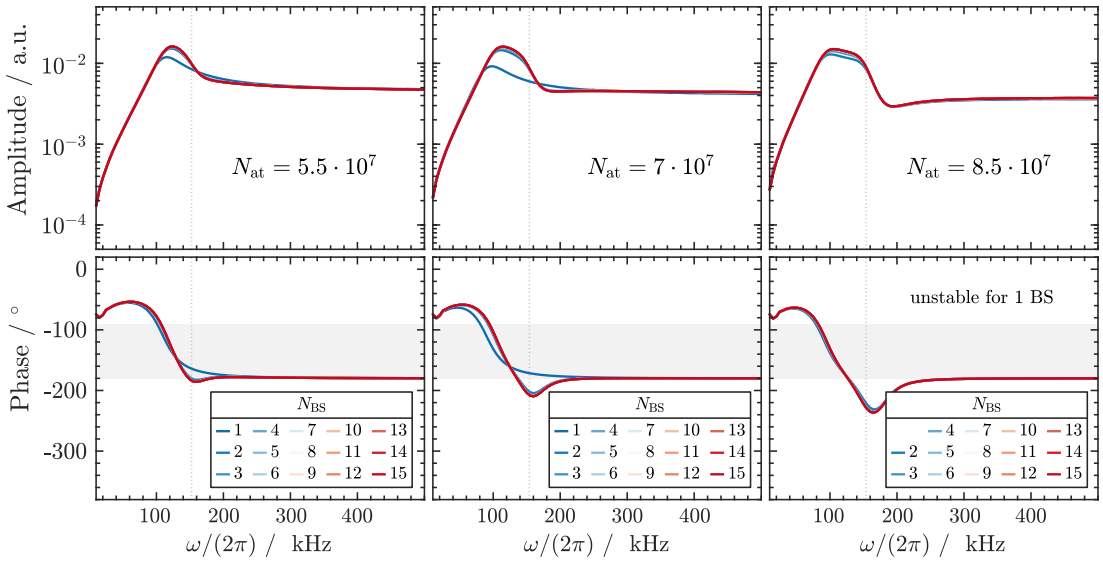

Figure B.4: Sweep of the number of atomic beam splitters in the system. Simulated atomic response for a variation of the number of beam splitters between 1 and 15 at three different atom numbers. Above $N_{\mathrm{at}} = 8 \cdot 10^7$ the simulation does not return a meaningful result for a single beam splitter in the asymmetric lattice. Parameters: reflectivity $R = 0.22$, incident power $P_{\mathrm{inc}} = 100\,\mu\mathrm{W}$, detuning $\Delta_{\mathrm{at,L}}/(2\pi) = -4.55\,\mathrm{GHz}$, atomic damping $\Gamma_{\mathrm{at}} = 0.3\,\omega_{\mathrm{m}}$ and atom numbers N_{at} as denoted in the plots.

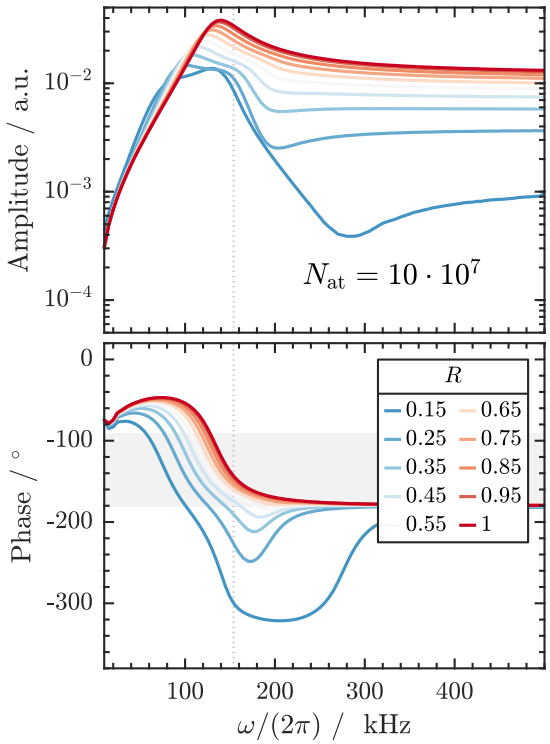

Figure B.5: Sweep of the reflectivity R. Simulated atomic response for a variation of the reflectivity R. With decreasing reflectivity the phase lag on resonance increases. Parameters: incident power $P_{\mathrm{inc}} = 100\,\mu\mathrm{W}$, detuning $\Delta_{\mathrm{at,L}}/(2\pi) = -4.55\,\mathrm{GHz}$, atomic damping $\Gamma_{\mathrm{at}} = 0.3\,\omega_{\mathrm{m}}$, number of atoms $N_{\mathrm{at}} = 10 \cdot 10^7$ and number of beam splitters $N_{\mathrm{BS}} = 10$.

In figure B.5 the atomic response for decreasing reflectivity R and hence increasing pump asymmetry is depicted. In the balanced lattice we recover the single beam splitter response and for increasing asymmetry the phase lag on resonance becomes more pronounced.

Considering the simulation of the asymmetric lattice shown in the right panel of figure 3.6 in section 3.3.2, we have seen that the phase lag at the resonator frequency exceeds the threshold lag of $\Delta\phi = -180°$ for atom numbers larger than $N_{\mathrm{at}} = 5.5 \cdot 10^7$. The development of the phase lag can also be observed in the atomic displacement explicitly. Figure B.6 shows how the beam splitter displacement from the equilibrium position $\xi_{\mathrm{eq}}(t) = x_j(t) - x_j^{ss}$ evolves in time at four distinct points in figure 3.6. For small atom numbers (on resonance, where $\omega/(2\pi) = 154\,\mathrm{kHz}$), all beam splitters oscillate in phase indicating that the intra-beam splitter interaction is negligible (top left panel in figure B.6). For atom numbers, where the phase lag exceeds $\Delta\phi = -180°$ on resonance (bottom left and top right panel) the beam splitters do not oscillate in phase any more but exhibit a phase shift throughout the ensemble. The shift becomes more pronounced for larger atom numbers. Evidently, the macroscopic phase lag that we observe on the outgoing light to the left is caused by the sum of the individual phase lags between the beam splitters, which only occurs for asymmetric lattice pumping and large atom numbers. At driving frequencies ω above resonance the system exhibits two oscillation modes that are completely out of phase (bottom right panel) and can lead to the destruction of the lattice for even higher atom numbers.

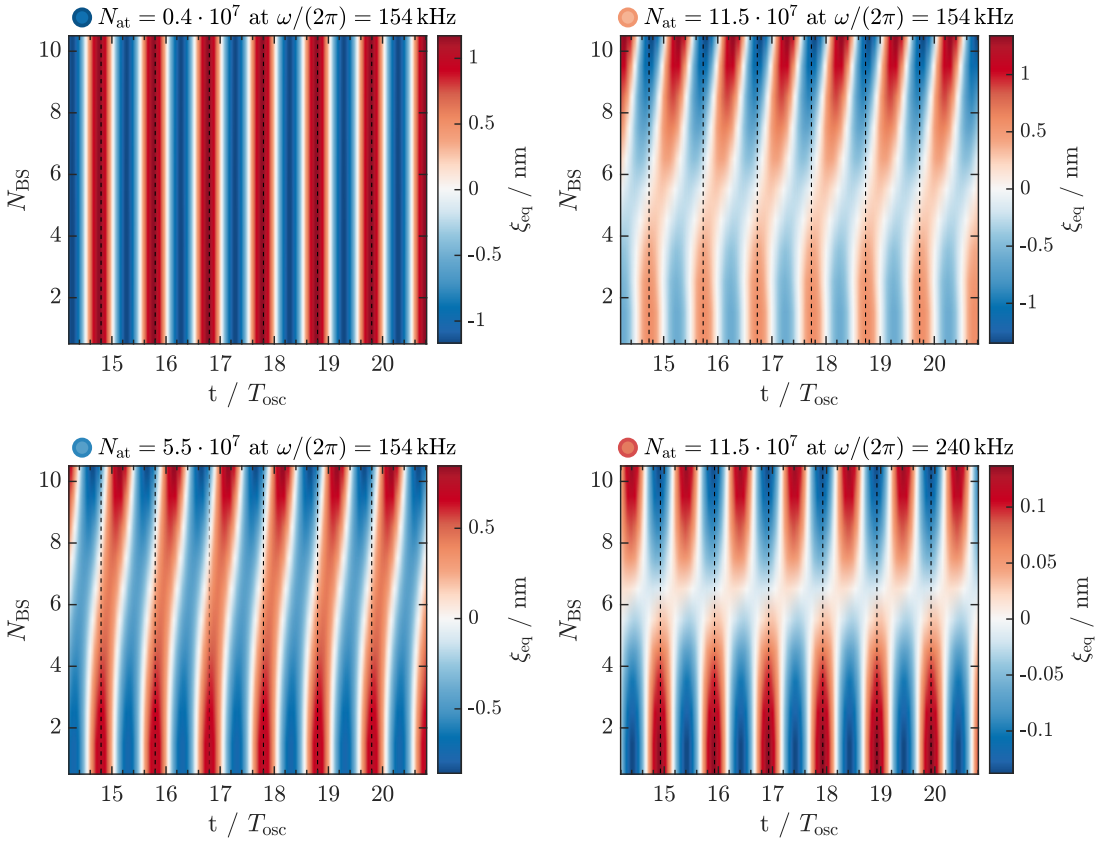

Figure B.6: Simulated beam splitter evolution in asymmetric lattice. The plots show the beam splitter displacements from their equilibrium position $\xi_{\mathrm{eq}} = x_j(t) - x_j^{ss}$ as a function of time in units of the oscillation period $T_{\mathrm{osc}} = 2\pi/\omega$. The titles show the corresponding atom number N_{at} and drive frequency ω that correspond to different points in the right panel of figure 3.6.

B.3 Cryogenic sympathetic cooling in PAC lattice

In order to test the performance of the PAC lattice we wanted to repeat the measurements presented in chapter 3.5 at cryogenic temperatures. After an extended warm-up period and multiple pump and flush cycles we were convinced that the blockage in our helium lines, which caused the cryostat to warm up in the first place, was dissolved. Unfortunately, shortly after the cooldown the blockage occurred again and caused the cryostat temperature to rise slowly. Because the sympathetic cooling experiments were performed on different days within one week, the blue detuned data were taken at $T_{\mathrm{MiM}}^{\mathrm{blue}} = 1.5\,\mathrm{K}$ and the red detuned data at $T_{\mathrm{MiM}}^{\mathrm{red}} = 11\,\mathrm{K}$. The temperature T_{MiM} refers to a temperature sensor that is placed inside the cryostat in direct proximity to the MiM system.
The measurements show qualitatively the same behaviour as the ones presented in 3.5 but this time the cooling performance in the red detuned PAC lattice is slightly better than in the blue detuned case. This can be seen in figure B.7, where the sympathetic cooling rates for all three lattice configurations that allow for cooling are depicted. The dashed lines in figures B.9 and B.8 denote the measured mode temperatures that were obtained by averaging the recorded time traces for all measurements (see exemplary trace in figure 3.16) before the initial cooldown. For the measurements at cryogenic temperatures we determined a homodyne calibration of $|\frac{\partial \phi_{\mathrm{x}}}{\partial x\mathrm{m}}| = (0.56 \pm 0.01)\,\mathrm{rad/nm}$. The sympathetic cooling rates were calculated according to equation (3.15) using the measured bath temperatures T_{bath} and mode temperatures T_{mode}. From the sympathetic cooling rates the hybrid cooperativities are calculated using equation (3.25) and the results are summarized here:

red/blue lattice	$T_{\mathrm{mode}}^{\mathrm{min}}$	$\Gamma_{\mathrm{sym}}^{\mathrm{max}}$	C_{hybrid}
without PAC	$(214.7 \pm 44.0)\,\mathrm{mK}$	$(4.8 \pm 1.0)\,\mathrm{Hz}$	(347 ± 72)
with $\mathrm{PAC}^{\mathrm{blue}}$	$(587.8 \pm 118.0)\,\mathrm{mK}$	$(1.8 \pm 0.4)\,\mathrm{Hz}$	(130 ± 29)
with $\mathrm{PAC}^{\mathrm{red}}$	$(489.5 \pm 103.0)\,\mathrm{mK}$	$(2.2 \pm 0.5)\,\mathrm{Hz}$	(159 ± 36)

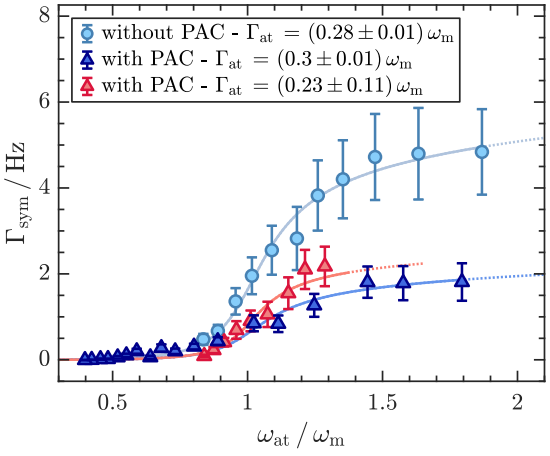

Figure B.7: Resonance behaviour of $\Gamma_{\mathrm{sym}}(\omega_{\mathrm{at}})$ for MOT cooling in red and blue detuned lattice. Sympathetic cooling rate Γ_{sym} calculated with equation (3.15) using the temperatures T_{mode} and T_{bath} from figures B.8 and B.9. Data points with decreasing Γ_{sym} for large ω_{at} are omitted. The solid lines are fits according to equation (3.17), which are used to obtain the atomic cooling rate Γ_{at} and to rescale the x-axis.

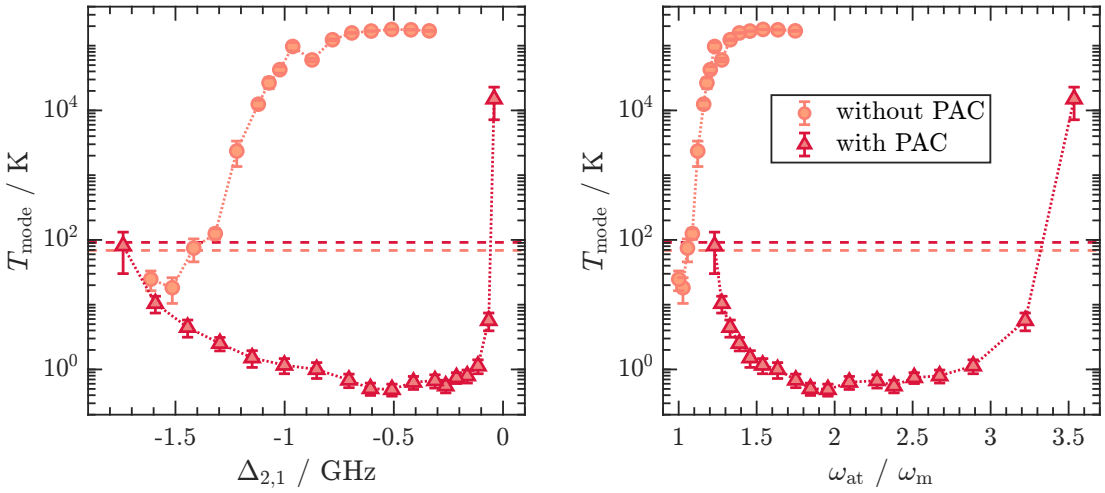

Figure B.8: Sympathetic cooling with and without pump asymmetry compensation in red detuned lattice at $T_{\mathrm{MiM}} = 11\,\mathrm{K}$. Minimum resonator mode temperature T_{mode} during sympathetic cooling with a high OD MOT as a function of the resonant lattice depth. **Left panel:** The lattice power is held constant and the detuning $\Delta_{2,1}$ is varied to tune the lattice depth. The circles show the resulting mode temperature due to coupling mediated via an imbalanced lattice and the triangles denote the measured mode temperature with applied auxiliary lattice beam. Dashed lines depict the measured bath temperatures $T_{\mathrm{bath}} = 68.8\,\mathrm{K}$ and $T_{\mathrm{bath}}^{\mathrm{PAC}} = 91.6\,\mathrm{K}$ from the time traces before the initial cooldown. **Right panel:** T_{mode} as a function of the (calibrated) atomic trapping frequency ω_{at} in units of the resonator frequency ω_{m}. Parameters: $P_{\mathrm{inc}} = 102.6\,\mu\mathrm{W}$, $P_{\mathrm{back}} = 21.6\,\mu\mathrm{W}$, $P_{\mathrm{aux}} = 102.6\,\mu\mathrm{W}$, $\phi_{\mathrm{aux,back}} = 0.77\,\pi$.

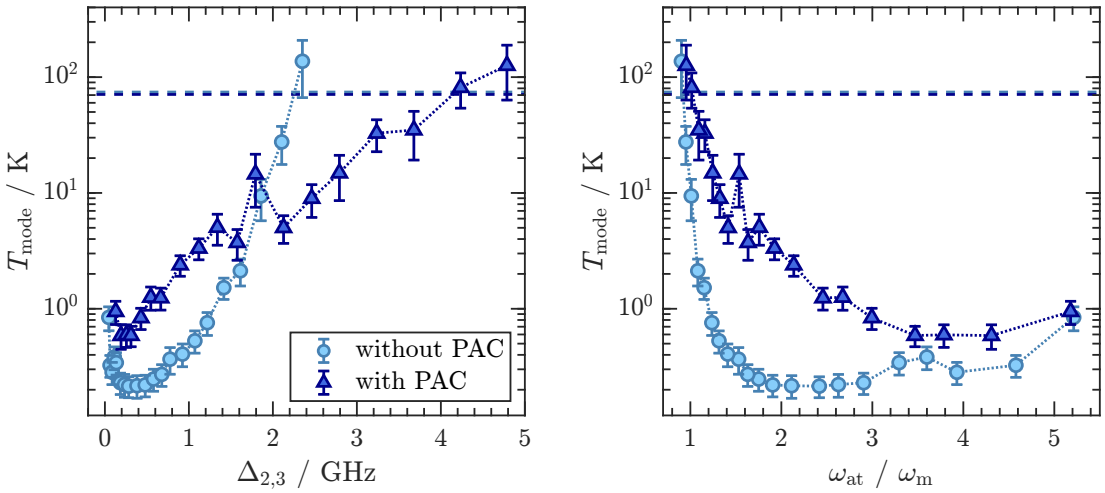

Figure B.9: Sympathetic cooling with and without pump asymmetry compensation in blue detuned lattice at $T_{\mathrm{MiM}} = 1.5\,\mathrm{K}$. Minimum resonator mode temperature T_{mode} during sympathetic cooling with a high OD MOT as a function of the resonant lattice depth. **Left panel:** The lattice power is held constant and the detuning $\Delta_{2,3}$ is varied to tune the lattice depth. The circles show the resulting mode temperature due to coupling mediated via an imbalanced lattice and the triangles denote the measured mode temperature in a balanced lattice. Dashed lines depict the measured bath temperatures $T_{\mathrm{bath}} = 74.4\,\mathrm{K}$ and $T_{\mathrm{bath}}^{\mathrm{PAC}} = 70.9\,\mathrm{K}$ from the time traces before the initial cooldown. **Right panel:** T_{mode} as a function of the (calibrated) atomic trapping frequency ω_{at} in units of the resonator frequency ω_{m}. Parameters: $P_{\mathrm{inc}} = 102\,\mu\mathrm{W}$, $P_{\mathrm{back}} = 22.6\,\mu\mathrm{W}$, $P_{\mathrm{aux}} = 102.6\,\mu\mathrm{W}$, $\phi_{\mathrm{aux,back}} = 0.57\,\pi$.

Appendix C

Pulsed optomechanics

C.1 Supplementary plots

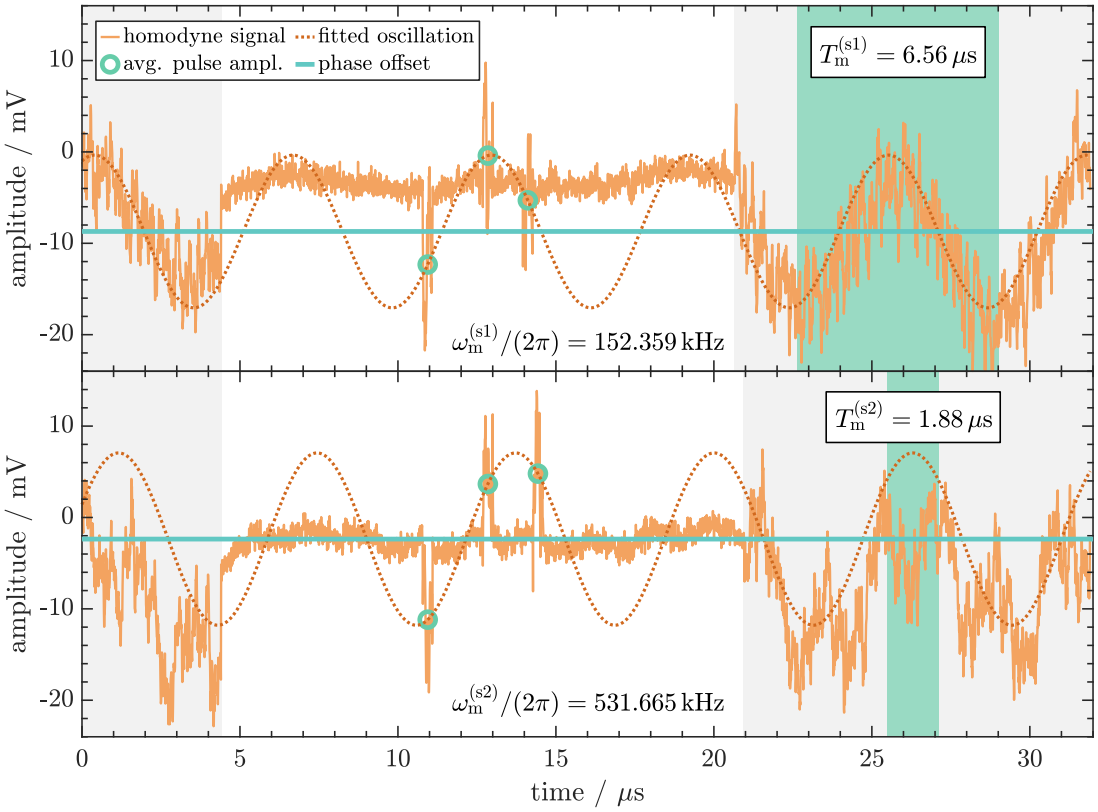

Figure C.1: Exemplary traces showing the excitation of the s1 and s2 mode. Both traces were recorded at different θ_t and were selected to illustrate the excitation of the first and second symmetric modes shown in the upper and lower panel, respectively. In both cases one can see, that the sinusoidal fit for the offset subtraction (only the three average pulse amplitudes are fitted) matches the the oscillation at the frequency of the fundamental mode.

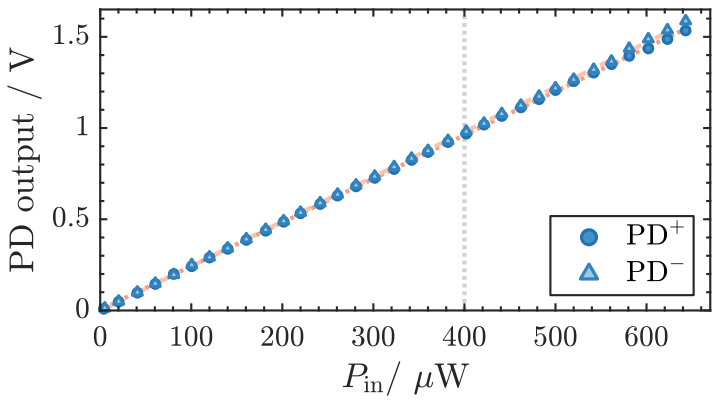

Figure C.2: Confirmation of the linear detector response for the HBPR-500M-10K-SI-FS. For increasing incident power P_{in} up to 644 µW on each detector PD$^+$ and PD$^-$ the output voltage was measured. Red dashed/dotted lines are linear fits to the data and the vertical dotted line denotes the linearity threshold specified by the manufacturer.

Bibliography

[1] T. D. Ladd, F. Jelezko, R. Laflamme, Y. Nakamura, C. Monroe and J. L. O'Brien: "Quantum computers", Nature **464**, 45–53 (2010), ISSN 0028-0836. 1

[2] E. Grumbling and M. Horowitz (editors): *Quantum Computing*, National Academies Press (2019), ISBN 978-0-309-47969-1. 1

[3] I. H. Deutsch: "Harnessing the Power of the Second Quantum Revolution", PRX Quantum **1**, 020101 (2020), ISSN 2691-3399.

[4] A. J. Daley, I. Bloch, C. Kokail, S. Flannigan, N. Pearson, M. Troyer and P. Zoller: "Practical quantum advantage in quantum simulation", Nature **607**, 667–676 (2022), ISSN 0028-0836. 1

[5] J. Chen: "Review on Quantum Communication and Quantum Computation", Journal of Physics: Conference Series **1865**, 022008 (2021), ISSN 1742-6588. 1

[6] N. Gisin, G. Ribordy, W. Tittel and H. Zbinden: "Quantum cryptography", Reviews of Modern Physics **74**, 145–195 (2002), ISSN 0034-6861. 1

[7] V. Giovannetti, S. Lloyd and L. Maccone: "Quantum-Enhanced Measurements: Beating the Standard Quantum Limit", Science **306**, 1330–1336 (2004), ISSN 0036-8075. 1, 2

[8] V. Giovannetti, S. Lloyd and L. Maccone: "Advances in quantum metrology", Nature Photonics **5**, 222–229 (2011), ISSN 1749-4885.

[9] C. Degen, F. Reinhard and P. Cappellaro: "Quantum sensing", Reviews of Modern Physics **89**, 035002 (2017), ISSN 0034-6861. 1

[10] R. P. Feynman: "Simulating physics with computers", International Journal of Theoretical Physics **21**, 467–488 (1982), ISSN 0020-7748. 1

[11] I. Georgescu, S. Ashhab and F. Nori: "Quantum simulation", Reviews of Modern Physics **86**, 153–185 (2014), ISSN 0034-6861. 1

[12] A. Aspuru-Guzik and P. Walther: "Photonic quantum simulators", Nature Physics **8**, 285–291 (2012), ISSN 1745-2473. 1

[13] J.-W. Pan, Z.-B. Chen, C.-Y. Lu, H. Weinfurter, A. Zeilinger and M. Żukowski: "Multiphoton entanglement and interferometry", Reviews of Modern Physics **84**, 777–838 (2012), ISSN 0034-6861. 1

[14] J. J. Morton and B. W. Lovett: "Hybrid solid-state qubits: The powerful role of electron spins", (2011). 1

[15] P. C. Maurer, G. Kucsko, C. Latta, L. Jiang, N. Y. Yao, S. D. Bennett, F. Pastawski, D. Hunger, N. Chisholm, M. Markham, D. J. Twitchen, J. I. Cirac and M. D. Lukin: "Room-Temperature Quantum Bit Memory Exceeding One Second", Science **336**, 1283–1286 (2012), ISSN 0036-8075.

[16] J. J. Pla, K. Y. Tan, J. P. Dehollain, W. H. Lim, J. J. L. Morton, F. A. Zwanenburg, D. N. Jamieson, A. S. Dzurak and A. Morello: "High-fidelity readout and control of a nuclear spin qubit in silicon", Nature **496**, 334–338 (2013), ISSN 0028-0836. 1

[17] T. Grünzweig, A. Hilliard, M. McGovern and M. F. Andersen: "Near-deterministic preparation of a single atom in an optical microtrap", Nature Physics **6**, 951–954 (2010), ISSN 1745-2473. 1

[18] A. M. Kaufman, B. J. Lester and C. A. Regal: "Cooling a Single Atom in an Optical Tweezer to Its Quantum Ground State", Physical Review X **2**, 041014 (2012), ISSN 2160-3308. 1

[19] R. Blatt and C. F. Roos: "Quantum simulations with trapped ions", Nature Physics **8**, 277–284 (2012), ISSN 1745-2473. 1

[20] I. Bloch, J. Dalibard and S. Nascimbène: "Quantum simulations with ultracold quantum gases", Nature Physics **8**, 267–276 (2012), ISSN 1745-2473. 1

[21] R. J. Schoelkopf and S. M. Girvin: "Wiring up quantum systems", Nature **451**, 664–669 (2008), ISSN 0028-0836. 1

[22] A. A. Houck, H. E. Türeci and J. Koch: "On-chip quantum simulation with superconducting circuits", Nature Physics **8**, 292–299 (2012), ISSN 1745-2473. 1

[23] M. Poot and H. S. van der Zant: "Mechanical systems in the quantum regime", Physics Reports **511**, 273–335 (2012), ISSN 03701573. 1, 2, 19, 26, 29

[24] M. Aspelmeyer, T. J. Kippenberg and F. Marquardt: "Cavity optomechanics", Reviews of Modern Physics **86**, 1391–1452 (2014). 1, 2, 4, 19, 28, 31, 34, 35, 56, 102

[25] W. H. Zurek: "Decoherence, einselection, and the quantum origins of the classical", Reviews of Modern Physics **75**, 715–775 (2003), ISSN 0034-6861. 1, 102

[26] G. Kurizki, P. Bertet, Y. Kubo, K. Mølmer, D. Petrosyan, P. Rabl and J. Schmiedmayer: "Quantum technologies with hybrid systems", Proceedings of the National Academy of Sciences **112**, 3866–3873 (2015), ISSN 0027-8424. 1, 2

[27] M. Wallquist, K. Hammerer, P. Rabl, M. Lukin and P. Zoller: "Hybrid quantum devices and quantum engineering", Physica Scripta **T137**, 014001 (2009), ISSN 0031-8949. 1

[28] Z.-L. Xiang, S. Ashhab, J. Q. You and F. Nori: "Hybrid quantum circuits: Superconducting circuits interacting with other quantum systems", Reviews of Modern Physics **85**, 623–653 (2013), ISSN 0034-6861. 1

[29] P. Treutlein, C. Genes, K. Hammerer, M. Poggio and P. Rabl: *Hybrid Mechanical Systems*, pages 327–351, Springer Berlin Heidelberg, Berlin, Heidelberg (2014), ISBN 978-3-642-55312-7. 1

[30] L. Tian, P. Rabl, R. Blatt and P. Zoller: "Interfacing Quantum-Optical and Solid-State Qubits", Physical Review Letters **92**, 247902 (2004), ISSN 0031-9007. 2

[31] A. S. Sørensen, C. H. van der Wal, L. I. Childress and M. D. Lukin: "Capacitive Coupling of Atomic Systems to Mesoscopic Conductors", Physical Review Letters **92**, 063601 (2004), ISSN 0031-9007.

[32] J. Verdú, H. Zoubi, C. Koller, J. Majer, H. Ritsch and J. Schmiedmayer: "Strong Magnetic Coupling of an Ultracold Gas to a Superconducting Waveguide Cavity", Physical Review Letters **103**, 043603 (2009), ISSN 0031-9007.

[33] D. Petrosyan, G. Bensky, G. Kurizki, I. Mazets, J. Majer and J. Schmiedmayer: "Reversible state transfer between superconducting qubits and atomic ensembles", Physical Review A **79**, 040304 (2009), ISSN 1050-2947.

[34] A. Imamoğlu: "Cavity QED Based on Collective Magnetic Dipole Coupling: Spin Ensembles as Hybrid Two-Level Systems", Physical Review Letters **102**, 083602 (2009), ISSN 0031-9007.

[35] J. H. Wesenberg, A. Ardavan, G. A. D. Briggs, J. J. L. Morton, R. J. Schoelkopf, D. I. Schuster and K. Mølmer: "Quantum Computing with an Electron Spin Ensemble", Physical Review Letters **103**, 070502 (2009), ISSN 0031-9007.

[36] D. Marcos, M. Wubs, J. M. Taylor, R. Aguado, M. D. Lukin and A. S. Sørensen: "Coupling Nitrogen-Vacancy Centers in Diamond to Superconducting Flux Qubits", Physical Review Letters **105**, 210501 (2010), ISSN 0031-9007. 2

[37] K. Stannigel, P. Rabl, A. S. Sørensen, M. D. Lukin and P. Zoller: "Optomechanical transducers for quantum-information processing", Physical Review A **84**, 042341 (2011), ISSN 1050-2947. 2

[38] M. Gao, Y. xi Liu and X.-B. Wang: "Coupling Rydberg atoms to superconducting qubits via nanomechanical resonator", Physical Review A **83**, 022309 (2011), ISSN 1050-2947.

[39] L. Tian: "Optoelectromechanical transducer: Reversible conversion between microwave and optical photons", Annalen der Physik **527**, 1–14 (2015), ISSN 00033804.

[40] Z. qi Yin, W. L. Yang, L. Sun and L. M. Duan: "Quantum network of superconducting qubits through an optomechanical interface", Physical Review A **91**, 012333 (2015), ISSN 1050-2947. 2

[41] A. D. Armour, M. P. Blencowe and K. C. Schwab: "Entanglement and Decoherence of a Micromechanical Resonator via Coupling to a Cooper-Pair Box", Physical Review Letters **88**, 148301 (2002), ISSN 0031-9007. 2

[42] K. Hammerer, M. Wallquist, C. Genes, M. Ludwig, F. Marquardt, P. Treutlein, P. Zoller, J. Ye and H. J. Kimble: "Strong Coupling of a Mechanical Oscillator and a Single Atom", Physical Review Letters **103**, 063005 (2009), ISSN 0031-9007. 40, 54

[43] K. Hammerer, M. Aspelmeyer, E. S. Polzik and P. Zoller: "Establishing Einstein-Poldosky-Rosen Channels between Nanomechanics and Atomic Ensembles", Physical Review Letters **102**, 020501 (2009), ISSN 0031-9007. 2, 54

[44] P. Rabl, P. Cappellaro, M. V. G. Dutt, L. Jiang, J. R. Maze and M. D. Lukin: "Strong magnetic coupling between an electronic spin qubit and a mechanical resonator", Physical Review B **79**, 041302 (2009), ISSN 1098-0121.

[45] B. Vogell, K. Stannigel, P. Zoller, K. Hammerer, M. T. Rakher, M. Korppi, A. Jöckel and P. Treutlein: "Cavity-enhanced long-distance coupling of an atomic ensemble to a micromechanical membrane", Physical Review A - Atomic, Molecular, and Optical Physics **87**, 23816 (2013), ISSN 10502947. 2, 54, 60, 61

[46] F. Bariani, J. Otterbach, H. Tan and P. Meystre: "Single-atom quantum control of macroscopic mechanical oscillators", Physical Review A **89**, 011801 (2014), ISSN 1050-2947.

[47] F. Bariani, S. Singh, L. F. Buchmann, M. Vengalattore and P. Meystre: "Hybrid optomechanical cooling by atomic Λ systems", Physical Review A **90**, 033838 (2014), ISSN 1050-2947. 54

[48] B. Vogell, T. Kampschulte, M. T. Rakher, A. Faber, P. Treutlein, K. Hammerer and P. Zoller: "Long distance coupling of a quantum mechanical oscillator to the internal states of an atomic ensemble", New Journal of Physics **17**, 043044 (2015), ISSN 1367-2630. 2, 40

[49] I. Yeo, P.-L. de Assis, A. Gloppe, E. Dupont-Ferrier, P. Verlot, N. S. Malik, E. Dupuy, J. Claudon, J.-M. Gérard, A. Auffèves, G. Nogues, S. Seidelin, J.-P. Poizat, O. Arcizet and M. Richard: "Strain-mediated coupling in a quantum dot–mechanical oscillator hybrid system", Nature Nanotechnology **9**, 106–110 (2014), ISSN 1748-3387. 2

[50] M. Montinaro, G. Wüst, M. Munsch, Y. Fontana, E. Russo-Averchi, M. Heiss, A. F. i Morral, R. J. Warburton and M. Poggio: "Quantum Dot Opto-Mechanics in a Fully Self-Assembled Nanowire", Nano Letters **14**, 4454–4460 (2014), ISSN 1530-6984. 2

[51] C. L. Degen, M. Poggio, H. J. Mamin, C. T. Rettner and D. Rugar: "Nanoscale magnetic resonance imaging", Proceedings of the National Academy of Sciences **106**, 1313–1317 (2009), ISSN 0027-8424. 2

[52] O. Arcizet, V. Jacques, A. Siria, P. Poncharal, P. Vincent and S. Seidelin: "A single nitrogen-vacancy defect coupled to a nanomechanical oscillator", Nature Physics **7**, 879–883 (2011), ISSN 1745-2473.

[53] S. Kolkowitz, A. C. B. Jayich, Q. P. Unterreithmeier, S. D. Bennett, P. Rabl, J. G. E. Harris and M. D. Lukin: "Coherent Sensing of a Mechanical Resonator with a Single-Spin Qubit", Science **335**, 1603–1606 (2012), ISSN 0036-8075.

[54] J. Teissier, A. Barfuss, P. Appel, E. Neu and P. Maletinsky: "Strain Coupling of a Nitrogen-Vacancy Center Spin to a Diamond Mechanical Oscillator", Physical Review Letters **113**, 020503 (2014), ISSN 0031-9007.

[55] P. Ovartchaiyapong, K. W. Lee, B. A. Myers and A. C. B. Jayich: "Dynamic strain-mediated coupling of a single diamond spin to a mechanical resonator", Nature Communications **5**, 4429 (2014), ISSN 2041-1723. 2

[56] A. D. O'Connell, M. Hofheinz, M. Ansmann, R. C. Bialczak, M. Lenander, E. Lucero, M. Neeley, D. Sank, H. Wang, M. Weides, J. Wenner, J. M. Martinis and A. N. Cleland: "Quantum ground state and single-phonon control of a mechanical resonator", Nature **464**, 697–703 (2010), ISSN 00280836. 2, 23, 102

[57] J.-M. Pirkkalainen, S. U. Cho, J. Li, G. S. Paraoanu, P. J. Hakonen and M. A. Sillanpää: "Hybrid circuit cavity quantum electrodynamics with a micromechanical resonator", Nature **494**, 211–215 (2013), ISSN 0028-0836.

[58] T. A. Palomaki, J. W. Harlow, J. D. Teufel, R. W. Simmonds and K. W. Lehnert: "Coherent state transfer between itinerant microwave fields and a mechanical oscillator", Nature **495**, 210–214 (2013), ISSN 0028-0836. 102

[59] J. M. Fink, M. Kalaee, A. Pitanti, R. Norte, L. Heinzle, M. Davanço, K. Srinivasan and O. Painter: "Quantum electromechanics on silicon nitride nanomembranes", Nature Communications **7** (2016), ISSN 20411723. 2

[60] Y.-J. Wang, M. Eardley, S. Knappe, J. Moreland, L. Hollberg and J. Kitching: "Magnetic Resonance in an Atomic Vapor Excited by a Mechanical Resonator", Physical Review Letters **97**, 227602 (2006), ISSN 0031-9007. 2

[61] D. Hunger, S. Camerer, T. W. Hänsch, D. König, J. P. Kotthaus, J. Reichel and P. Treutlein: "Resonant Coupling of a Bose-Einstein Condensate to a Micromechanical Oscillator", Physical Review Letters **104**, 143002 (2010), ISSN 0031-9007.

[62] A. Jöckel, A. Faber, T. Kampschulte, M. Korppi, M. T. Rakher and P. Treutlein: "Sympathetic cooling of a membrane oscillator in a hybrid mechanical–atomic system", Nature Nanotechnology **10**, 55–59 (2015), ISSN 1748-3387. 2, 29, 54, 55, 58, 59

[63] C. Montoya, J. Valencia, A. A. Geraci, M. Eardley, J. Moreland, L. Hollberg and J. Kitching: "Resonant interaction of trapped cold atoms with a magnetic cantilever tip", Physical Review A **91**, 063835 (2015), ISSN 1050-2947.

[64] C. B. Møller, R. A. Thomas, G. Vasilakis, E. Zeuthen, Y. Tsaturyan, M. Balabas, K. Jensen, A. Schliesser, K. Hammerer and E. S. Polzik: "Quantum back-Action-evading measurement of motion in a negative mass reference frame", Nature **547**, 191–195 (2017), ISSN 14764687. 29, 54, 104

[65] P. Christoph, T. Wagner, H. Zhong, R. Wiesendanger, K. Sengstock, A. Schwarz and C. Becker: "Combined feedback and sympathetic cooling of a mechanical oscillator coupled to ultracold atoms", New Journal of Physics **20**, 093020 (2018), ISSN 1367-2630. 2, 29, 55, 63

[66] L. Pezzè, A. Smerzi, M. K. Oberthaler, R. Schmied and P. Treutlein: "Quantum metrology with nonclassical states of atomic ensembles", Reviews of Modern Physics **90**, 035005 (2018), ISSN 0034-6861. 2

[67] S. Chu: "Cold atoms and quantum control", Nature **416**, 206–210 (2002), ISSN 00280836. 2, 6

[68] K. Hammerer, K. Stannigel, C. Genes, P. Zoller, P. Treutlein, S. Camerer, D. Hunger and T. W. Hänsch: "Optical lattices with micromechanical mirrors", Physical Review A **82**, 021803 (2010), ISSN 1050-2947. 2, 54

[69] D. Hunger, S. Camerer, M. Korppi, A. Jöckel, T. W. Hänsch and P. Treutlein: "Coupling ultracold atoms to mechanical oscillators", Comptes Rendus Physique **12**, 871–887 (2011), ISSN 16310705.

[70] J. S. Bennett, L. S. Madsen, M. Baker, H. Rubinsztein-Dunlop and W. P. Bowen: "Coherent control and feedback cooling in a remotely coupled hybrid atom–optomechanical system", New Journal of Physics **16**, 083036 (2014), ISSN 1367-2630. 2, 54, 57, 58, 61

[71] S. Camerer, M. Korppi, A. Jöckel, D. Hunger, T. W. Hänsch and P. Treutlein: "Realization of an optomechanical interface between ultracold atoms and a membrane", Physical Review Letters **107**, 223001 (2011), ISSN 00319007. 2

[72] A. Vochezer, T. Kampschulte, K. Hammerer and P. Treutlein: "Light-Mediated Collective Atomic Motion in an Optical Lattice Coupled to a Membrane", Physical Review Letters **120**, 073602 (2018), ISSN 0031-9007. 2, 54, 57, 62, 63, 71, 94

[73] A. Faber: "Sympathetic cooling and self-oscillations in a hybrid atom-membrane system", Universität Basel, PhD Thesis (2016). 57, 59, 62, 64, 65, 69, 71, 74, 94

[74] P. Christoph: "Feedback-assisted sympathetic cooling in a hybrid atomic-mechanical system", Universität Hamburg, PhD Thesis (2018), ISBN 978-3-8439-3596-8. 2, 6, 11, 12, 13, 15, 16, 17, 20, 21, 26, 27, 33, 54, 56, 57, 59, 60, 62, 63, 72, 87, 88, 92, 94, 99, 101

[75] J. K. Asbóth, H. Ritsch and P. Domokos: "Collective Excitations and Instability of an Optical Lattice due to Unbalanced Pumping", Physical Review Letters **98**, 203008 (2007), ISSN 0031-9007. 3, 54, 57, 62, 64

[76] J. K. Asbóth, H. Ritsch and P. Domokos: "Optomechanical coupling in a one-dimensional optical lattice", Physical Review A **77**, 063424 (2008), ISSN 1050-2947. 3, 54, 57, 62, 64, 65, 66, 67, 68, 69

[77] T. Wagner: "Realization of a Hybrid Quantum System Consisting of Ultra-cold Atoms and a Nanomechanical Oscillator", Universität Hamburg, PhD Thesis (2020), ISBN 978-3-8439-4599-8. 3, 6, 11, 13, 14, 15, 20, 23, 30, 33, 55, 62, 63, 72, 87, 99

[78] V. B. Braginsky, Y. I. Vorontsov and K. S. Thorne: "Quantum Nondemolition Measurements", Science **209**, 547–557 (1980), ISSN 0036-8075. 4, 19, 103, 104

[79] M. R. Vanner, I. Pikovski, G. D. Cole, M. S. Kim, C. Brukner, K. Hammerer, G. J. Milburn and M. Aspelmeyer: "Pulsed quantum optomechanics", Proceedings of the National Academy of Sciences of the United States of America **108**, 16182–16187 (2011), ISSN 00278424. 4, 104, 108, 110

[80] M. R. Vanner, J. Hofer, G. D. Cole and M. Aspelmeyer: "Cooling-by-measurement and mechanical state tomography via pulsed optomechanics", Nature Communications **4**, 2295 (2013), ISSN 2041-1723. 4, 104, 106, 109

[81] M. R. Vanner, I. Pikovski and M. S. Kim: "Towards optomechanical quantum state reconstruction of mechanical motion", Annalen der Physik **527**, 15–26 (2015), ISSN 00033804. 4, 102, 107, 122

[82] W. Happer: "Optical Pumping", Reviews of Modern Physics **44**, 169–249 (1972), ISSN 0034-6861. 6

[83] H. F. Hess: "Evaporative cooling of magnetically trapped and compressed spin-polarized hydrogen", Physical Review B **34**, 3476–3479 (1986), ISSN 01631829. 6

[84] C. Chin, R. Grimm, P. Julienne and E. Tiesinga: "Feshbach resonances in ultracold gases", Reviews of Modern Physics **82**, 1225–1286 (2010), ISSN 00346861. 6

[85] R. Grimm, M. Weidemüller and Y. B. Ovchinnikov: "Optical Dipole Traps for Neutral Atoms", Advances in Atomic, Molecular and Optical Physics **42**, 95–170 (2000), ISSN 1049250X. 6, 9, 16

[86] A. Hemmerich and T. W. Hänsch: "Two-dimesional atomic crystal bound by light", Physical Review Letters **70**, 410–413 (1993), ISSN 0031-9007. 6

[87] B. Yang, H. Sun, C. J. Huang, H. Y. Wang, Y. Deng, H. N. Dai, Z. S. Yuan and J. W. Pan: "Cooling and entangling ultracold atoms in optical lattices", Science **369**, 550–553 (2020), ISSN 10959203. 6

[88] S. V. Frank, A. Negretti, T. Berrada, R. Bücker, S. Montangero, J. F. Schaff, T. Schumm, T. Calarco and J. Schmiedmayer: "Interferometry with non-classical motional states of a Bose-Einstein condensate", Nature Communications **5**, 1–6 (2014), ISSN 20411723. 6

[89] S. Riedl, M. Lettner, C. Vo, S. Baur, G. Rempe and S. Dürr: "Bose-Einstein condensate as a quantum memory for a photonic polarization qubit", Physical Review A - Atomic, Molecular, and Optical Physics **85**, 1–11 (2012), ISSN 10502947. 6

[90] Y. Tsaturyan, A. Barg, E. S. Polzik and A. Schliesser: "Ultracoherent nanomechanical resonators via soft clamping and dissipation dilution", Nature Nanotechnology **12**, 776–783 (2017), ISSN 1748-3387. 6, 52

[91] E. E. Wollman, C. U. Lei, A. J. Weinstein, J. Suh, A. Kronwald, F. Marquardt, A. A. Clerk and K. C. Schwab: "Quantum squeezing of motion in a mechanical resonator", Science **349**, 952–955 (2015), ISSN 10959203. 6, 102

[92] R. Riedinger, A. Wallucks, I. Marinković, C. Löschnauer, M. Aspelmeyer, S. Hong and S. Gröblacher: "Remote quantum entanglement between two micromechanical oscillators", Nature **556**, 473–477 (2018), ISSN 14764687. 6, 102

[93] R. Norte, J. Moura and S. Gröblacher: "Mechanical Resonators for Quantum Optomechanics Experiments at Room Temperature", Physical Review Letters **116**, 147202 (2016), ISSN 0031-9007. 6, 27, 29

[94] C. Reinhardt, T. Müller, A. Bourassa and J. C. Sankey: "Ultralow-Noise SiN Trampoline Resonators for Sensing and Optomechanics", Physical Review X **6**, 021001 (2016), ISSN 2160-3308. 27, 29

[95] T. P. Purdy, K. E. Grutter, K. Srinivasan and J. M. Taylor: "Quantum correlations from a room-temperature optomechanical cavity", Science **356**, 1265–1268 (2017), ISSN 10959203. 6

[96] A. Bick: "Interfacing Ultracold Atoms and a Cryogenic Micromechanical Oscillator", Universität Hamburg, PhD Thesis (2015), ISBN 978-3-8439-2106-0. 6, 7, 8, 10, 12, 40, 60

[97] C. Staarmann: "Towards a Hybrid Quantum System", Universität Hamburg, PhD Thesis (2016), ISBN 978-3-8439-3050-5. 6, 7, 8, 28

[98] D. A. Steck: "Rubidium 87 D Line Data", pages 1–29 (2003). 9, 13, 16, 42, 47

[99] A. Bick, C. Staarmann, P. Christoph, O. Hellmig, J. Heinze, K. Sengstock and C. Becker: "The role of mode match in fiber cavities", Review of Scientific Instruments **87**, 013102 (2016), ISSN 0034-6748. 12, 22, 27

[100] C. F. Klein: "The role of pump asymmetry compensation in quantum hybrid systems", Universität Hamburg, Master Thesis (2020). 15, 28, 64, 68, 82, 84

[101] M. Greiner: "Ultracold quantum gases in three-dimensional optical lattice potentials", Ludwig-Maximilians-Universität München, PhD Thesis (2003). 16

[102] H. Andersen: "Bose–Einstein condensates in optical lattices", University of Aarhus, PhD Thesis (2008). 16, 17

[103] H. P. Yuen and V. W. S. Chan: "Noise in homodyne and heterodyne detection", Optics Letters **8**, 177 (1983), ISSN 0146-9592. 18, 111

[104] H. Bachor and T. C. Ralph: *A Guide to Experiments in Quantum Optics*, Wiley (2019), ISBN 9783527411931. 18, 19, 20

[105] A. A. Clerk, M. H. Devoret, S. M. Girvin, F. Marquardt and R. J. Schoelkopf: "Introduction to quantum noise, measurement, and amplification", Reviews of Modern Physics **82**, 1155–1208 (2010), ISSN 00346861. 19

[106] S. Vyatchanin and E. Zubova: "Quantum variation measurement of a force", Physics Letters A **201**, 269–274 (1995), ISSN 03759601. 19

[107] D. Mason, J. Chen, M. Rossi, Y. Tsaturyan and A. Schliesser: "Continuous force and displacement measurement below the standard quantum limit", Nature Physics **15**, 745–749 (2019), ISSN 1745-2473. 20

[108] H. Yu, L. McCuller, M. Tse and et al.: "Quantum correlations between light and the kilogram-mass mirrors of LIGO", Nature **583**, 43–47 (2020), ISSN 0028-0836. 20

[109] V. B. Braginsky, V. Y. I. and K. F. Y.: "Optimal quantum measurements in detectors of gravitation radiation", JETP Letters **27**, 276–280 (1978). 20, 104

[110] T. Wagner: "Homodyne Detection of a Nanomechanical Oscillator for Thermometry and Active Feedback Cooling", Universität Hamburg, Master Thesis (2016). 21, 22

[111] J. Chan, T. P. Alegre, A. H. Safavi-Naeini, J. T. Hill, A. Krause, S. Gröblacher, M. Aspelmeyer and O. Painter: "Laser cooling of a nanomechanical oscillator into its quantum ground state", Nature **478**, 89–92 (2011), ISSN 00280836. 23, 102

[112] J. D. Teufel, T. Donner, D. Li, J. W. Harlow, M. S. Allman, K. Cicak, A. J. Sirois, J. D. Whittaker, K. W. Lehnert and R. W. Simmonds: "Sideband cooling of micromechanical motion to the quantum ground state", Nature **475**, 359–363 (2011), ISSN 00280836. 23, 102

[113] M. Rossi, D. Mason, J. Chen, Y. Tsaturyan and A. Schliesser: "Measurement-based quantum control of mechanical motion", Nature **563**, 53–58 (2018), ISSN 14764687. 23, 29, 102, 104

[114] J. Guo, R. Norte and S. Gröblacher: "Feedback Cooling of a Room Temperature Mechanical Oscillator close to its Motional Ground State", Physical Review Letters **123**, 223602 (2019), ISSN 10797114. 23

[115] S. A. Saarinen, N. Kralj, E. C. Langman, Y. Tsaturyan and A. Schliesser: "Laser cooling a membrane-in-the-middle system close to the quantum ground state from room temperature", Optica **10**, 364 (2023), ISSN 2334-2536. 23, 29

[116] R. Vijay, C. MacKlin, D. H. Slichter, S. J. Weber, K. W. Murch, R. Naik, A. N. Korotkov and I. Siddiqi: "Stabilizing Rabi oscillations in a superconducting qubit using quantum feedback", Nature **490**, 77–80 (2012), ISSN 00280836. 23

[117] D. J. Wilson, V. Sudhir, N. Piro, R. Schilling, A. Ghadimi and T. J. Kippenberg: "Supplementary: Measurement-based control of a mechanical oscillator at

its thermal decoherence rate - Supplementary Information", Nature **524**, 325–329 (2015), ISSN 14764687. 24

[118] J. Petermann: "Simulations and Fabrication of Optical Fiber Cavities for a Quantum Hybrid Experiment", Universität Hamburg, Master Thesis (2017). 27

[119] H. Zhong, G. Fläschner, A. Schwarz, R. Wiesendanger, P. Christoph, T. Wagner, A. Bick, C. Staarmann, B. Abeln, K. Sengstock and C. Becker: "A millikelvin all-fiber cavity optomechanical apparatus for merging with ultra-cold atoms in a hybrid quantum system", Review of Scientific Instruments **88**, 023115 (2017), ISSN 10897623. 27

[120] M. Aspelmeyer, S. Gröblacher, K. Hammerer and N. Kiesel: "Quantum optomechanics—throwing a glance [Invited]", Journal of the Optical Society of America B **27**, A189 (2010), ISSN 0740-3224. 28

[121] J. C. Sankey, C. Yang, B. M. Zwickl, A. M. Jayich and J. G. Harris: "Strong and tunable nonlinear optomechanical coupling in a low-loss system", Nature Physics **6**, 707–712 (2010), ISSN 17452481. 28, 29

[122] J. D. Thompson, B. M. Zwickl, a M Jayich, F. Marquardt, S. M. Girvin and J. G. E. Harris: "Strong dispersive coupling of a high-finesse cavity to a micromechanical membrane.", Nature **452**, 72–5 (2008), ISSN 1476-4687.

[123] A. M. Jayich, J. C. Sankey, B. M. Zwickl, C. Yang, J. D. Thompson, S. M. Girvin, A. A. Clerk, F. Marquardt and J. G. E. Harris: "Dispersive optomechanics: a membrane inside a cavity", New Journal of Physics **10**, 095008 (2008), ISSN 1367-2630. 32

[124] D. J. Wilson, C. A. Regal, S. B. Papp and H. J. Kimble: "Cavity optomechanics with stoichiometric SiN films", Physical Review Letters **103** (2009), ISSN 00319007. 29, 32

[125] T. P. Purdy, R. W. Peterson and C. A. Regal: "Observation of Radiation Pressure Shot Noise on a Macroscopic Object", Science **339**, 801–804 (2013), ISSN 0036-8075. 29

[126] R. W. Peterson, T. P. Purdy, N. S. Kampel, R. W. Andrews, P. L. Yu, K. W. Lehnert and C. A. Regal: "Laser Cooling of a Micromechanical Membrane to the Quantum Backaction Limit", Physical Review Letters **116** (2016), ISSN 10797114. 29

[127] T. M. Karg, B. Gouraud, C. T. Ngai, G.-L. Schmid, K. Hammerer and P. Treutlein: "Light-mediated strong coupling between a mechanical oscillator and atomic spins 1 meter apart", Science **369**, 174–179 (2020), ISSN 0036-8075. 29, 42, 52, 53, 54, 102

[128] G.-L. Schmid, C. T. Ngai, M. Ernzer, M. B. Aguilera, T. M. Karg and P. Treutlein: "Coherent Feedback Cooling of a Nanomechanical Membrane with Atomic Spins", Physical Review X **12**, 011020 (2022), ISSN 2160-3308. 29

[129] D. J. Wilson: "Cavity Optomechanics with High-Stress Silicon Nitride Films", California Institute of Technology, PhD Thesis (2012). 32, 33

[130] V. Dumont, S. Bernard, C. Reinhardt, A. Kato, M. Ruf and J. C. Sankey: "Flexure-tuned membrane-at-the-edge optomechanical system", Optics Express **27**, 25731 (2019), ISSN 10944087. 32, 33

[131] M. Aspelmeyer, T. J. Kippenberg and F. Marquardt: *Cavity Optomechanics*, Springer-Verlag Berlin Heidelberg (2014), ISBN 978-3-642-55311-0. 34

[132] P. Rohse, J. Butlewski, F. Klein, T. Wagner, C. Friesen, A. Schwarz, R. Wiesendanger, K. Sengstock and C. Becker: "A cavity optomechanical locking scheme based on the optical spring effect", Review of Scientific Instruments **91** (2020), ISSN 10897623. 37, 38, 39

[133] K. Hammerer, A. S. Sørensen and E. S. Polzik: "Quantum interface between light and atomic ensembles", Reviews of Modern Physics **82**, 1041–1093 (2010), ISSN 0034-6861. 40

[134] C. Schellong: "Präparation und Manipulation von mF-Zuständen in einem mehrkomponentigen Bose-Einstein-Kondensat", Universität Hamburg, Bachelor Thesis (2019). 40

[135] J. Hahne: "Untersuchung von Faraday-Rotation zur Kopplung interner Freiheitsgrade eines BEC an einen nanomechanischen Oszillator", Universität Hamburg, Bachelor Thesis (2019). 40, 46, 50, 51

[136] C. Becker: "Multi component Bose-Einstein Condensates", Universität Hamburg, PhD Thesis (2008). 41

[137] M. Kubasik, M. Koschorreck, M. Napolitano, S. R. de Echaniz, H. Crepaz, J. Eschner, E. S. Polzik and M. W. Mitchell: "Polarization-based light-atom quantum interface with an all-optical trap", Physical Review A **79**, 043815 (2009), ISSN 1050-2947. 41, 45, 50, 52

[138] I. H. Deutsch and P. S. Jessen: "Quantum control and measurement of atomic spins in polarization spectroscopy", Optics Communications **283**, 681–694 (2010), ISSN 00304018. 42

[139] S. R. de Echaniz, M. Koschorreck, M. Napolitano, M. Kubasik and M. W. Mitchell: "Hamiltonian design in atom-light interactions with rubidium ensembles: A quantum-information toolbox", Physical Review A **77**, 032316 (2008), ISSN 1050-2947. 42, 43, 44

[140] M. Koschorreck: "Generation of Spin Squeezing in an Ensemble of Cold Rubidium 87", Universitat Politècnica de Catalunya, PhD Thesis (2010). 42

[141] J. M. Geremia, J. K. Stockton and H. Mabuchi: "Tensor polarizability and dispersive quantum measurement of multilevel atoms", Physical Review A **73**, 042112 (2006), ISSN 1050-2947. 43

[142] M. Kubasik: "Towards Spin Squeezing in Cold Atomic Ensembles", Universitat Politècnica de Catalunya, PhD Thesis (2009). 44, 126

[143] F. Dalfovo, S. Giorgini, L. P. Pitaevskii and S. Stringari: "Theory of Bose-Einstein condensation in trapped gases", Reviews of Modern Physics **71**, 463–512 (1999), ISSN 0034-6861. 45

[144] T. M. Karg: "Strong light-mediated coupling between a membrane oscillator and an atomic spin ensemble", Universität Basel, PhD Thesis (2020). 47, 54

[145] L.-M. Duan, J. I. Cirac, P. Zoller and E. S. Polzik: "Quantum Communication between Atomic Ensembles Using Coherent Light", Physical Review Letters **85**, 5643–5646 (2000), ISSN 0031-9007. 48

[146] J. H. Müller, P. Petrov, D. Oblak, C. L. G. Alzar, S. R. de Echaniz and E. S. Polzik: "Diffraction effects on light–atomic-ensemble quantum interface", Physical Review A **71**, 033803 (2005), ISSN 1050-2947. 49

[147] B. Q. Baragiola, L. M. Norris, E. Montaño, P. G. Mickelson, P. S. Jessen and I. H. Deutsch: "Three-dimensional light-matter interface for collective spin squeezing in atomic ensembles", Physical Review A **89**, 033850 (2014), ISSN 1050-2947. 49

[148] M. Hashimoto and M. Ohtsu: "Modulation transfer and optical Stark effect in a rubidium atomic clock pumped by a semiconductor laser", Journal of the Optical Society of America B **6**, 1777 (1989), ISSN 0740-3224. 50

[149] Y. Tsaturyan: "Ultracoherent soft-clamped mechanical resonators for quantum cavity optomechanics", University of Copenhagen, PhD Thesis (2019). 52

[150] P.-L. Yu, K. Cicak, N. S. Kampel, Y. Tsaturyan, T. P. Purdy, R. W. Simmonds and C. A. Regal: "A phononic bandgap shield for high- Q membrane microresonators", Applied Physics Letters **104**, 023510 (2014), ISSN 0003-6951. 52

[151] C. Genes, H. Ritsch, M. Drewsen and A. Dantan: "Atom-membrane cooling and entanglement using cavity electromagnetically induced transparency", Physical Review A **84**, 051801 (2011), ISSN 1050-2947. 54

[152] Z. Yi, G. xiang Li, S. ping Wu and Y. ping Yang: "Ground-state cooling of an oscillator in a hybrid atom-optomechanical system", Optics Express **22**, 20060 (2014), ISSN 1094-4087. 54

[153] F. Momeni and M. H. Naderi: "Atomic quadrature squeezing and quantum state transfer in a hybrid atom–optomechanical cavity with two Duffing mechanical oscillators", Journal of the Optical Society of America B **36**, 775 (2019), ISSN 0740-3224. 54

[154] F. Bariani, H. Seok, S. Singh, M. Vengalattore and P. Meystre: "Atom-based coherent quantum-noise cancellation in optomechanics", Physical Review A **92**, 043817 (2015), ISSN 1050-2947. 54

[155] N. Mann, M. R. Bakhtiari, A. Pelster and M. Thorwart: "Nonequilibrium Quantum Phase Transition in a Hybrid Atom-Optomechanical System", Physical Review Letters **120**, 063605 (2018), ISSN 0031-9007. 54

[156] N. Mann, A. Pelster and M. Thorwart: "Tuning the order of the nonequilibrium quantum phase transition in a hybrid atom-optomechanical system", New Journal of Physics **21**, 113037 (2019), ISSN 1367-2630.

[157] C. Gao and Z. Liang: "Steady-state phase diagram of quantum gases in a lattice coupled to a membrane", Physical Review A **99**, 013629 (2019), ISSN 2469-9926. 54

[158] D. J. Larson, J. C. Bergquist, J. J. Bollinger, W. M. Itano and D. J. Wineland: "Sympathetic cooling of trapped ions: A laser-cooled two-species nonneutral ion plasma", Physical Review Letters **57**, 70–73 (1986), ISSN 0031-9007. 55

[159] J. Schmidt, P. Weckesser, F. Thielemann, T. Schaetz and L. Karpa: "Optical Traps for Sympathetic Cooling of Ions with Ultracold Neutral Atoms", Physical Review Letters **124**, 053402 (2020), ISSN 0031-9007. 55

[160] F. Schreck, G. Ferrari, K. L. Corwin, J. Cubizolles, L. Khaykovich, M.-O. Mewes and C. Salomon: "Sympathetic cooling of bosonic and fermionic lithium gases towards quantum degeneracy", Physical Review A **64**, 011402 (2001), ISSN 1050-2947. 55

[161] M. Bohman, V. Grunhofer, C. Smorra, M. Wiesinger, C. Will, M. J. Borchert, J. A. Devlin, S. Erlewein, M. Fleck, S. Gavranovic, J. Harrington, B. Latacz, A. Mooser, D. Popper, E. Wursten, K. Blaum, Y. Matsuda, C. Ospelkaus, W. Quint, J. Walz and S. Ulmer: "Sympathetic cooling of a trapped proton mediated by an LC circuit", Nature **596**, 514–518 (2021), ISSN 0028-0836. 55

[162] A. Jöckel: "Sympathetic cooling of a membrane oscillator in a hybrid mechanical-atomic system", Universität Basel, PhD Thesis (2014). 56, 57, 59, 61

[163] I. H. Deutsch, R. J. C. Spreeuw, S. L. Rolston and W. D. Phillips: "Photonic band gaps in optical lattices", Physical Review A **52**, 1394–1410 (1995), ISSN 1050-2947. 65, 66

[164] G. Birkl, M. Gatzke, I. H. Deutsch, S. L. Rolston and W. D. Phillips: "Bragg Scattering from Atoms in Optical Lattices", Physical Review Letters **75**, 2823–2826 (1995), ISSN 0031-9007. 65

[165] M. Weidemüller, A. Görlitz, T. W. Hänsch and A. Hemmerich: "Local and global properties of light-bound atomic lattices investigated by Bragg diffraction", Physical Review A **58**, 4647–4661 (1998), ISSN 1050-2947. 65

[166] A. Xuereb, P. Domokos, J. Asbóth, P. Horak and T. Freegarde: "Scattering theory of cooling and heating in optomechanical systems", Physical Review A **79**, 053810 (2009), ISSN 1050-2947. 66

[167] M. Schlosshauer: *Decoherence and the Quantum-To-Classical Transition*, Springer Berlin Heidelberg (2007), ISBN 978-3-540-35773-5. 102

[168] C. F. Ockeloen-Korppi, E. Damskägg, J.-M. Pirkkalainen, M. Asjad, A. A. Clerk, F. Massel, M. J. Woolley and M. A. Sillanpää: "Stabilized entanglement of massive mechanical oscillators", Nature **556**, 478–482 (2018), ISSN 0028-0836. 102

[169] J.-M. Pirkkalainen, E. Damskägg, M. Brandt, F. Massel and M. Sillanpää: "Squeezing of Quantum Noise of Motion in a Micromechanical Resonator", Physical Review Letters **115**, 243601 (2015), ISSN 0031-9007. 102

[170] F. Lecocq, J. Clark, R. Simmonds, J. Aumentado and J. Teufel: "Quantum Nondemolition Measurement of a Nonclassical State of a Massive Object", Physical Review X **5**, 041037 (2015), ISSN 2160-3308. 102

[171] T. A. Palomaki, J. D. Teufel, R. W. Simmonds and K. W. Lehnert: "Entangling Mechanical Motion with Microwave Fields", Science **342**, 710–713 (2013), ISSN 0036-8075. 102

[172] A. P. Reed, K. H. Mayer, J. D. Teufel, L. D. Burkhart, W. Pfaff, M. Reagor, L. Sletten, X. Ma, R. J. Schoelkopf, E. Knill and K. W. Lehnert: "Faithful conversion of propagating quantum information to mechanical motion", Nature Physics **13**, 1163–1167 (2017), ISSN 1745-2473. 102

[173] P. Cohadon, a. Heidmann and M. Pinard: "Cooling of a Mirror by Radiation Pressure", Physical Review Letters **83**, 3174–3177 (1999), ISSN 0031-9007. 102

[174] D. J. Wilson, V. Sudhir, N. Piro, R. Schilling, A. Ghadimi and T. J. Kippenberg: "Measurement-based control of a mechanical oscillator at its thermal decoherence rate", Nature **524**, 325–329 (2015). 102

[175] H. M. Wiseman and G. J. Milburn: *Quantum Measurement and Control*, Cambridge University Press (2009), ISBN 978-0-521-80442-4. 102, 107, 110

[176] M. Rossi, D. Mason, J. Chen and A. Schliesser: "Observing and Verifying the Quantum Trajectory of a Mechanical Resonator", Physical Review Letters **123**, 163601 (2019), ISSN 0031-9007. 102

[177] V. B. Braginsky and Y. I. Vorontsov: "Quantum-mechanical limitations in macroscopic experiments and modern experimental technique", Soviet Physics Uspekhi **17**, 644–650 (1975), ISSN 0038-5670. 103

[178] K. S. Thorne, R. W. P. Drever, C. M. Caves, M. Zimmermann and V. D. Sandberg: "Quantum Nondemolition Measurements of Harmonic Oscillators", Physical Review Letters **40**, 667–671 (1978), ISSN 0031-9007. 103

[179] G. Vasilakis, H. Shen, K. Jensen, M. Balabas, D. Salart, B. Chen and E. S. Polzik: "Generation of a squeezed state of an oscillator by stroboscopic backaction-evading measurement", Nature Physics **11**, 389–392 (2015), ISSN 1745-2473. 104

[180] C. Ockeloen-Korppi, E. Damskägg, J.-M. Pirkkalainen, A. Clerk, M. Woolley and M. Sillanpää: "Quantum Backaction Evading Measurement of Collective Mechanical Modes", Physical Review Letters **117**, 140401 (2016), ISSN 0031-9007.

[181] V. Sudhir, R. Schilling, S. Fedorov, H. Schütz, D. Wilson and T. Kippenberg: "Quantum Correlations of Light from a Room-Temperature Mechanical Oscillator", Physical Review X **7**, 031055 (2017), ISSN 2160-3308. 104

[182] N. Kampel, R. Peterson, R. Fischer, P.-L. Yu, K. Cicak, R. Simmonds, K. Lehnert and C. Regal: "Improving Broadband Displacement Detection with Quantum Correlations", Physical Review X **7**, 021008 (2017), ISSN 2160-3308. 104

[183] J. B. Hertzberg, T. Rocheleau, T. Ndukum, M. Savva, A. A. Clerk and K. C. Schwab: "Back-action-evading measurements of nanomechanical motion", Nature Physics **6**, 213–217 (2010), ISSN 1745-2473. 104

[184] J. Suh, A. J. Weinstein, C. U. Lei, E. E. Wollman, S. K. Steinke, P. Meystre, A. A. Clerk and K. C. Schwab: "Mechanically detecting and avoiding the quantum fluctuations of a microwave field", Science **344**, 1262–1265 (2014), ISSN 0036-8075. 104

[185] I. Shomroni, L. Qiu, D. Malz, A. Nunnenkamp and T. J. Kippenberg: "Optical backaction-evading measurement of a mechanical oscillator", Nature Communications **10**, 2086 (2019), ISSN 2041-1723. 104

[186] J. T. Muhonen, G. R. L. Gala, R. Leijssen and E. Verhagen: "State preparation and tomography of a nanomechanical resonator with fast light pulses", Physical Review Letters **123**, 113601 (2019), ISSN 10797114. 104, 106, 119, 123

[187] G. R. L. Gala: "Glancing at tiny vibrations", Eindhoven University of Technology (2020), ISBN 9783540773405. 105, 106, 107

[188] J. Bennett: "Quantum optomechanics in the unresolved sideband regime", University of Queensland, PhD Thesis (2017). 106

[189] M. Fox: *Quantum Optics - An Introduction*, Oxford University Press (2006), ISBN 978–0–19–856672–4. 106

[190] D. T. Smithey, M. Beck, M. G. Raymer and A. Faridani: "Measurement of the Wigner distribution and the density matrix of a light mode using optical homodyne tomography: Application to squeezed states and the vacuum", Physical Review Letters **70**, 1244–1247 (1993), ISSN 0031-9007. 107

[191] U. Leonhardt: *Measuring the Quantum State of Light*, Cambridge University Press (1997), ISBN 0-521-49730-2. 107, 109

[192] F. Schwabl: *Quantum Mechanics*, Springer Berlin Heidelberg (2007), ISBN 978-3-540-71932-8. 107

[193] A. I. Lvovsky and M. G. Raymer: "Continuous-variable optical quantum-state tomography", Reviews of Modern Physics **81**, 299–332 (2009), ISSN 00346861. 109

[194] C. M. Caves and G. J. Milburn: "Quantum-mechanical model for continuous position measurements", Physical Review A **36**, 5543–5555 (1987), ISSN 0556-2791. 110

[195] R. Kumar, E. Barrios, A. MacRae, E. Cairns, E. Huntington and A. Lvovsky: "Versatile wideband balanced detector for quantum optical homodyne tomography", Optics Communications **285**, 5259–5267 (2012), ISSN 00304018. 113

[196] C. F. Klein: “Herstellung und Charakterisierung von Fasercavities zum Einsatz in MiM-Systemen”, Universität Hamburg, Bachelor Thesis (2018). 123

[197] W. Wieczorek, S. G. Hofer, J. Hoelscher-Obermaier, R. Riedinger, K. Hammerer and M. Aspelmeyer: “Optimal State Estimation for Cavity Optomechanical Systems”, Physical Review Letters **114**, 223601 (2015), ISSN 0031-9007. 124

[198] K. Ma, J. Kong, Y. Wang and X.-M. Lu: “Review of the Applications of Kalman Filtering in Quantum Systems”, Symmetry **14**, 2478 (2022), ISSN 2073-8994. 124

[199] M. Brunelli, D. Malz, A. Schliesser and A. Nunnenkamp: “Stroboscopic quantum optomechanics”, Physical Review Research **2** (2020), ISSN 2643-1564. 124

Danksagung

Ich möchte mich hier gerne bei allen bedanken, die mich im Verlauf meiner Doktorarbeit unterstützt und das Anfertigen der Arbeit ermöglicht haben.
Zunächst möchte ich mich bei den Professoren Klaus Sengstock und Roland Wiesendanger bedanken, für das entgegengebrachte Vertrauen, die vielen Freiheiten und die exzellenten Bedingungen, unter denen ich in den vergangenen Jahren an einem außerodentlich interessanten Projekt arbeiten durfte. Es hat mir immer viel Freude bereitet, auch wenn oder gerade weil wir stets neue Wege einschlagen mussten - dadurch habe ich viel gelernt. Weiterhin möchte ich mich für die Übernahme der Gutachten der Dissertation bedanken.
Ein großer Dank gilt der gesamten Arbeitsgruppe, deren Teil ich bereits seit meiner Masterarbeit sein durfte. Vielen Dank für die immerwährende Hilfsbereitschaft, die stets freundschaftliche Atmosphäre, die anregenden Diskussionen und die schöne gemeinsame Zeit auf Tagungen und Gruppenausfahrten nach Dänemark.
Ein besonderer Dank gebührt dem *NanoBEC*-Team und all seinen Mitgliedern mit denen ich über die Zeit zusammenarbeiten durfte - Philipp Rohse, Tobias Wagner, Clara Schellong, Josina Hahne, Cody Friesen, Felix Klein, Alexander Schwarz und Christoph Becker - Ich hatte viel Spaß mit Euch und konnte einiges von Euch lernen!
Besonders hervorheben möchte ich dabei Christoph Becker und Felix Klein, mit denen ich die meiste Zeit verbringen durfte:

Lieber Christoph, vielen Dank für die zahlreichen Diskussionen, unendlich vielen Ideen, das stets offene Ohr für alle Probleme und Fragen, die freundschaftlichen sowie professionellen Ratschläge, den Zuspruch sowie allen anderen Quatsch über den wir uns köstlich amüsiert haben!

Lieber Felix, Du hast die Zeit am Experiment für mich zu einer ganz besonderen gemacht. Ich bin unglaublich froh darüber, dass ich mit Dir zusammen arbeiten und mich immer wieder von Deiner unerschütterlichen positiven Ausstrahlung und Deiner Energie anstecken lassen durfte. Vielen Dank für die unzähligen gemeinsamen Stunden im Labor, am TiSa, am Cryo und wo wir sonst noch alleine verzweifelt wären - mit Dir schien keine Herausforderung zu groß. Vielen Dank auch für die nie endende moralische Unterstützung in der Endphase der Promotion.

Außerdem möchte ich mich bei meinen Freunden und meiner Familie bedanken, die mich immer unterstützt haben und viel Verständnis dafür hatten, dass ich gerade im letzten halben Jahr so gut wie keine Zeit für sie hatte. Vielen Dank für die vielen gemeinsamen Stunden, die ein wunderbarer Ausgleich und eine willkommene Abwechslung zur Arbeit waren.
Zu guter Letzt bin ich auch meiner Freundin Melina einen ganz besonders großen Dank schuldig, für die permanente Unterstützung und den Zuspruch in all den Jahren sowie das Aushalten all meiner Launen.